Science
AAAS

Supplementary Materials for

Synthesis of Triple Stranded Porphyrin Nanobelts

Arnau Rodríguez-Rubio,[1]† He Zhu,[1]† Ka Man Cheung,[1]† Igor Rončević,[2] Lene A. Gödde,[1] Janko Hergenhahn,[1] Joshua L. Field,[1] Prakhar Gupta,[1] Wojciech Stawski,[3] Henrik Gotfredsen,[1] Joseph Straw,[4] Matthew Edmondson,[4] James N. O'Shea,[4] Alex Saywell,[4]* and Harry L. Anderson[1]*

[1]Department of Chemistry, University of Oxford, Chemistry Research Laboratory, Oxford, UK
[2]Department of Chemistry, The University of Manchester, Oxford Road, Manchester, UK
[3] Institute of Organic Chemistry II and New Materials, Ulm University, Albert-Einstein-Allee 11, 89081 Ulm, Germany
[4]School of Physics & Astronomy, University of Nottingham, Nottingham, UK

† These authors contributed equally

*Correspondence to: harry.anderson@chem.ox.ac.uk, alex.saywell@nottingham.ac.uk

Table of Contents

Section 1. Compound Codes

Porphyrin oligomers are described by compound codes, as illustrated by the examples ***ls*-P2$_{tBu}$Br$_2$**, **P1$_{OOct}$Br$_2$** and **P1$_{MesBu}$Br$_2$**, drawn in Figure S1. The label '***ls***' denotes 'linear singly-linked' and is omitted for monomers (N = 1). Similarly, '***cf***' stands for 'cyclic fused'. The solubilizing side chain is indicated by a subscript (*e.g.* **OOct** for -OC$_8$H$_{17}$). Most compounds used in this work are Ni(II) porphyrins and in these cases the metal is omitted from the compound code; in cases where different metalloporphyrins are used it is indicated, e.g. **Zn-*ls*-P2$_{OOct}$**. The suffix **Br$_2$**, e.g. in ***ls*-P6$_{OOct}$Br$_2$**, indicates that terminal *meso* positions are brominated.

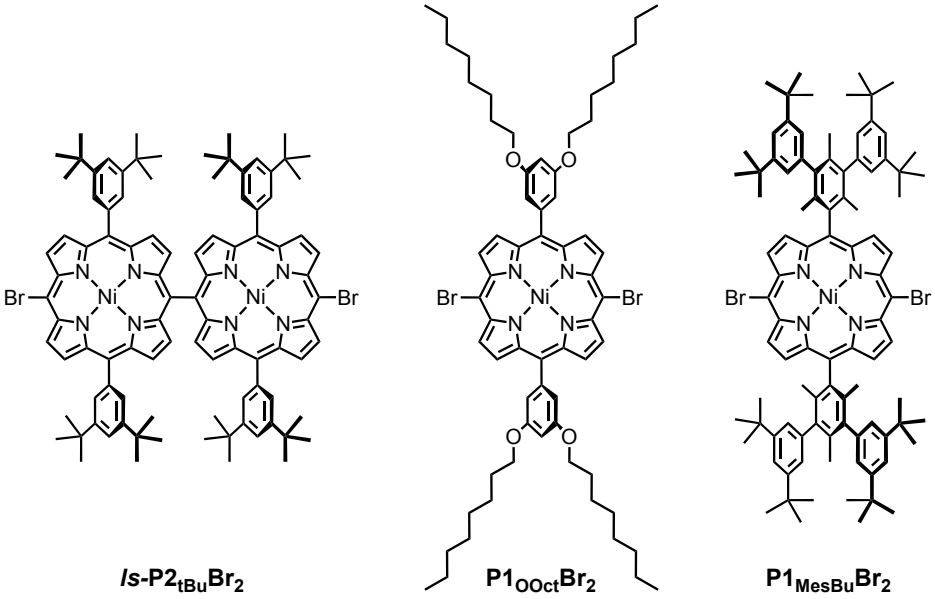

***ls*-P2$_{tBu}$Br$_2$** **P1$_{OOct}$Br$_2$** **P1$_{MesBu}$Br$_2$**

Figure S1. Examples of compound codes.

Section 2. General Methods

Commercially available reagents from Alfa Aesar, Fluorochem, Sigma Aldrich, Strem Chemicals and TCI were used as received. Reactions, unless otherwise stated, were carried out in oven-dried glassware under argon atmosphere. Anhydrous dichloromethane (DCM), *N*,*N*-dimethylformamide (DMF), toluene, tetrahydrofuran (THF), 1,4-dioxane and triethylamine (TEA) were purified by a MBraun MNSPS-5 Bench-Top solvent purification system under nitrogen atmosphere (H_2O content < 20 ppm as determined by Karl-Fischer titration). All other solvents used for extraction or flash column chromatography (silica gel: SiO_2, 60 Å, 40–63 μm) are HPLC grade and dried over appropriate drying agents when required. Thin layer chromatography (TLC) was carried out on aluminum-backed silica gel 60 F_{254} plates (Merck) and visualized under UV irradiation either at 254 or 365 nm. Petroleum ether (pet. ether) boiling point range of 40–60 °C was used for chromatography. Size exclusion chromatography (SEC) was carried out using Bio-Rad Bio-Beads S-X1 (1%, cross linkage, 40–80 μm bead size) under gravity. Evaporation of solvents was performed at 20–60 °C and 5–1010 mbar. Reported yield refer to pure compounds dried under high vacuum (< 0.1 mbar).

^{1}H and ^{13}C nuclear magnetic resonance (NMR) spectra were recorded on Bruker AVIII HD 400, AVIII HD 500 and a Bruker NEO 600 (with a broadband helium cryo-probe) spectrometers at 400 MHz, 500 MHz and 600 MHz (^{1}H) and 101 MHz, 126 MHz and 151 MHz (^{13}C), respectively at 298 K unless otherwise stated. ^{1}H NMR chemical shifts were reported in ppm to the nearest 0.01 ppm relative to $SiMe_4$ (δ = 0) and coupling constants (J) are in Hertz. Spectra were referenced internally to residual solvent protons in the deuterated solvent using the reported values (δ = 5.32 for dichloromethane-d_2, 7.26 for chloroform-d and 2.09 for tolune-d_8). Multiplicities are reported in

accordance with the following: s = singlet; d = doublet; dd = doublet of doublet; t = triplet and m = multiplet. ^{13}C chemical shifts were reported in ppm to the nearest 0.1 ppm relative to $SiMe_4$ ($\delta = 0$) and were referenced internally with respect to carbons in the solvents ($\delta = 53.8$ for dichloromethane-*d2*, 77.2 for chloroform-*d* and 20.4 for toluene-*d8*). ^1H assignments were made using 2D NMR methods (COSY, NOESY, HSQC, HMBC).

MALDI-ToF MS spectra were measured using Bruker MALDI Autoflex Speed spectrometer utilizing *trans*-2-[3-(4-*tert*-butylphenyl-2-methyl-2-propenylidene]malononitrile (DCTB) as matrix.

UV−vis−NIR spectra in solution were recorded with a Perkin-Elmer Lambda 20 with temperature control by a PTP-1 Peltier unit or a JASCO V-770 spectrometer using Infrasil® Quartz 1 cm cuvettes at 298 K. UV−vis−NIR−MIR spectra were recorded with JASCO V-770 spectrometer with a pathlength of 1 cm at 298 K.

Recycling GPC was carried out either on a Shimadzu recycling GPC system equipped with a LC-20 AD pump, SPD-20A UV detector and a set of JAIGEL 3H (20 × 600 mm) and JAIGEL 4H (20 × 600 mm) columns in toluene + 1% pyridine as eluent at a flow rate of 3.5 mL min^{-1}; or on a JAIGEL LaboACE LC-7080Plus equipped with a P-LA80 pump, UV-vis 4ch 800LA detector and a set of JAIGEL 3HR (20 × 600 mm) and JAIGEL 4HR (20 × 600 mm) columns in toluene + 1% pyridine as eluent at a flow rate of 10.0 mL min^{-1}. Analytical GPC was carried out on an Agilent 1260 Infinity II LC system equipped with a 1260 Iso Pump, G1315C DAD and a set of JAIGEL 3HA (8 × 500 mm) and JAIGEL 4HA (8 × 500 mm) columns in THF + pyridine 1% as eluent at a flow of 1.0 mL min^{-1}.

Section 3. Synthesis of Previously Reported Compounds

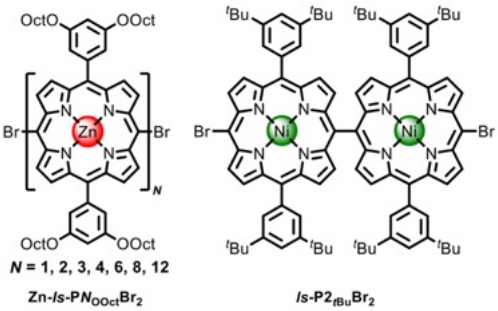

Figure S2. Structures of previously reported compounds used in this study.

Zn-*ls*-P*N*$_{OOct}$Br$_2$ (*37*) and ***ls*-P2$_{tBu}$Br$_2$** (*51*) were synthesized as previously reported.

Section 4. Synthetic Procedures and Compound Characterization

Section 4.1. Synthesis of *ls*-P*N*Br$_2$ oligomers

Zn-P1$_{OOct}$Bpin$_2$

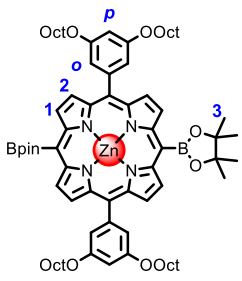

To a Schlenk flask under argon charged with **Zn-P1$_{OOct}$Br$_2$** (150 mg, 0.125 mmol) and $PdCl_2(PPh_3)_2$ (17.6 mg, 25.1 µmol) was added dry THF (14 mL) and dry NEt_3 (0.35 mL), which had been previously subjected to three rounds of freeze-pump-thaw degassing. To this was added pinacol borane (0.73 mL, 5.0 mmol) and the reaction stirred at 60 °C for 2 hours. The mixture was then passed through a short silica plug using $CHCl_3$ as the eluent, followed by SEC (toluene eluent) to remove excess pinacol borane. The crude mixture was then purified by flash column chromatography on silica gel petrol ether/CH_2Cl_2 (1:1) to give **Zn-P1$_{OOct}$Bpin$_2$** as a purple powder (68.8 mg, 42%).

^{1}H NMR (600 MHz, $CDCl_3$) δ_H 9.92 (d, J = 4.6 Hz, 4H, $\mathbf{H_1}$), 9.21 (d, J = 4.6 Hz, 4H, $\mathbf{H_2}$), 7.39 (d, J = 2.3 Hz, 4H, $\mathbf{H_o}$), 6.91 (t, J = 2.3 Hz, 2H, $\mathbf{H_p}$), 4.13 (t, J = 6.6 Hz, 8H, $\mathbf{H_{Oct}}$), 1.85 (m, 32H, $\mathbf{H_{Oct}}$, $\mathbf{H_3}$), 1.55 – 1.48 (m, 8H, $\mathbf{H_{Oct}}$), 1.41 – 1.25 (m, 32H, $\mathbf{H_{Oct}}$), 0.87 (t, J = 6.9 Hz, 12H, $\mathbf{H_{Oct}}$).

^{13}C NMR (151 MHz, $CDCl_3$) δ_C 158.2, 153.4, 149.9, 144.7, 132.8, 132.5, 120.6, 114.4, 101.2, 85.2, 68.4, 31.8, 29.4, 29.4, 29.3, 26.1, 25.4, 22.7, 14.1.

MALDI-TOF *m/z* 1289.042, ($C_{76}H_{106}B_2N_4O_8Zn$, M^+ requires 1289.75)

***ls*-P2$_{OOct}$Br$_2$**

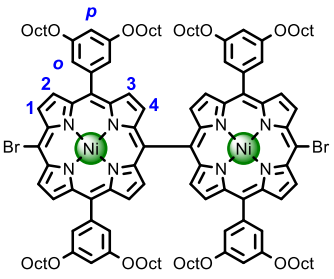

To a solution of **Zn-*ls*-P2$_{OOct}$Br$_2$** (400 mg, 0.18 mmol) in CH_2Cl_2 (24 mL) in an ice bath (0 °C) was added TFA (0.27 mL, 3.6 mmol, 20 equiv.). The reaction mixture was stirred at 0 °C until full demetallation of starting material was observed by MS analysis (usually around 30 min), followed by addition of triethylamine (1.0 mL) to quench the excess TFA. The resulting mixture was filtered on silica using pentane/CH_2Cl_2 (1:1) as eluent. Crude **H$_2$-*ls*-P2$_{OOct}$Br$_2$** and Ni(acac)$_2$ (530 mg, 1.8 mmol, 10 equiv.) in 1,3-xylene (10 mL) was evacuated and backfilled with argon three times, followed by stirring at 130 °C under argon for 2 h. The resulting mixture was concentrated and purified by flash column chromatography on silica gel using pentane/CH_2Cl_2 (1:1) as eluent to give the desired product ***ls*-P2$_{OOct}$Br$_2$** (339 mg, 86% over two steps).

^{1}H NMR (600 MHz, $CDCl_3$) δ_H 9.57 (d, J = 5.0 Hz, 4H, $\mathbf{H_1}$), 8.94 (d, J = 5.0 Hz, 4H, $\mathbf{H_2}$), 8.58 (d, J = 5.0 Hz, 4H, $\mathbf{H_3}$), 7.97 (d, J = 5.0 Hz, 4H, $\mathbf{H_4}$), 7.13 (d, J = 2.3 Hz, 8H, $\mathbf{H_o}$), 6.74 (t, J = 2.3 Hz, 4H, $\mathbf{H_p}$), 4.01 (t, J = 6.6 Hz, 16H, $\mathbf{H_{Oct}}$), 1.78 (m, 16H, $\mathbf{H_{Oct}}$), 1.45 – 1.40 (m, 16H, $\mathbf{H_{Oct}}$), 1.33 – 1.17 (m, 64H, $\mathbf{H_{Oct}}$), 0.81 (t, J = 6.9 Hz, 24H, $\mathbf{H_{Oct}}$).

^{13}C NMR (151 MHz, $CDCl_3$) δ_C 158.5, 147.0, 143.5, 142.4, 142.3, 142.0, 134.1, 133.4, 133.3, 132.9, 129.8, 120.3, 115.8, 113.4, 103.1, 101.2, 68.3, 31.8, 29.3, 29.3, 29.2, 26.0, 22.6, 14.0.

MALDI-ToF *m/z* = 2215.133 ($C_{128}H_{164}Br_2N_8Ni_2O_8$, M^+ requires 2214.974)

UV-vis (CH_2Cl_2, 298 K) λ_{max} (ε / 10^4 M^{-1} cm^{-1}): 421 (16.4), 447 (17.5), 539 (3.92)

***ls*-P3$_{OOct}$Br$_2$**

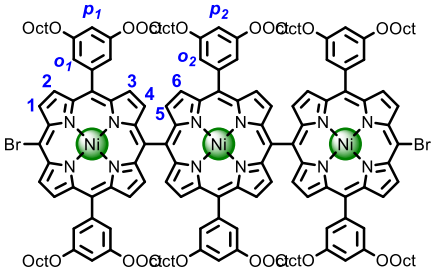

To a solution of **Zn-*ls*-P3$_{OOct}$Br$_2$** (28 mg, 8.6 µmol) in CH_2Cl_2 (1.1 mL) in an ice bath (0 °C) was added TFA (13 µL, 171 µmol, 20 equiv.). The reaction mixture was stirred at 0 °C until full demetallation of starting material was observed by MS analysis (usually around 30 min), followed by addition of triethylamine (1.0 mL) to quench the excess TFA. The resulting mixture was filtered on silica using pentane/CH_2Cl_2 (1:1) as eluent. Crude **H$_2$-*ls*-P3$_{OOct}$Br$_2$** and Ni(acac)$_2$ (38 mg, 0.13 mmol, 15 equiv.) in 1,3-xylene (2.0 mL) was evacuated and backfilled with argon three times, followed by stirring at 130 °C under argon for 2 h. The resulting mixture was concentrated and purified by flash column chromatography on silica gel using pentane/CH_2Cl_2 (1:1) as eluent to give the desired product ***ls*-P3$_{OOct}$Br$_2$** (26 mg, 93% over two steps).

^{1}H NMR (600 MHz, $CDCl_3$) δ_H 9.59 (d, J = 4.9 Hz, 4H, $\mathbf{H_1}$), 8.96 (d, J = 4.9 Hz, 4H, $\mathbf{H_2}$), 8.67 (d, J = 5.0 Hz, 4H, $\mathbf{H_6}$), 8.63 (d, J = 4.9 Hz, 4H, $\mathbf{H_3}$), 8.12 – 8.01 (m, 8H, $\mathbf{H_4}$, $\mathbf{H_5}$), 7.20 – 7.15 (m, 12H, $\mathbf{H_{o1}}$, $\mathbf{H_{o2}}$), 6.76 (t, J = 2.3 Hz, 4H, $\mathbf{H_{p1}}$), 6.66 (t, J = 2.4 Hz, 2H, $\mathbf{H_{p2}}$), 4.03 (t, J = 6.6 Hz, 16H, $\mathbf{H_{Oct}}$), 3.94 (t, J = 6.5 Hz, 8H, $\mathbf{H_{Oct}}$), 1.80 (p, J = 6.7 Hz, 16H, $\mathbf{H_{Oct}}$), 1.70 (p, J = 6.7 Hz, 8H, $\mathbf{H_{Oct}}$), 1.48 – 1.40 (m, 16H, $\mathbf{H_{Oct}}$), 1.37 – 1.09 (m, 104H, $\mathbf{H_{Oct}}$), 0.82 (t, J = 6.9 Hz, 24H, $\mathbf{H_{Oct}}$), 0.75 (t, J = 6.8 Hz, 12H, $\mathbf{H_{Oct}}$).

^{13}C NMR (151 MHz, $CDCl_3$) δ_C 158.7, 158.6, 147.3, 146.9, 142.9, 142.6, 142.5, 142.2, 134.4, 134.1, 133.5, 133.4, 133.0, 132.5, 130.2, 129.9, 120.8, 120.4, 116.5, 116.3, 113.5, 113.4, 103.3, 101.3, 101.2, 68.5, 68.4, 31.9, 31.8, 29.5, 29.4, 29.4, 29.4, 29.3, 29.3, 26.2, 26.1, 22.8, 22.7, 14.2, 14.1.

MALDI-ToF *m/z* = 3246.858 ($C_{192}H_{246}Br_2N_{12}Ni_3O_{12}$, M^+ requires 3249.543)

UV-vis (CH_2Cl_2, 298 K) λ_{max} (ε / 10^4 M^{-1} cm^{-1}): 416 (15.1), 463 (15.0), 544 (4.81)

_ls_-P4$_{OOct}$Br$_2$

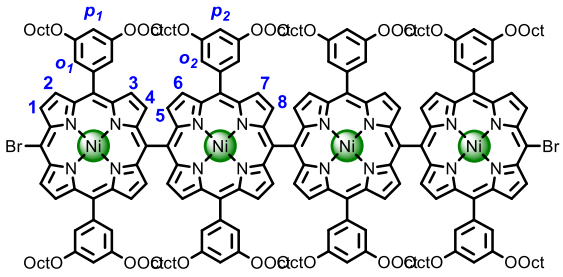

To a solution of **Zn-_ls_-P4$_{OOct}$Br$_2$** (39 mg, 9.0 µmol) in CH_2Cl_2 (5.0 mL) in an ice bath (0 °C) was added TFA (28 µL, 360 µmol, 40 equiv.). The reaction mixture was stirred at 0 °C until full demetallation of starting material was observed by MS analysis (usually around 30 min), followed by addition of triethylamine (1.0 mL) to quench the excess TFA. The resulting mixture was filtered on silica using pentane/CH_2Cl_2 (1:1) as eluent. Crude **H$_2$-_ls_-P4$_{OOct}$Br$_2$** and Ni(acac)$_2$ (53 mg, 0.18 mmol, 20 equiv.) in 1,3-xylene (5.0 mL) was evacuated and backfilled with argon three times, followed by stirring at 130 °C under argon for 2 h. The resulting mixture was concentrated and purified by flash column chromatography on silica gel using pentane/CH_2Cl_2 (1:1) as eluent to give the desired product **_ls_-P4$_{OOct}$Br$_2$** (27 mg, 70% over two steps).

^{1}H NMR (600 MHz, $CDCl_3$) δ_H 9.60 (d, J = 5.1 Hz, 4H, **H$_1$**), 8.97 (d, J = 5.0 Hz, 4H, **H$_2$**), 8.73 (d, J = 4.9 Hz, 4H, **H$_6$**), 8.70 (d, J = 5.0 Hz, 4H, **H$_7$**), 8.65 (d, J = 4.9 Hz, 4H, **H$_3$**), 8.19 (d, J = 5.0 Hz, 4H, **H$_5$**), 8.11 (d, J = 5.0 Hz, 4H, **H$_4$**), 8.10 (d, J = 5.0 Hz, 4H, **H$_8$**), 7.21 (d, J = 2.2 Hz, 8H, **H$_{o2}$**), 7.18 (d, J = 2.3 Hz, 8H, **H$_{o1}$**), 6.77 (t, J = 2.3 Hz, 4H, **H$_{p1}$**), 6.69 (t, J = 2.3 Hz, 4H, **H$_{p2}$**), 4.04 (t, J = 6.6 Hz, 16H, **H$_{Oct}$**), 3.97 (t, J = 6.6 Hz, 16H, **H$_{Oct}$**), 1.81 (p, J = 6.7 Hz, 16H, **H$_{Oct}$**), 1.73 (p, J = 6.7 Hz, 16H, **H$_{Oct}$**), 1.48 – 1.09 (m, 160H, **H$_{Oct}$**), 0.91 – 0.81 (m, 24H, **H$_{Oct}$**), 0.76 (t, J = 6.9 Hz, 24H, **H$_{Oct}$**).

MALDI-ToF m/z = 4277.913 ($C_{256}H_{328}Br_2N_{16}Ni_4O_{16}$, M^+ requires 4278.112)

UV-vis (CH_2Cl_2, 298 K) λ_{max} (ε / 10^4 M^{-1} cm^{-1}): 415 (7.30), 470 (7.31), 534 (2.48), 562 (3.43)

_ls_-P6$_{OOct}$Br$_2$

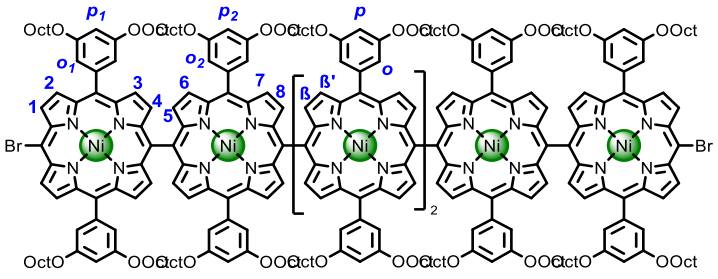

To a solution of **Zn-_ls_-P6$_{OOct}$Br$_2$** (40 mg, 6.2 µmol) in CH_2Cl_2 (1.8 mL) in an ice bath (0 °C) was added TFA (0.6 mL). The reaction mixture was stirred at 0 °C until full demetallation of starting material was observed by MS analysis (usually around 30 min), followed by addition of triethylamine (1.0 mL) to quench the excess TFA. The resulting mixture was filtered on silica using pentane/CH_2Cl_2 (1:1) as eluent. Crude **H$_2$-_ls_-P6$_{OOct}$Br$_2$** and Ni(acac)$_2$ (100 mg, 341 µmol, 55 equiv.) in 1,3-xylene (1.8 mL) was evacuated and backfilled with argon three times, followed by stirring at 130 °C under argon for 2 h. The resulting mixture was concentrated and purified by flash column chromatography on silica gel using pentane/CH_2Cl_2 (1:1) as eluent to give the desired product **_ls_-P6$_{OOct}$Br$_2$** (28 mg, 70% over two steps).

^{1}H NMR (600 MHz, $CDCl_3$) δ_H 9.61 (d, J = 5.0 Hz, 4H, **H$_1$**), 8.98 (d, J = 5.0 Hz, 4H, **H$_2$**), 8.80 – 8.75 (m, 12H, **H$_7$**, **H$_{ß'}$**), 8.72 (d, J = 5.0 Hz, 4H, **H$_6$**), 8.67 (d, J = 4.9 Hz, 4H, **H$_3$**), 8.27 – 8.21 (m, 12H, **H$_8$**, **H$_ß$**), 8.13 (d, J = 5.0 Hz, 4H, **H$_5$**), 8.11 (d, J = 4.9 Hz, 4H, **H$_4$**), 7.27 (d, J = 1.9 Hz, 8H, **H$_o$**), 7.23 (d, J = 2.3 Hz, 8H, **H$_{o2}$**), 7.20 (d, J = 2.2 Hz, 8H, **H$_{o1}$**), 6.79 (t, J = 2.3 Hz, 4H, **H$_{p1}$**), 6.72 (t, J = 2.2 Hz, 4H, **H$_p$**), 6.70 (t, J = 2.3 Hz, 4H, **H$_{p2}$**), 4.11 – 3.93 (m, 48H, **H$_{Oct}$**), 1.88 – 1.70 (m, 48H, **H$_{Oct}$**), 1.51 – 1.13 (m, 240H, **H$_{Oct}$**), 0.86 – 0.74 (m, 72H, **H$_{Oct}$**).

^{13}C NMR (151 MHz, $CDCl_3$) δ_C 158.7, 158.6, 158.6, 147.4, 147.2, 147.2, 147.0, 143.7, 143.0, 143.0, 142.7, 142.6, 142.3, 134.5, 134.3, 134.1, 133.5, 133.4, 133.1, 132.6, 120.9, 120.5, 116.9, 116.9, 116.8, 116.6, 116.3, 113.5, 113.5, 103.3, 101.4, 101.3, 68.5, 68.4, 68.4, 31.9, 31.9, 29.5, 29.5, 29.5, 29.4, 29.4, 29.3, 26.2, 26.2, 22.8, 22.7, 14.2, 14.2.

MALDI-ToF m/z = 6334.393 ($C_{384}H_{492}Br_2N_{24}Ni_6O_{24}$, M^+ requires 6337.257)

UV-vis (CH_2Cl_2, 298 K) λ_{max} (ε / 10^4 M^{-1} cm^{-1}): 413 (40.1), 478 (43.4), 549 (20.4), 582 (8.75)

***ls*-P12$_{OOct}$Br$_2$**

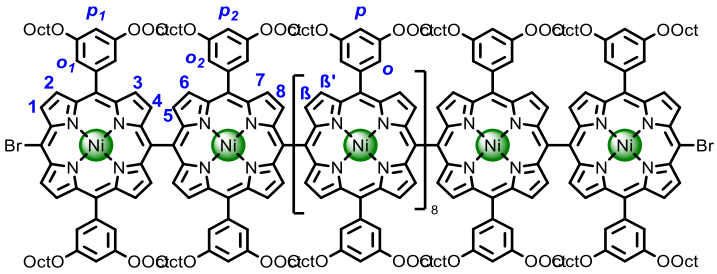

To a solution of **Zn-*ls*-P12$_{OOct}$Br$_2$** (33 mg, 2.6 μmol) in CH_2Cl_2 (0.5 mL) in an ice bath (0 °C) was added TFA (0.35 mL). The reaction mixture was stirred at 0 °C until full demetallation of starting material was observed by MS analysis (usually around 30 min), followed by addition of triethylamine (1.0 mL) to quench the excess TFA. The resulting mixture was filtered on silica using pentane/CH_2Cl_2 (1:1) as eluent. Crude **H$_2$-*ls*-P12$_{OOct}$Br$_2$** and Ni(acac)$_2$ (46 mg, 157 μmol, 60 equiv.) in 1,3-xylene (0.6 mL) was evacuated and backfilled with argon three times, followed by stirring at 130 °C under argon for 2 h. The resulting mixture was concentrated and purified by flash column chromatography on silica gel using pentane/CH_2Cl_2 (1:1) as eluent to give the desired product ***ls*-P12$_{OOct}$Br$_2$** (31 mg, 94% over two steps).

^{1}H NMR (600 MHz, $CDCl_3$) δ_H 9.63 (d, J = 4.9 Hz, 4H, **H$_1$**), 9.00 (d, J = 4.9 Hz, 4H, **H$_2$**), 8.86 – 8.76 (m, 36H, **H$_7$**, **H$_{ß'}$**), 8.73 (d, J = 5.0 Hz, 4H, **H$_6$**), 8.69 (d, J = 4.9 Hz, 4H, **H$_3$**), 8.31 – 8.23 (m, 36H, **H$_8$**, **H$_ß$**), 8.15 (d, J = 4.9 Hz, 4H, **H$_5$**), 8.13 (d, J = 4.9 Hz, 4H, **H$_4$**), 7.36 – 7.27 (m, 32H, **H$_o$**), 7.25 (d, J = 2.4 Hz, 8H, **H$_{o2}$**), 7.22 (d, J = 2.3 Hz, 8H, **H$_{o1}$**), 6.80 (t, J = 2.3 Hz, 4H, **H$_{p1}$**), 6.78 – 6.73 (m, 16H, **H$_p$**), 6.72 (t, J = 2.3 Hz, 4H, **H$_{p2}$**), 4.12 – 3.95 (m, 96H, **H$_{Oct}$**), 1.87 – 1.73 (m, 96H, **H$_{Oct}$**), 1.51 – 1.15 (m, 480H, **H$_{Oct}$**), 0.89 – 0.77 (m, 144H, **H$_{Oct}$**).

^{13}C NMR (151 MHz, $CDCl_3$) δ_C 158.7, 158.7, 158.6, 147.4, 147.2, 147.0, 143.7, 143.1, 143.0, 142.7, 142.6, 142.3, 134.4, 134.1, 133.6, 133.4, 133.1, 132.6, 120.9, 120.9, 120.5, 116.9, 116.6, 116.3, 113.5, 113.5, 103.3, 101.4, 101.3, 68.5, 68.4, 68.4, 31.9, 31.9, 31.9, 29.5, 29.5, 29.5, 29.4, 29.4, 29.3, 29.3, 26.2, 26.2, 26.2, 22.8, 22.7, 22.7, 14.2, 14.2, 14.2.

MALDI-ToF m/z = 12527.396 ($C_{768}H_{984}Br_2N_{48}Ni_{12}O_{48}$, M^+ requires 12519.672)

UV-vis (CH_2Cl_2, 298 K) λ_{max} (ε / 10^4 M^{-1} cm^{-1}): 410 (61.5), 483 (72.0), 552 (38.3), 585 (18.6)

MesBu-aldehyde

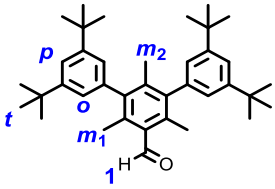

1-Bpin-3,5-di-*tert*-butylbenzene (2.5 g, 7.8 mmol, 2.4 equiv.), 3,5-dibromo-2,4,6-trimethylbenzaldehyde (1.00 g, 3.3 mmol, 1 equiv.) and Sphos G2 Pd (235 mg, 326.8 μmol, 0.1 equiv.) were mixed in a 500 mL two-neck round bottom flask and it was evacuated and backfilled with argon for three times before the addition of 1,4-dioxane (0.21 L). A 2M solution of K_3PO_4 (27.8 g, 40 equiv., 130 mmol) in water (42 mL) was sparged for 1 h. The solution was heated to 80 °C and the degassed K_3PO_4 solution was added into the mixture. The reaction proceeded at 80 °C for 2 h with stirring and monitored by TLC (pet. ether/dichloromethane, v/v, 4:1) until all the starting materials had been consumed, at which point the solution was allowed to cool to room temperature. The crude reaction solution was concentrated and diluted with dichloromethane (30 mL). The organic phase was extracted and washed twice with water (100 mL × 2) and dried over Na_2SO_4. The residue was purified through a silica column chromatography (pet. ether/ dichloromethane, *v/v*, 4:1). **MesBu-aldehyde** (0.89 g, 52%) was yielded as a white solid.

^{1}H NMR (600 MHz, $CDCl_3$) δ_H 10.71 (s, 1H, **H$_1$**), 7.37 (t, J = 1.9 Hz, 2H, **H$_p$**), 6.99 (d, J = 1.8 Hz, 4H, **H$_o$**), 2.26 (s, 6H, **H$_{m1}$**), 1.70 (s, 3H, **H$_{m2}$**), 1.34 (s, 36H, **H$_t$**).

^{13}C NMR (151 MHz, $CDCl_3$) δ_C 195.58, 151.09, 142.69, 140.43, 139.89, 137.09, 132.14, 123.69, 120.36, 35.06, 31.68, 20.55, 17.88.

HR MS: m/z = 525.4088 ($C_{38}H_{52}O$, $[M+H]^+$ requires 525.4091)

H_2-P1$_{MesBu}$

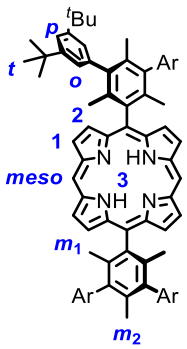

Dipyrromethane (0.33 g, 2.3 mmol, 2.0 equiv.) and **MesBu-aldehyde** (1.2 g, 2.3 mmol, 2.0 equiv.) were added into a 1 L round-bottom flask followed by chloroform (356 mL) and the solution was degassed with argon for 20 min. Boron trifluoride etherate (BF_3OEt_2, 0.19 mL, 1.5 mmol, 1.3 equiv.) was added dropwise, and the reaction was stirred in the dark for 3 h. DDQ (771 mg, 3.4 mmol, 3.0 equiv.) was added and the mixture was stirred for another 20 minutes. The reaction was quenched by the addition of triethylamine (3.6 mL). The solution was then concentrated under reduced pressure and purified by a silica column chromatography (pet. ether/dichloromethane, *v/v*, 4:1) to yield **P1$_{MesBu}$** (0.485 g, 33%) as a red-purple solid.

^{1}H NMR (600 MHz, $CDCl_3$) δ_H 10.23 (s, 2H, **H$_{meso}$**), 9.39 (d, J = 4.5 Hz, 4H, **H$_1$**), 9.15 (d, J = 4.5 Hz, 4H, **H$_2$**), 7.36 (t, J = 1.9 Hz, 4H, **H$_p$**), 7.33 (d, J = 1.9 Hz, 8H, **H$_o$**), 2.03 (s, 6H, **H$_{m2}$**), 1.55 (s, 12H, **H$_{m1}$**), 1.38 (s, 72H, **H$_t$**), –2.96 (s, 2H, **H$_3$**).

^{13}C NMR (151 MHz, $CDCl_3$) δ_C 150.73, 141.40, 140.78, 138.33, 136.69, 134.46, 131.91, 130.49, 124.19, 119.93, 118.98, 104.70, 35.10, 31.80, 20.80, 20.05.

MALDI-ToF *m/z* = 1299.933 ($C_{94}H_{114}N_4$, M^+ requires 1299.901)

Zn-P1$_{MesBu}$

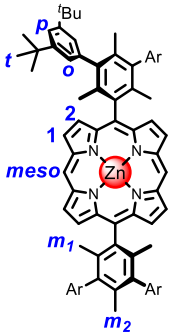

H_2-P1$_{MesBu}$ (0.70 g, 0.54 mmol, 1.0 equiv.) was dissolved again in chloroform (30 mL) and zinc acetate dihydrate (0.24 g, 1.1 mmol, 2.0 equiv.) in methanol (5mL) was added. The mixture was stirred in room temperature under atmosphere for 3 hours. Subsequently, the solvent was removed and the residue was purified by a silica column chromatography (pet. ether/dichloromethane, *v/v*, gradient elution from 10:1 to 6:1). The product **Zn-P1$_{MesBu}$** was obtained as pink solid (0.70 g, 95%).

^{1}H NMR (400 MHz, $CDCl_3$) δ_H 10.25 (s, 2H, **H$_{meso}$**), 9.45 (d, J = 4.4 Hz, 4H, **H$_1$**), 9.23 (d, J = 4.4 Hz, 4H, **H$_2$**), 7.36 – 7.34 (m, 12H, **H$_o$**, **H$_p$**), 2.04 (s, 6H, **H$_{m2}$**), 1.53 (s, 12H, **H$_{m1}$**), 1.38 (s, 72H, **H$_t$**).

^{13}C NMR (101 MHz, CD_2Cl_2) δ_C 150.83, 150.50, 149.69, 141.68, 140.80, 139.63, 136.63, 134.18, 132.21, 131.82, 124.33, 120.08, 119.94, 105.69, 35.14, 31.84, 20.75, 19.99.

MALDI-ToF *m/z* = 1360.808 ($C_{94}H_{112}N_4Zn$, M^+ requires 1360.849)

P1$_{MesBu}$

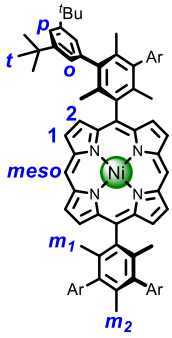

H_2-P1$_{MesBu}$ (0.71 g, 0.54 mmol, 1 equiv.) and $Ni(acac)_2(H_2O)_2$ (0.79 g, 2.71 mmol, 5 equiv.) were added into a 100 mL round-bottom flask followed by the addition of *m*-xylene (50 mL). The mixture was stirred at 130 °C overnight and the reaction was monitored by TLC (pet. ether/dichloromethane, *v/v*, 5:1). The resulting solution was concentrated under reduced pressure and purified through a short silica plug (pet. ether/dichloromethane, *v/v*, 5:1) to yield **P1$_{MesBu}$** (0.55 g, 76%) as a red-purple solid.

^{1}H NMR (600 MHz, $CDCl_3$) δ_H 9.93 (s, 2H, **H$_{meso}$**), 9.22 (d, J = 4.7 Hz, 4H, **H$_1$**), 9.05 (d, J = 4.6 Hz, 4H, **H$_2$**), 7.35 (t, J = 1.9 Hz, 4H, **H$_p$**), 7.29 (d, J = 1.9 Hz, 8H, **H$_o$**), 1.99 (s, 6H, **H$_{m2}$**), 1.49 (s, 12H, **H$_{m1}$**), 1.37 (s, 72H, **H$_t$**).

^{13}C NMR (151 MHz, $CDCl_3$) δ_C 150.69, 143.24, 142.87, 141.34, 140.75, 138.13, 136.30, 134.32, 132.41, 131.78, 124.23, 119.88, 118.40, 104.92, 35.09, 31.77, 20.46, 19.98.

MALDI-ToF *m/z* = 1354.770 ($C_{94}H_{112}N_4Ni$, M^+ requires 1354.814)

$P1_{MesBu}Br_2$

$P1_{MesBu}$ (125 mg, 92 μmol, 1.0 equiv.) was added into a 250 mL round-bottom flask followed by the addition of dichloromethane (50 mL) with pyridine (0.5 mL). It was cooled to 0 °C in an ice bath and to the stirred mixture, a solution of N-bromosuccinimide (36.1 mg, 203 μmol, 2.2 equiv.) in dichloromethane (10 mL) was added dropwise. The reaction mixture was stirred at 0 °C for 15 minutes, then acetone (10 mL) was added to quench the excess N-bromosuccinimide. The resulting mixture was concentrated under reduced pressure and purified by a silica plug (chloroform) to yield **$P1_{MesBu}Br_2$** (130 mg, 93%).

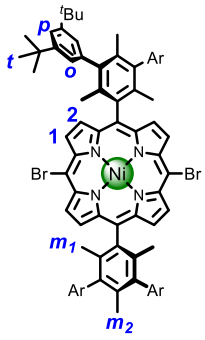

^{1}H NMR (600 MHz, $CDCl_3$) δ_H 9.50 (d, J = 4.9 Hz, 4H, $\mathbf{H_1}$), 8.85 (d, J = 4.9 Hz, 4H, $\mathbf{H_2}$), 7.35 (t, J = 1.9 Hz, 4H, $\mathbf{H}_p$), 7.25 (d, J = 1.9 Hz, 8H, $\mathbf{H}_o$), 1.96 (s, 6H, $\mathbf{H}_{m2}$), 1.49 (s, 12H, $\mathbf{H}_{m1}$), 1.36 (s, 72H, $\mathbf{H}_t$).

^{13}C NMR (151 MHz, $CDCl_3$) δ_C 150.77, 143.67, 143.06, 141.07, 140.85, 137.22, 136.09, 134.70, 133.90, 133.20, 124.13, 120.17, 119.97, 102.78, 35.09, 31.76, 20.45, 19.96.

MALDI-ToF m/z = 1514.285 ($C_{94}H_{110}N_4NiBr_2$, M^+ requires 1514.628)

Zn-*ls*-$P2_{MesBu}$

Zn-$P1_{MesBu}$ (705 mg, 517 μmol, 1 equiv.) was dissolved in dichloromethane (85 mL). Bis(trifluoroacetoxy)iodobenzene (111 mg, 259 μmol, 0.5 equiv.) was added to the solution. The mixture kept stirring at room temperature for 40 minutes. Then, sodium borohydride (196 mg, 5.17 mmol, 10 equiv.) in methanol (10 mL) was added to the mixture and the mixture was kept stirring for another 30 minutes. After passing through a silica plug eluted with chloroform, the solvent was removed. The residue was purified by size-exclusion chromatography (Bio-Beads, S-X1) (toluene + 1% pyridine). **Zn-*ls*-$P2_{MesBu}$** (330 mg, 47%) was yield as dark red solid.

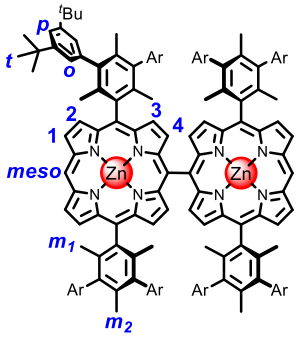

^{1}H NMR (400 MHz, $CDCl_3$) δ_H 10.22 (s, 2H, $\mathbf{H}_{meso}$), 9.45 (d, J = 4.5 Hz, 4H, $\mathbf{H_1}$), 9.16 (d, J = 4.4 Hz, 4H, $\mathbf{H_2}$), 8.74 (d, J = 4.6 Hz, 4H, $\mathbf{H_3}$), 8.05 (d, J = 4.6 Hz, 4H, $\mathbf{H_4}$), 7.32– 7.30 (m, 16H, $\mathbf{H}_o$), 7.13 (t, J = 1.7 Hz, 8H, $\mathbf{H}_p$), 1.90 (s, 12H, $\mathbf{H}_{m2}$), 1.62 (s, 24H, $\mathbf{H}_{m1}$), 1.40 (s, 72H, $\mathbf{H}_t$), 1.24 (s, 72H, $\mathbf{H}_t$).

^{13}C NMR (101 MHz, CD_2Cl_2) δ_C 154.88, 151.00, 150.76, 149.93, 149.86, 141.81, 140.68, 140.05, 136.48, 134.31, 133.94, 132.07, 131.54, 130.76, 124.35, 124.14, 121.11, 119.98, 119.88, 105.62, 35.13, 35.04, 31.86, 31.76, 29.89, 21.03, 19.83.

MALDI-ToF m/z = 2723.461 ($C_{188}H_{222}N_8Zn_2$, M^+ requires 2723.614)

Zn-*ls*-$P2_{MesBu}Br_2$

Zn-*ls*-$P2_{MesBu}$ (368 mg, 135 μmol, 1.0 equiv.) was added into a 250 mL round-bottom flask followed by chloroform (140 mL) and pyridine (1.4 mL). It was cooled to 0 °C in an ice bath and to the stirred mixture, a solution of N-bromosuccinimide (52.9 mg, 297 μmol, 2.2 equiv.) in chloroform (28 mL) was added dropwise. The reaction mixture was stirred at 0 °C for 15 minutes until it turned green, then acetone (10 mL) was added to quench the excess N-bromosuccinimide. The resulting mixture was concentrated under reduced pressure and purified by a silica plug (chloroform) to yield **Zn-*ls*-$P2_{MesBu}Br_2$** (382 mg, 98%).

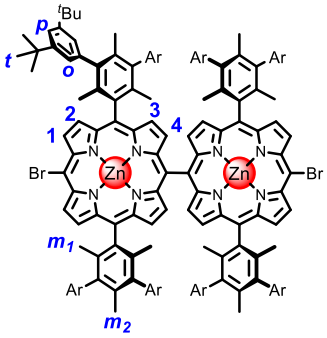

^{1}H NMR (400 MHz, $CDCl_3$) δ_H 9.88 (d, J = 4.7 Hz, 4H, $\mathbf{H_1}$), 9.13 (d, J = 4.7 Hz, 4H, $\mathbf{H_2}$), 8.75 (d, J = 4.6 Hz, 4H, $\mathbf{H_3}$), 8.13 (d, J = 4.6 Hz, 4H, $\mathbf{H_4}$), 7.31 (t, J = 1.8 Hz, 8H, $\mathbf{H}_p$), 7.29 (t, J = 1.6 Hz, 8H, $\mathbf{H}_o$), 7.10 (t, J = 1.6 Hz, 8H, $\mathbf{H}_o$), 1.87 (s, 12H, $\mathbf{H}_{m2}$), 1.59 (s, 24H, $\mathbf{H}_{m1}$), 1.38 (s, 72H, $\mathbf{H}_t$), 1.22 (s, 72H, $\mathbf{H}_t$).

MALDI-ToF m/z = 2881.477 ($C_{188}H_{220}N_8Zn_2Br_2$, M^+ requires 2881.458)

***ls*-P2$_{MesBu}$Br$_2$**

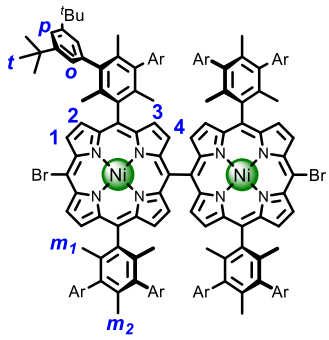

Zn-*ls*-P2$_{MesBu}$Br$_2$ (349 mg, 0.12 mmol, 1 equiv.) was dissolved in of chloroform (16 mL). Trifluoroacetic acid (0.56 mL, 7.26 mmol, 60 equiv.) was added to the solution. The mixture kept stirring at room temperature overnight. Then, sodium bicarbonate aqueous solution (20 mL) was added. The mixture was extracted with water and brine. The organic phase was collected and the solvent was removed. The residue was dissolved again in of *m*-xylene (12 mL). $Ni(acac)_2(H_2O)_2$ (177 mg, 0.61 mmol, 5 equiv.) was added. The mixture was stirred at 130 °C overnight. The solvent was removed and the residue was purified by silica column chromatography using pure chloroform. The product ***ls*-P2$_{MesBu}$Br$_2$** was recrystallized from CH_2Cl_2 and methanol (303 mg, 87%).

^{1}H NMR (600 MHz, $CDCl_3$) δ_H 9.63 (d, J = 5.0 Hz, 4H, $\mathbf{H_1}$), 8.93 (d, J = 5.0 Hz, 4H, $\mathbf{H_2}$), 8.60 (d, J = 4.9 Hz, 4H, $\mathbf{H_3}$), 8.09 (d, J = 4.9 Hz, 4H, $\mathbf{H_4}$), 7.29 (t, J = 1.8 Hz, 8H, $\mathbf{H_p}$), 7.22 (t, J = 1.6 Hz, 8H, $\mathbf{H_o}$), 7.06 (t, J = 1.6 Hz, 8H, $\mathbf{H_o}$), 1.85 (s, 12H, $\mathbf{H_{m2}}$), 1.53 (s, 24H, $\mathbf{H_{m1}}$), 1.35 (s, 72H, $\mathbf{H_t}$), 1.22 (s, 72H, $\mathbf{H_t}$).

^{13}C NMR (151 MHz, CD_2Cl_2) δ_C 150.66, 150.64, 147.26, 144.11, 142.81, 142.55, 141.14, 140.72, 137.94, 137.45, 136.00, 134.67, 134.49, 133.63, 132.67, 132.28, 128.30, 126.17, 124.13, 123.98, 120.53, 119.86, 115.99, 103.00, 35.07, 34.97, 31.76, 31.67, 21.48, 20.61, 19.86.

MALDI-ToF m/z = 2867.908 ($C_{188}H_{220}N_8Ni_2Br_2$, M^+ requires 2867.453)

Section 4.2. Optimization of Reaction Conditions for Yamamoto (Cyclo)Oligomerization

Table S1. List of ***ls*-P2$_{OOct}$Br$_2$** (cyclo)oligomerization conditions and their respective outcomes.

Entry	Solvents	Concentration	Temperature	Catalyst	Outcome
1[*]	DMF:THF:Pyridine (3:1:0.05)	1 mM	60 °C	$Ni(COD)_2$ (20 eq.) 2,2-bipyridine (20 eq.)	GPC trace in Figure S5a
2	DMF:THF:Pyridine (3:1:0.05)	10 mM	60 °C	$Ni(COD)_2$ (20 eq.) 2,2-bipyridine (20 eq.)	Significant linear oligomerization, larger rings favored
3	DMF:THF:Pyridine (3:1:0.05)	0.1 mM	60 °C	$Ni(COD)_2$ (20 eq.) 2,2-bipyridine (20 eq.)	Almost no linear oligomerization, smaller rings favored
4	DMF:THF (3:1)	1 mM	60 °C	$Ni(COD)_2$ (20 eq.) 2,2-bipyridine (20 eq.)	Same as Entry 1
5	DMF:THF:Pyridine (3:1:0.05)	1 mM	60 °C	$Ni(^{t\text{-}Bu}stb)_3$ (20 eq.) 2,2-bipyridine (20 eq.)	No oligomerization
6	DMF:THF:Pyridine (3:1:0.05)	1 mM	60 °C	$Ni(COD)_2$ (5 eq.) 2,2-bipyridine (5 eq.)	No oligomerization
7	DMF:THF:Pyridine (3:1:0.05)	1 mM	25 °C[†]	$Ni(COD)_2$ (20 eq.) 2,2-bipyridine (20 eq.)	Less linear oligomerization, smaller rings favored

[*] Standard conditions. [†] Catalyst solution stirred at 60 °C for 1h, then cooled down to 25 °C before addition of porphyrin oligomer.

As expected for a macrocyclization reaction, increasing the concentration (Table S1 entry 2) led to diminished yields of cyclic species, whereas lowering it had the opposite effect (Table S1 entry 3). The active catalyst species in Ni(0)-catalyzed Yamamoto couplings is believed to be [Ni(COD)(2,2'-bipyridine)] (*52*). However, the use of pyridine as a solvent does not seem to affect the performance of polymerization (Table S1 entry 4). The use of an air-stable Ni(0) source (Table S1 entry 5) completely shut down the reaction and resulted in unreacted ***ls*-P2$_{OOct}$Br$_2$**. Similarly, reducing the amount of catalyst to 5 equivalents (Table S1 entry 6) hindered the polymerization. Activation of the catalyst at 60 °C followed by cooling down to room temperature to perform the oligomerization (Table S1 entry 7), had a similar effect to diluting the reaction and favored cyclic species.

Section 4.3. Standard Procedure for Yamamoto (Cyclo)Oligomerization

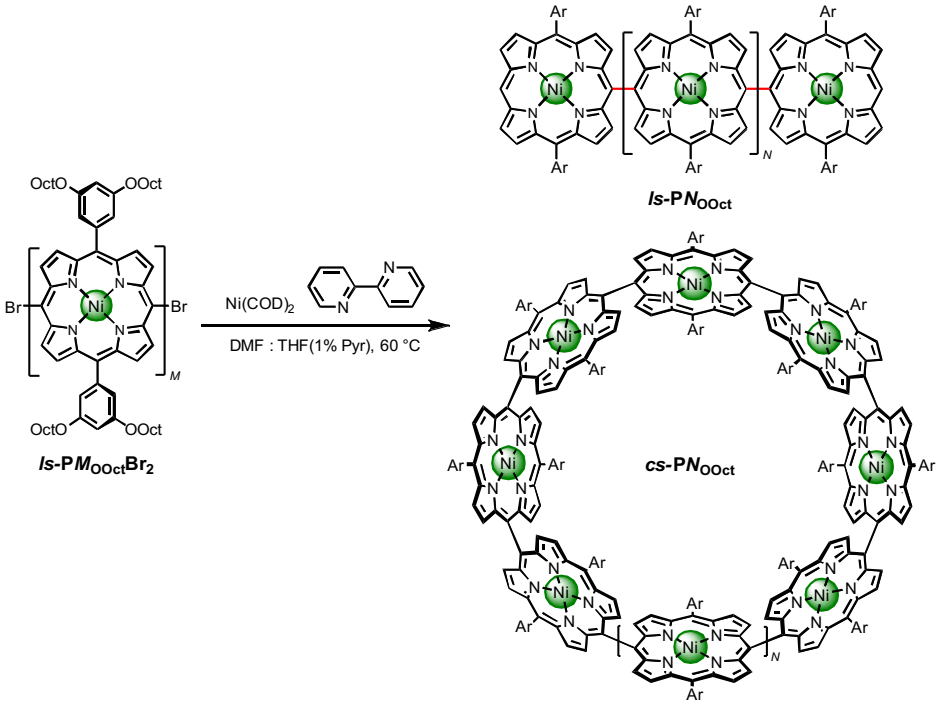

Figure S3. Standard synthetic route towards ***cs*-P*N*$_{OOct}$** from Ni(II) porphyrin oligomers.

Method. $Ni(COD)_2$ (100 mg, 37 µmol, 20 equiv.) and 2,2'-bipyridine (57 mg, 37 µmol, 20 equiv.) were dissolved in dry DMF (14 mL) and degassed by three freeze-thaw cycles. This solution was stirred under argon at 60 °C for 1 h, when the solution had turned from yellow into deep purple. ***ls*-P2$_{OOct}$Br$_2$** (40 mg, 18 µmol, 1.0 equiv.) was dissolved in dry THF (4.5 mL) and pyridine (230 µL) and degassed by three freeze-thaw cycles. The porphyrin solution was then added into the flask containing the catalyst mixture and stirred under argon at 60 °C overnight. After cooling to room temperature, the crude reaction mixture was filtered on silica using CH_2Cl_2 as eluent. This solution was evaporated under vacuum and the crude mixture of oligomers separated by recycling GPC in toluene + 1% pyridine.

Isolated yields: ***cs*-P6$_{OOct}$** (1.9 mg, 5%), ***cs*-P8$_{OOct}$** (3.5 mg, 9%), ***cs*-P10$_{OOct}$** (5.7 mg, 15%), ***cs*-P12$_{OOct}$** (4.5 mg, 12%), ***cs*-P14$_{OOct}$** (2.0 mg, 5%).

Results. The degree of polymerization was measured by analytical GPC (Figures S5 –S9). The polymerization of dimer (Figure S5a) featured two Gaussian-type distributions, which hinted at the formation of two types of products (*i.e.* cyclic and linear). Cyclic oligomers usually display smaller hydrodynamic volumes, which result in longer retention times compared to their linear counterparts (*36*). Short porphyrin oligomers ($N = 1 – 4$) gave cyclic products in yields up to 46% (when considering the sum of all cyclic compounds). Prime-numbered porphyrin nanorings were obtained from mixtures of oligomers (Table S2, Figure S6b). Interestingly, neither ***ls*-P6$_{OOct}$Br$_2$** nor ***ls*-P12$_{OOct}$Br$_2$** produced their cyclic counterparts (***cs*-P6** and ***cs*-P12** respectively), as evidenced by Figure S7b and Figure S8, which seems to indicate that cyclization of a fully C-C linked chain is not possible (see Section 7.2 for discussion of the reaction mechanism). Figure S9 shows that coupling of zinc porphyrins does not form cyclic oligomers.

Section 4.4. Synthesis of *cs*-P*N*$_{OOct}$

Table S2. List of Yamamoto (cyclo)oligomerizations using different size **OOct** oligomers and their detected cyclic species and isolated yields.

***ls*-P*N*$_{OOct}$Br$_2$**	**Detected cyclic species *N* for *cs*-P*N* (*isolated yield*)***
P1Br$_2$	**7** (*4%*), **8** (*4%*), **9** (*4%*), **10** (*2%*)
***ls*-P2Br$_2$**	**6** (*5%*), **8** (*9%*), **10** (*15%*), **12** (*12%*), **14** (*5%*), **16**, **18**
***ls*-P3Br$_2$**	**6** (*5%*), **9** (*13%*), **12** (*9%*), **15** (*4%*), **18**, **21**
***ls*-P2Br$_2$ + *ls*-P3Br$_2$**	**6** (*2%*), **7** (*2%*), **8** (*3%*), **9** (*5%*), **10** (*6%*), **11** (*4%*), **12** (*4%*), **13** (*4%*)
***ls*-P4Br$_2$**	**8** (*6%*), **12** (*12%*), **16**, **20**, **24**
***ls*-P6Br$_2$**	**12**, **18**, **24**, **30**
***ls*-P12Br$_2$**	No ***cs*-P*N*** detected

* Yields calculated by max. theoretical mass, *i.e.* assuming that all ***ls*-P*N*Br$_2$** was converted to a single ***cs*-P*N***.

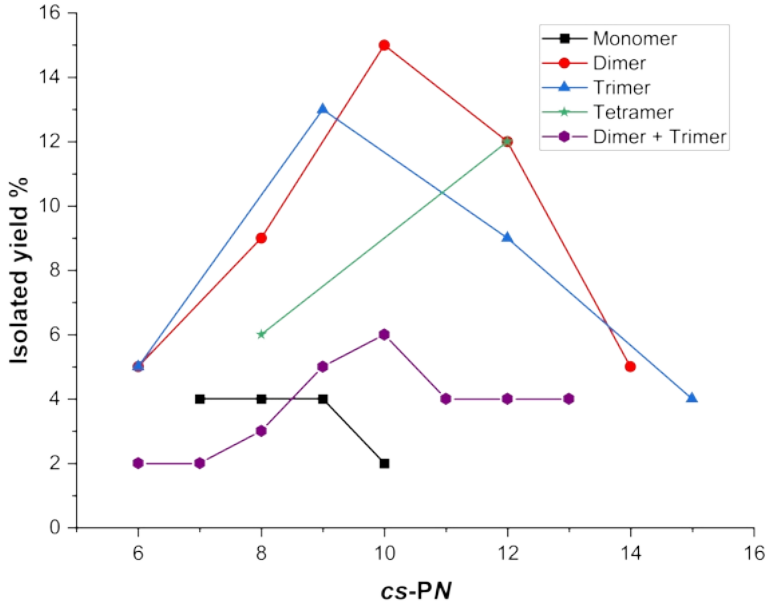

Figure S4. Summary of cyclic products and yields obtained *via* Yamamoto (cyclo)oligomerizations of different size **OOct** starting oligomers.

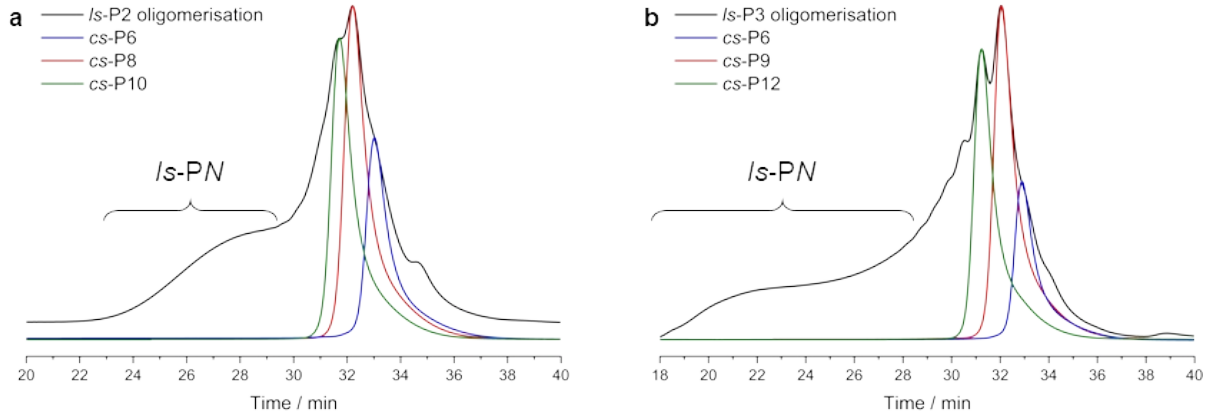

Figure S5. Analytical GPC traces of the crude reaction mixtures and main purified cyclic products from Yamamoto (cyclo)oligomerization of a) ***ls*-P2$_{OOct}$Br$_2$** and b) ***ls*-P3$_{OOct}$Br$_2$**.

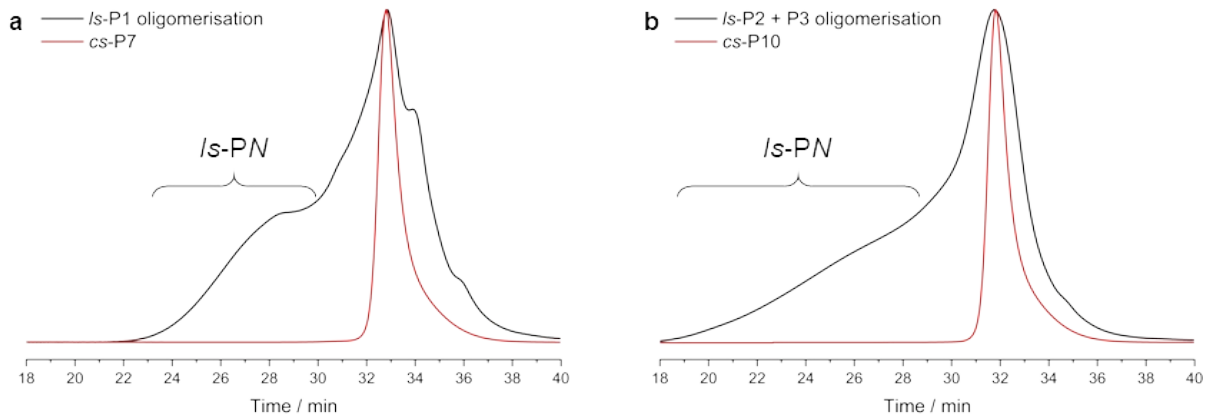

Figure S6. Analytical GPC traces of the crude reaction mixtures and main purified cyclic product from Yamamoto (cyclo)oligomerization of a) ***ls*-P1$_{OOct}$Br$_2$** and b) ***ls*-P2$_{OOct}$Br$_2$** + ***ls*-P3$_{OOct}$Br$_2$**.

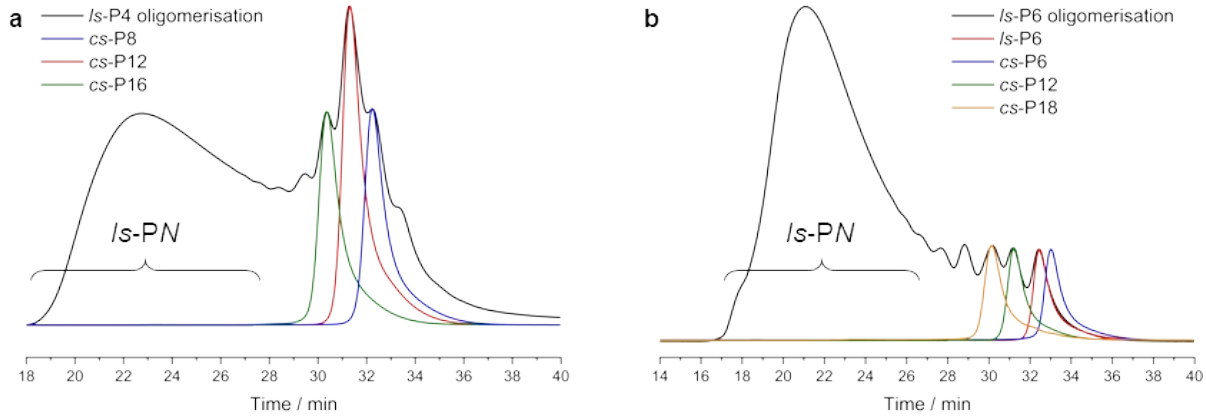

Figure S7. Analytical GPC traces of the crude reaction mixtures and purified cyclic product from Yamamoto (cyclo)oligomerization of a) ***ls*-P4$_{OOct}$Br$_2$** and b) ***ls*-P6$_{OOct}$Br$_2$**. Note that coupling of ***ls*-P6$_{OOct}$Br$_2$** does not give ***cs*-P6$_{OOct}$Br$_2$**.

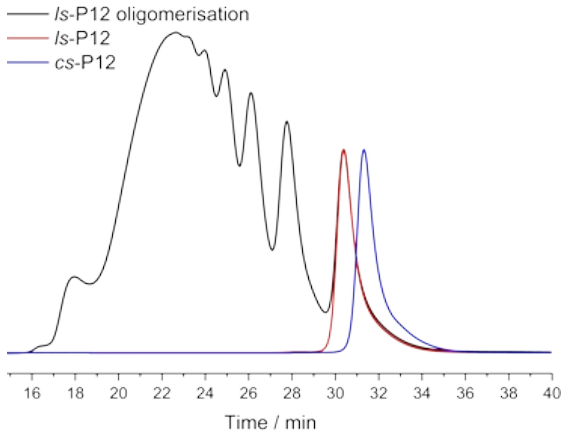

Figure S8. Analytical GPC trace of the crude reaction mixture from Yamamoto (cyclo)oligomerization of ***ls*-P12$_{OOct}$Br$_2$**, showing that ***cs*-P12$_{OOct}$** is not formed from ***ls*-P12$_{OOct}$Br$_2$.**

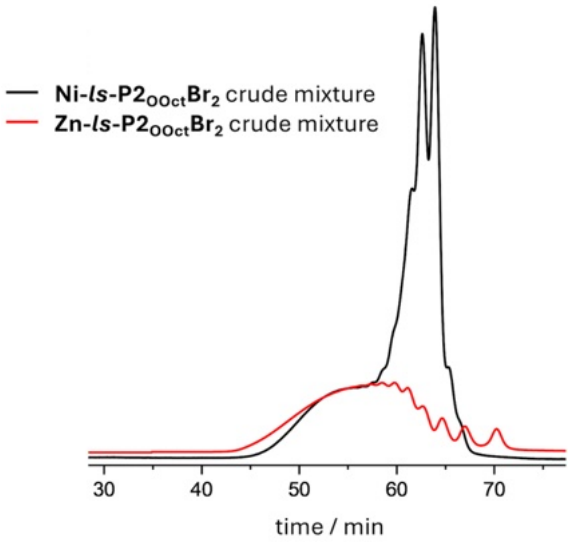

Figure S9. GPC traces of the crude reaction mixtures from (cyclo)oligomerisation of Ni(II) ***ls*-P2$_{OOct}$Br$_2$** (black) and Zn(II) (**Zn-*ls*-P2$_{OOct}$Br$_2$**, red), showing that the zinc complex does not form cyclic oligomers.

***cs*-P6$_{OOct}$**

^{1}H NMR (600 MHz, CD_2Cl_2) δ_H 9.95 (d, J = 4.8 Hz, 12H, **H$_{ß\ in}$**), 9.13 (d, J = 4.8 Hz, 12H, **H$_{ß',\ in}$**), 7.85 (d, J = 5.0 Hz, 12H, **H$_{ß',\ out}$**), 6.86 (s, 6H, **H$_{p\ in}$**), 6.60 (d, J = 4.9 Hz, 12H, **H$_{ß\ out}$**), 6.42 (s, 6H, **H$_{p\ out}$**), 6.33 (s, 12H, **H$_{o\ out}$**), 4.30 – 3.93 (br m, 24H, **H$_{Oct\ in}$**), 3.62 (t, J = 6.2 Hz, 24H, **H$_{Oct\ out}$**), 1.97 – 1.81 (m, 24H, **H$_{Oct\ in}$**), 1.44 – 1.16 (m, 168H, **H$_{Oct}$**), 1.13 – 0.69 (m, 132H, **H$_{Oct}$**), 0.47 – 0.30 (m, 36H, **H$_{Oct\ in}$**). Note: **H$_{o\ in}$** is missing from the ^{1}H NMR at room temperature due to rotation of the phenyl ring leading to broadening of the peak.

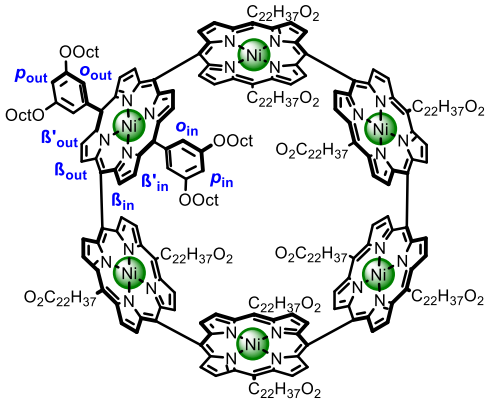

MALDI-ToF m/z = 6178.111 ($C_{384}H_{492}N_{24}Ni_6O_{24}$, M^+ requires 6177.422)

UV-vis (CH_2Cl_2, 298 K) λ_{max} (ε / 10^4 M^{-1} cm^{-1}): 416 (19.8), 488 (27.4), 552 (6.85), 639 (4.72)

***cs*-P7$_{OOct}$**

^{1}H NMR (500 MHz, TCE-d_2, 368 K) δ_H 8.57 (s, 28H, **H$_{ß'}$**), 8.29 (s, 28H, **H$_{ß}$**), 7.02 (s, 28H, **H$_{o}$**), 6.69 (s, 14H, **H$_{p}$**), 3.95 (t, J = 6.6 Hz, 56H, **H$_{Oct}$**), 1.71 (p, J = 7.0 Hz, 56H, **H$_{Oct}$**), 1.40 – 1.01 (m, 280H, **H$_{Oct}$**), 0.67 (t, J = 6.4 Hz, 84H, **H$_{Oct}$**).

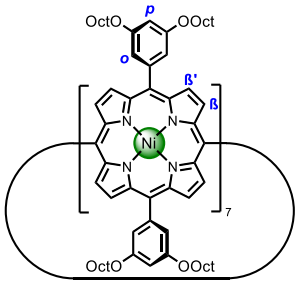

MALDI-ToF m/z = 7211.984 ($C_{448}H_{574}N_{28}Ni_7O_{28}$, M^+ requires 7208.989)

UV-vis (CH_2Cl_2, 298 K) λ_{max} (ε / 10^4 M^{-1} cm^{-1}): 416 (31.4), 481 (35.7), 551 (10.9), 623 (5.15)

***cs*-P8$_{OOct}$**

^{1}H NMR (600 MHz, CD_2Cl_2) δ_H 9.76 (d, J = 4.9 Hz, 16H, **H$_{ß\ in}$**), 9.19 (d, J = 4.9 Hz, 16H, **H$_{ß',\ in}$**), 8.03 (d, J = 5.1 Hz, 16H, **H$_{ß',\ out}$**), 6.87 (t, J = 2.2 Hz, 8H, **H$_{p\ in}$**), 6.70 (d, J = 5.1 Hz, 16H, **H$_{ß\ out}$**), 6.65 – 6.45 (br m, 16H, **H$_{o\ out}$**), 6.41 (t, J = 2.3 Hz, 8H, **H$_{p\ out}$**), 4.42 – 3.90 (br m, 32H, **H$_{Oct\ in}$**), 3.63 (t, J = 6.0 Hz, 32H, **H$_{Oct\ out}$**), 1.97 – 1.79 (br m, 32H, **H$_{Oct\ in}$**), 1.49 – 0.63 (m, 416H, **H$_{Oct}$**) 0.58 – 0.13 (br m, 32H, **H$_{Oct}$**). Note: **H$_{o\ in}$** is missing from the ^{1}H NMR at room temperature due to slow rotation of the phenyl ring leading to broadening of the peak. It can be detected as a broad singlet at 7.66 ppm by VT ^{1}H NMR at 95 °C in toluene-d_8 (see Section 4.7).

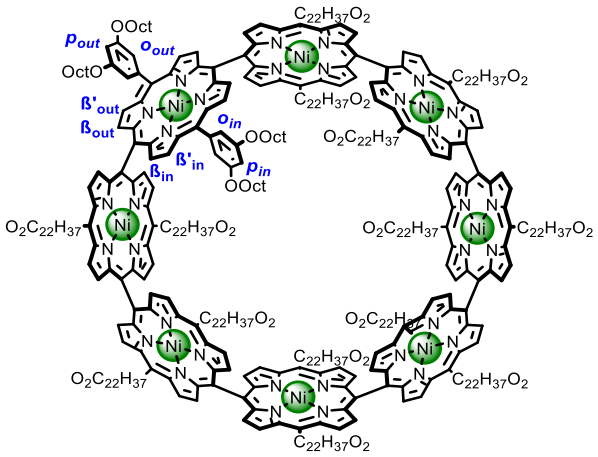

^{13}C NMR (151 MHz, CD_2Cl_2) δ_C 159.5 (from HMBC), 158.7, 145.0, 144.1, 142.4, 142.1, 141.4, 141.3, 135.0, 134.0, 133.5, 132.8, 121.1, 119.8, 113.8, 113.5, 113.0, 101.6, 101.3, 68.9, 68.3, 32.2, 31.8, 30.1, 29.8, 29.7, 29.4, 29.3, 29.3, 26.5, 26.1, 23.0, 22.6, 14.3, 13.9.

MALDI-ToF m/z = 8249.767 ($C_{512}H_{656}N_{32}Ni_8O_{32}$, M^+ requires 8239.558)

UV-vis (CH_2Cl_2, 298 K) λ_{max} (ε / 10^4 M^{-1} cm^{-1}): 415 (28.6), 481 (36.0), 562 (12.4), 603 (3.17)

***cs*-P9$_{OOct}$**

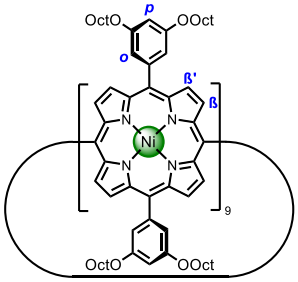

^{1}H NMR (600 MHz, CD_2Cl_2) δ_H 8.65 (d, J = 5.0 Hz, 36H, **H$_{ß'}$**), 8.31 – 8.18 (m, 36H, **H$_{ß}$**), 7.06 (d, J = 2.2 Hz, 36H, **H$_o$**), 6.64 (t, J = 2.2 Hz, 18H, **H$_p$**), 3.93 (t, J = 6.7 Hz, 72H, **H$_{Oct}$**), 1.68 (p, J = 6.8 Hz, 72H, **H$_{Oct}$**), 1.36 – 1.28 (m, 72H, **H$_{Oct}$**), 1.23 – 1.10 (m, 144H, **H$_{Oct}$**), 1.10 – 1.02 (m, 144H, **H$_{Oct}$**), 0.62 (t, J = 7.1 Hz, 108H, **H$_{Oct}$**).

^{13}C NMR (151 MHz, CD_2Cl_2) δ_C 159.1, 145.3, 142.1, 142.0, 134.3, 133.3, 120.6, 114.2, 113.5, 101.4, 68.6, 32.0, 29.6, 29.6, 29.5, 26.3, 22.9, 14.1.

MALDI-ToF m/z = 9273.126 ($C_{576}H_{738}N_{36}Ni_9O_{36}$, M^+ requires 9269.128)

UV-vis (CH_2Cl_2, 298 K) λ_{max} (ε / 10^4 M^{-1} cm^{-1}): 414 (45.4), 482 (55.7), 562 (20.9)

***cs*-P10$_{OOct}$**

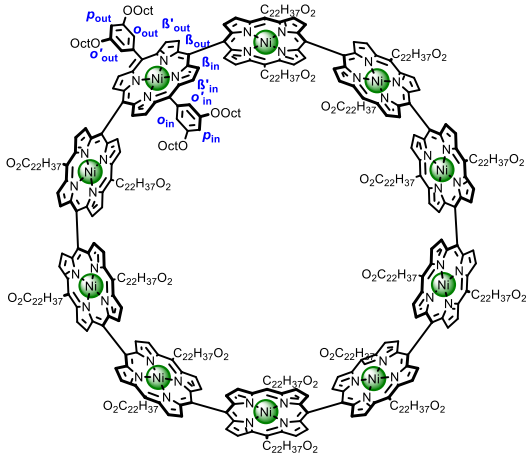

^{1}H NMR (500 MHz, CD_2Cl_2, 233 K) δ_H 9.51 (s, 20H, **H$_{ß\ in}$**), 9.14 (s, 20H, **H$_{ß',\ in}$**), 8.16 (s, 20H, **H$_{ß',\ out}$**), 8.08 (s, 10H, **H$_{o\ in}$**), 7.04 (s, 10H, **H$_{o\ out}$**), 6.92 (s, 20H, **H$_{ß\ out}$**), 6.81 (s, 10H, **H$_{p\ in}$**), 6.76 (s, 10H, **H$_{o',\ in}$**), 6.42 (s, 10H, **H$_{p\ out}$**), 6.30 (s, 10H, **H$_{o',\ out}$**), 4.22 (s, 20H, **H$_{Oct}$**), 3.97 (s, 20H, **H$_{Oct}$**), 3.69 (s, 20H, **H$_{Oct}$**), 3.59 (s, 20H, **H$_{Oct}$**), 1.87 (s, 20H, **H$_{Oct}$**), 1.75 (s, 20H, **H$_{Oct}$**), 1.61 – 0.56 (m, 530H, **H$_{Oct}$**), 0.25 (s, 30H, **H$_{Oct}$**).

MALDI-ToF m/z = 10313.377 ($C_{640}H_{820}N_{40}Ni_{10}O_{40}$, M^+ requires 10299.698)

UV-vis (CH_2Cl_2, 298 K) λ_{max} (ε / 10^4 M^{-1} cm^{-1}): 412 (48.0), 477 (54.6), 555 (21.7)

***cs*-P11$_{OOct}$**

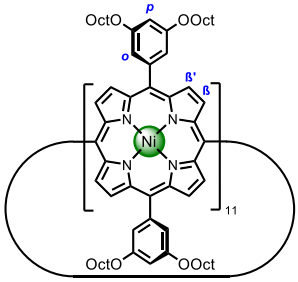

^{1}H NMR (600 MHz, CD_2Cl_2) δ_H 8.71 (br s, 44H, **H$_{ß'}$**), 8.27 (br s, 44H, **H$_{ß}$**), 7.14 (br s, 44H, **H$_o$**), 6.67 (br s, 22H, **H$_p$**), 3.99 – 3.93 (m, 88H, **H$_{Oct}$**), 1.75 – 1.66 (m, 88H, **H$_{Oct}$**), 1.43 – 1.01 (m, 440H, **H$_{Oct}$**), 0.73 – 0.67 (m, 132H, **H$_{Oct}$**).

^{13}C NMR (151 MHz, CD_2Cl_2) δ_C 159.1, 146.0, 142.5, 142.3, 134.4, 133.2, 120.8, 115.1, 113.6, 101.4, 68.7, 32.1, 29.7, 29.6, 29.5, 26.4, 22.9, 14.1.

MALDI-ToF m/z = 11342.312 ($C_{704}H_{902}N_{44}Ni_{11}O_{44}$, M^+ requires 11329.268)

UV-vis (CH_2Cl_2, 298 K) λ_{max} (ε / 10^4 M^{-1} cm^{-1}): 412 (63.4), 483 (76.2), 561 (31.8)

***cs*-P12$_{OOct}$**

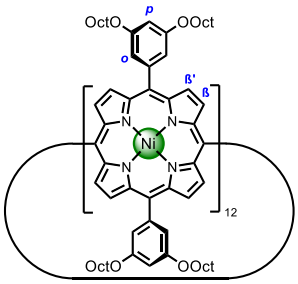

^{1}H NMR (600 MHz, CD_2Cl_2) δ_H 8.72 (br s, 48H, **H$_{ß'}$**), 8.26 (br s, 48H, **H$_{ß}$**), 7.15 (br s, 48H, **H$_o$**), 6.68 (br s, 24H, **H$_p$**), 3.97 (t, J = 6.8 Hz, 96H, **H$_{Oct}$**), 1.71 (p, J = 6.7 Hz, 96H, **H$_{Oct}$**), 1.35 (q, J = 7.8 Hz, 96H, **H$_{Oct}$**), 1.30 – 1.01 (m, 384H, **H$_{Oct}$**), 0.71 (t, J = 6.9 Hz, 144H, **H$_{Oct}$**).

^{13}C NMR (151 MHz, CD_2Cl_2) δ_C 159.1, 146.1, 142.6, 142.4, 134.3, 133.2, 120.8, 115.3, 113.6, 101.4, 68.7, 32.1, 29.7, 29.6, 29.5, 26.4, 22.9, 14.1.

MALDI-ToF m/z = 12378.101 ($C_{768}H_{984}N_{48}Ni_{12}O_{48}$, M^+ requires12359.837)

UV-vis (CH_2Cl_2, 298 K) λ_{max} (ε / 10^4 M^{-1} cm^{-1}): 410 (45.0), 478 (56.6), 553 (24.5)

***cs*-P13$_{OOct}$**

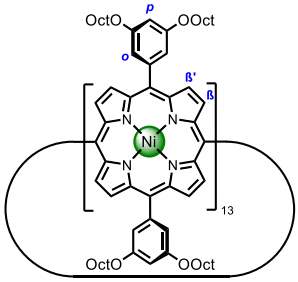

^{1}H NMR (600 MHz, CD_2Cl_2) δ_H 8.74 (d, J = 4.9 Hz, 52H, **H**ß'), 8.27 (d, J = 5.0 Hz, 52H, **H**ß), 7.18 (d, J = 2.3 Hz, 52H, **H**$_o$), 6.69 (t, J = 2.3 Hz, 26H, **H**$_p$), 4.03 – 3.95 (m, 104H, **H**$_{Oct}$), 1.72 (p, J = 6.7 Hz, 104H, **H**$_{Oct}$), 1.43 – 1.08 (m, 520H, **H**$_{Oct}$), 0.73 (t, J = 7.1 Hz, 156H, **H**$_{Oct}$).
^{13}C NMR (151 MHz, CD_2Cl_2) δ_C 159.1, 146.5, 142.8, 134.4, 133.1, 120.9, 113.6, 101.4, 68.7, 32.1, 29.7, 29.7, 29.5, 26.4, 22.9, 14.2.
MALDI-ToF m/z = 13403.259 ($C_{832}H_{1066}N_{52}Ni_{13}O_{52}$, M^+ requires 13389.407)
UV-vis (CH_2Cl_2, 298 K) λ_{max} (ε / 10^4 M^{-1} cm^{-1}): 411 (71.3), 483 (86.5), 559 (37.8)

***cs*-P14$_{OOct}$**

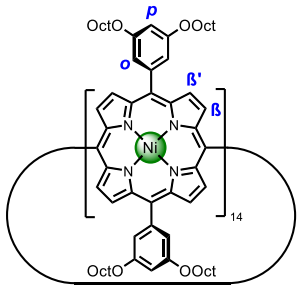

^{1}H NMR (600 MHz, CD_2Cl_2) δ_H 8.75 (d, J = 5.0 Hz, 56H, **H**ß'), 8.27 (d, J = 4.9 Hz, 56H, **H**ß), 7.19 (d, J = 2.1 Hz, 56H, **H**$_o$), 6.69 (d, J = 2.2 Hz, 28H, **H**$_p$), 3.99 (t, J = 6.6 Hz, 112H, **H**$_{Oct}$), 1.72 (p, J = 6.7 Hz, 112H, **H**$_{Oct}$), 1.37 (p, J = 7.4 Hz, 112H, **H**$_{Oct}$), 1.32 – 1.09 (m, 448H, **H**$_{Oct}$), 0.73 (t, J = 4.2 Hz, 168H, **H**$_{Oct}$).
MALDI-ToF m/z = 14429.071 ($C_{896}H_{1148}N_{56}Ni_{14}O_{56}$, M^+ requires 14419.977)

***cs*-P15$_{OOct}$**

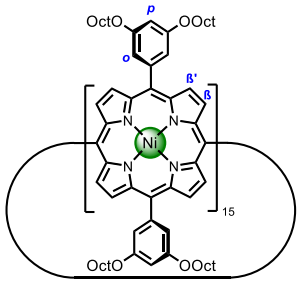

^{1}H NMR (600 MHz, CD_2Cl_2) δ_H 8.76 (d, J = 5.0 Hz, 60H, **H**ß'), 8.27 (d, J = 5.1 Hz, 60H, **H**ß), 7.20 (d, J = 1.8 Hz, 60H, **H**$_o$), 6.70 (d, J = 2.3 Hz, 30H, **H**$_p$), 3.99 (t, J = 6.7 Hz, 120H, **H**$_{Oct}$), 1.73 (p, J = 6.9 Hz, 120H, **H**$_{Oct}$), 1.37 (p, J = 6.7 Hz, 120H, **H**$_{Oct}$), 1.32 – 1.10 (m, 480H, **H**$_{Oct}$), 0.74 (t, J = 6.8 Hz, 180H, **H**$_{Oct}$).
^{13}C NMR (151 MHz, CD_2Cl_2) δ_C 159.1, 146.8, 142.9, 134.3, 133.0, 130.0, 121.1, 113.7, 101.4, 68.7, 32.1, 29.7, 29.7, 29.5, 26.4, 22.9, 14.2.
MALDI-ToF m/z = 15453.384 ($C_{960}H_{1230}N_{60}Ni_{15}O_{60}$, M^+ requires 15449.547)
UV-vis (CH_2Cl_2, 298 K) λ_{max} (ε / 10^4 M^{-1} cm^{-1}): 407 (28.1), 482 (36.4), 554 (16.9)

Section 4.5. Synthesis of *cs*-PN_{tBu}

Table S3. List of products obtained from ***ls*-P2$_{tBu}$Br$_2$** Yamoto (cyclo)oligomerization and isolated yields.

***ls*-PN_{tBu}Br$_2$**	**Detected cyclic species *N* for *cs*-P*N*** (*isolated yield*)
***ls*-P2Br$_2$**	**6** (*5%*), **8** (*18%*), **10** (*13%*), **12** (*8%*), **14** (*4%*), **16** (*2%*), **18** (*1%*)

<u>*cs*-P6$_{tBu}$</u>

^{1}H NMR (600 MHz, CD_2Cl_2) δ_H 9.90 (d, J = 4.9 Hz, 12H, **H$_{ß\ in}$**), 8.99 (d, J = 4.9 Hz, 12H, **H$_{ß',\ in}$**), 7.93 (d, J = 5.0 Hz, 12H, **H$_{ß',\ out}$**), 7.81 (d, J = 1.9 Hz, 6H, **H$_{p\ in}$**), 7.43 (t, J = 1.8 Hz, 6H, **H$_{p\ out}$**), 7.11 (br s, 12H, **H$_{o\ out}$**), 6.91 (d, J = 5.0 Hz, 12H, **H$_{ß\ out}$**), 1.27 (s, 108H, **H$_1$**), 1.15 (s, 108H, **H$_2$**). Note: **H$_{o\ in}$** is missing from the ^{1}H NMR at room temperature due to rotation of the phenyl ring leading to broadening of the peak.

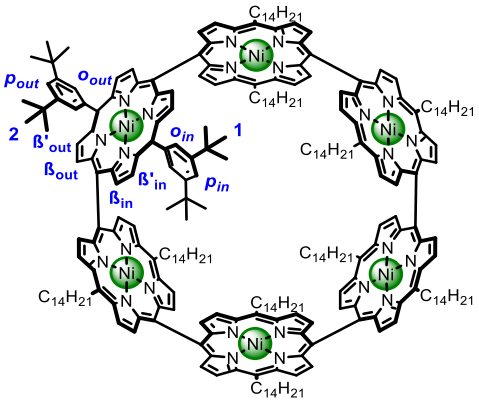

MALDI-ToF m/z = 4449.056 ($C_{288}H_{300}N_{24}Ni_6$, M^+ requires 4479.082)

UV-vis (CH_2Cl_2, 298 K) λ_{max} (ε / 10^4 M^{-1} cm^{-1}): 417 (17.8), 491 (23.2), 552 (6.16), 646 (5.40)

<u>*cs*-P8$_{tBu}$</u>

^{1}H NMR (600 MHz, CD_2Cl_2) δ_H 9.80 (d, J = 4.9 Hz, 16H, **H$_{ß\ in}$**), 9.12 (d, J = 4.9 Hz, 16H, **H$_{ß',\ in}$**), 7.93 (d, J = 5.2 Hz, 16H, **H$_{ß',\ out}$**), 7.85 (br s, 8H, **H$_{p\ in}$**), 7.39 (br s, 8H, **H$_{p\ out}$**), 7.35 – 7.21 (m, 16H, **H$_{o\ out}$**), 6.70 (d, J = 5.2 Hz, 16H, **H$_{ß\ out}$**), 1.53 (s, 144H, **H$_1$**), 1.06 (s, 144H, **H$_2$**). Note: **H$_{o\ in}$** is missing from the ^{1}H NMR at room temperature due to rotation of the phenyl ring leading to broadening of the peak.

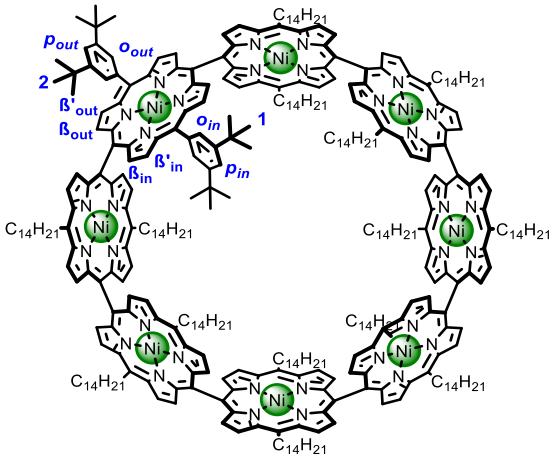

^{13}C NMR (151 MHz, CD_2Cl_2) δ_C 150.0, 149.1, 144.9, 144.1, 142.5, 141.8, 139.9, 138.9, 134.9, 134.0, 133.4, 132.9, 129.2, 128.5, 122.4, 122.1, 121.4, 121.1, 113.4, 35.4, 34.9, 31.9, 31.5.

MALDI-ToF m/z = 5934.646 ($C_{384}H_{400}N_{32}Ni_8$, M^+ requires 5932.713)

UV-vis (CH_2Cl_2, 298 K) λ_{max} (ε / 10^4 M^{-1} cm^{-1}): 415 (35.2), 479 (43.8), 561 (14.7), 604 (3.99)

<u>*cs*-P10$_{tBu}$</u>

^{1}H NMR (500 MHz, CD_2Cl_2, 263 K) δ_H 8.65 (d, J = 4.8 Hz, 20H), 8.40 (d, J = 8.0 Hz, 20H), 7.83 (t, J = 7.9 Hz, 30H), 7.33 (t, J = 7.4 Hz, 20H), 7.22 (d, J = 7.4 Hz, 20H), 7.16 (d, J = 7.4 Hz, 20H), 7.14 (d, J = 7.7 Hz, 10H), 1.34 – 1.18 (m, 360H).

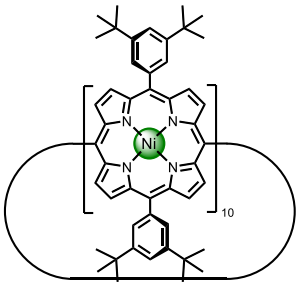

MALDI-ToF m/z = 7413.881 ($C_{480}H_{500}N_{40}Ni_{10}$, M^+ requires 7415.391)

UV-vis (CH_2Cl_2, 298 K) λ_{max} (ε / 10^4 M^{-1} cm^{-1}): 411 (53.2), 478 (68.7), 556 (26.9)

***cs*-P12$_{tBu}$**

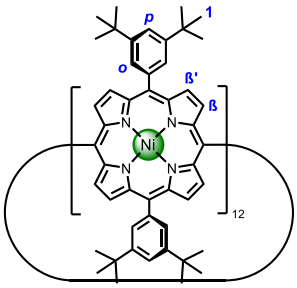

^{1}H NMR (600 MHz, CD_2Cl_2) δ_H 8.65 (br s, 48H, **H$_{ß'}$**), 8.28 (br s, 48H, **H$_ß$**), 7.87 (br s, 48H, **H$_o$**), 7.65 (br s, 24H, **H$_p$**), 1.35 (s, 432H, **H$_1$**).
^{13}C NMR (151 MHz, CD_2Cl_2) δ_C 149.5, 146.1, 143.1, 139.8, 134.1, 133.3, 129.0, 122.2, 121.8, 115.4, 35.2, 31.7.
MALDI-ToF *m/z* = 8896.634 ($C_{576}H_{600}N_{48}Ni_{12}$, M^+ requires 8899.069)
UV-vis (CH_2Cl_2, 298 K) λ_{max} (ε / 10^4 M^{-1} cm^{-1}): 409 (43.6), 479 (58.9), 554 (25.1)

***cs*-P14$_{tBu}$**

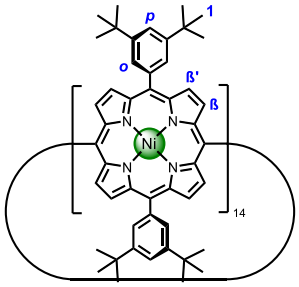

^{1}H NMR (600 MHz, CD_2Cl_2) δ_H 8.67 (br s, 56H, **H$_{ß'}$**), 8.28 (br s, 56H, **H$_ß$**), 7.91 (br s, 56H, **H$_o$**), 7.66 (br s, 28H, **H$_p$**), 1.36 (s, 504H, **H$_1$**).
^{13}C NMR (151 MHz, CD_2Cl_2) δ_H 149.5, 146.5, 143.3, 140.0, 134.2, 133.2, 129.0, 122.4, 121.8, 115.9, 35.2, 31.7.
MALDI-ToF *m/z* = 10384.546 ($C_{672}H_{700}N_{56}Ni_{14}$, M^+ requires 10381.747)
UV-vis (CH_2Cl_2, 298 K) λ_{max} (ε / 10^4 M^{-1} cm^{-1}): 407 (64.8), 480 (89.9), 553 (40.6)

Section 4.6. Synthesis of *cs*-P*N*$_{MesBu}$

Table S4. List of Yamamoto (cyclo)oligomerizations using different size ***ls*-PN$_{MesBu}$Br$_2$** oligomers and their detected cyclic species and isolated yields.

***ls*-PN$_{MesBu}$Br$_2$**	**Detected cyclic species *N* for *cs*-P*N*** (*isolated yield*)*
***ls*-P2Br$_2$**	**8** (*0.5%*), **10** (*2.7%*), **12** (*3.8%*), **14**
P1Br$_2$ + *ls*-P2Br$_2$	**8** (*0.8%*), **9** (*1.1%*), **10** (*1.8%*), **11** (*2.4%*), **12** (*1.2%*)

* Yields calculated by max. theoretical mass

***cs*-P8$_{MesBu}$**

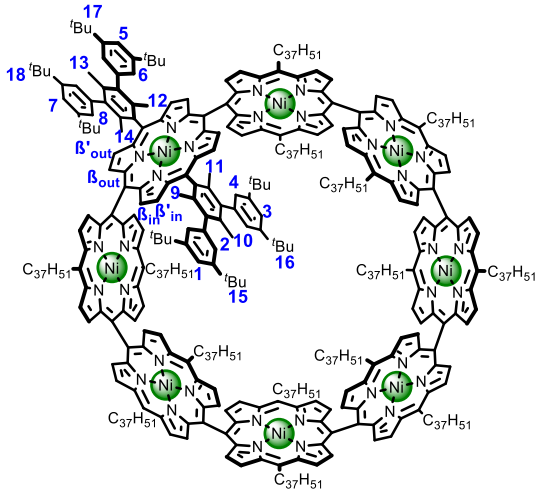

^{1}H NMR (600 MHz, CD_2Cl_2) δ_H 9.75 (d, *J* = 4.5 Hz, 16H, **H$_{ß\ in}$**), 9.03 (d, *J* = 4.8 Hz, 16H, **H$_{ß',\ in}$**), 8.11 (d, *J* = 5.0 Hz, 16H, **H$_{ß',\ out}$**), 7.47 (d, *J* = 1.7 Hz, 8H, **H$_3$**), 7.45 (d, *J* = 2.0 Hz, 16H, **H$_4$**), 7.37 (t, *J* = 1.8 Hz, 8H, **H$_1$**), 7.27 (t, *J* = 1.8 Hz, 8H, **H$_7$**), 7.23 (d, *J* = 1.8 Hz, 16H, **H$_2$**), 7.10 (br s, 16H, **H$_{ß\ out}$**), 6.89 (d, *J* = 1.8 Hz, 16H, **H$_8$**), 6.60 (br s, 16H, **H$_6$**), 6.47 (br s, 8H, **H$_5$**), 2.54 (s, 24H, **H$_{11}$**), 1.97 (s, 24H, **H$_{10}$**), 1.61 (s, 24H, **H$_{13}$**), 1.42 (s, 144H, **H$_{16}$**), 1.34 (s, 168H, **H$_{15}$**, **H$_9$**), 1.31 (s, 24H, **H$_{12}$**), 1.26 (s, 144H, **H$_{18}$**), 0.69 (s, 24H, **H$_{14}$**), 0.49 (br s, 144H, **H$_{17}$**).
MALDI-ToF *m/z* = 10835.504 ($C_{752}H_{880}N_{32}Ni_8$, M^+ requires 10836.476)
UV-vis (CH_2Cl_2, 298 K) λ_{max} (ε / 10^4 M^{-1} cm^{-1}): 413 (42.3), 491 (54.8), 549 (17.8), 634 (8.02).

***cs*-P9$_{MesBu}$**

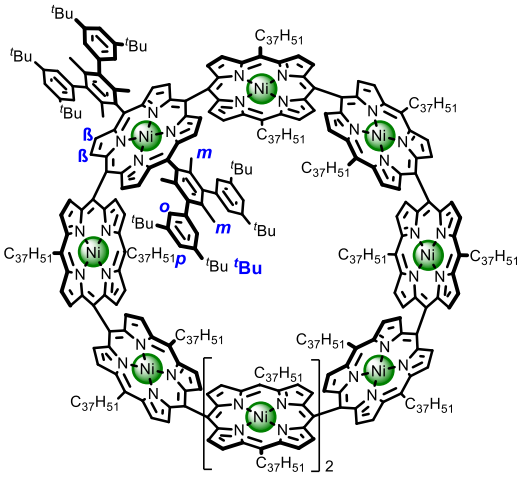

^{1}H NMR (400 MHz, $CDCl_3$) δ_H 10.24 (d, J = 4.4 Hz, 2H, **Hß**), 10.15 (d, J = 4.4 Hz, 2H, **Hß**), 9.83–9.82 (m, 4H), 9.71 (d, J = 4.4 Hz, 2H, **Hß**), 9.61 (d, J = 4.4 Hz, 2H, **Hß**), 9.36 (d, J = 4.4 Hz, 2H, **Hß**), 9.27 (d, J = 4.4 Hz, 2H, **Hß**), 9.22 (d, J = 4.4 Hz, 2H, **Hß**), 9.11 – 9.03 (m, 12H), 8.92 (d, J = 4.4 Hz, 2H, **Hß**), 8.81 (d, J = 4.4 Hz, 2H, **Hß**), 8.63 (d, J = 4.4 Hz, 2H, **Hß**), 8.41 (d, J = 4.4 Hz, 2H, **Hß**), 8.34 (d, J = 4.4 Hz, 2H, **Hß**), 8.24 (br s, 4H), 8.17 (d, J = 4.4 Hz, 2H, **Hß**), 8.12 – 8.09 (m, 4H), 7.76 (d, J = 4.4 Hz, 2H, **Hß**), 7.68 (d, J = 4.4 Hz, 2H, **Hß**), 7.57 – 7.41 (m, 32H), 7.36 – 7.31 (m, 28H), 7.22 (s, 28H), 7.23 – 7.19 (m, 24H), 7.14 – 7.10 (m, 11H), 7.03 (br s, 4H), 6.89 – 6.74 (m, 24H), 6.62 (s, 2H), 6.43 (s, 2H), 6.32 (d, J = 4.4 Hz, 2H, **Hß**), 6.21 – 6.18 (m, 3H), 5.91 (s, 2H), 5.79 (s, 1H), 5.68 (s, 1H), 2.69 (s, 6H), 2.62 (s, 6H), 2.56 (s, 6H), 2.55 (s, 6H), 2.25 (s, 6H), 2.05 – 1.98 (m, 36H), 1.84 – 1.82 (m, 12H), 1.70 – 1.68 (m, 18H), 1.47 – 1.39 (m, 160H), 1.33 – 1.22 (m, 280H), 1.16 – 1.15 (m, 24H), 1.11 – 1.10 (m, 24H), 0.93 (s, 24H), 0.91 – 0.85 (m, 32H), 0.82 (s, 18H), 0.72 (s, 18H), 0.66 (s, 18H), 0.60 (s, 6H), 0.52 (s, 18H), 0.04 (s, 18H), –0.42 (s, 18H), –0.47 (s, 18H).

MALDI-ToF m/z = 12196.287 ($C_{846}H_{990}N_{36}Ni_9$, M^+ requires 12190.339)

UV-vis (CH_2Cl_2, 298 K) λ_{max} (ε / 10^4 M^{-1} cm^{-1}): 414 (58.9), 488 (72.0), 565 (26.9), 619 (9.1)

***cs*-P10$_{MesBu}$**

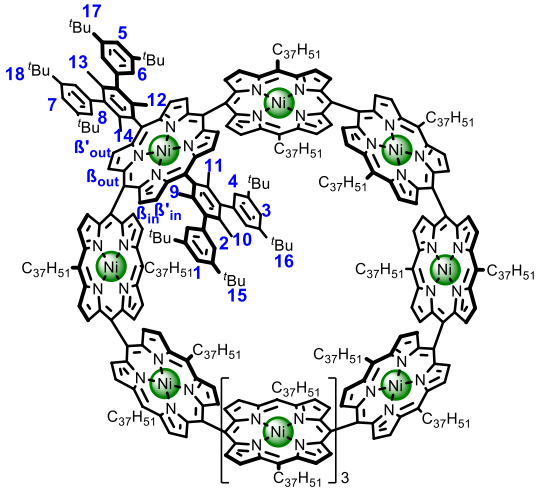

^{1}H NMR (600 MHz, CD_2Cl_2) δ_H 9.61 (d, J = 4.8 Hz, 20H, **Hß in**), 9.10 (d, J = 4.8 Hz, 20H, **Hß' in**), 8.19 (d, J = 5.1 Hz, 20H, **Hß' out**), 7.48 (t, J = 1.9 Hz, 10H, **H$_3$**), 7.43 (d, J = 1.8 Hz, 20H, **H$_4$**), 7.39 (t, J = 1.8 Hz, 10H, **H$_1$**), 7.27 (t, J = 1.8 Hz, 10H, **H$_7$**), 7.24 (d, J = 1.7 Hz, 20H, **H$_2$**), 7.16 (d, J = 5.1 Hz, 20H, **Hß out**), 6.90 (d, J = 1.9 Hz, 20H, **H$_8$**), 6.65 (d, J = 1.7 Hz, 20H, **H$_6$**), 6.62 (t, J = 1.8 Hz, 10H, **H$_5$**), 2.52 (s, 30H, **H$_{11}$**), 1.96 (s, 30H, **H$_{10}$**), 1.61 (s, 30H, **H$_{13}$**), 1.41 (s, 180H, **H$_{16}$**), 1.36 (s, 210H, **H$_{15}$**, **H$_9$**), 1.33 (s, 30H, **H$_{12}$**), 1.24 (s, 180H, **H$_{18}$**), 0.95 (s, 30H, **H$_{14}$**), 0.53 (s, 180H, **H$_{17}$**).

MALDI-ToF m/z = 13548.605 ($C_{940}H_{1100}N_{40}Ni_{10}$, M^+ requires 13545.149)

UV-vis (CH_2Cl_2, 298 K) λ_{max} (ε / 10^4 M^{-1} cm^{-1}): 412 (119), 483 (141), 560 (57.8)

***cs*-P11$_{MesBu}$**

^{1}H NMR (400 MHz, CD_2Cl_2) δ_H 8.68 (s, 44H, **H$_{ß'}$**), 8.41 (br s, 44H, **H$_{ß}$**), 7.23 (s, 44H, **H$_p$**), 7.08 (br s, 88H, **H$_o$**), 1.78 (s, 66H, **H$_{m1}$**), 1.52 (s, 132H, **H$_{m2}$**), 1.17 (br s, 792H, **T^u_b**).

MALDI-ToF *m*/*z* = 14908.223 ($C_{1034}H_{1210}N_{44}Ni_{11}$, M^+ requires 14899.950)

UV-vis (CH_2Cl_2, 298 K) λ_{max} (ε / 10^4 M^{-1} cm^{-1}): 410 (58.4), 485 (69.1), 560 (29.8)

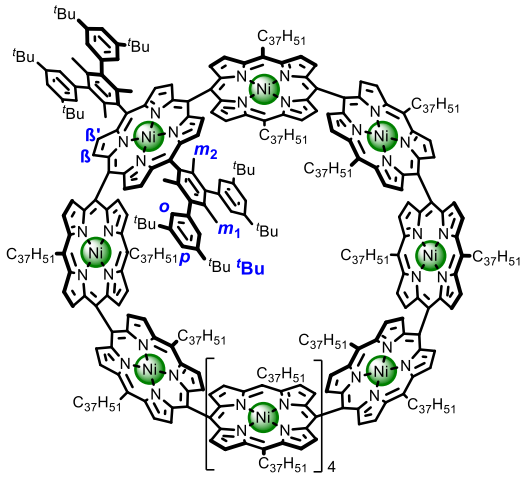

***cs*-P12$_{MesBu}$**

^{1}H NMR (500 MHz, $C_2D_2Cl_4$) δ_H 8.71 (s, 48H, **H$_{ß'}$**), 8.43 (br s, 48H, **H$_{ß'}$**), 7.25 (s, 48H, **H$_p$**), 7.11 (s, 96H, **H$_o$**), 1.85 (s, 72H, **H$_{m1}$**), 1.66 (s, 144H, **H$_{m2}$**), 1.24 (s, 864H, **H$^t_{Bu}$**).

MALDI-ToF *m*/*z* = 16249.175 ($C_{1128}H_{1320}N_{48}Ni_{12}$, M^+ requires 16254.595)

UV-vis (CH_2Cl_2, 298 K) λ_{max} (ε / 10^4 M^{-1} cm^{-1}): 409 (70.5), 482 (83.2), 556 (37.4)

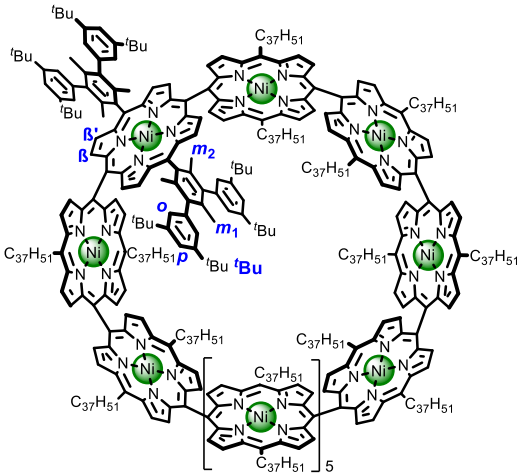

Section 4.7. Dynamics and Variable-Temperature NMR Spectra of *cs*-P*N* Nanorings

Meso–meso singly-linked porphyrin nanorings display different ^{1}H NMR spectra depending on the number of porphyrins. Even-numbered small rings such as ***cs*-P6$_{OOct}$** and ***cs*-P8$_{OOct}$** present four signals for the β environments of the porphyrins, while bigger rings such as ***cs*-P12$_{OOct}$** or ***cs*-P14$_{OOct}$** have only two resonances for these environments. This can be explained by considering the conformation of even-numbered porphyrin nanorings. *Meso-meso* linked porphyrins adopt 70° – 90° dihedral angles, which leads to a conformation of alternating porphyrins pointing inside the cavity of the macrocycle (Figure S10). Rotation along the *meso–meso* bond interconverts inside into outside environments. In smaller rings, the rotation of this bond is hindered by the clashing of the solubilizing groups of the porphyrin in the cavity of the ring, thus making inside and outside environments non-equivalent.

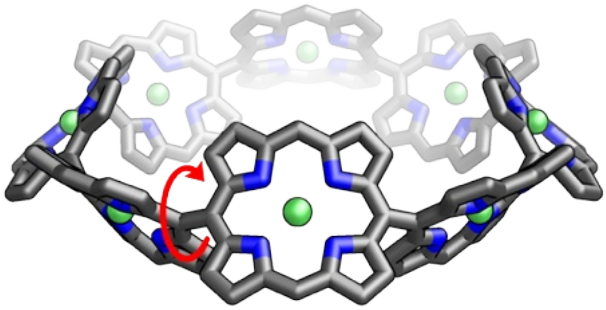

Figure S10. Chemical structure of ***cs*-P8** showing alternating porphyrin units pointing inside the ring, red arrow indicates the rotation of the *meso–meso* bond.

Rotation of porphyrin–aryl bonds also causes broadening of some of the signals of the solubilizing groups. This is most noticeable in *ortho* (***o*$_{in}$** and ***o*$_{out}$**) environments. At 298 K, the ^{1}H spectrum of ***cs*-P8$_{OOct}$** displays only one broad signal corresponding to the outside protons ***o*$_{out}$**, while the peak for ***o*$_{in}$** is so broad that disappears into the baseline (Figure S11). At 368 K (95 °C), the ^{1}H NMR resonances of both signals become sharper allowing assignment of the signal corresponding to ***o*$_{in}$** at 7.66 ppm as a broad singlet. Similarly, the signal for **H$_{a\ in}$** is poorly resolved at 298 K and coalesces into a triplet upon heating.

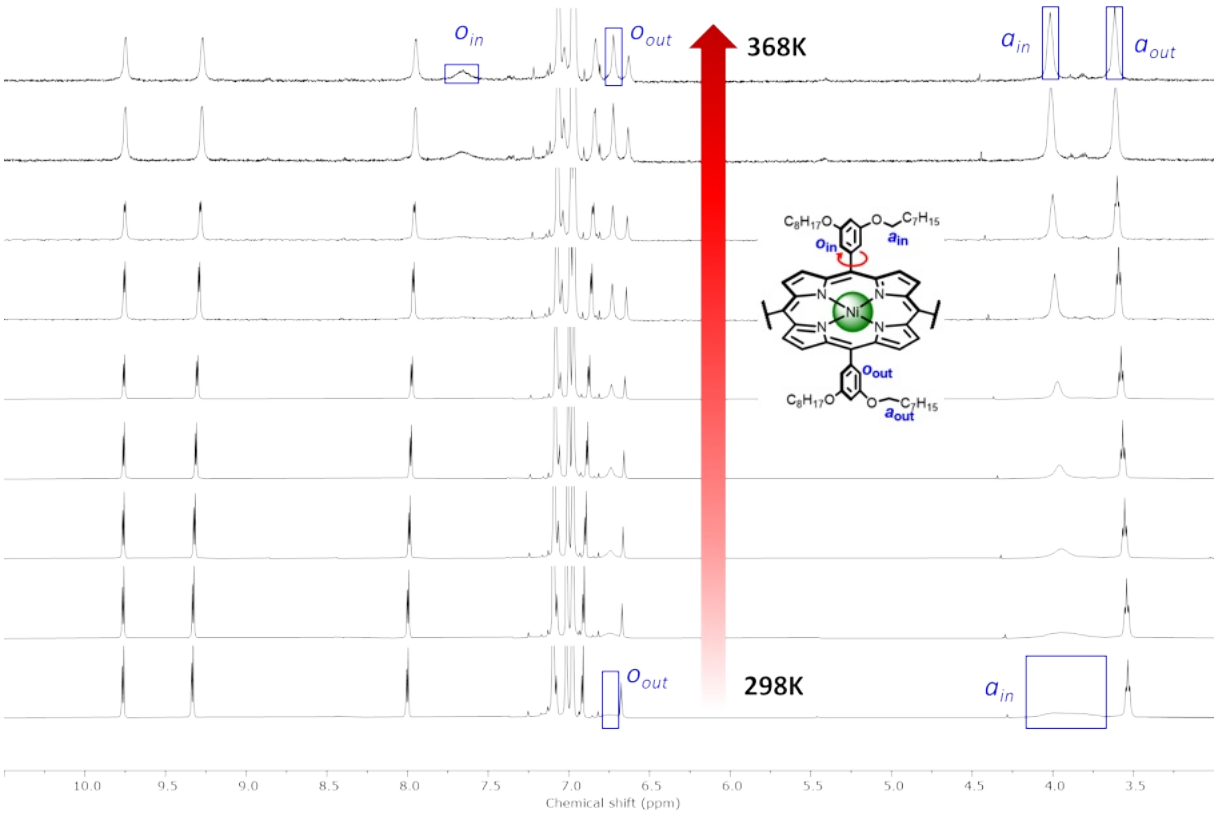

Figure S11. VT ^{1}H NMR of ***cs*-P8$_{OOct}$** (Tol-d_8, 500 MHz, 298–368 K), red arrow indicates the rotation of the porphyrin–phenyl bond.

The case of ***cs*-P10$_{OOct}$** is particularly interesting as both the *meso-meso* and porphyrin-aryl rotation rates are slow on the NMR time scale at room temperature, which makes the ^{1}(Figure S12b). Cooling the sample to 233 K stops the dynamics and splits the signals, leading to a 'frozen' conformation that displays separate signals for each aromatic environment (Figure S12c). On the other hand, heating up the sample to 368 K in TCE-d_2 resulted in a spectrum (Figure S12a) where inside and outside environments coalesce, similar to ***cs*-P12$_{OOct}$** and ***cs*-P14$_{OOct}$**.

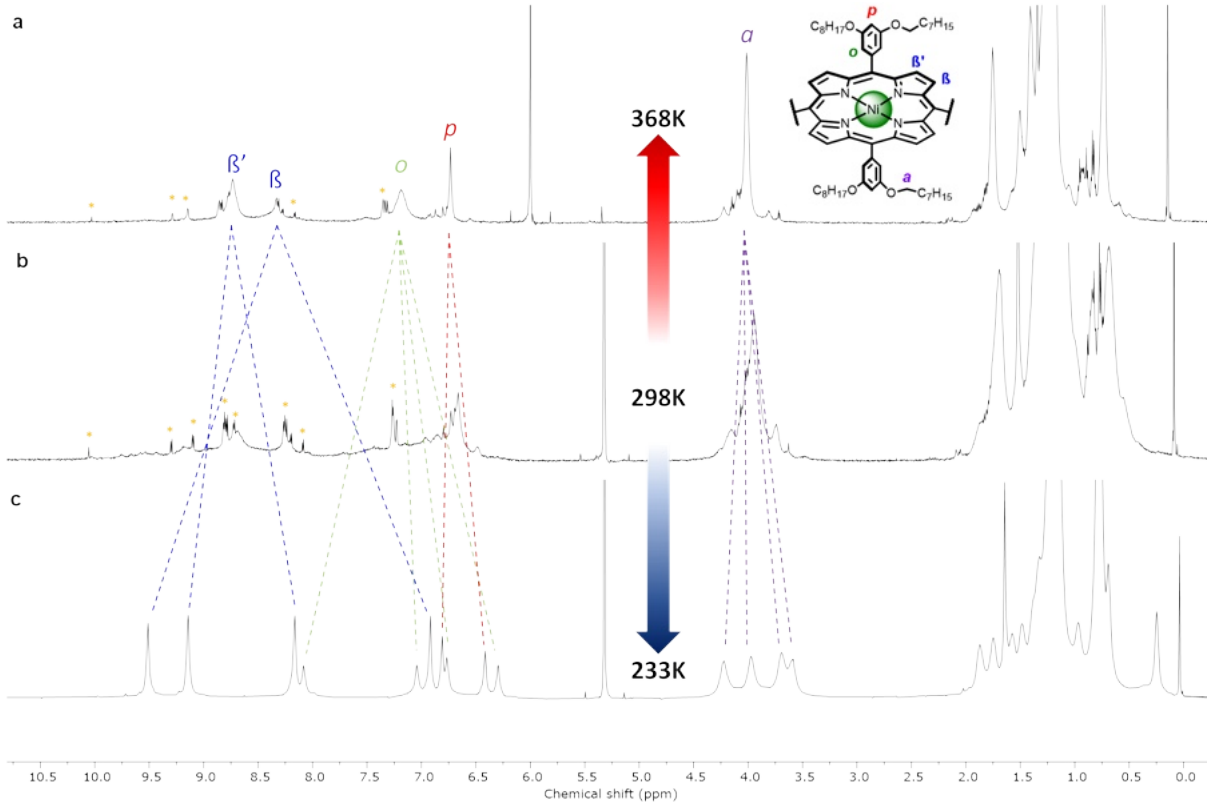

Figure S12. VT ^{1}H NMR of ***cs*-P10$_{OOct}$** a) TCE-d_2, 500 MHz, 368 K b) CD_2Cl_2, 500 MHz, 298 K c) CD_2Cl_2, 500 MHz, 233 K. * Denotes a linear porphyrin oligomer impurity.

One would expect the same sort of behavior from odd-numbered rings; however, due to their odd number of repeat units, they cannot adopt an alternating geometry such as Figure S10. Their lower symmetry leads them to continuously rotate along the *meso-meso* bond to alleviate the steric congestion inside the ring, making inside and outside environments equivalent. Thus, their NMR spectra are simplified and similar to ***cs*-P12$_{OOct}$** (*e.g.* Figure S68). Nevertheless, we encountered some very sterically crowded rings where this rotation is severely slowed down and led to broad NMR spectra. For example, ***cs*-P7$_{OOct}$** was measured at 368 K (Figure S60) to get coalescence of the signals. On the other hand, ***cs*-P9$_{MesBu}$** bears bulky solubilizing chains and displayed a 'frozen' low-symmetry conformation where 36 different β signals were observed (Figure S84).

Section 4.8. Standard Procedure for Porphyrin Nanobelts *cf*-P*N*$_{MesBu}$

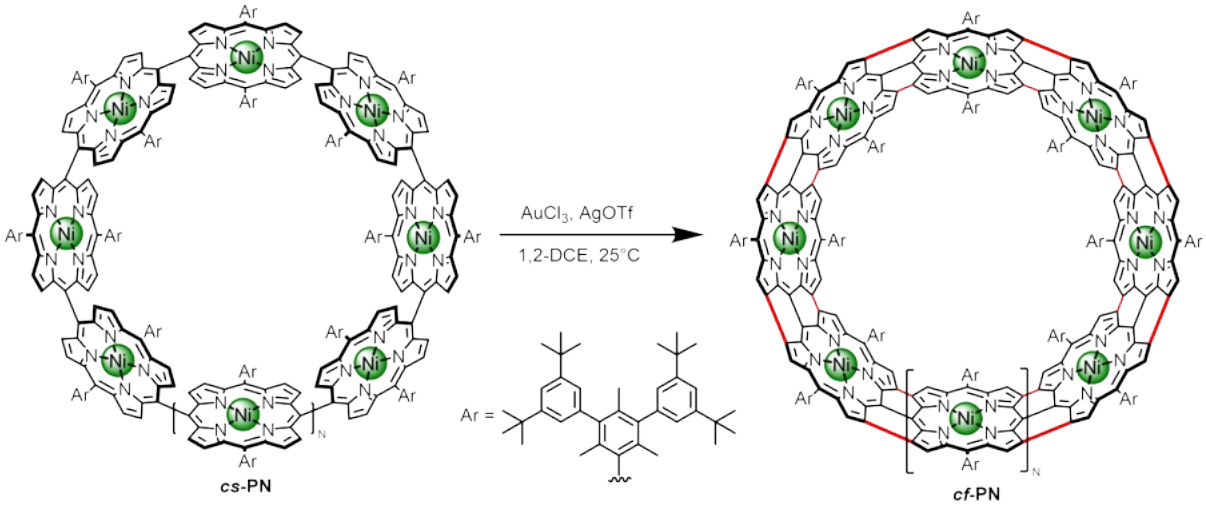

A stock solution of $AuCl_3$ (6.7 mg, 22 µmol, 160 equiv.) and AgOTf (28.5 mg, 111 µmol, 800 equiv.) was prepared by suspending in dry 1,2-dichloroethane (2.3 mL). ***cs*-P8$_{MesBu}$** (1.5 mg, 0.14 µmol) was dissolved in dry 1,2-dichloroethane (1.2 mL). An aliquot (230 µL, 16 equiv. $AuCl_3$, 80 equiv. AgOTf) of the oxidant stock solution was added under vigorous stirring at room temperature. The reaction was monitored by UV-vis spectroscopy after 15 minutes. The fully fused product is characterized by an absorption band at 700–800 nm. When required, further aliquots were added (14 µL, 1 equiv. $AuCl_3$, 5 equiv. AgOTf) and the reaction monitored after each addition until the starting material had fully fused. The reaction was then quenched by the addition of triethylamine (1 mL) and the product precipitated by adding methanol (20 mL). The resulting suspension was centrifuged, the supernatant discarded and the product obtained as a black solid (1.4 mg, 95%).

***cf*-P8$_{MesBu}$**

^{1}H NMR (400 MHz, CD_2Cl_2) δ_H 9.70 (s, 16H, **H**$_{p\ in}$), 9.30 (s, 32H, **H**$_{o\ in}$), 8.77 (s, 32H, **H**ß), 7.94 (s, 48H, **H**$_{m\ in}$), 7.11 (s, 16H, **H**$_{p\ out}$), 6.83 (s, 32H, **H**$_{o\ out}$), 3.54 (s, 288H, **H**$_{t\mathrm{Bu}\ in}$), 2.58 (s, 48H, **H**$_m$), 1.09 (s, 288H, **H**$_{t\mathrm{Bu}\ out}$), –0.46 (s, 48H, **H**$_{m\ out}$).

MALDI-ToF *m*/*z* = 10805.103 ($C_{752}H_{848}N_{32}Ni_8$, M^+ requires 10804.113)

UV-vis (Tol-d_8, 298 K) λ_{max} (ε / 10^4 M^{-1} cm^{-1}): 434 (44.5), 742 (105), 1388 (80.6)

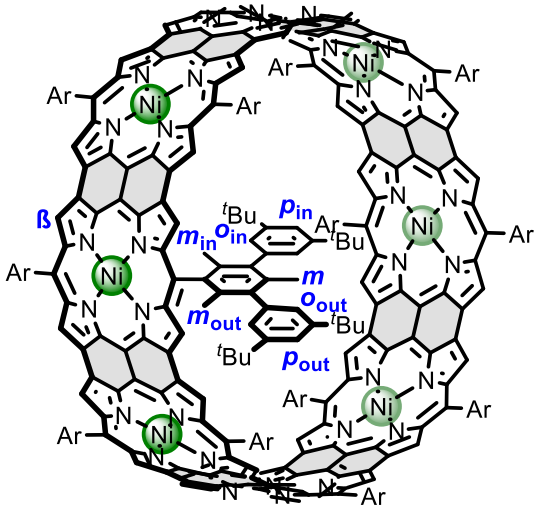

***cf*-P9$_{MesBu}$**

Yield: 94% (1.8 mg) from ***cs*-P9$_{MesBu}$** (1.9 mg, 0.16 µmol)

^{1}H NMR (400 MHz, CD_2Cl_2) δ_H 7.57 (s, 18H, **H$_{p\ out}$**), 7.18 (s, 36H, **H$_{o\ out}$**), 5.64 (s, 18H, **H$_{p\ in}$**), 5.42 (s, 36H, **H$_{o\ in}$**), 5.39 (s, 36H, **H$_{ß}$**), 3.39 (s, 54H, **H$_{m\ out}$**), 1.58 (s, 324H, **H$_{t Bu\ out}$**), 1.13 (s, 54H, **H$_m$**), –0.41 (s, 324H, **H$_{t Bu\ in}$**), –2.12 (s, 54H, **H$_{m\ in}$**).

MALDI-ToF *m/z* = 12159.591 ($C_{846}H_{954}N_{36}Ni_9$, M^+ requires 12154.071)

UV-vis (Tol-*d*$_8$, 298 K) λ_{max} (ε / 10^4 M^{-1} cm^{-1}): 427 (51.6), 758 (125), 1518 (134), 1833 (41.4), 1711 (29.3), 1776 (37.4), 1832 (41.4)

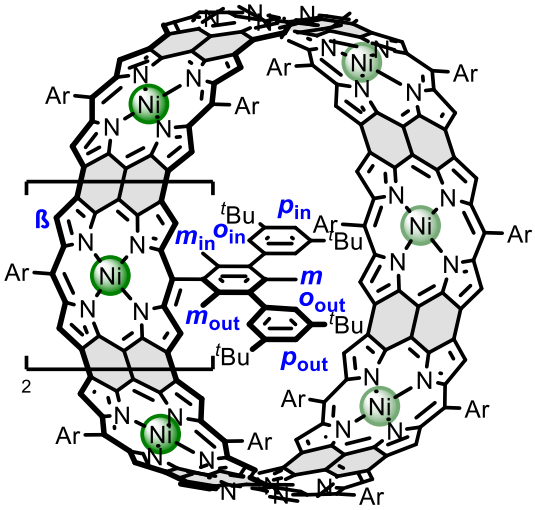

***cf*-P10$_{MesBu}$**

Yield: 93% (1.9 mg) from ***cs*-P10$_{MesBu}$** (2.1 mg, 0.16 µmol)

^{1}H NMR (400 MHz, CD_2Cl_2) δ_H 8.75 (s, 20H, **H$_{p\ in}$**), 8.39 (s, 40H, **H$_{o\ in}$**), 7.73 (s, 40H, **H$_{ß}$**), 7.12 (s, 20H, **H$_{p\ out}$**), 6.80 (s, 40H, **H$_{o\ out}$**), 5.49 (s, 60H, **H$_{m\ in}$**), 2.66 (s, 360H, **H$_{t Bu\ in}$**), 2.22 (s, 60H, **H$_m$**), 1.12 (s, 360H, **H$_{t Bu\ out}$**), 0.20 (s, 60H, **H$_{m\ out}$**).

MALDI-ToF *m/z* = 13505.766 ($C_{940}H_{1060}N_{40}Ni_{10}$, M^+ requires 13504.718)

UV-vis (Tol-*d*$_8$, 298 K) λ_{max} (ε / 10^4 M^{-1} cm^{-1}): 427 (59.4), 759 (143), 1551 (134)

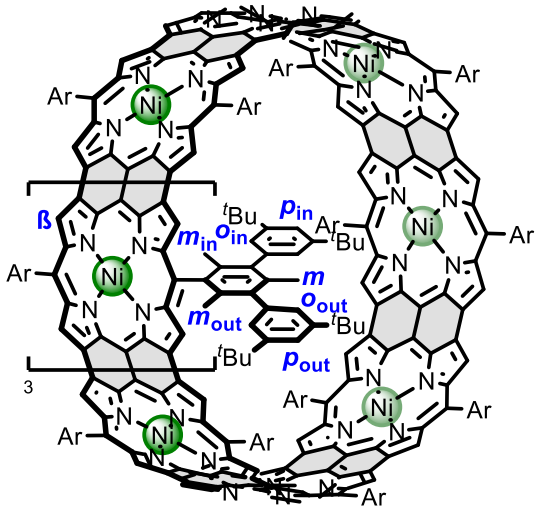

***cf*-P11$_{MesBu}$**

Yield: 96% (2.6 mg) from ***cs*-P11$_{MesBu}$** (2.8 mg, 0.19 µmol)

^{1}H NMR (400 MHz, CD_2Cl_2) δ_H 7.51 (s, 22H, **H$_{p\ out}$**), 7.15 (s, 44H, **H$_{o\ out}$**), 6.16 (s, 22H, **H$_{p\ in}$**), 6.00 (s, 44H, **H$_{ß}$**), 5.94 (s, 44H, **H$_{o\ in}$**), 2.89 (s, 66H, **H$_{m\ out}$**), 1.52 (s, 396H, **H$_{t Bu\ out}$**), 1.40 (s, 66H, **H$_m$**), 0.07 (s, 396H, **H$_{t Bu\ in}$**), –0.66 (s, 66H, **H$_{m\ in}$**).

MALDI-ToF *m/z* = 14864.721 ($C_{1034}H_{1166}N_{44}Ni_{11}$, M^+ requires 14855.485)

UV-vis (Tol-*d*$_8$, 298 K) λ_{max} (ε / 10^4 M^{-1} cm^{-1}): 424 (54.6), 773 (124), 1634 (127), 1781 (43.4), 1877 (48.1), 1933 (56.1)

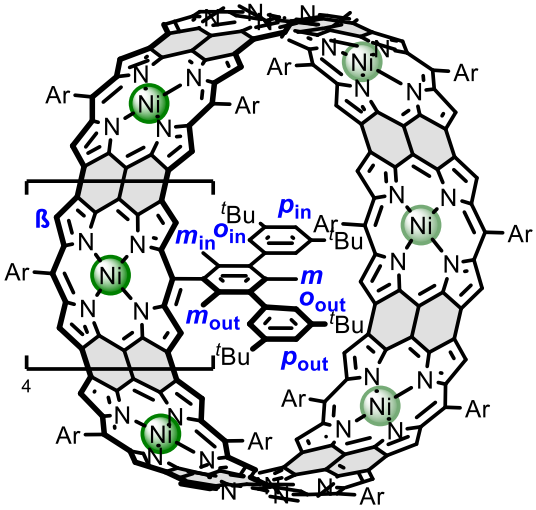

***cf*-P12$_{MesBu}$**

Yield: 94% (2.8 mg) from ***cs*-P12$_{MesBu}$** (3.0 mg, 0.19 µmol)

^{1}H NMR (400 MHz, CD_2Cl_2) δ_H 8.12 (s, 24H, **H$_{p\ in}$**), 7.80 (s, 48H, **H$_{p\ in}$**), 7.25 (s, 48H, **Hß**), 7.20 (s, 24H, **H$_{p\ out}$**), 6.87 (s, 48H, **H$_{o\ out}$**), 3.96 (s, 72H, **H$_{m\ in}$**), 2.03 (s, 504H, **H$_{t\mathrm{Bu\ in}}$**, **H$_m$**), 1.19 (s, 432H, **H$_{t\mathrm{Bu\ out}}$**), 0.79 (s, 72H, **H$_{m\ out}$**).

MALDI-ToF *m*/*z* = 16198.868 ($C_{1128}H_{1272}N_{48}Ni_{12}$, M^+ requires 16206.484)

UV-vis (Tol-*d*$_8$, 298K) λ_{max} (ε / 10^4 M^{-1} cm^{-1}): 420 (76.7), 771 (183), 1667 (185)

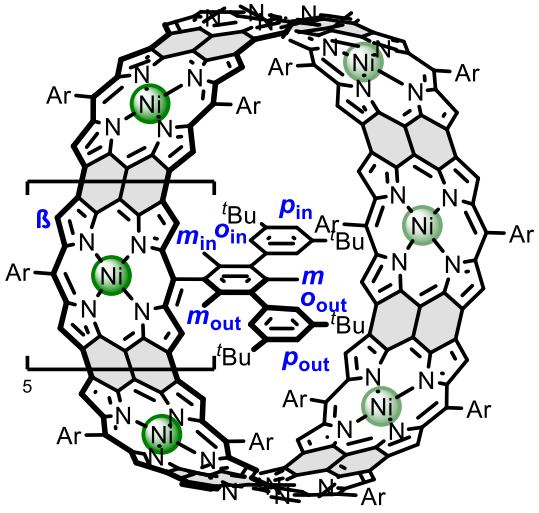

Section 4.9. Comparison of ^{1}H NMR spectra of *cf*-P*N*$_{MesBu}$ Nanobelts

Table S5. ^{1}**H NMR chemical shifts for *cf*-P*N*$_{MesBu}$ (400 MHz, CD_2Cl_2 /CS_2, 298 K).**

^{1}H NMR δ (ppm)	ß	*Me*$_{in}$	*Me*$_{out}$	*Me*	*o*$_{in}$	*o*$_{out}$	*p*$_{in}$	*p*$_{out}$	^{t}Bu$_{in}$	^{t}Bu$_{out}$
***cf*-P8**	8.77	7.95	–0.46	2.57	9.30	6.82	9.69	7.10	3.54	1.09
***cf*-P9**	5.39	–2.12	3.39	1.13	5.42	7.18	5.64	7.57	–0.41	1.58
***cf*-P10**	7.73	5.49	0.20	2.22	8.39	6.80	8.75	7.12	2.66	1.12
***cf*-P11**	6.00	–0.66	2.90	1.40	5.94	7.15	6.15	7.51	0.07	1.53
***cf*-P12**	7.24	3.97	0.78	2.03	7.80	6.86	8.11	7.18	2.04	1.19

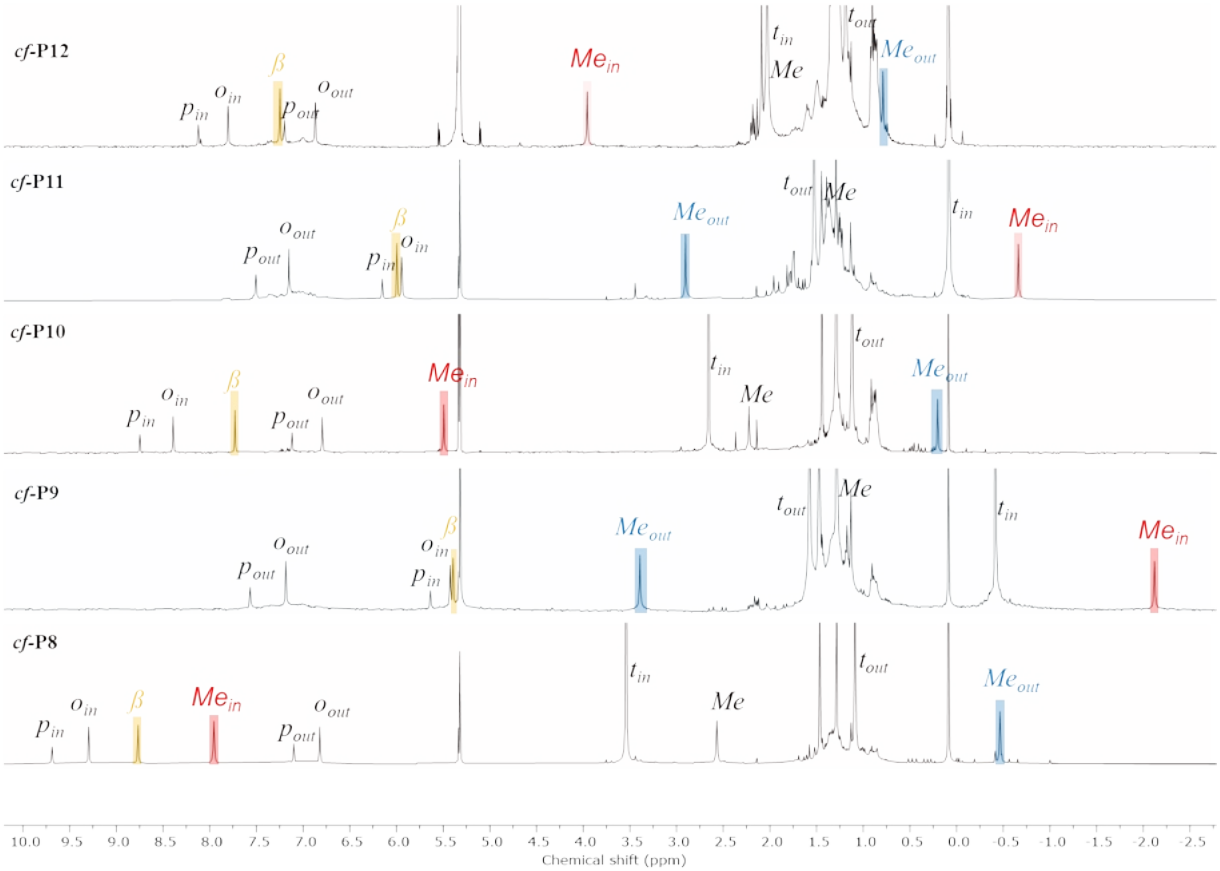

Figure S13. ^{1}H NMR spectra of ***cf*-P*N*$_{MesBu}$** (CD_2Cl_2/CS_2, 298 K, 400 MHz).

The shifts induced by global (anti)aromatic ring currents, Δδ (Table S6) were estimated by comparing the ^{1}H NMR resonances *Me*$_{in}$, *Me*$_{out}$, *o*$_{in}$, *o*$_{out}$, *p*$_{in}$ and *p*$_{out}$ in ***cf*-P*N*$_{MesBu}$** with the corresponding resonances of **MesBu** (Figure S14) recorded under identical conditions.

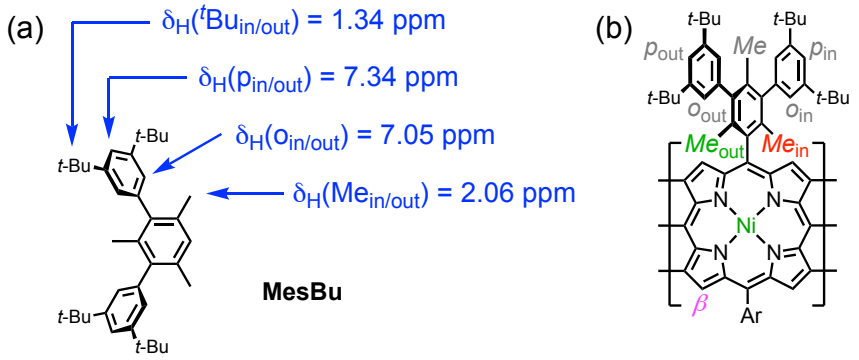

Figure S14. **(a)** Structure of the **MesBu** reference compound and ^{1}H NMR chemical shift of the methyl group (CD_2Cl_2, 298 K, 400 MHz). (b) Labelling scheme for ***cf*-P*N*$_{MesBu}$**.

Table S6. Experimental ^{1}H NMR Δδ values for ***cf*-P*N*$_{MesBu}$** (400 MHz, CD_2Cl_2, 298 K) from comparison with **MesBu** reference compound (Fig. S14).

^{1}H NMR δ (ppm)	***Me*$_{in}$**	***Me*$_{out}$**	***o*$_{in}$**	***o*$_{out}$**	***p*$_{in}$**	***p*$_{out}$**	**^{t}Bu$_{in}$**	**^{t}Bu$_{out}$**
***cf*-P8**	5.88	–2.52	2.25	–0.22	2.36	–0.23	2.20	–0.25
***cf*-P9**	–4.18	1.33	–1.63	0.13	–1.70	0.23	–1.75	0.24
***cf*-P10**	3.43	–1.86	1.34	–0.25	1.41	–0.22	1.32	–0.22
***cf*-P11**	–2.72	0.83	–1.11	0.10	–1.18	0.17	–1.27	0.18
***cf*-P12**	1.90	–1.27	0.75	–0.18	0.78	–0.15	0.69	–0.15

Table S7. Computed Δδ values for ***cf*-P*N*$_{MesBu}$** (DFT, OX-B3LYP/def2-SVP) from comparison with **MesBu** reference compound (Fig. S14).

^{1}H NMR δ (ppm)	***Me*$_{in}$**	***Me*$_{out}$**	***o*$_{in}$**	***o*$_{out}$**	***p*$_{in}$**	***p*$_{out}$**	**^{t}Bu$_{in}$**	**^{t}Bu$_{out}$**
***cf*-P8**	8.46	–2.99	3.46	–0.07	3.54	–0.24	3.41	–0.28
***cf*-P9**	–5.74	1.78	–2.06	0.23	–2.24	0.30	–2.15	0.27
***cf*-P10**	4.90	–2.11	2.15	–0.11	2.23	–0.17	2.05	–0.23
***cf*-P11**	–3.82	1.29	–1.32	0.22	–1.52	0.29	–1.49	0.25
***cf*-P12**	2.71	–1.43	1.30	–0.09	1.33	–0.10	1.28	–0.16

Computational details. All calculations utilized the OX-B3LYP/def2-SVP level of theory, which has been tuned to describe extended conjugation in porphyrin nanobelts (*23*). To reduce the computational load, only a single **MesBu** group was included. Geometries of ***cf*-P*N*$_{MesBu}$** (N = 7–12) were optimized and their chemical shifts were compared with **MesBu**. No scaling was done. Calculations were done using Gaussian16 (*53*). Output files are included at a separate piece of Supplementary Material and are available from Zenodo: 10.5281/zenodo. 15675187 *(49)*.

OX-B3LYP reproduces the experimental Δδ values very well (Figure S15), with a mean absolute error of 0.48 ppm. Linear regression between computed and experimental Δδ values reveals that OX-B3LYP overestimates the ring current by about 30% ($\Delta\delta_{exp}$ = 0.73 $\Delta\delta_{calc}$ + 0.16 ppm; R^2 = 0.9937), which may be attributed to distortion of the nanobelts (a) due to the presence of 2N **MesBu** groups and (b) due to temperature, which may cause them to assume an elliptical shape. Both of these effects reduce magnitude of the ring current by reducing symmetry, and neither of them are accounted for in calculations, which include only a single **MesBu** group and a single geometry of the nanobelt.

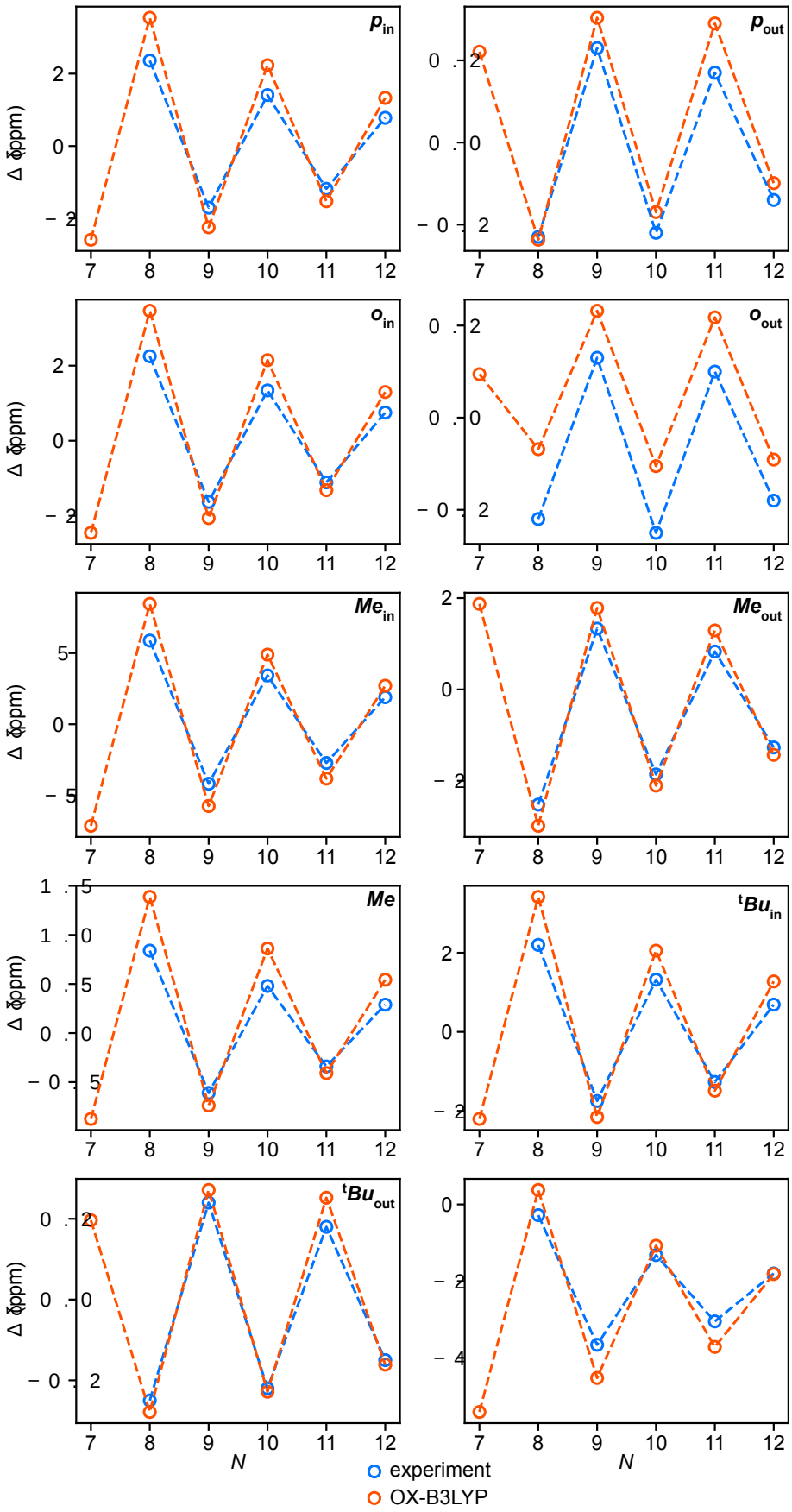

Figure S15. Measured (blue) and computed (orange) Δδ values for ***cf*-P*N*$_{\mathbf{MesBu}}$** relative to **MesBu** for $N = 8$–12. Computed values for $N = 7$ are also included.

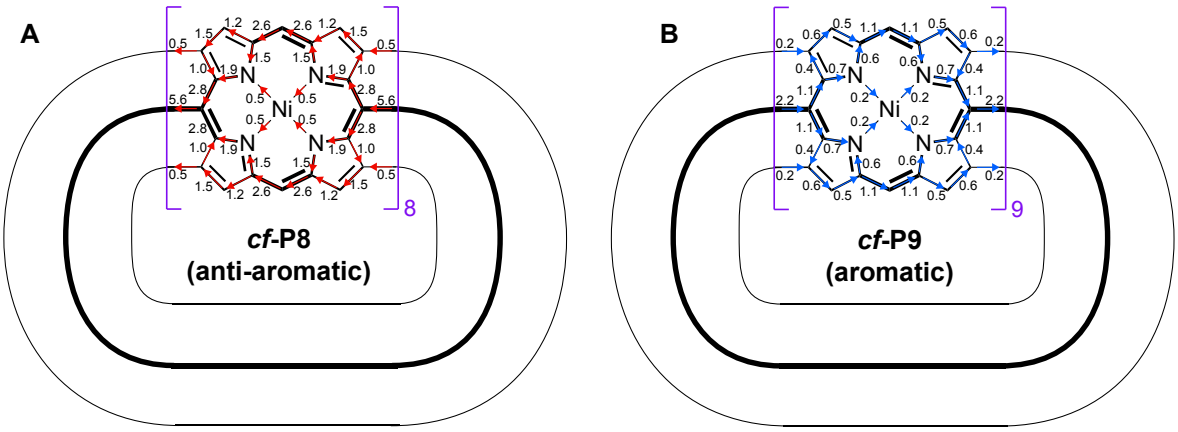

Figure S16. Bond currents in (A) ***cf*-P8** and (B) ***cf*-P9**. Currents were calculated at the OX-B3LYP/def2-SVP level of theory using optimized nanobelt geometries without side-chains. Bond current calculations were done using SYSMOIC *(46)*. Integration limits for current density (2.65 Å around each bond) were chosen so that the integrated bond currents approximately obey Kirchhoff's law. Integrated ring currents are given in units of the benzene ring current (12 nA/T). For both systems, the shown currents were calculated from the density associated with HOMO and HOMO–1 due to system size; in our previous work (*23*) we found that this accounts for 80–90% of the total bond current.

Section 4.10. Biot-Savart Law Analysis of ^{1}H NMR spectra of *cf*-P*N*$_{MesBu}$ Nanobelts

In order to compare the magnitudes of the ring currents in the different ***cf*-P*N*$_{MesBu}$** nanobelts, we analyzed the data in Table S6 using the ring current loop model developed by Jirasek et al. (*18*) (the model and its implementation are described, together with the corresponding MATLAB scripts in the Supplementary Information to ref. *18*). In brief, the Bio-Savart law enables one to calculate the magnetic field at any point in space arising from a current flowing between two points in space. Based on the DFT-optimized geometries of the neutral ***cf*-P8$_{MesBu}$**, ***cf*-P9$_{MesBu}$**, ***cf*-P10$_{MesBu}$**, ***cf*-P11$_{MesBu}$** and ***cf*-P12$_{MesBu}$**, we construct a current loop model consisting of linear segments of infinitely thin wire following the conjugated path of the nanoring (Figure S17). We then calculate the ring current geometric factor (RCGF, Table S8) for the ^{1}H resonances listed in Table S6 assuming a fixed ring current of 1 nA. Finally, the experimentally observed chemical shift difference (Δδ) from Table S6 are plotted against the RCGF values to give a straight line passing through the origin (Figures S18–22). In each case, the gradient of this line is the ring current susceptibility *I*/*B* (Table S9). The excellent fits to a straight line in Figures S18–22 show that the experimental Δδ values fit well to a global ring current model.

Table S8. Ring current geometric factors (RCGFs) for the ^{1}H resonances listed in Table S6.

RCGF (ppm T / nA)	***Me*$_{in}$**	***Me*$_{out}$**	***o*$_{in}$**	***o*$_{out}$**	***p*$_{in}$**	***p*$_{out}$**	**^{t}Bu$_{in}$**	**^{t}Bu$_{out}$**
***cf*-P8**	–0.0454	0.0552	–0.0031	0.0574	–0.0050	0.0548	–0.0053	–0.0454
***cf*-P9**	–0.0486	0.0548	–0.0046	0.0574	–0.0062	0.0552	–0.0065	–0.0486
***cf*-P10**	–0.0635	0.0337	–0.0195	0.0455	–0.0138	0.0425	–0.0145	–0.0635
***cf*-P11**	–0.0536	0.0541	–0.0067	0.0582	–0.0078	0.0564	–0.0082	–0.0536
***cf*-P12**	–0.0658	0.0378	–0.0188	0.0480	–0.0143	0.0457	–0.0150	–0.0658

Table S9. Ring current susceptibility calculated from the experimental data in Table S6 using the Bio-Savart law and a ring current loop model, based on the RCGDs in Table S8.

nanobelt	*I*/*B* (nA/T)
***cf*-P8**	41.9
***cf*-P9**	–29.8
***cf*-P10**	31.3
***cf*-P11**	–20.0
***cf*-P12**	17.2

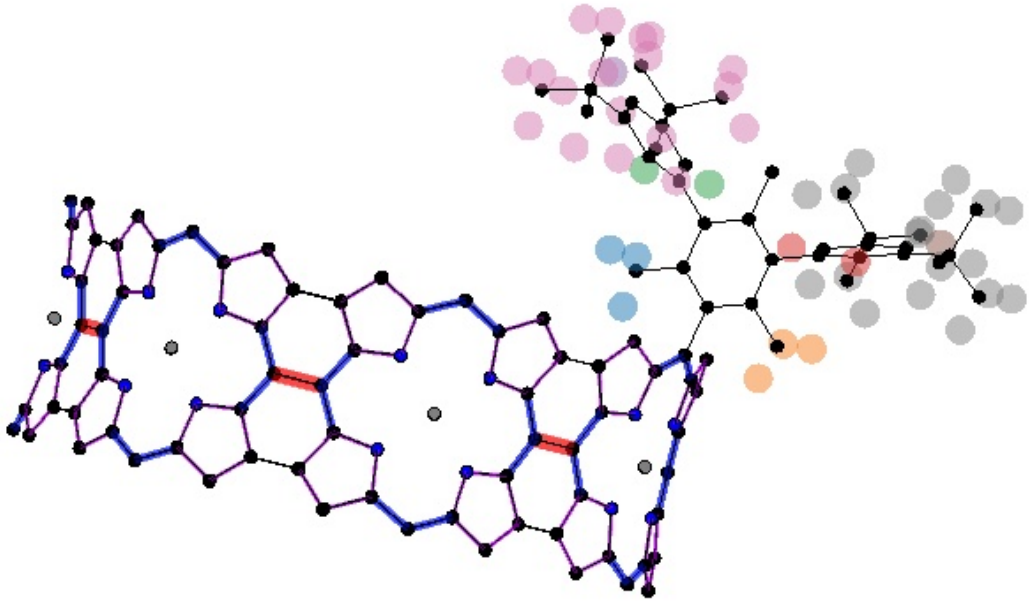

Figure S17. Illustration of the ring current model, as applied to ***cf*-P7**.

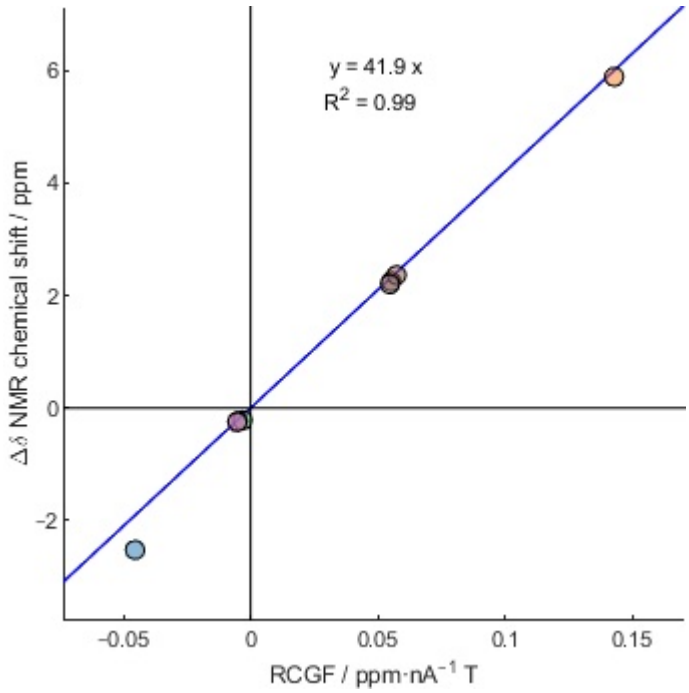

Figure S18. Ring current model fit for ***cf*-P8**.

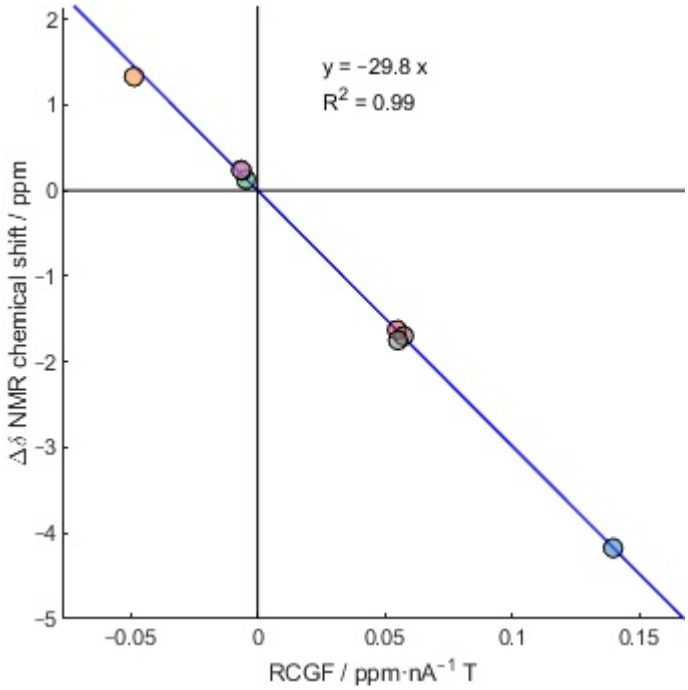

Figure S19. Ring current model fit for ***cf*-P9**.

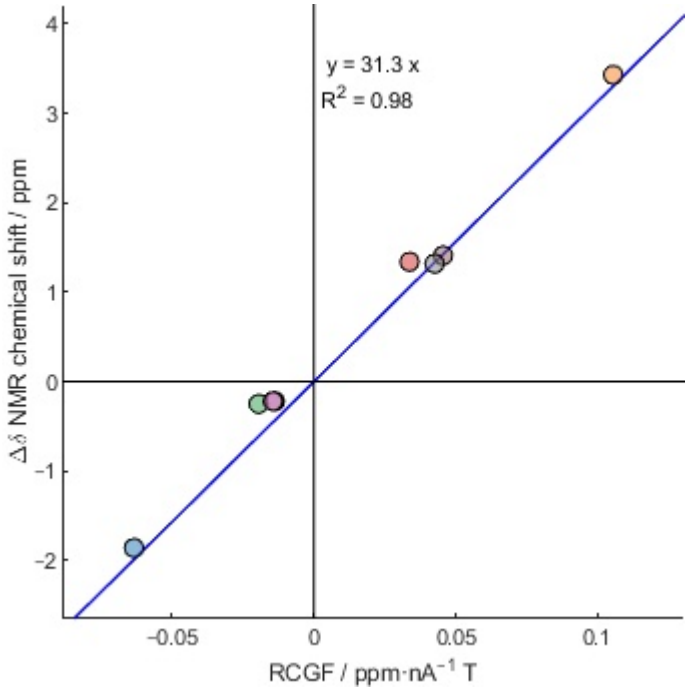

Figure S20. Ring current model fit for ***cf*-P10**.

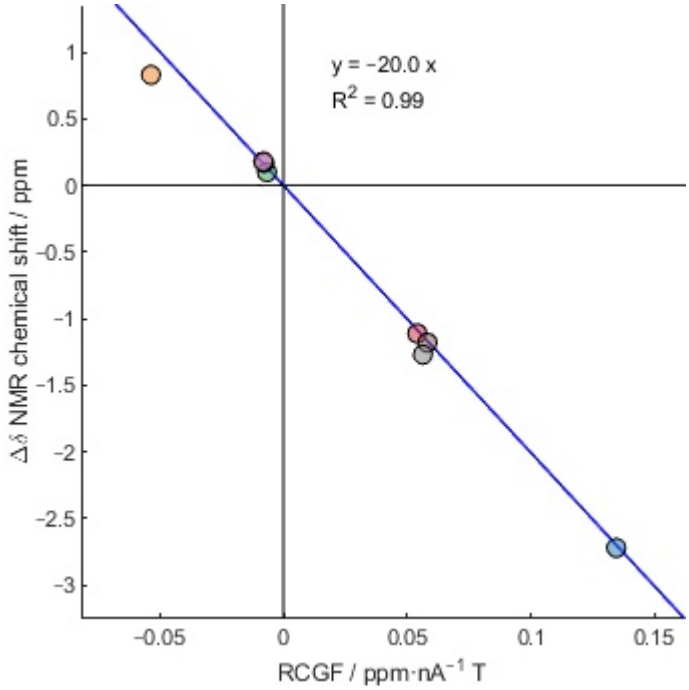

Figure S21. Ring current model fit for ***cf*-P11**.

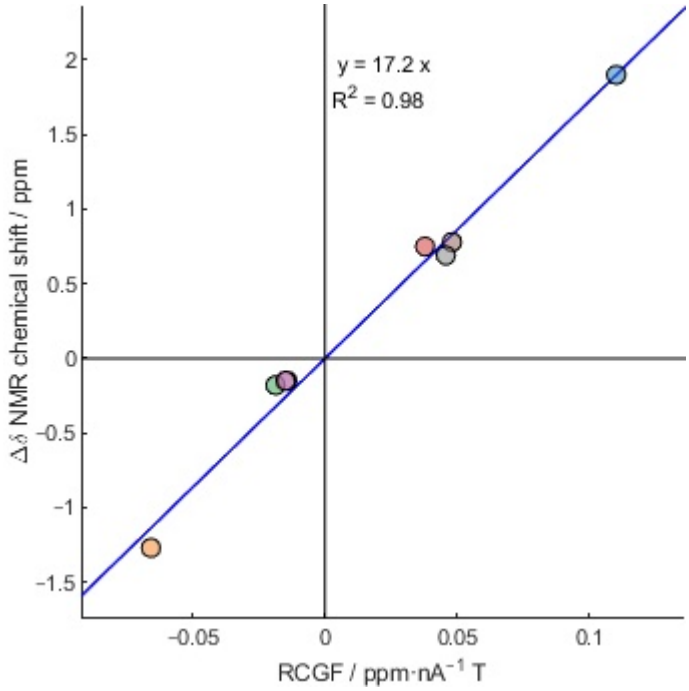

Figure S22. Ring current model fit for ***cf*-P12**.

Section 5. Scanning Tunnelling Microscopy

Section 5.1. Experimental Methods

STM image acquisition. Scanning tunneling microscopy (STM) image acquisition was performed using a Scienta Omicron POLAR low-temperature STM system operating under ultra-high vacuum (UHV) conditions. The UHV system has a base pressure of sub 3×10^{-10} mbar. The STM measurement stage was cooled with liquid helium (4.7 K). All STM images were measured in constant current mode with electrochemically etched tungsten tips that may be coated in gold during tip optimization (achieved via controlled indentation into the Au(111) substrate). Image acquisition parameters (sample bias and current set-point) are stated within figure captions. Au(111) on mica surfaces (Georg Albert PVD GmbH) were prepared by cycles of argon ion sputtering (30 minutes at a pressure of around 1×10^{-5} mbar) and annealing (~520 °C). Annealing temperatures were estimated by thermocouple measurements close to the heating stage.

Electrospray deposition. All molecules (***cs*-P8$_{OOct}$**, ***cs*-P12$_{OOct}$**, and ***cs*-P18$_{OOct}$**) were deposited upon a clean Au(111)/mica substrate held under vacuum via electrospray ionization (Molecularspray Ltd, UHV4i source). Solutions of the material (40 µg/mL for ***cs*-P8$_{OOct}$**, ***cs*-P12$_{OOct}$**, and ***cs*-P18$_{OOct}$**) were prepared in toluene/methanol (4:1 volume ratio) and were deposited using the method described in our previous work (*33-35*). A chamber pressure of around 4×10^{-7} mbar was obtained within the deposition chamber by varying the solvent flow rate/ionization voltage. Sub-monolayer coverages were achieved, as determined by regular XPS measurement of the C 1*s* and Au 4*f* regions and compared with prior depositions where the presence of a sub-monolayer coverage had been characterized by STM [Deposition times: ***cs*-P18$_{OOct}$** and ***cs*-P8$_{OOct}$** = 40 minutes; ***cs*-P12$_{OOct}$** = 80 minutes]. Samples were transported between the STM and X-ray photoelectron spectroscopy (XPS) UHV systems using a vacuum suitcase operating at a pressure of $< 1 \times 10^{-10}$ mbar.

XPS acquisition. XPS measurements were acquired using a SPECS DeviSim near ambient pressure XPS (NAP-XPS) instrument operating in ultra-high vacuum (UHV) mode at a pressure $< 1 \times 10^{-9}$ mbar. Spectra were measured using a Phoibos 150 NAP hemispherical analyzer with 20 eV pass energy and monochromatic Al Kα X-rays (1486.7 eV).

Section 5.2. Characterization via STM and XPS

XPS characterization of the ***cs*-P8$_{OOct}$** species following electrospray deposition onto a clean Au(111) surface is shown in Figure S23. Within the Ni 2*p* region (Figure S23a) peaks at 855.5 and 872.8 eV are assigned to the spin-orbit splitting of the Ni 2*p* signal and the smaller satellite feature (~863 eV) is assigned (based upon previous work) (*54, 55*) to a signature of the metal-organic interaction between the Ni and surrounding N atoms within the macrocycles of the porphyrin sub-units of ***cs*-P8$_{OOct}$**. The N 1*s* XPS region displays a single peak at 399.1 eV (Figure S23b), assigned to the single nitrogen environment of the four N atoms withing the macrocycle of each porphyrin sub-unit. XPS analysis demonstrates that the metalated core of the porphyrin sub-units are intact following electrospray deposition.

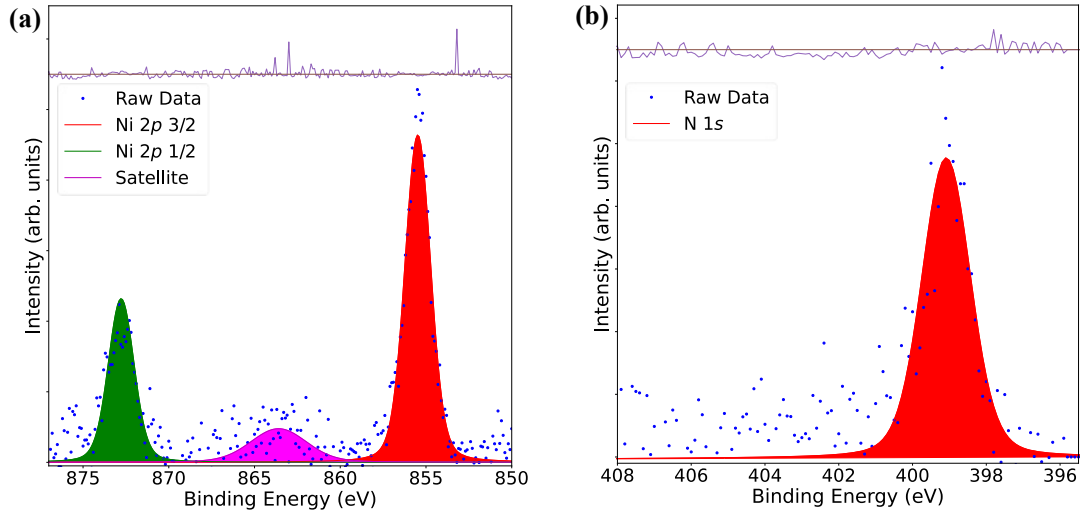

Figure S23. XPS characterization of ***cs*-P8$_{OOct}$** on Au(111). (a) Ni 2*p* region showing the presence of the $2p_{3/2}$ and $2p_{1/2}$ peaks (855.5 and 872.8 eV, respectively) as well as a small satellite feature (~863 eV) which is indicative of a metal-organic interaction. (b) N 1*s* region showing a single feature (399.1 eV) corresponding to the expected nitrogen environment for the metalated porphyrin units within the cyclic polymer.

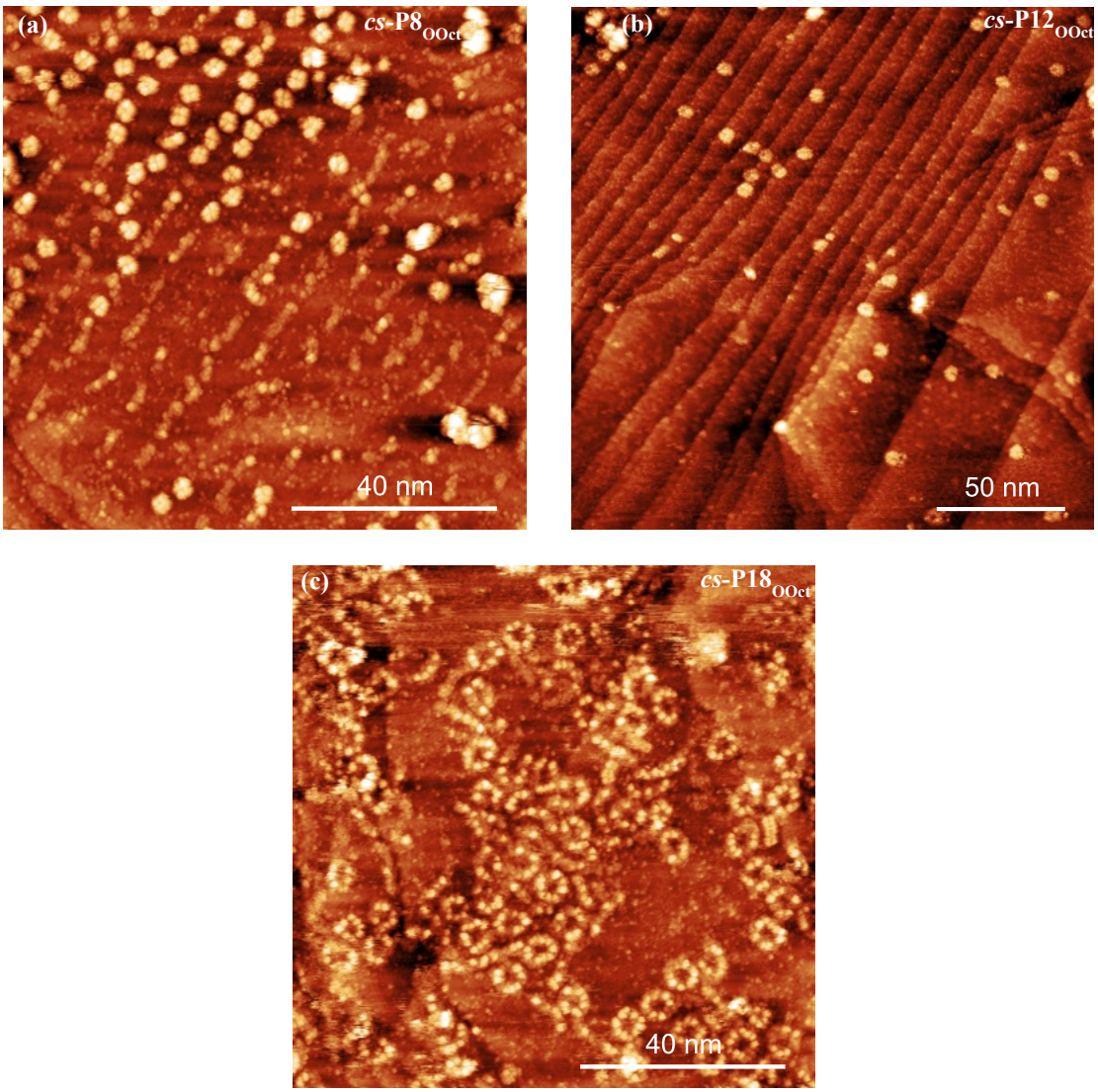

Figure S24. STM topographs of (a) ***cs*-P8$_{OOct}$**, (b) ***cs*-P12$_{OOct}$**, and (c) ***cs*-P18$_{OOct}$** on Au(111) following electrospray deposition. Within each image distinct topographic features can be identified corresponding to the cyclic polymer species. [Image parameters: (a) bias = –2 V, set-point current = 9 pA; (b, c) 2 V, 20 pA]

Following electrospray deposition of the ***cs*-P*N*** rings, STM topographs were recorded to provide details of the large-scale surface morphology. Overview images for ***cs*-P8$_{OOct}$**, ***cs*-P12$_{OOct}$**, and ***cs*-P18$_{OOct}$** are shown in Figure S24. High resolution STM topographs for ***cs*-P8$_{OOct}$**, ***cs*-P12$_{OOct}$**, ***cs*-P18$_{OOct}$** are shown in Figure S25. For each of the ***cs*-P*N*** variants distinct topographical features can be identified; the number of features within each ring corresponding to half the number of porphyrin sub-units (i.e. ***cs*-P8$_{OOct}$**, 4 features; ***cs*-P12$_{OOct}$**, 6 features; ***cs*-P18$_{OOct}$**, 9 features). This observation is in agreement with the single-crystal X-ray crystallography data discussed within the main manuscript (Figure 3D) where the macrocycle of ***cs*-P8$_{tBu}$** exhibits a highly twisted geometry and neighbouring porphyrin units are almost orthogonal. Such a twisted geometry would occlude the visibility within STM constant current topographs of alternate porphyrins around the cyclic polymer; the periodic variation in porphyrin height relative to the substrate leads to only half of the sub-units being clearly imaged.

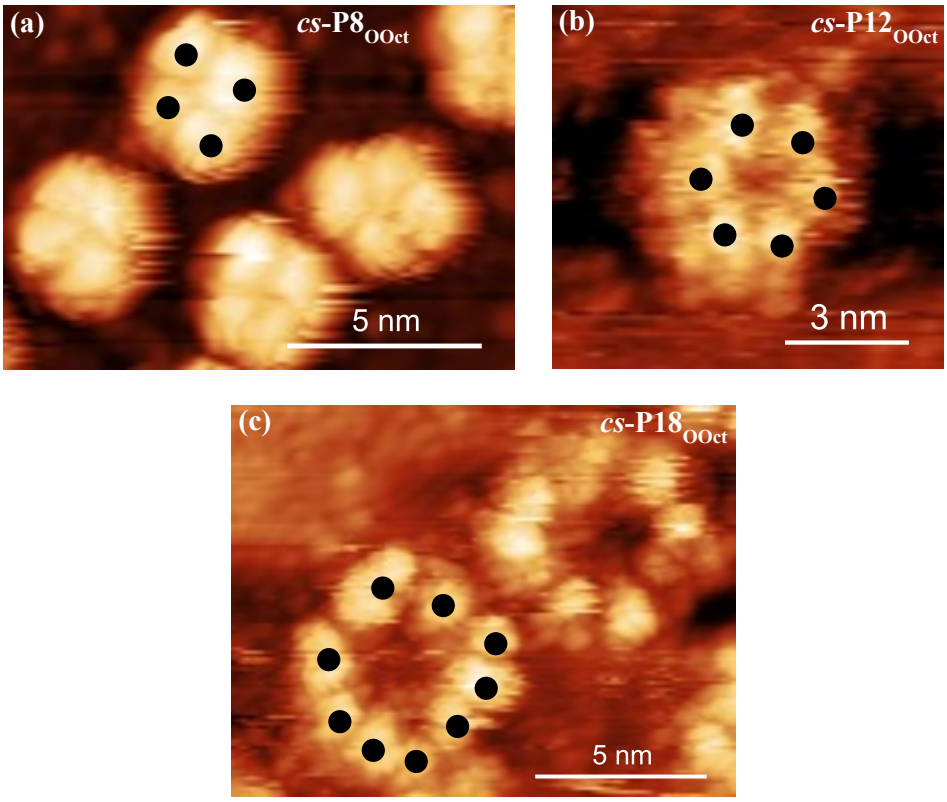

Figure S25. STM topographs of (a) ***cs*-P8$_{OOct}$**, (b) ***cs*-P12$_{OOct}$**, (c) ***cs*-P18$_{OOct}$** on Au(111) following electrospray deposition. Within each image distinct topographic features can be identified corresponding to every other porphyrin sub-unit within the cyclic polymer. [Image parameters: (a) bias = –2 V, set-point current = 9 pA; (b) –1.2 V, 20 pA; (c) 2 V, 20 pA]

The dimensions of the nanoring structures were measured from line profiles acquired along the long and short axes of the rings (as shown in Figure S26). Peak-to-peak measurements were obtained to determine the separation between the features corresponding to the position of the nanoring circumference. Measurements were performed on data acquired with both 'forward' and 'backward' scan directions. An average of the two measurements was taken, to minimize the effect of drift. The circumference of the rings was estimated using the Ramanujan approximation for the circumference of an ellipse:

$$C \approx \pi[3(a+b) - \sqrt{(3a+b)(a+3b)}],$$

where C is the circumference of the ellipse, with a and b being the radii of the long- and short-axis of the ellipse, respectively.

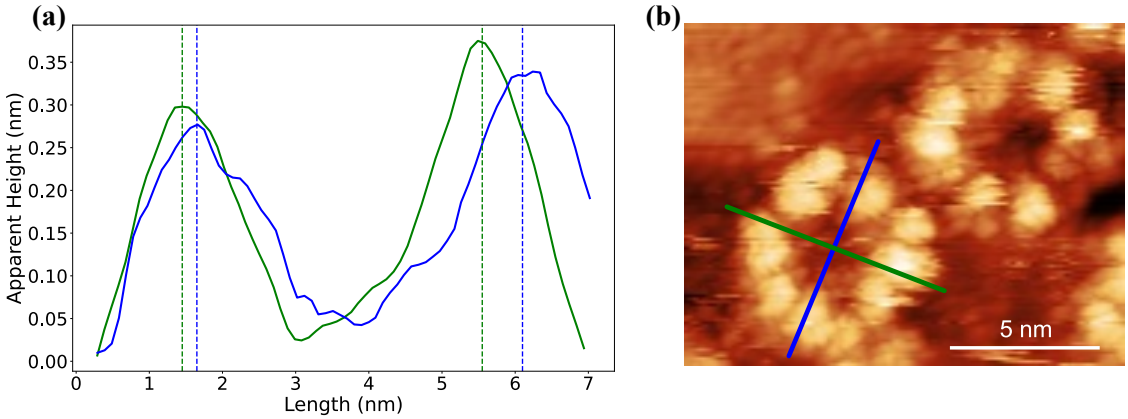

Figure S26. Dimensions of ***cs*-P18$_{OOct}$** on Au(111) following electrospray deposition characterized by STM. (a) Line profiles acquired for the long (a) and short (b) axes of a nanoring structure following deposition on Au(111); line profile locations are shown within the forwards scan of the STM image, (b) STM image (bias = 2 V, set-point current = 20 pA). Peak-to-peak separation on the blue and green line profiles are 4.5 nm and 4.1 nm respectively. These measurements were averaged with the same measurements taken on the backwards scan to produce a drift-compensated measurement for a and b.

The measured dimensions for ***cs*-P8$_{OOct}$**, ***cs*-P12$_{OOct}$**, ***cs*-P18$_{OOct}$** are shown in Figure S27. The average dimensions for C, a, and b are shown in Table S10.

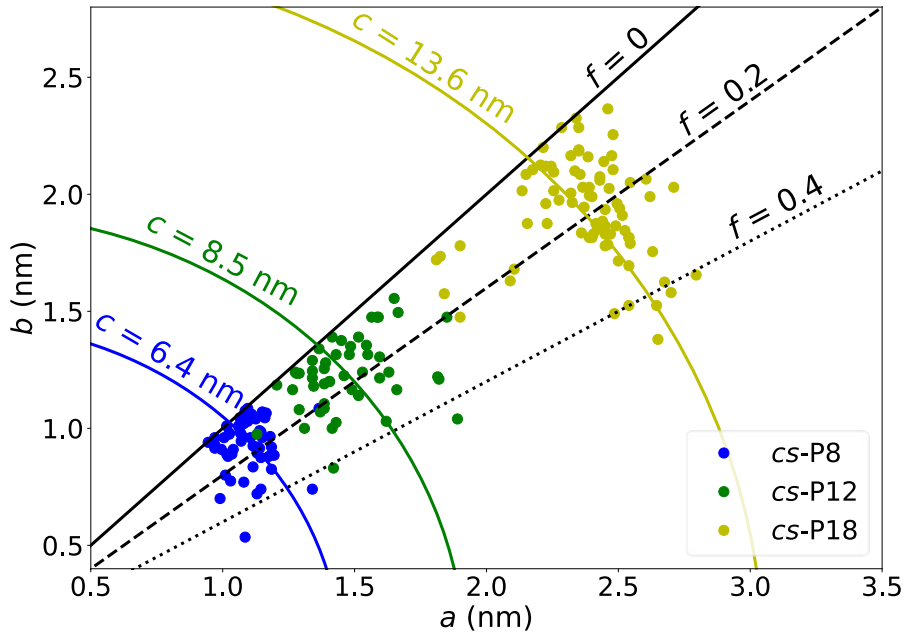

Figure S27. Plot of experimentally measured long (a) versus short (b) radii for three ***cs*-P*N*** species. $f = 1 - b/a$ indicates the ellipticity or flattening factor of the nanorings. The blue arcs correspond to ellipses of fixed circumference calculated using the Ramanujan's approximations – the values are equivalent to the average circumference. The solid black line indicates circular geometries ($a = b, f = 0$). The dotted lines represent $f =$, 0.2 and 0.4, the shape becoming more elliptical with increasing f value.

Table S10. Measured values for *C* (circumference), *a* and *b* (radii of the long- and short-axis) for the electrospray deposited species ***cs*-P8$_{OOct}$, *cs*-P12$_{OOct}$, *cs*-P18$_{OOct}$** on Au(111). For each species, *n* individual rings were measured.

cs*-P*N	*a* (nm)	*b* (nm)	*C* (nm) Experiment	*C* (nm) Predicted*	*n*
***cs*-P8$_{OOct}$**	1.1 ± 0.1	0.9 ± 0.1	6.4 ± 0.5	6.5	59
***cs*-P12$_{OOct}$**	1.5 ± 0.2	1.2 ± 0.2	8.5 ± 0.8	9.8	50
***cs*-P18$_{OOct}$**	2.4 ± 0.2	1.9 ± 0.2	13.6 ± 0.9	14.6	79

* Ni···Ni circumference from DFT calculations.

Figure S27 highlights the distribution of nanoring dimensions, alongside the average circumference and black solid/ dashed lines representing the flattening factor *f* :

$$f = \frac{a-b}{a}.$$

It can be seen that for increasing *N* the spread in flattening factor increases, indicating an increase in ring flexibility with increased number of porphyrin sub-units. There is excellent agreement between the experimentally measured and predicted values of the nanoring circumference (Table S10).

Section 6. X-Ray Crystallography

ls-P2$_{t\text{Bu}}$Br$_2$

Crystals were grown by diffusing methanol vapor into a solution of ***ls*-P2$_{t\text{Bu}}$Br$_2$** in *ortho*-dichlorobenzene (*o*-DCB) and *n*-hexane. X-ray data collection for ***ls*-P2$_{t\text{Bu}}$Br$_2$** was performed at the Department of Chemistry, University of Oxford using a (Rigaku) Oxford Diffraction SuperNova diffractometer at 150 K and subsequently reduced using CrysAlisPro. After transferring a suspension of crystals in mother liquor to NVH oil (MiTeGen, LLC) smeared over a glass slide, a suitable crystal was very quickly (in few seconds) placed on a 50 μm MiTeGen loop and mounted on a goniometer head. The crystals suffer from immediate solvent loss, which destroys their crystallinity. Moreover, they dissolve in all types of tested cryoprotecting oils, and the best results were observed when NVH oils were used.

The structure was solved with the Superflip (*56*) charge-flipping algorithm and refined by full-matrix least-squares procedures using the SHELXTL (version 2018/3) (*57*) software package through the OLEX2 graphical interface (*57*). All non-hydrogen atoms, including those in disordered parts, were refined anisotropically.

The structure was modelled with aid of several restraints placed both on appropriate distances (SADI) and displacement parameters (SIMU, RIGU). *Tert*-butyl groups were modelled after introducing appropriate restrains on their 1,2- and 1,3- distances. The current model involves three *o*-DCB molecules Two of the disordered *o*-DCB molecules were treated with appropriate restraints put on the 1,2- and 1,3-distances assuming 6-fold symmetry of the phenyl rings, after splitting into two parts. One *o*-DCB and a solvent molecule, which seems to be *n*-hexane lie in the same place were modelled with support of the PART -1 option, additionally being treated with a list of geometrical and ADP restraints provided by the FragmentDB tool.

The beta angle is very close to 90 degrees. Attempts to process the data in orthorhombic cell resulted in unreasonably high R_{int} (>40%), so the beta angle seems to be randomly close to 90 degrees and the cell is truly monoclinic.

The crystallographic data have been deposited with the Cambridge Crystallographic Data Center (CCDC 2463702), and copies of these data can be obtained free of charge from the Cambridge Crystallographic Data Center via www.ccdc.cam.ac.uk/data_request/cif

Table S11. Measurement and refinement details for ***ls*-P2$_{t\mathrm{Bu}}$Br$_2$**.

Identification code	***ls*-P2$_{t\mathrm{Bu}}$Br$_2$**
CCDC deposition number	2463702
Empirical formula	$C_{112.61}H_{113.39}Br_2Cl_{5.07}N_8Ni_2$
Formula weight	2035.88
Temperature/K	150.00(10)
Crystal system	monoclinic
Space group	$P2_1/c$
a/Å	12.7428(2)
b/Å	27.9258(6)
c/Å	29.1800(3)
α/°	90
β/°	90.0910(10)
γ/°	90
Volume/Å^3	10383.8(3)
Z	4
ρ_{calc}g/cm^3	1.302
μ/mm^{-1}	2.941
F(000)	4229.0
Crystal size/mm^3	0.2 × 0.18 × 0.02
Radiation	Cu Kα (λ = 1.54184)
2Θ range for data collection/°	6.33 to 152.61
Reflections collected	131637
Independent reflections	21495 [R_{int} = 0.0475, R_{sigma} = 0.0249]
Data/restraints/parameters	21495/1695/1478
Goodness-of-fit on F^2	1.085
Final R indexes [I>=2σ (I)]	R_1 = 0.0751, wR_2 = 0.1919
Final R indexes [all data]	R_1 = 0.0918, wR_2 = 0.2066
Largest diff. peak/hole / e Å^{-3}	1.03/–1.06

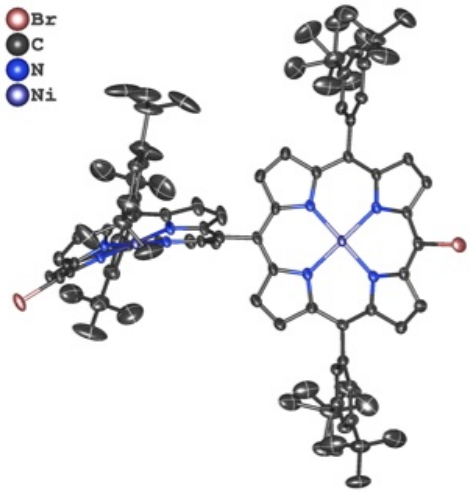

Figure S28. Displacement ellipsoid plot of the asymmetric unit of ***ls*-P2$_{t\mathrm{Bu}}$Br$_2$**with hydrogens and solvent omitted for clarity. Thermal ellipsoids were set to 50% probability level.

***cs*-P8$_{t\mathrm{Bu}}$**

Crystals were grown by diffusing acetone vapor into a solution of ***cs*-P8$_{t\mathrm{Bu}}$** in *o*-DCB. X-ray data collection for ***cs*-P8$_{t\mathrm{Bu}}$** was performed at the Department of Chemistry, University of Oxford using Rigaku Synergy DW diffractometer equipped with rotating anode source and HyPix-Arc 150° detector at 100 K and subsequently reduced using CrysAlisPro. After transferring suspension of crystals in mother liquor to Paratone oil smeared over a glass slide, a suitable crystal was very quickly (few seconds) placed on a 50 μm MiTeGen loop and mounted on a goniometer head. The crystals suffer from immediate solvent loss, which destroys their crystallinity. Moreover, they dissolve in all types of tested cryoprotecting oils, and the best results were observed when Paratone or NVH oils were used.

The crystals diffract very weakly (large unit cells, disorder, solvent loss) and as such, high-flux X-ray source was crucial for the measurement. Diffraction experiments took several attempts and the best dataset was selected for structure solution and refinement. Due to challenging nature of the crystals, the resolution of the dataset is 1.0 Å (data were trimmed during processing). Its molecular weight is larger than simple proteins (e.g. insulin), placing it beyond what is traditionally considered 'small molecule crystallography'. Although the data quality and achieved resolution do not enable detailed analysis of structural parameters (bond lengths, angles), the model provides information about connectivity, shape and packing of the nanoring in the solid state; therefore, the obtained structure is fit for purpose, considering the complexity and novelty of the sample.

The asymmetric unit involves two halves of the two crystallographically independent molecules. The current model also involves two *o*-DCB molecules per asymmetric unit, however, solvent masking had to be used as well, and many other solvent (*o*-DCB and acetone) molecules are not included in the model.

The structures were solved with Superflip (*56*) charge-flipping algorithm and refined by full-matrix least-squares procedures using SHELXTL (version 2018/3) (*57*) software package through the OLEX2 graphical interface (*58*). All non-hydrogen atoms, including those in disordered parts, were refined anisotropically.

The structure was modelled with aid of several restraints placed both on appropriate distances (SADI) and displacement parameters (SIMU, RIGU). *Tert*-butyl groups were modelled with aid of residuals (RESI), after introducing appropriate restrains on their 1,2- and 1,3-distances. Aryl groups were restrained as well, additionally using FLAT command. The current model involves two *o*-DCB molecules (one of them disordered and modelled accordingly, upon splitting into two components). Other solvent molecules (partially visible during the refinement, but their modelling did not provide satisfactory results) attributed to acetone and *o*-DCB were masked using Olex2 (*58*) subroutine, which indicated presence of 4962 electrons in solvent-accessible voids per unit cell.

Table S12. Measurement and refinement details for ***cs*-P8$_{t\mathrm{Bu}}$**.

Identification code	***cs*-P8$_{t\mathrm{Bu}}$**
CCDC deposition number	2463698
Empirical formula	$C_{396}H_{408}Cl_4N_{32}Ni_8$
Formula weight	6227
Temperature/K	100.00(10)
Crystal system	monoclinic
Space group	P2/c
a/Å	57.4377(4)
b/Å	17.67065(12)
c/Å	54.5459(3)
α/°	90
β/°	112.2071(7)
γ/°	90
Volume/Å^3	51255.4(6)
Z	4
ρ_{calc}g/cm^3	0.807
μ/mm^{-1}	0.815
F(000)	13200
Crystal size/mm^3	0.4 × 0.4 × 0.2
Radiation	Cu Kα (λ = 1.54184)
2Θ range for data collection/°	3.258 to 100.874
Reflections collected	933308
Independent reflections	53471 [R_{int} = 0.0657, R_{sigma} = 0.0213]
Data/restraints/parameters	53471/12314/3958
Goodness-of-fit on F^2	1.038
Final *R* indexes [*I*>=2σ (*I*)]	R_1 = 0.1759, wR_2 = 0.4694
Final *R* indexes [all data]	R_1 = 0.1888, wR_2 = 0.4864
Largest diff. peak/hole / e Å^{-3}	3.62/–1.17

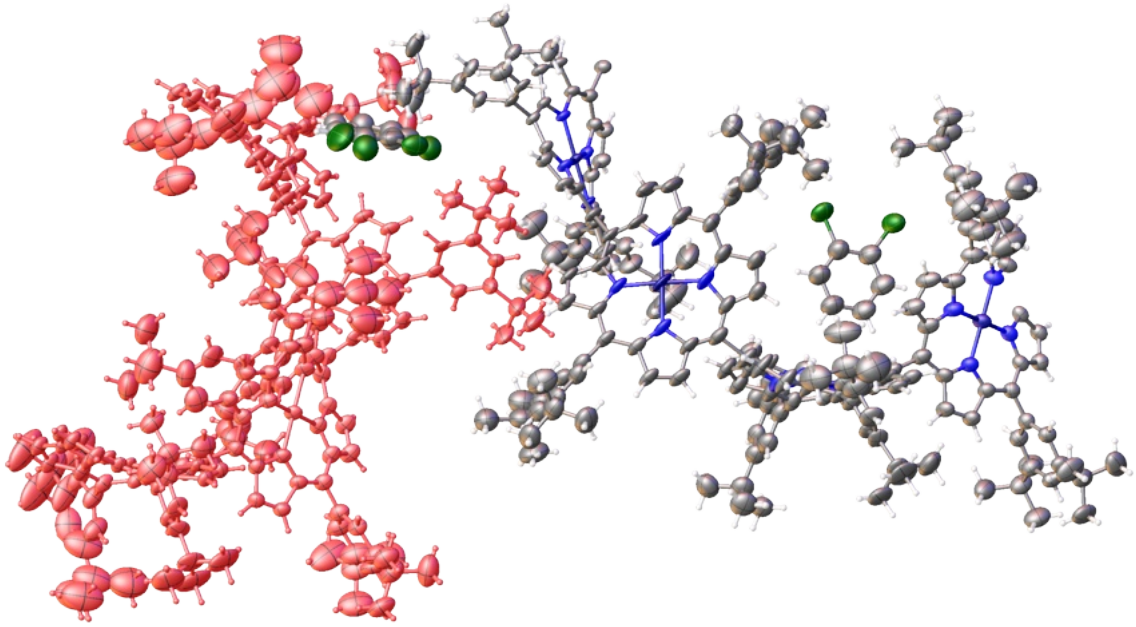

Figure S29. Displacement ellipsoid plot of the asymmetric unit. Two crystallographically independent halves of the ring were indicated with different color code. Ellipsoids were set to 50% probability level.

Responses to the A and B level alerts are given below.

Alert level A

```
THETM01_ALERT_3_A  The value of sine(theta_max)/wavelength is less than 0.550
           Calculated sin(theta_max)/wavelength =    0.5000
```

Author Response: The crystals diffracted poorly despite large size and the use of high-flux rotating anode source coupled with HYPix150 detector. The best crystal gave diffraction up to ca. 1.0 Angstroem resolution. Data were trimmed accordingly duringnthe processing stage. Despite many data collection attempts, quality of the crystals was repeatedly poor. The purpose of this structure is to show connectivity and as such, the obtained model is fit for purpose and publishable. No geometrical parameters are discussed. It is an extremely large molecule, beyond what is traditionally considered small molecule crystallography - its molecular mass is larger than that of simple proteins such as insulin.

```
PLAT084_ALERT_3_A High wR2 Value (i.e. > 0.25) ..................       0.49 Report
```

Author Response: The crystal quality wa very poor (see response to the other level A alert). The best crystal was not single and diffracted poorly. Attempts to treat the dataset as twinned did not give satisfactory results. However, the model serves as a proof of connectivity and as such, the obtained model is fit for purpose, useful and publishable.

PLAT971_ALERT_2_A Check Calcd Resid. Dens. 1.00Ang From Ni2 3.56 eA-3

Author Response: Close to heavy atom (Ni). Likely a consequence of poor data quality (see responses to the previous alerts).

PLAT973_ALERT_2_A Check Calcd Positive Resid. Density on Ni7 2.71 eA-3

Author Response: Close to heavy atom (Ni). Likely a consequence of poor data quality (see responses to the previous alerts).

PLAT973_ALERT_2_A Check Calcd Positive Resid. Density on Ni1 2.62 eA-3

Author Response: Close to heavy atom (Ni). Likely a consequence of poor data quality (see responses to the previous alerts).

Alert level B

PLAT082_ALERT_2_B High R1 Value ..... 0.18 Report

Author Response: Consequence of poor data qualit - see response to the A level alerts.

PLAT097_ALERT_2_B Large Reported Max. (Positive) Residual Density 3.62 eA-3

Author Response: Close to heavy atom (Ni). Likely a consequence of poor data quality (see responses to the previous alerts).

PLAT971_ALERT_2_B Check Calcd Resid. Dens. 0.85Ang From Ni8 2.84 eA-3

Author Response: Close to heavy atom (Ni). Likely a consequence of poor data quality (see responses to the previous alerts).

PLAT971_ALERT_2_B Check Calcd Resid. Dens. 0.87Ang From Ni3 2.77 eA-3

Author Response: Close to heavy atom (Ni). Likely a consequence of poor data quality (see responses to the previous alerts).

PLAT971_ALERT_2_B Check Calcd Resid. Dens. 0.75Ang From Ni5 2.52 eA-3

Author Response: Close to heavy atom (Ni). Likely a consequence of poor data quality (see responses to the previous alerts).

Section 7. Computational Modelling

Section 7.1. Strain calculations by DFT

Method. Geometries of *meso-meso* linked nickel-porphyrin rings and possible intermediate structures were optimized using density functional theory at the PBE0+GD3BJ level of theory with def2-SVP basis set on H, C and N atoms and the def2-TZVP basis set on Ni atoms (*59, 60*). Solubilizing groups on all porphyrins were capped and calculations were done with phenyl groups instead to reduce the computational cost. Due to the size of these systems, it was not possible to confirm the energy minima with frequency calculations but all calculations were converged within the maximum force thresholds ($max(F) < 0.000450$ and $RMS(F) < 0.00030$ in atomic units). All calculations were carried out in Gaussian 16 (*53*).

The strain energies were calculated by homodesmotic reactions, in which a cyclic structure is broken up into multiple linear fragments and equivalent bonds are broken and formed such that the reaction energy corresponds to the ring strain energy. For the *meso-meso* linked nickel-porphyrin rings, the strain energies were calculated by:

$$E_{Strain} = E(\boldsymbol{c}\text{-}\mathbf{PN}) + N \times E(\boldsymbol{l}\text{-}\mathbf{P2}) - N \times E(\boldsymbol{l}\text{-}\mathbf{P3})$$

Results. The resulting strain energies of ***c*-P*N*** are plotted in Figure S30 and listed in Tables S13 and S14. The strain energies in the *meso-meso* linked nickel-porphyrin rings are considerably lower in their previously studied zinc counterparts (*35*). The strain energy of ***cs*-P8** is only 84 kJ mol^{-1}, which is lower than many previously synthesized porphyrin rings such as a butadiyne-linked zinc porphyrin six-ring (*61*). Furthermore, the ring strain energy approaches zero for larger ring sizes with $N \geq 16$ with both ***cs*-P16** and ***cs*-P24** having strain energies of less than 5 kJ mol^{-1}.

The reason for the considerably lower strain in the nickel-containing porphyrin rings is the buckling of the porphyrin due to the nickel ion. The smaller size of Ni(II) compared to Zn(II) leads to a distortion of the porphyrin, which naturally leads to a curved structure for a *meso-meso* singly linked oligomer chain without introducing strain. The angle between two singly-linked nickel-porphyrins is about 16° in comparison to about 0° for a zinc-porphyrin dimer, as determined from their DFT optimized structures (see Figure S30b).

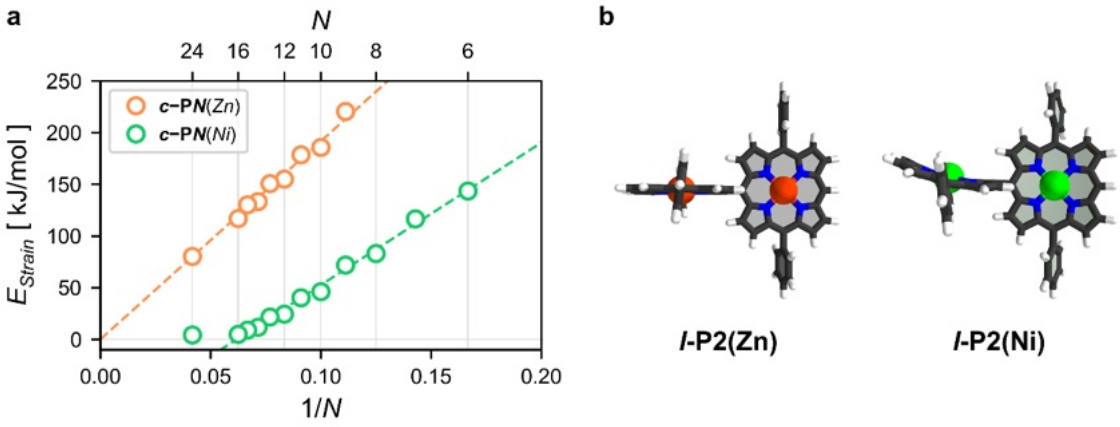

Figure S30. a) Strain energies for *meso-meso* singly-linked porphyrin rings calculated from homodesmotic reactions. b) DFT optimized structures of *meso-meso* linked zinc-porphyrin and nickel-porphyrin dimers.

There is a modest alternation pattern in strain between rings with an even and an odd number of porphyrin units with the odd-numbered rings having a higher strain energy (Figure 30a). This is presumably due to the necessarily smaller dihedral angle between adjacent porphyrins in the odd-numbered porphyrin rings.

Table S13. Electronic and strain energies for the cyclic and linear oligo nickel porphyrin compounds.

	Energy [Hartrees]	E_{Strain} [kJ mol^{-1}]
***ls*-P2**	–5910.940292	-
***ls*-P3**	–8865.822469	-
***cs*-P6**	–17729.238333	143.7
***cs*-P8**	–23639.025716	83.2
***cs*-P9**	–26593.912132	72.1
***cs*-P10**	–29548.804128	46.3
***cs*-P11**	–32503.688571	40.3
***cs*-P12**	–35458.576760	24.6
***cs*-P13**	–38413.459702	22.5
***cs*-P14**	–41368.345912	12.0
***cs*-P15**	–44323.229232	8.95
***cs*-P16**	–47278.112941	4.93
***cs*-P24**	–70917.170486	4.51
[Ni(bipy)(P1)$_2$]	–13823.334046	-
c-P12/[Ni(bipy)]$_3$	–41466.470995	8.7
c-P12/[Ni(bipy)]$_2$	–39463.833785	29.2
c-P12/[Ni(bipy)]$_1$	–37461.202759	33.5

Table S14. Electronic and strain energies for the cyclic and linear oligo zinc porphyrin compounds.

	Energy [Hartrees]	E_{Strain} [kJ·mol^{-1}]
Zn-*ls*-P4	–11058.770283	-
Zn-*ls*-P5	–13823.168415	-
Zn-*cs*-P9	–24879.499222	220.4
Zn-*cs*-P10	–27643.910586	185.8
Zn-*cs*-P11	–30408.311332	178.8
Zn-*cs*-P12	–33172.718479	155.2
Zn-*cs*-P13	–35937.118318	150.7
Zn-*cs*-P14	–38701.523079	133.4
Zn-*cs*-P15	–41465.922388	130.2
Zn-*cs*-P16	–44230.325615	116.8
Zn-*cs*-P24	–66345.524490	80.5

Section 7.2. Proposed Mechanism for Yamamoto (Cyclo)Oligomerization

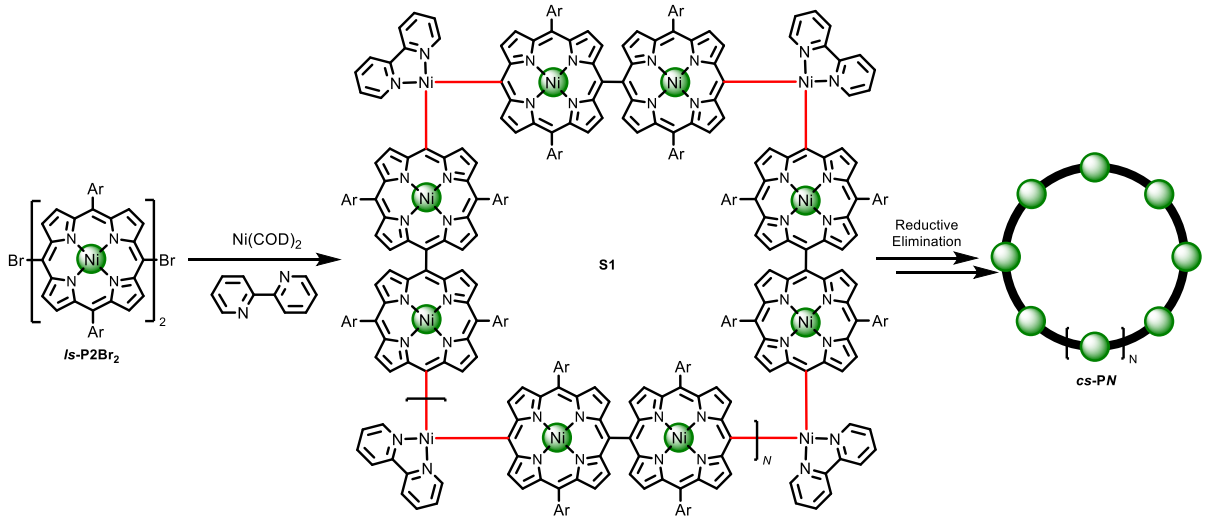

Figure S31. Proposed mechanism for Yamamoto (cyclo)oligomerization of ***ls*-P2Br$_2$**.

The strain energy of potential reaction intermediates in the formation of ***cs*-P12** (see Figure S31 and Figure S32) were calculated using the following equations:

$$E_{Strain} = E_A - E_B$$

$$E_A = E(\boldsymbol{cs}\textbf{-P12}/[\textbf{Ni(bipy)}]_{\boldsymbol{m}}) + (12 - m) \times E(\boldsymbol{ls}\textbf{-P2})$$

$$E_B = (12 - 2m) \times E(\boldsymbol{ls}\textbf{-P3}) + m \times E([\textbf{Ni(bipy)}(\textbf{P1})_{\textbf{2}}])$$

The initial triangular trimer species formed from three ***ls*-P4** and **[Ni(bipy)]** each has very low strain (8.7 kJ mol^{-1}) which makes it a likely intermediate. Subsequent reductive eliminations of **[Ni(bipy)]** result in an increase in strain energy (29.2 kJ mol^{-1} and 33.5 kJ mol^{-1}). The final elimination step to form ***cs*-P12** is energetically favored with a decrease in strain from 33.5 kJ mol^{-1} to 24.6 kJ mol^{-1}.

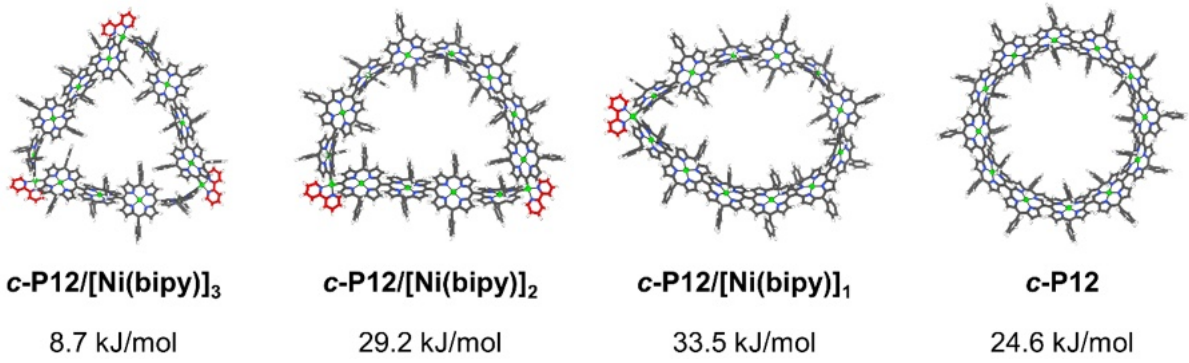

Figure S32. DFT optimized structures of possible reaction intermediates in the formation of ***cs*-P12** and strain energies calculated from homodesmotic reactions.

Section 7.3. Electronic Structure Calculations

Chemical shifts from DFT calculations (using OX-B3LYP/def2-SVP) are given in Table S7 and compared with experimental data in Figure S15. Integrated bond currents are provided in Figure S16. Calculated optical transitions from TD-DFT are shown in Figure S116.

Section 8. NMR and Mass Spectra

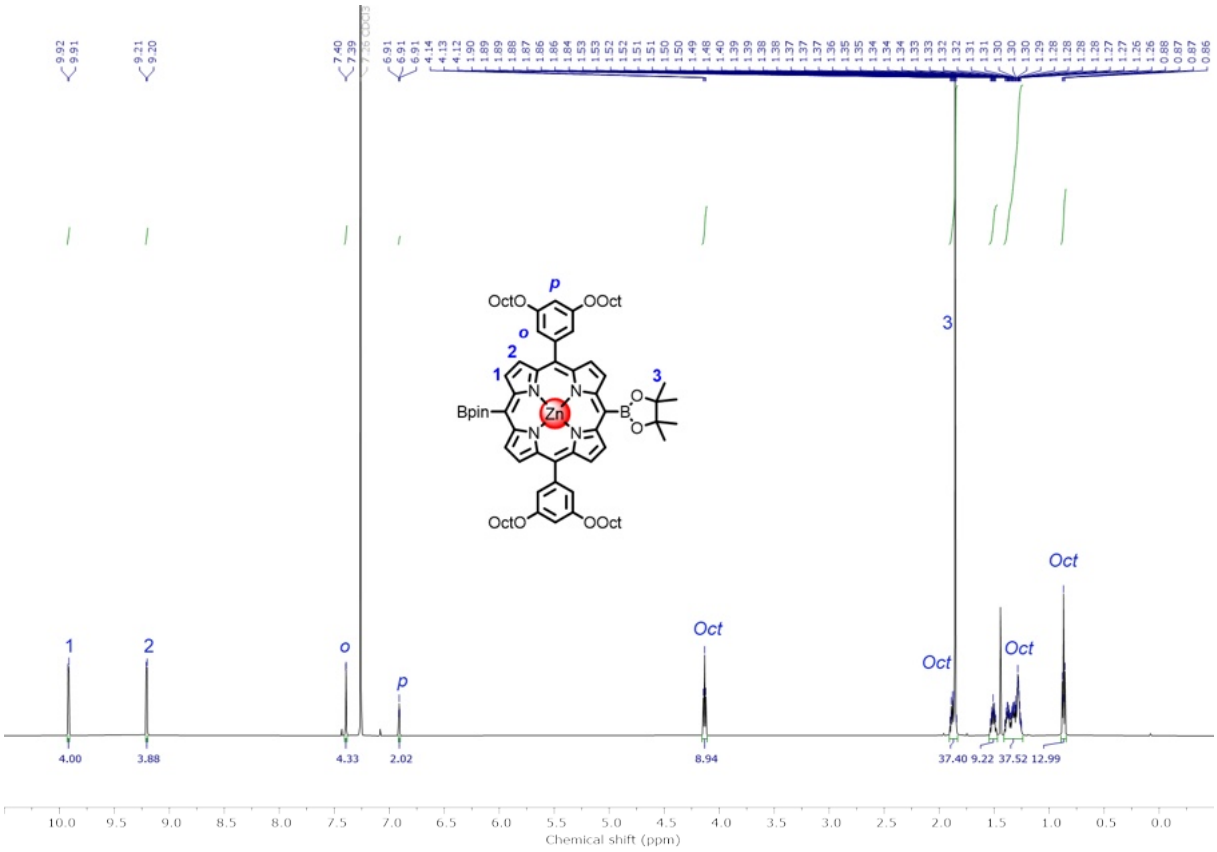

Figure S33. ^{1}H NMR (600 MHz) spectrum of **Zn-P1$_{OOct}$Bpin$_2$** ($CDCl_3$, 298 K).

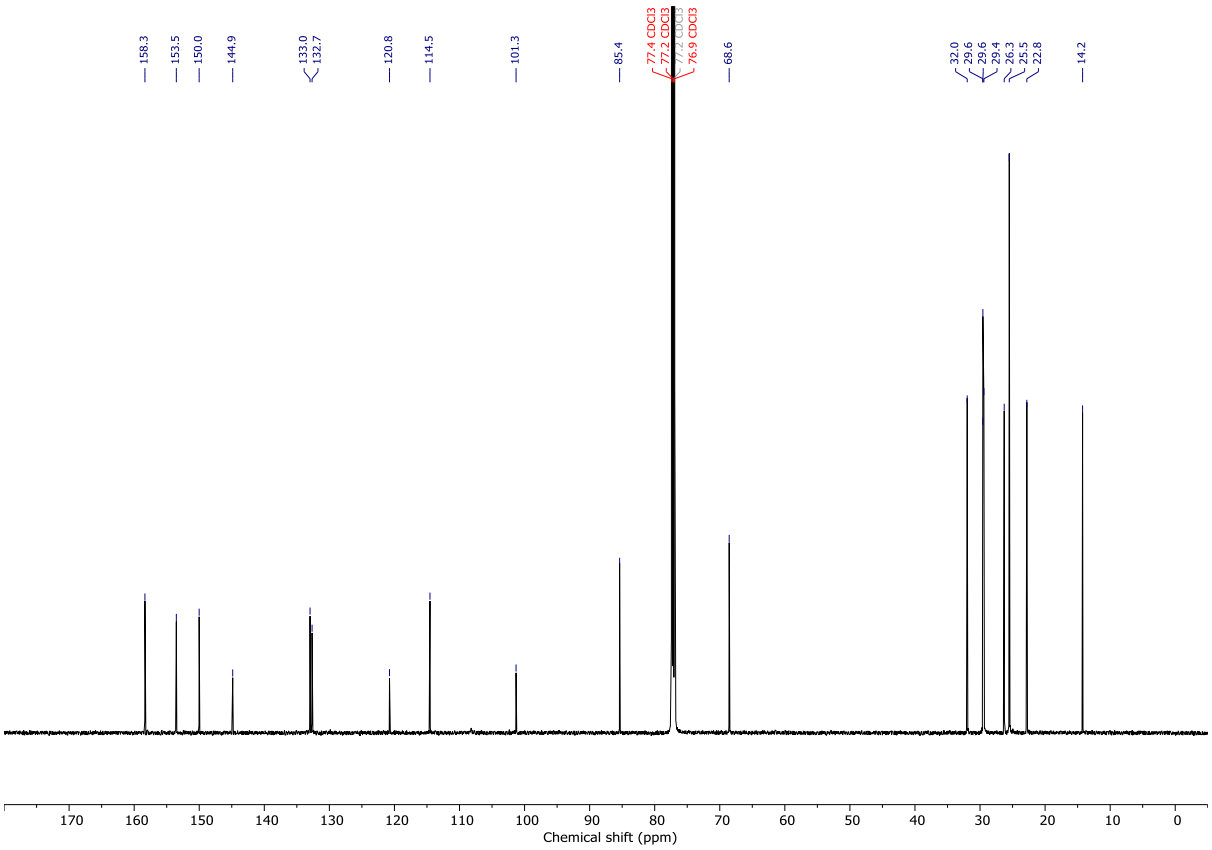

Figure S34. ^{13}C NMR (151 MHz) spectrum of **Zn-P1$_{OOct}$Bpin$_2$** ($CDCl_3$, 298 K).

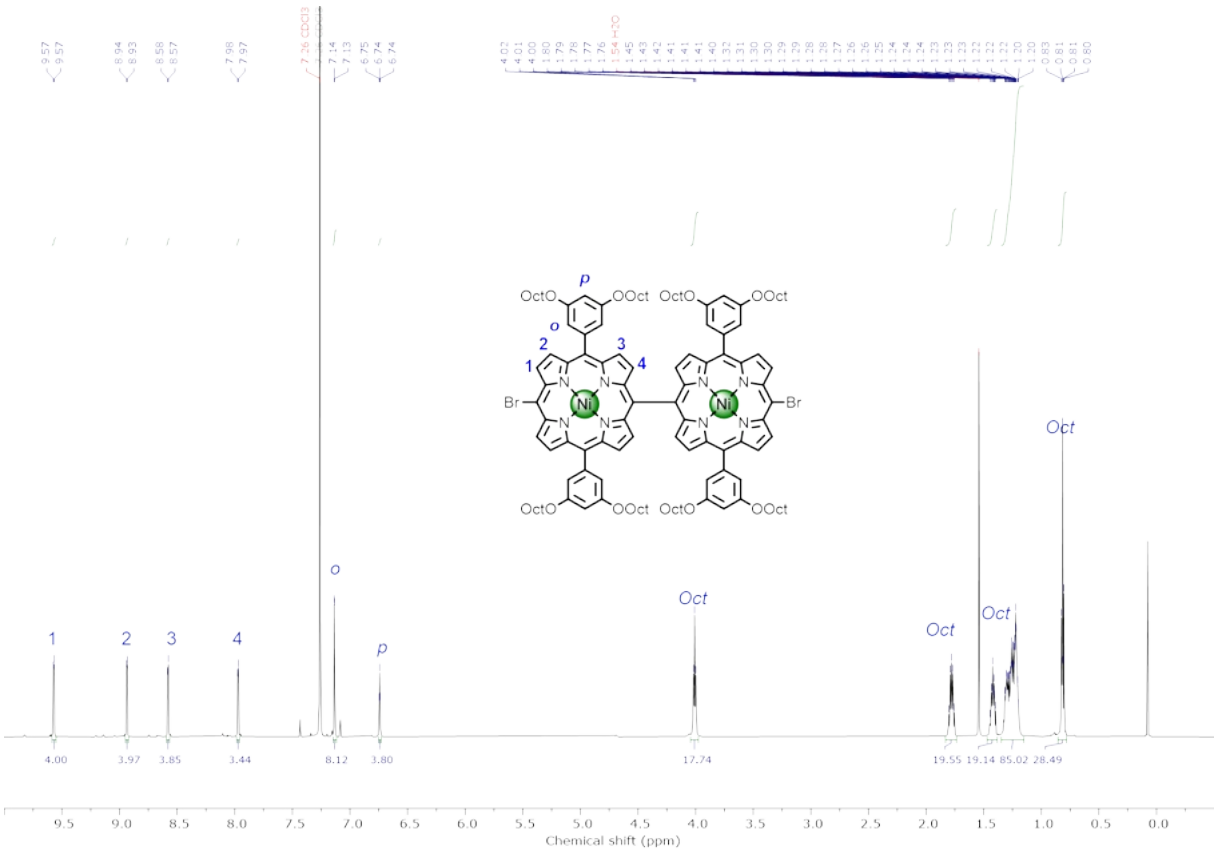

Figure S35. ^{1}H NMR (600 MHz) spectrum of ***ls*-P2$_{\mathbf{OOct}}$Br$_{\mathbf{2}}$** ($CDCl_3$, 298 K).

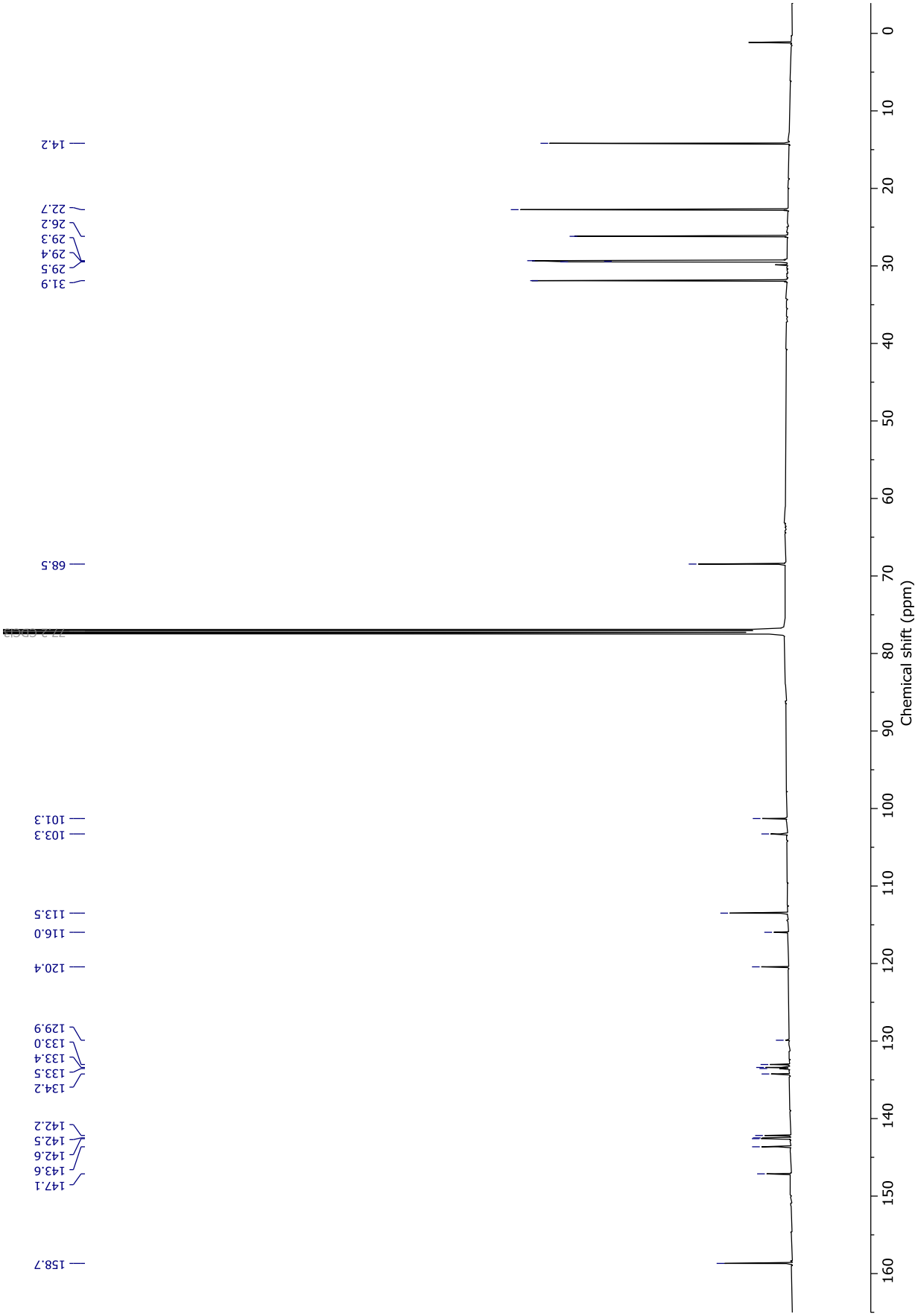

Figure S36. ^{13}C NMR (151 MHz) spectrum of ***ls*-P2$_{OOct}$Br$_2$** ($CDCl_3$, 298 K).

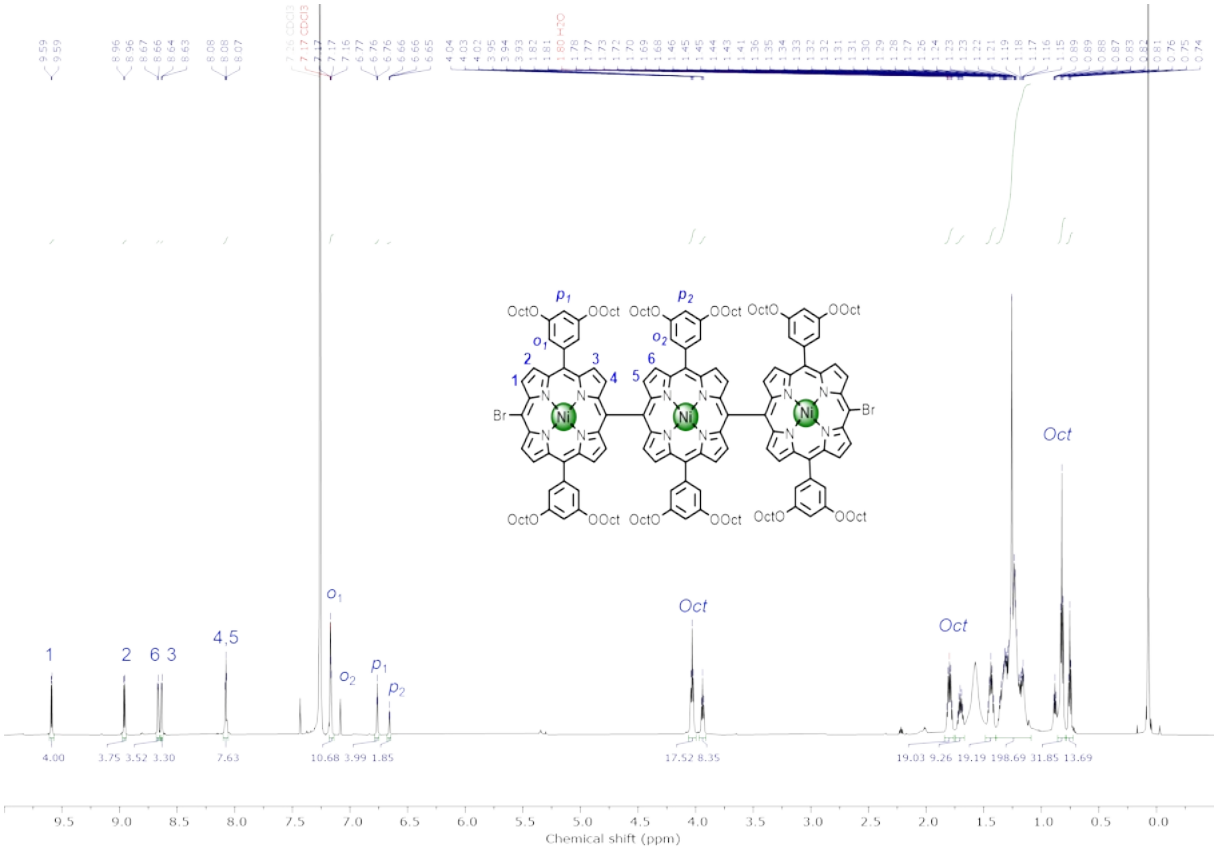

Figure S37. ^{1}H NMR (600 MHz) spectrum of ***ls*-P3$_{OOct}$Br$_2$** ($CDCl_3$, 298 K).

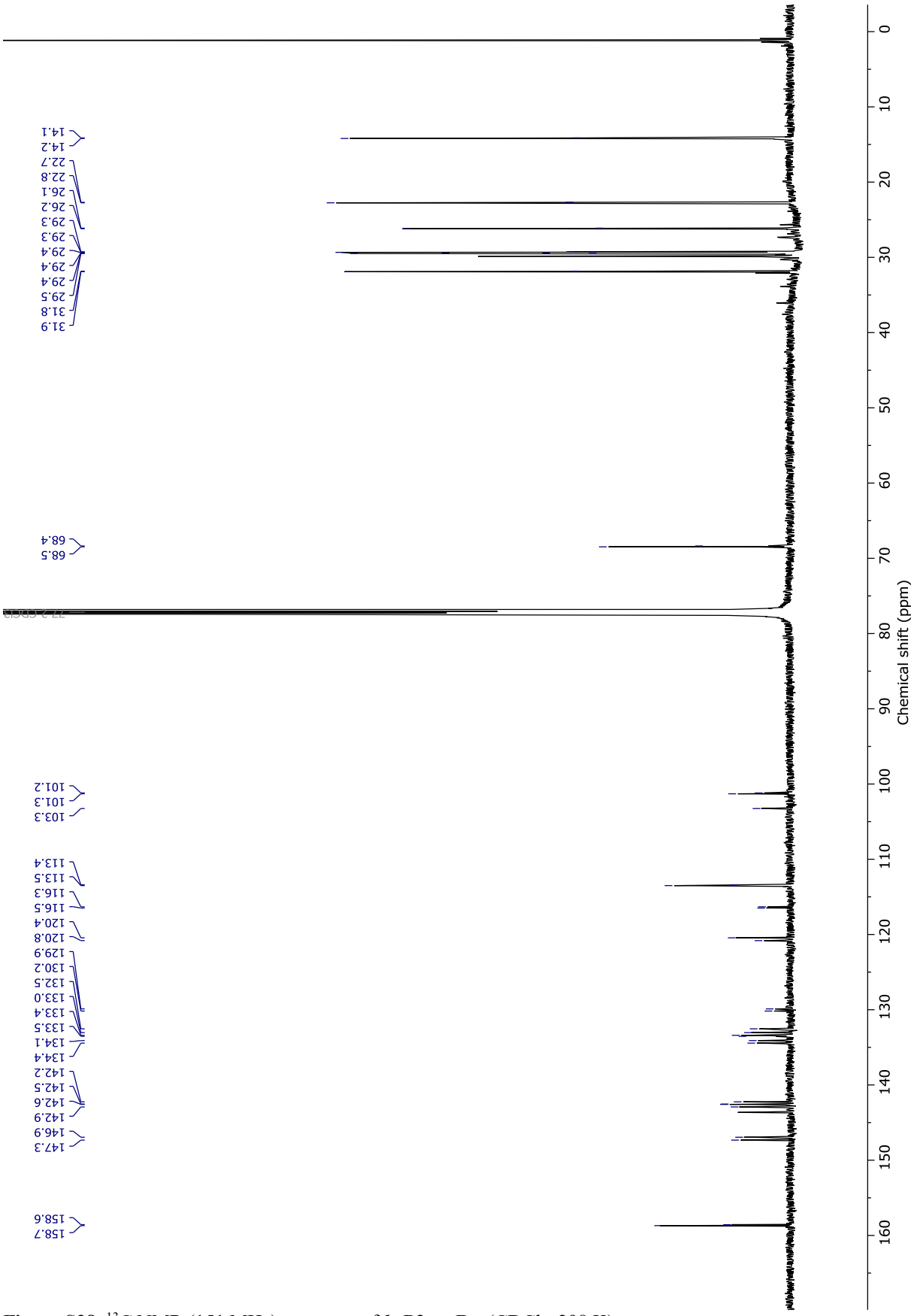

Figure S38. ^{13}C NMR (151 MHz) spectrum of ***ls*-P3$_{OOct}$Br$_2$** ($CDCl_3$, 298 K).

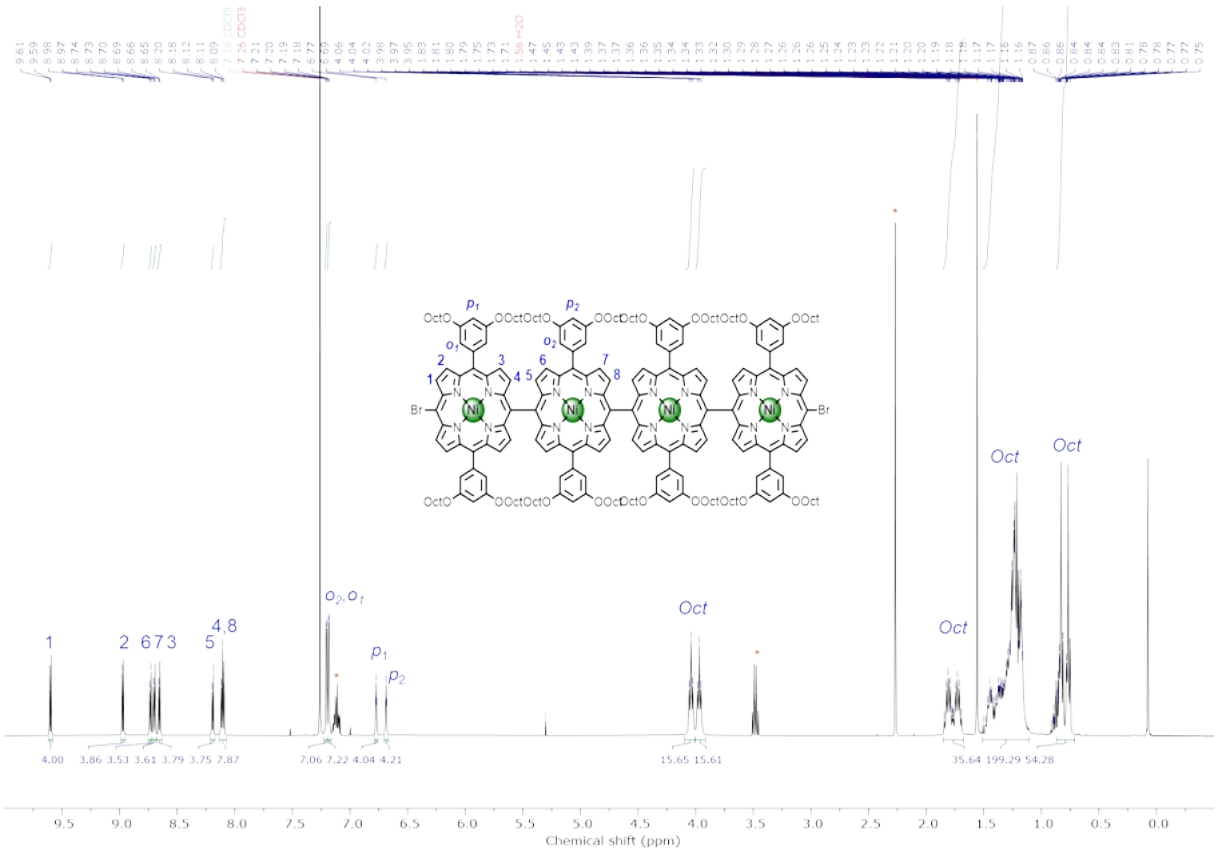

Figure S39. ^{1}H NMR (600 MHz) spectrum of ***ls*-P4$_{OOct}$Br$_2$** ($CDCl_3$, 298 K).

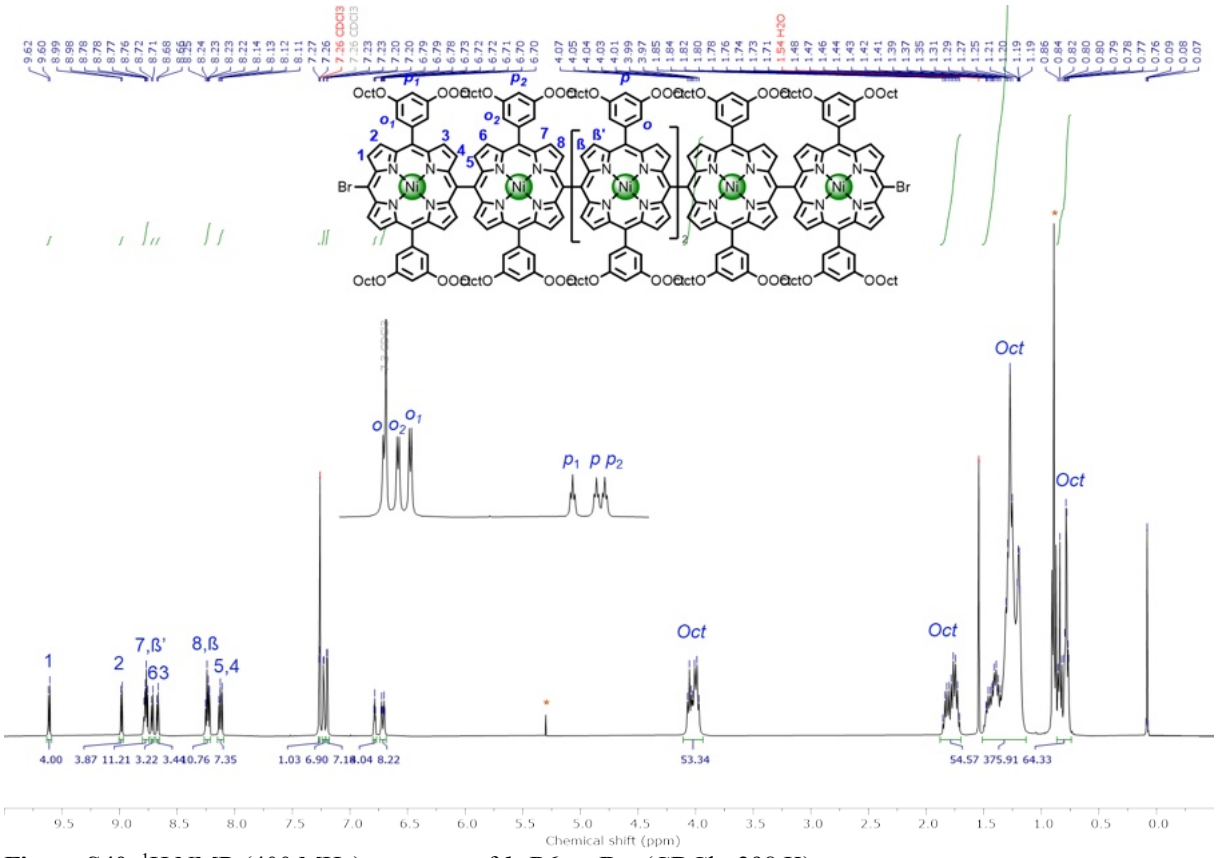

Figure S40. ^{1}H NMR (400 MHz) spectrum of ***ls*-P6$_{OOct}$Br$_2$** ($CDCl_3$, 298 K).

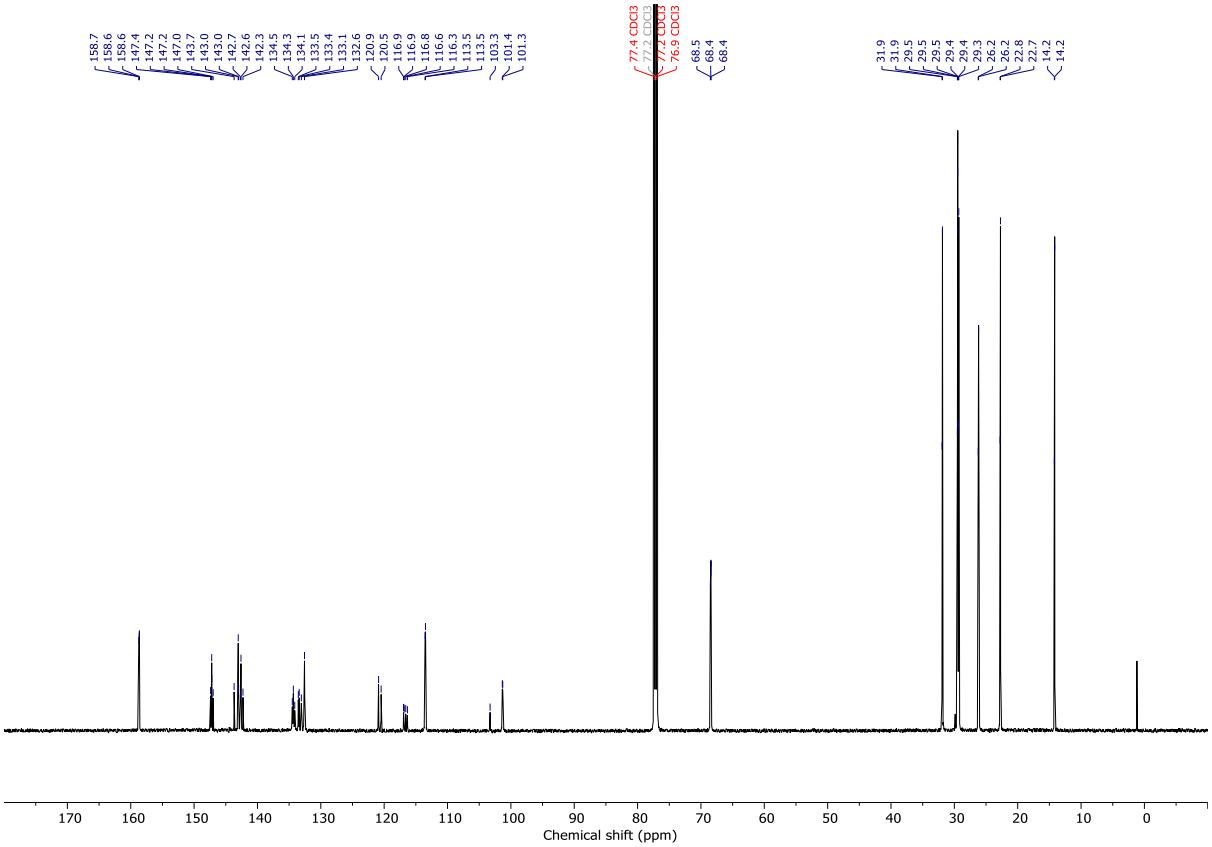

Figure S41. ^{13}C NMR (151 MHz) spectrum of ***ls*-P6$_{OOct}$Br$_2$** ($CDCl_3$, 298 K).

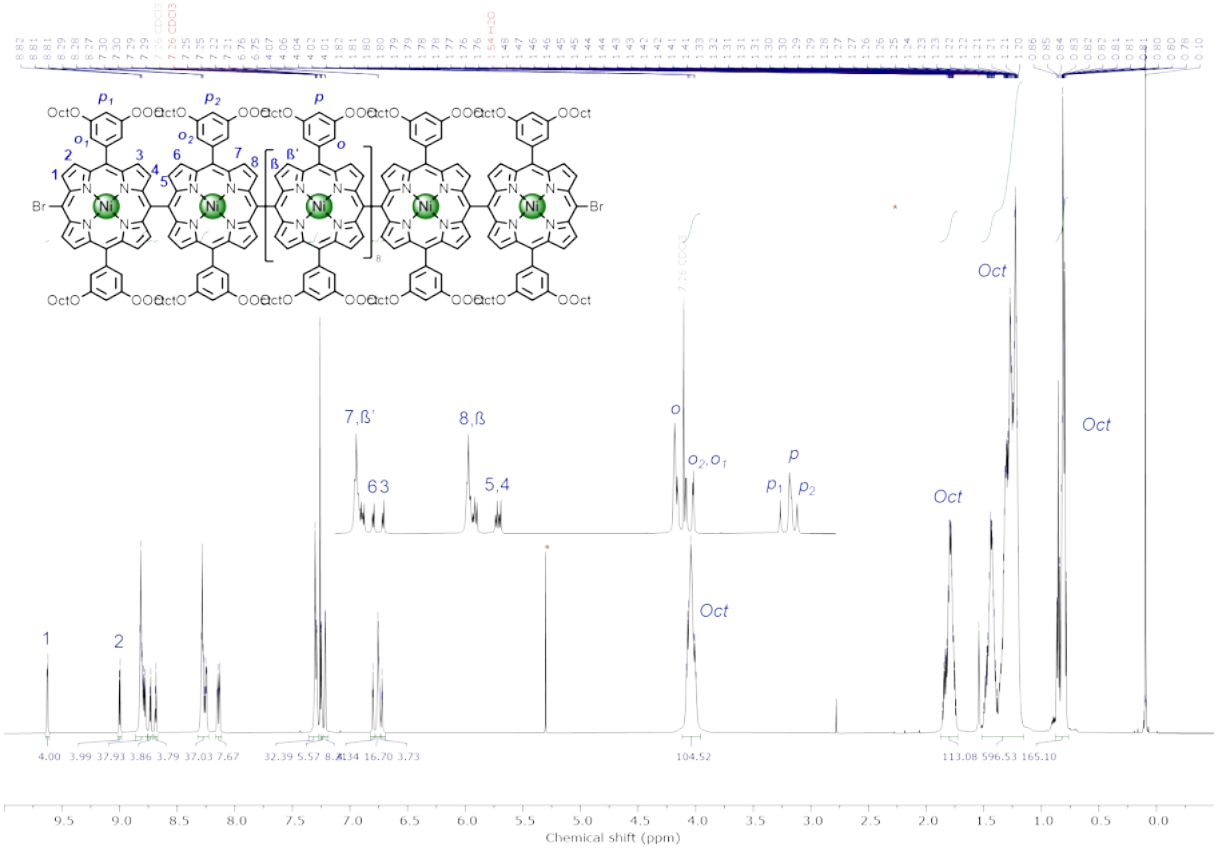

Figure S42. ^{1}H NMR (600 MHz) spectrum of ***ls*-P12$_{OOct}$Br$_2$** ($CDCl_3$, 298 K).

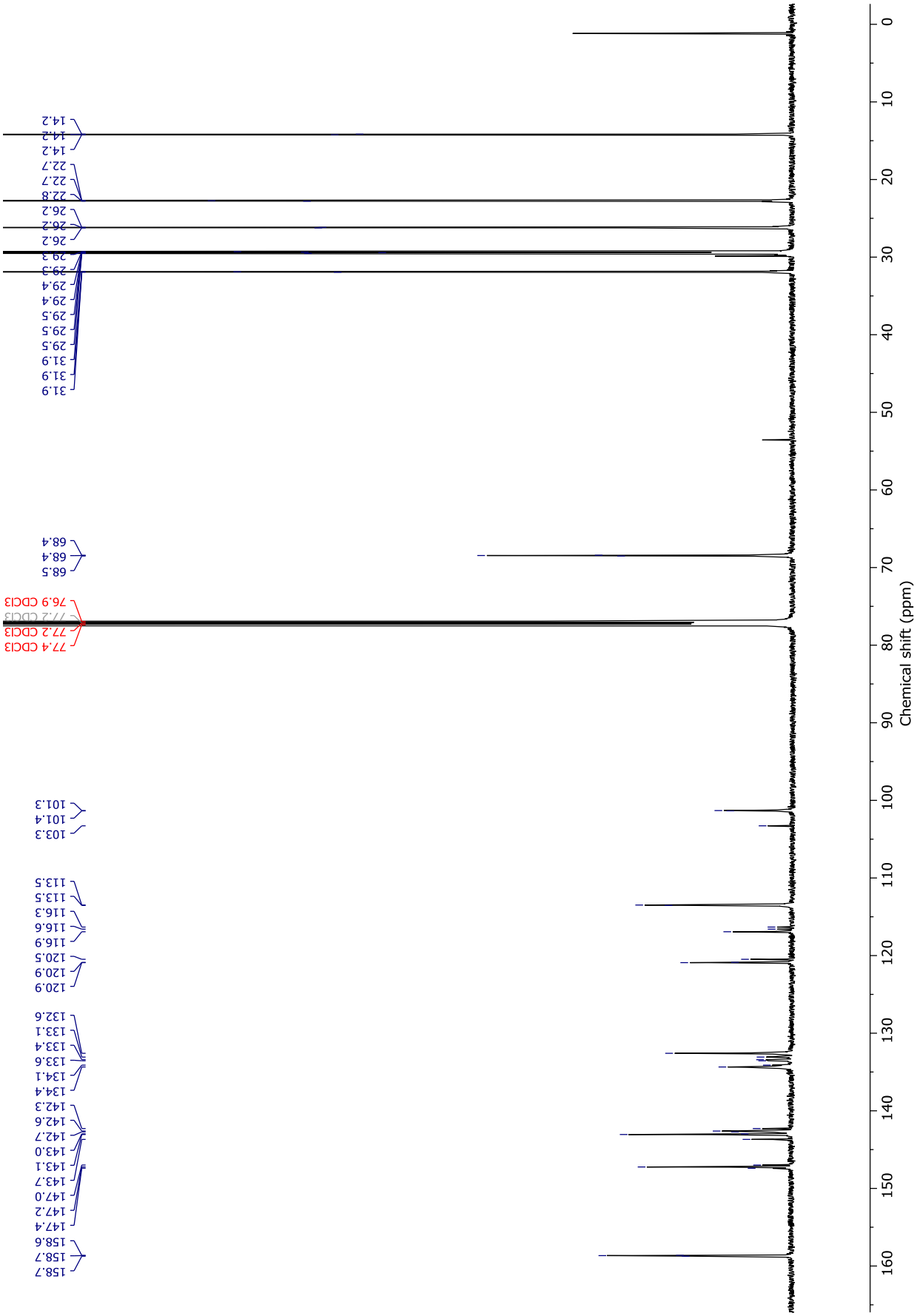

Figure S43. ^{13}C NMR (151 MHz) spectrum of ***ls*-P12$_{OOct}$Br$_2$** ($CDCl_3$, 298 K).

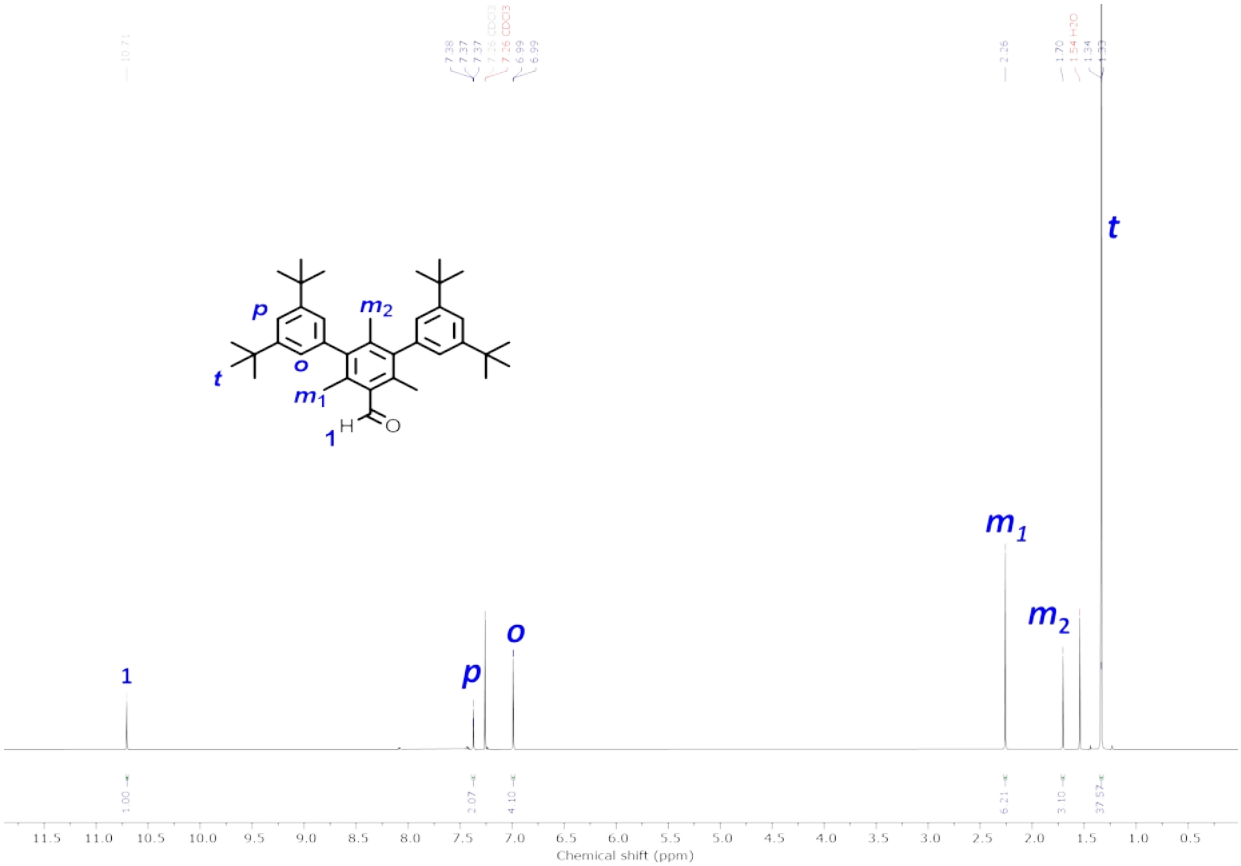

Figure S44. ^{1}H NMR (600 MHz) spectrum of **MesBu-aldehyde** ($CDCl_3$, 298 K).

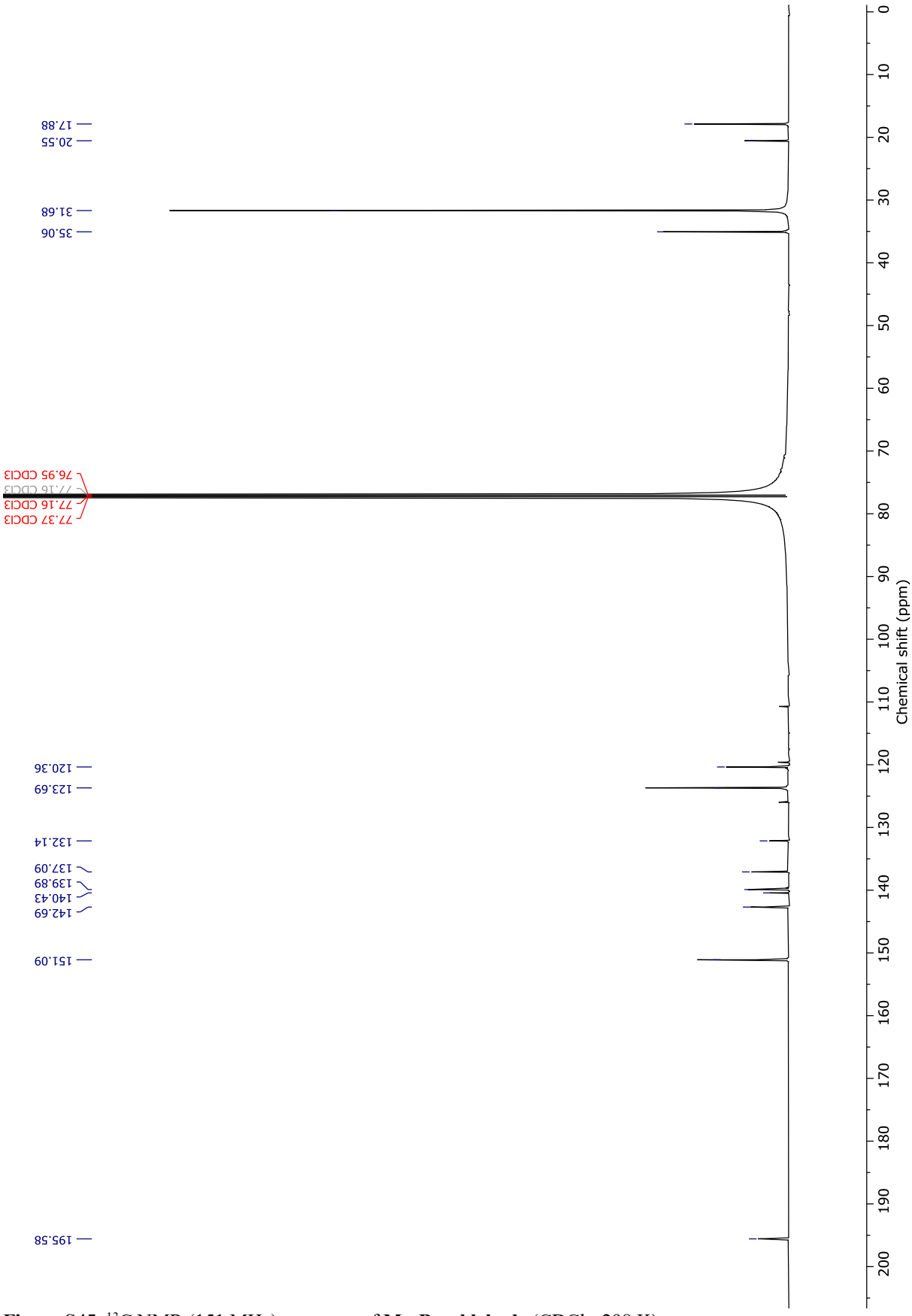

Figure S45. ^{13}C NMR (151 MHz) spectrum of **MesBu-aldehyde** ($CDCl_3$, 298 K).

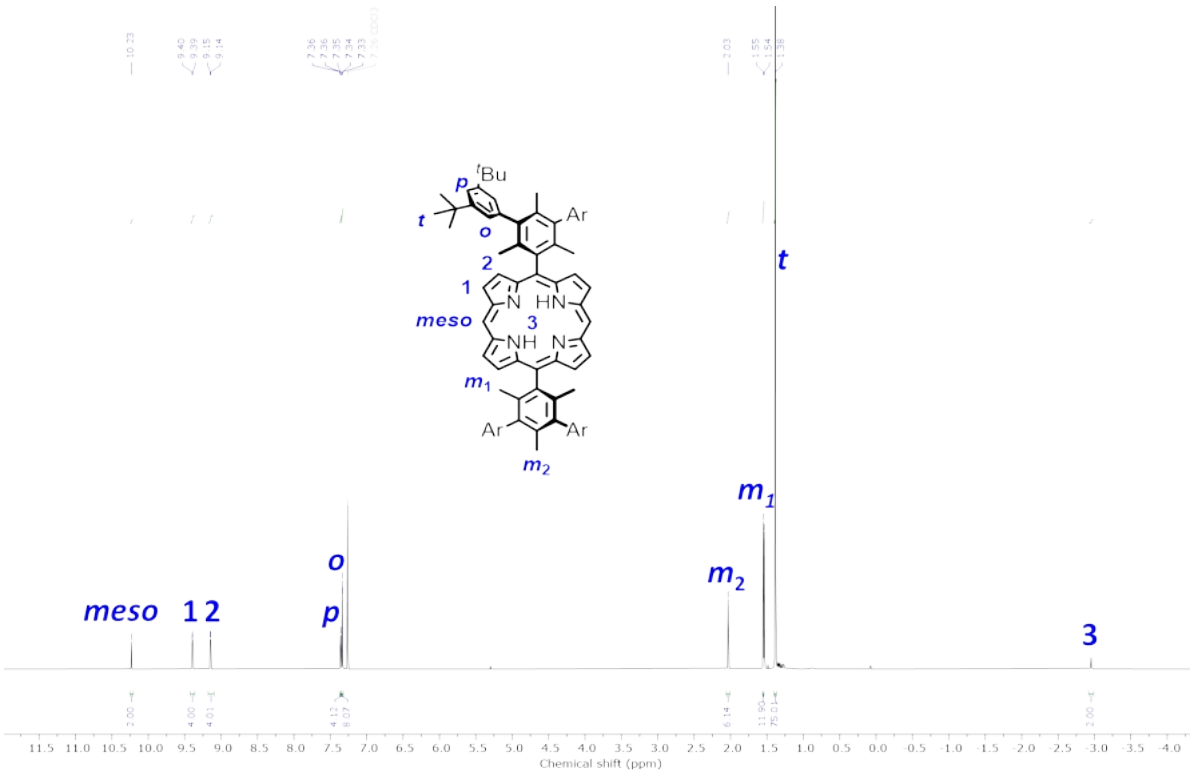

Figure S46. ^{1}H NMR (600 MHz) spectrum of **H$_2$-P1$_{MesBu}$** ($CDCl_3$, 298 K).

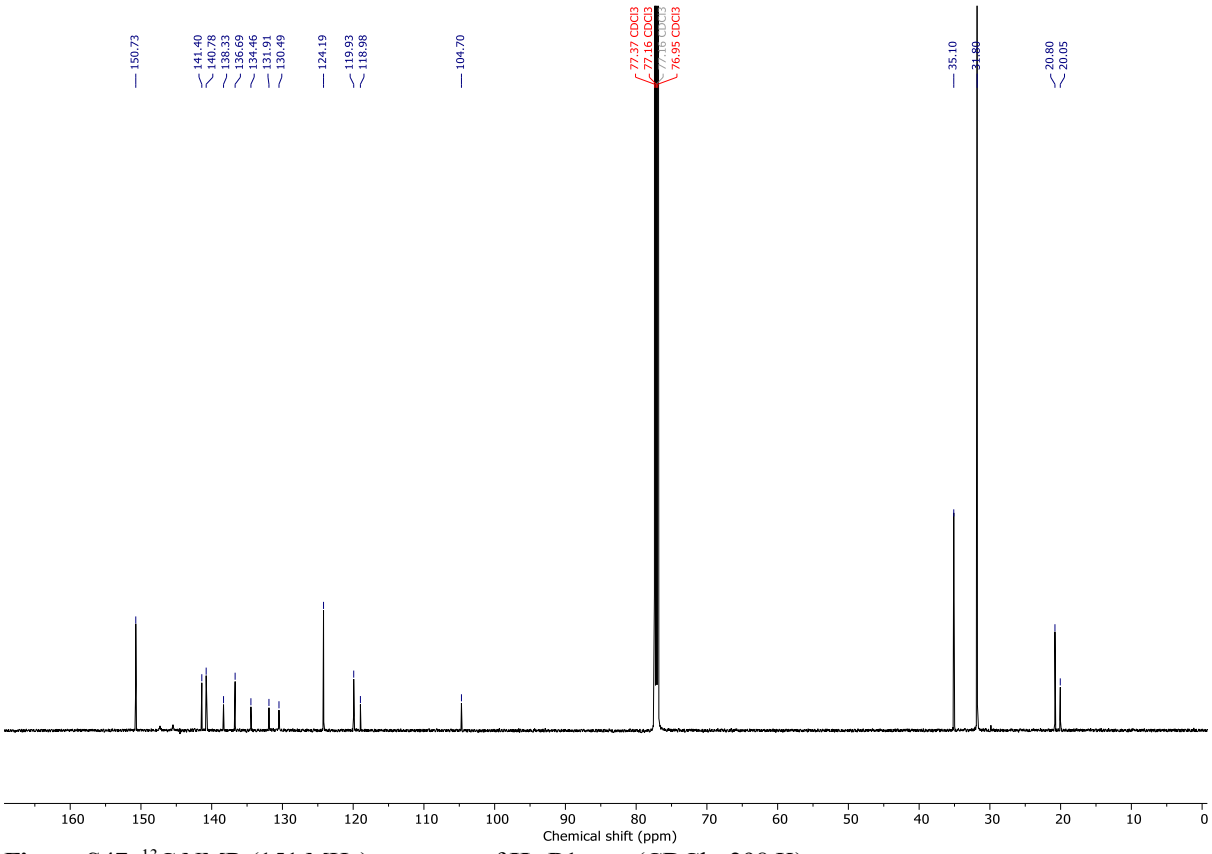

Figure S47. ^{13}C NMR (151 MHz) spectrum of **H$_2$-P1$_{MesBu}$** ($CDCl_3$, 298 K).

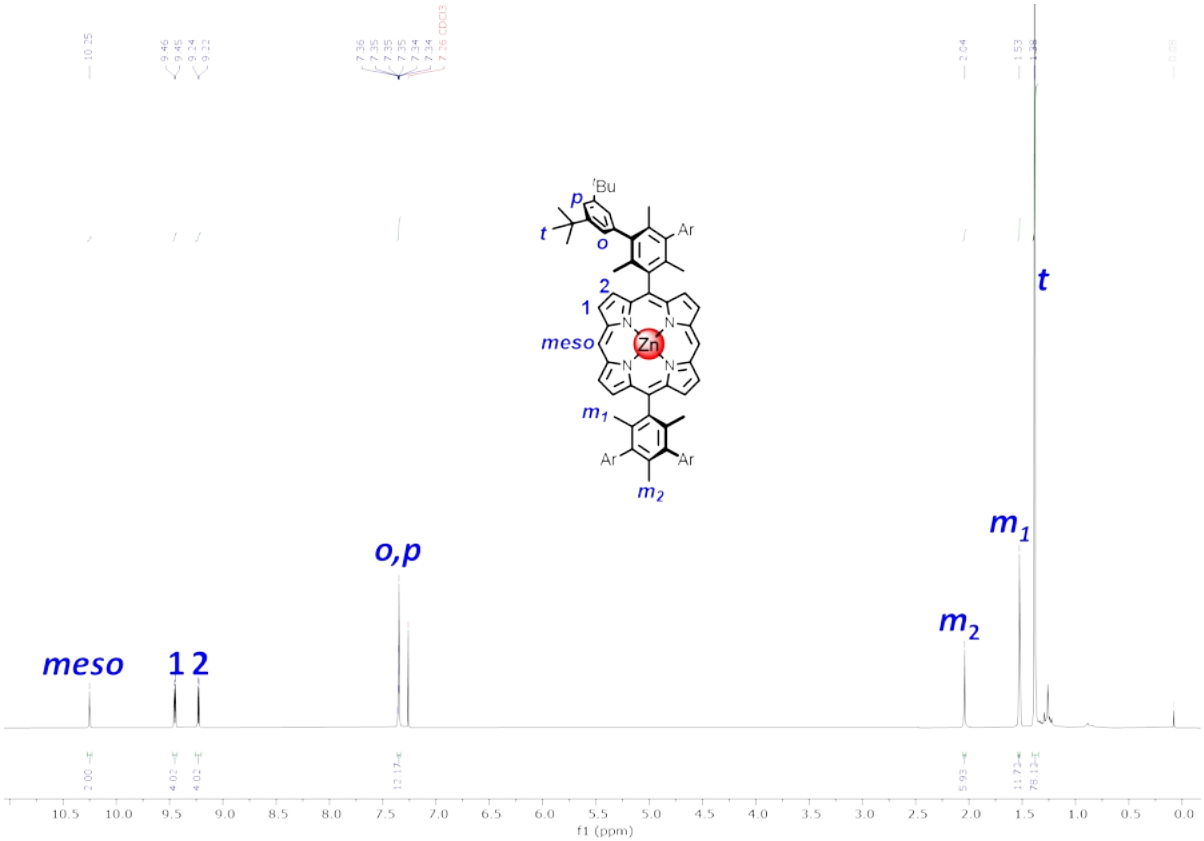

Figure S48. ^{1}H NMR (400 MHz) spectrum of **Zn-P1$_{\mathbf{MesBu}}$** ($CDCl_3$, 298 K).

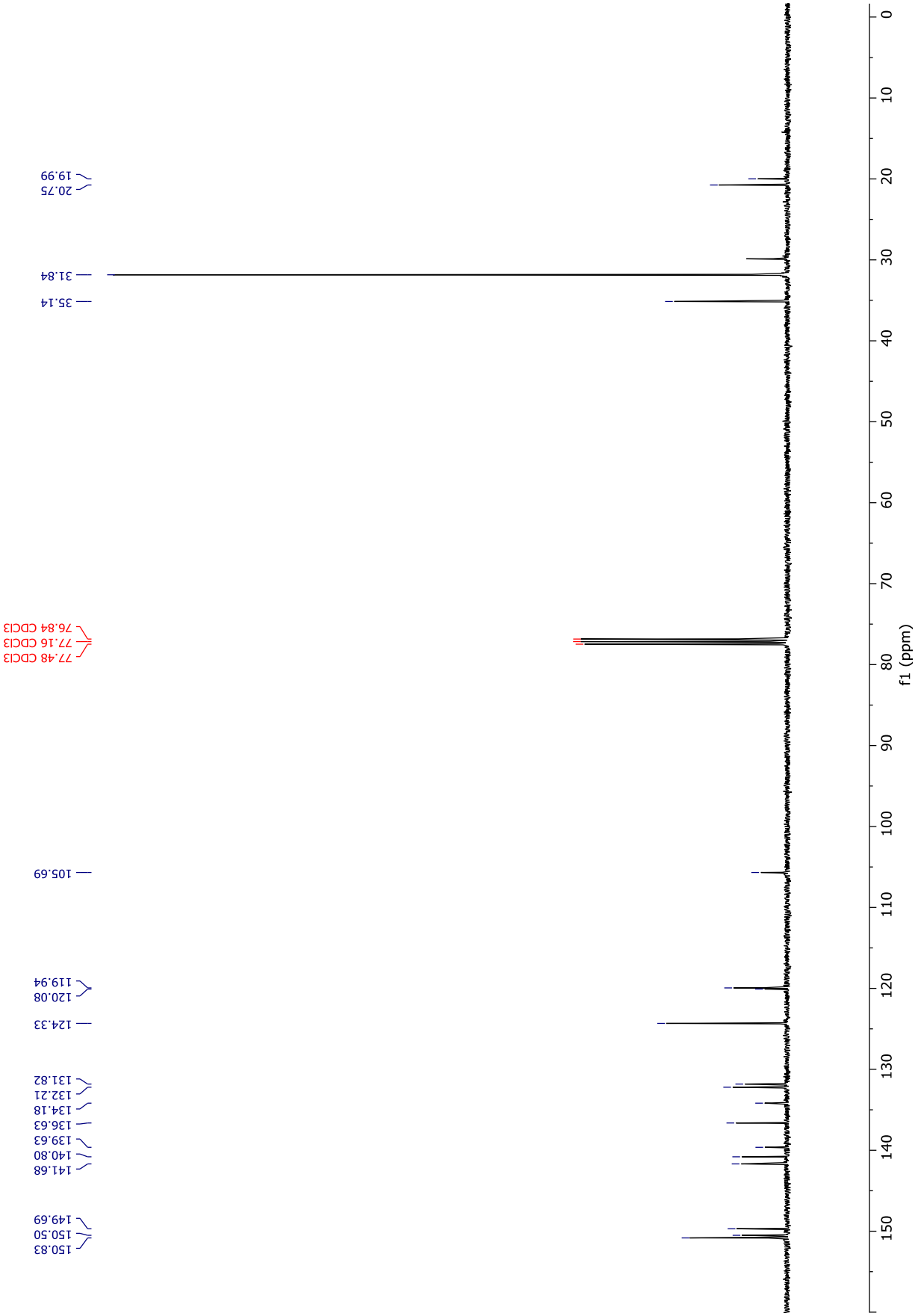

Figure S49. ^{13}C NMR (101 MHz) spectrum of **Zn-P1$_{MesBu}$** ($CDCl_3$, 298 K).

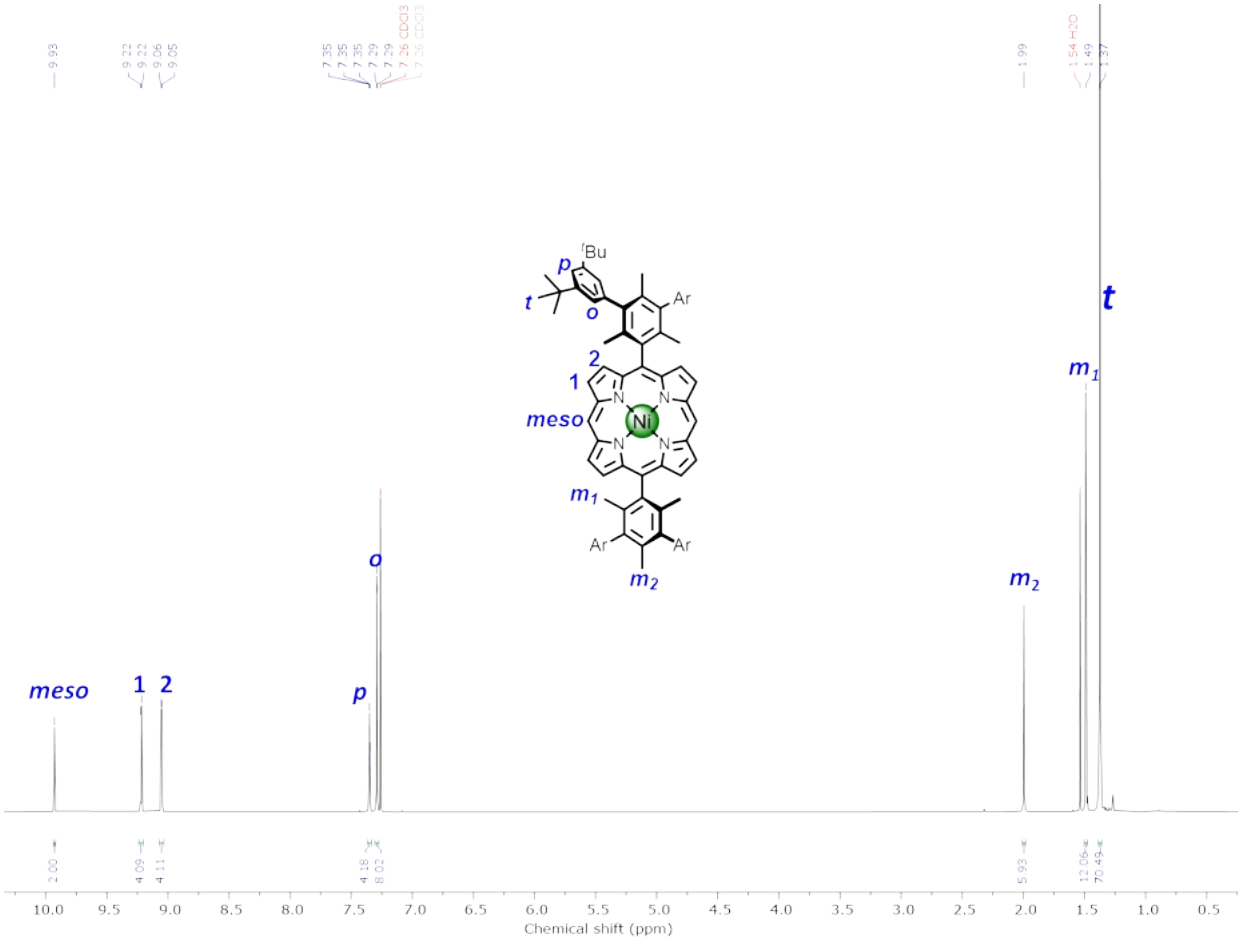

Figure S50. ^{1}H NMR (600 MHz) spectrum of **P1$_{MesBu}$** ($CDCl_3$, 298 K).

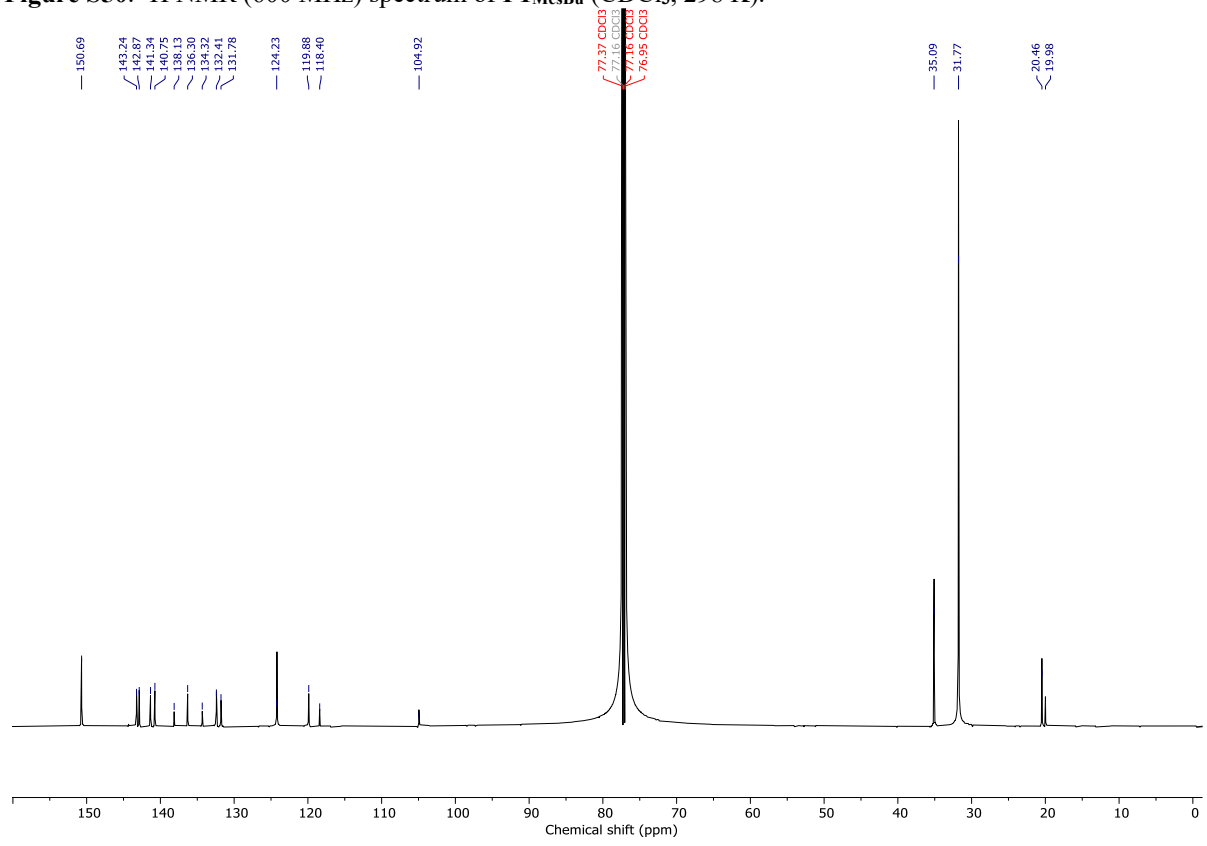

Figure S51. ^{13}C NMR (151 MHz) spectrum of **P1$_{MesBu}$** ($CDCl_3$, 298 K).

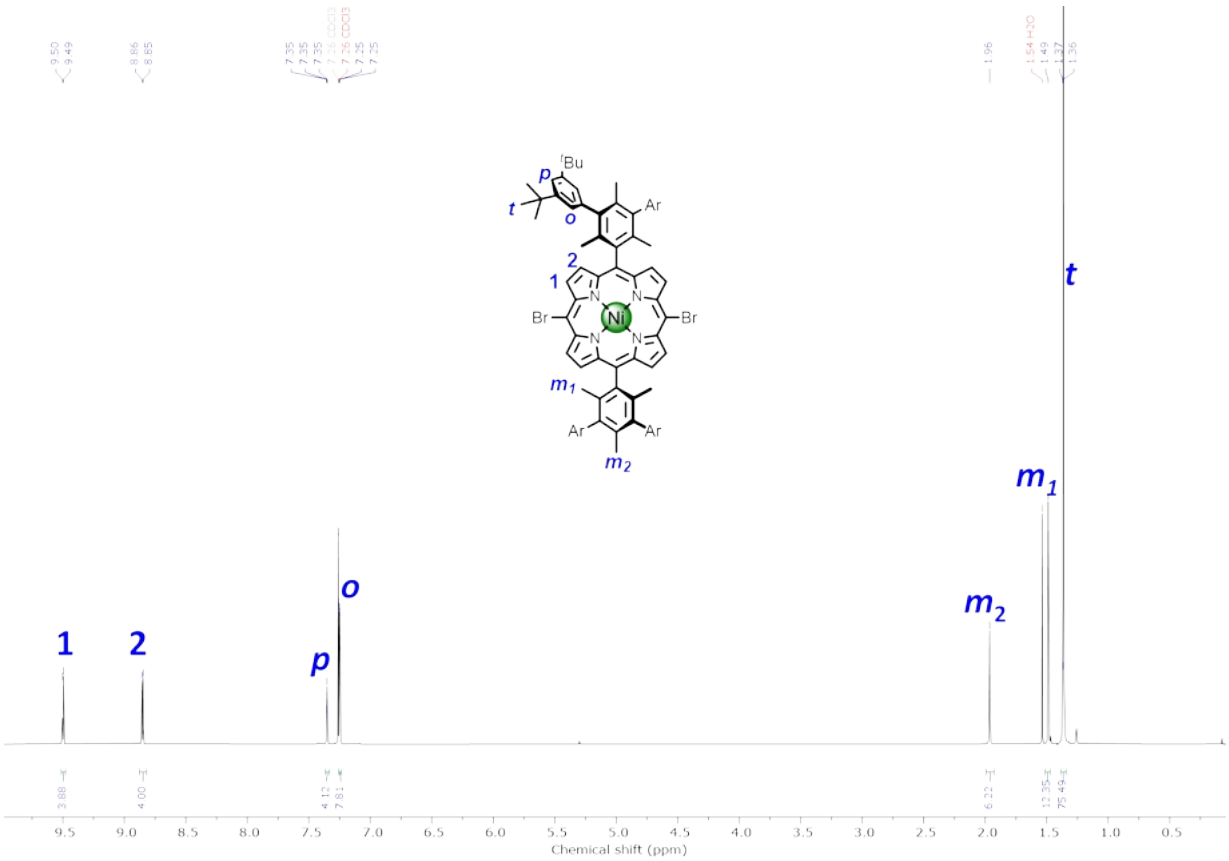

Figure S52. ^{1}H NMR (600 MHz) spectrum of **P1$_{MesBu}$Br$_2$** ($CDCl_3$, 298 K).

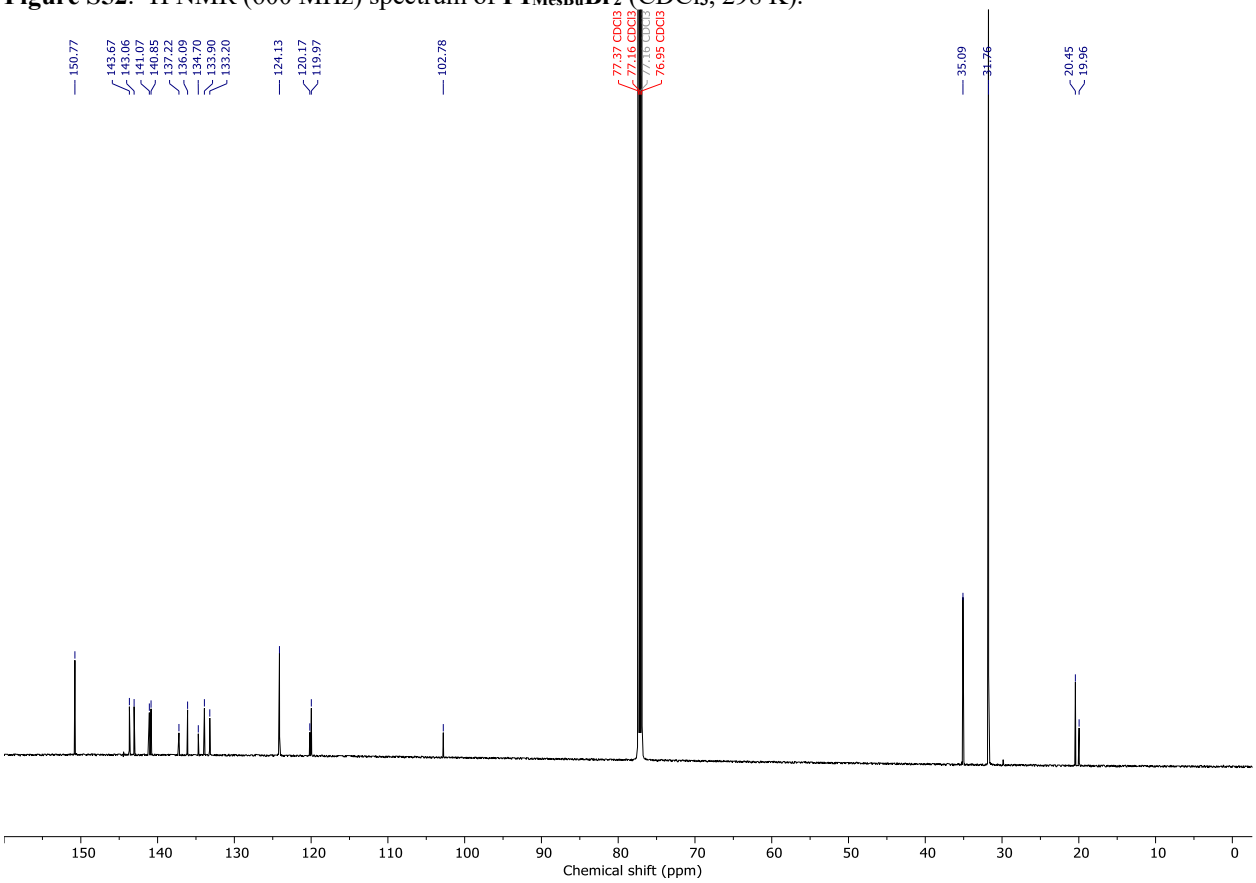

Figure S53. ^{13}C NMR (151 MHz) spectrum of **P1$_{MesBu}$Br$_2$** ($CDCl_3$, 298 K).

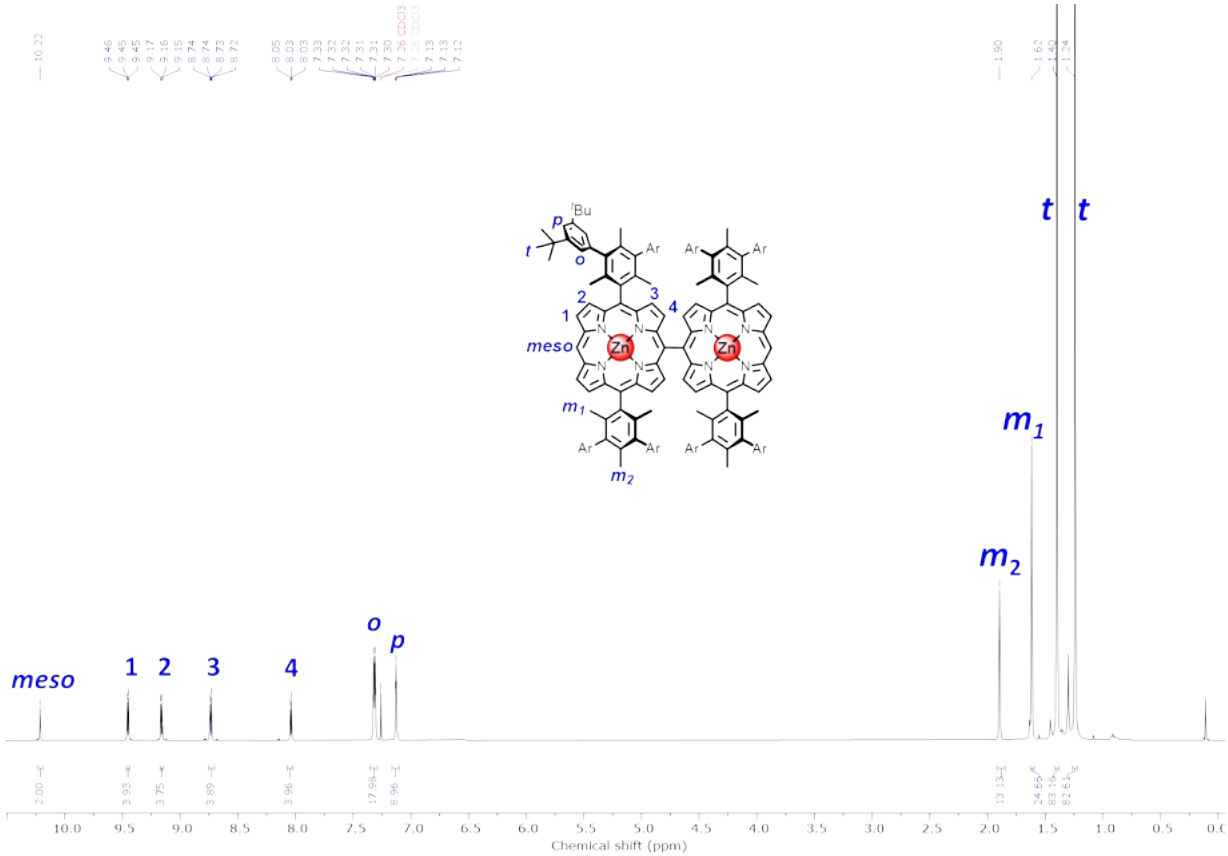

Figure S54. ^{1}H NMR (400 MHz) spectrum of **Zn-*ls*-P2$_{MesBu}$** ($CDCl_3$, 298 K).

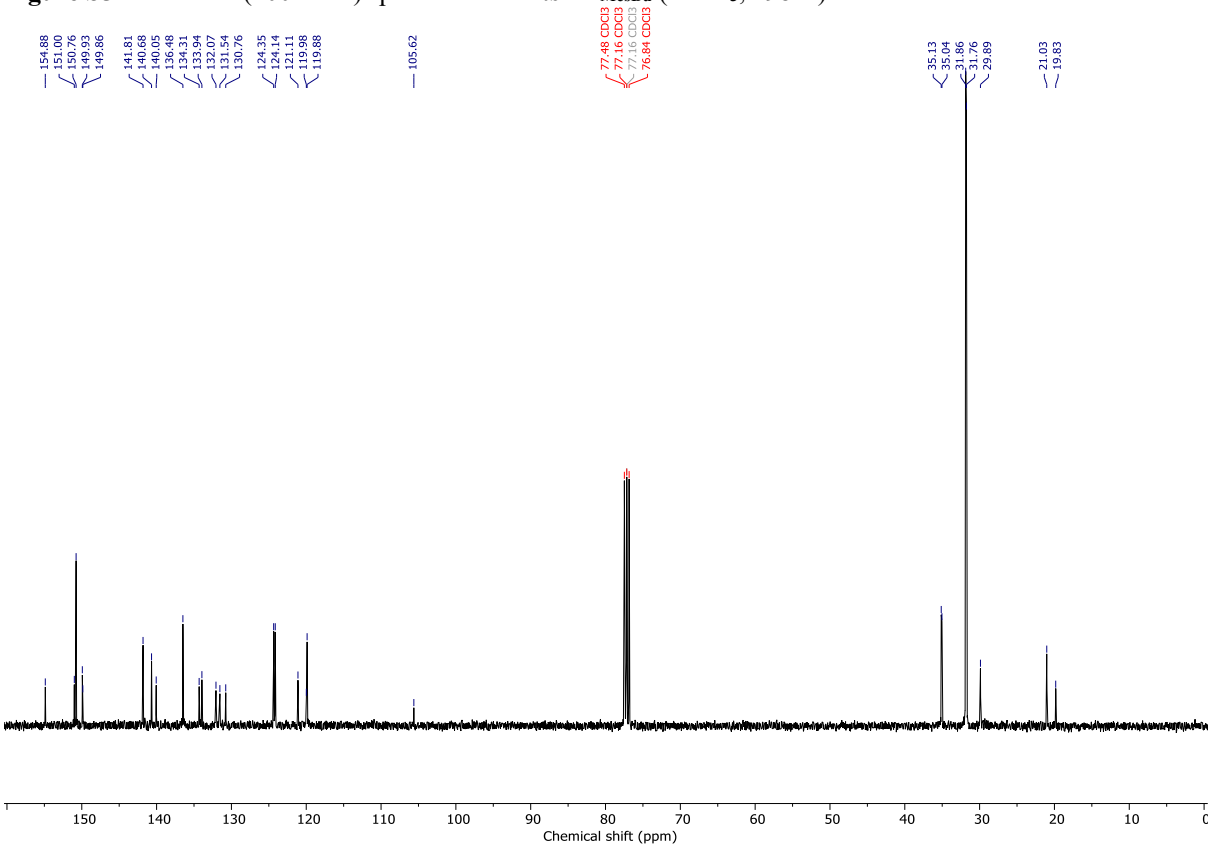

Figure S55. ^{13}C NMR (101 MHz) spectrum of **Zn-*ls*-P2$_{MesBu}$** ($CDCl_3$, 298 K).

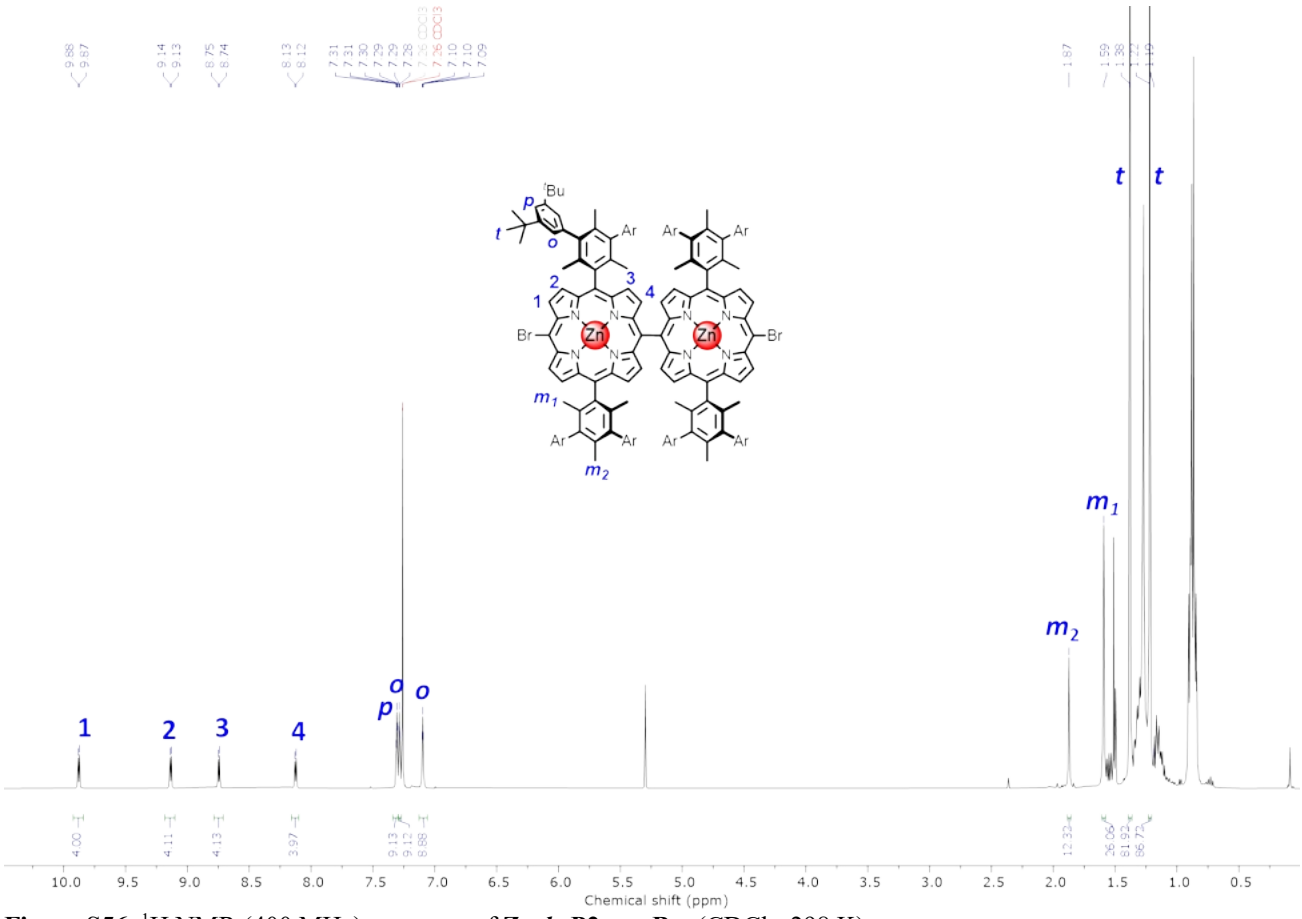

Figure S56. ^{1}H NMR (400 MHz) spectrum of **Zn-*ls*-P2$_{\mathbf{MesBu}}$Br$_2$** ($CDCl_3$, 298 K).

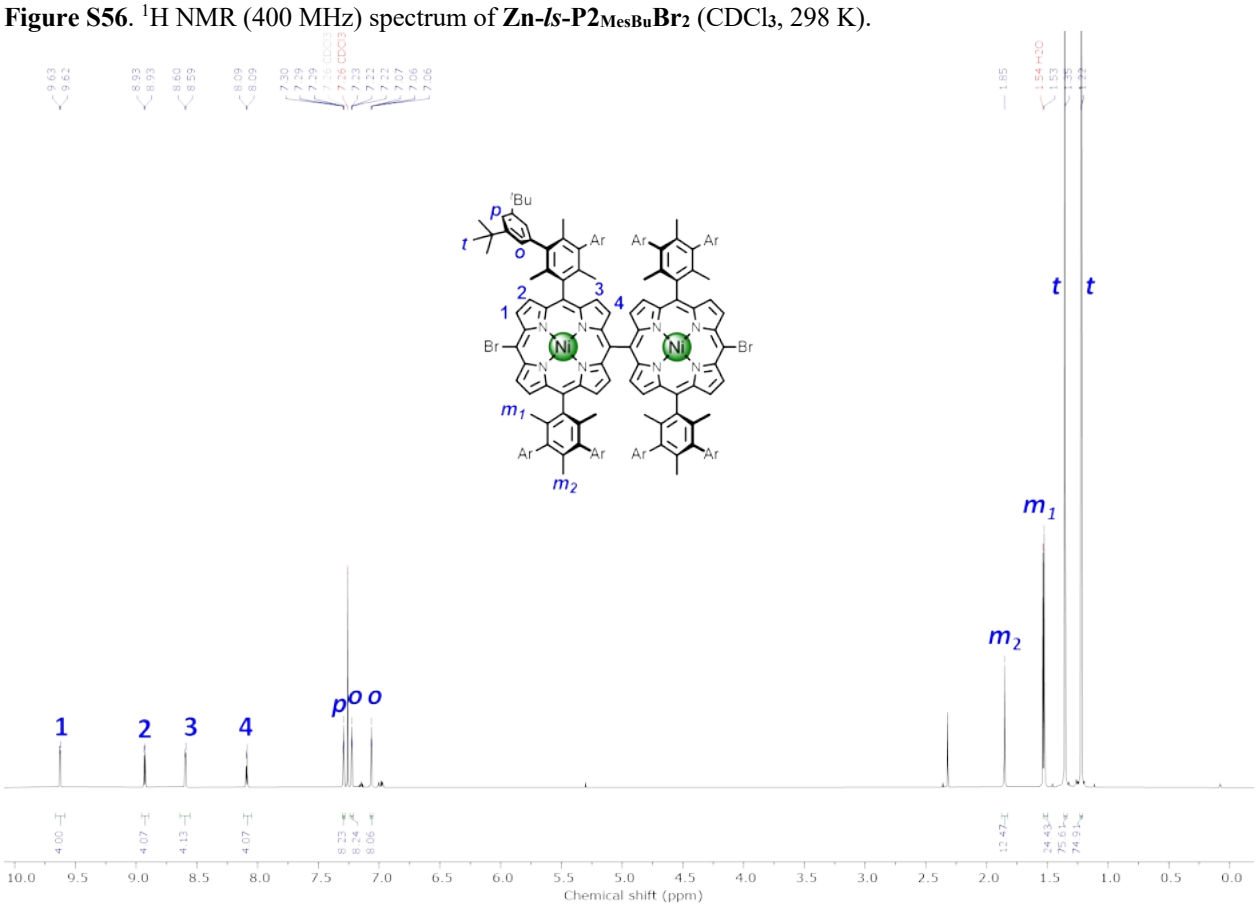

Figure S57. ^{1}H NMR (600 MHz) spectrum of ***ls*-P2$_{\mathbf{MesBu}}$Br$_2$** ($CDCl_3$, 298 K).

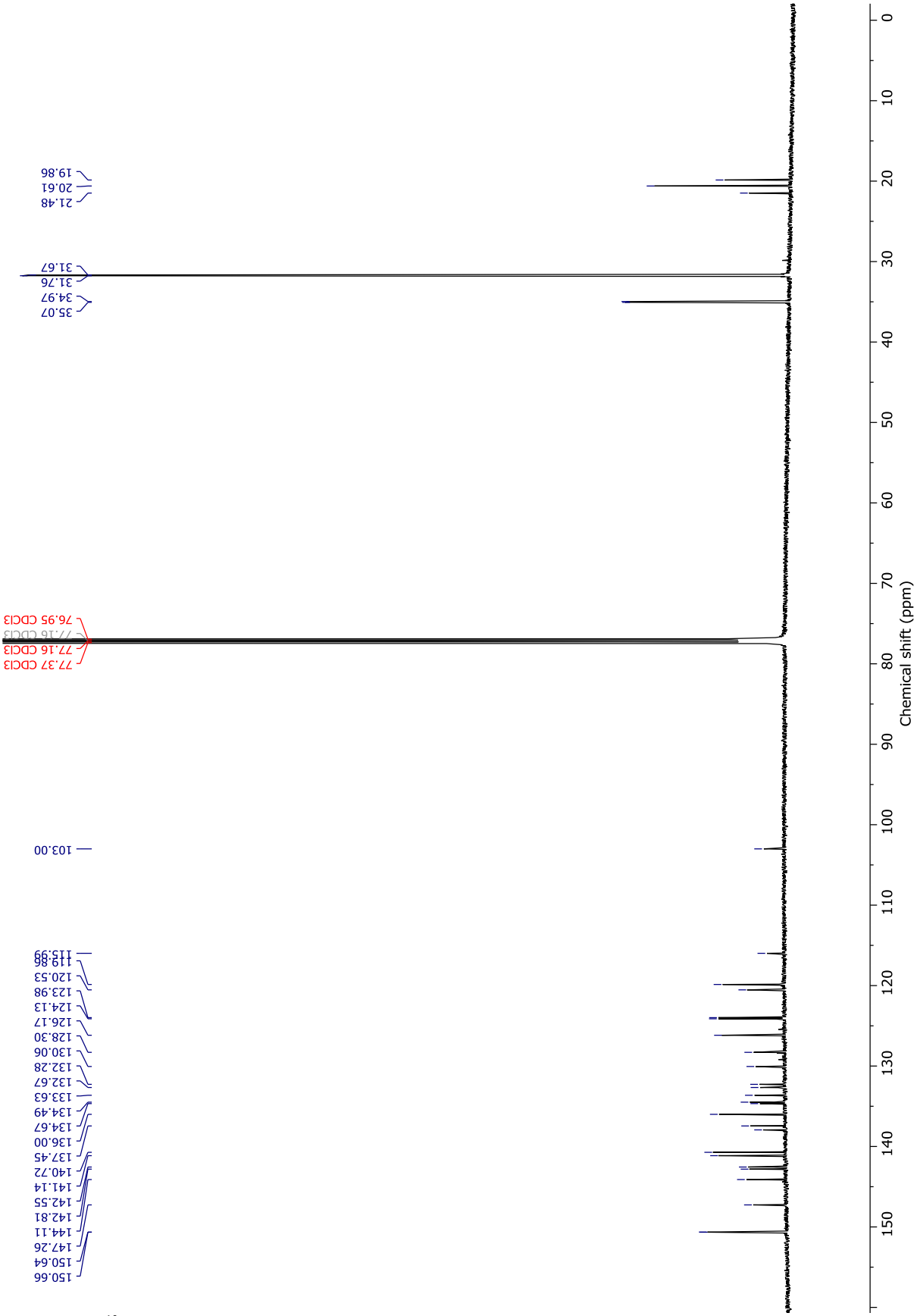

Figure S58. ^{13}C NMR (151 MHz) spectrum of ***ls*-P2$_{MesBu}$Br$_2$** ($CDCl_3$, 298 K).

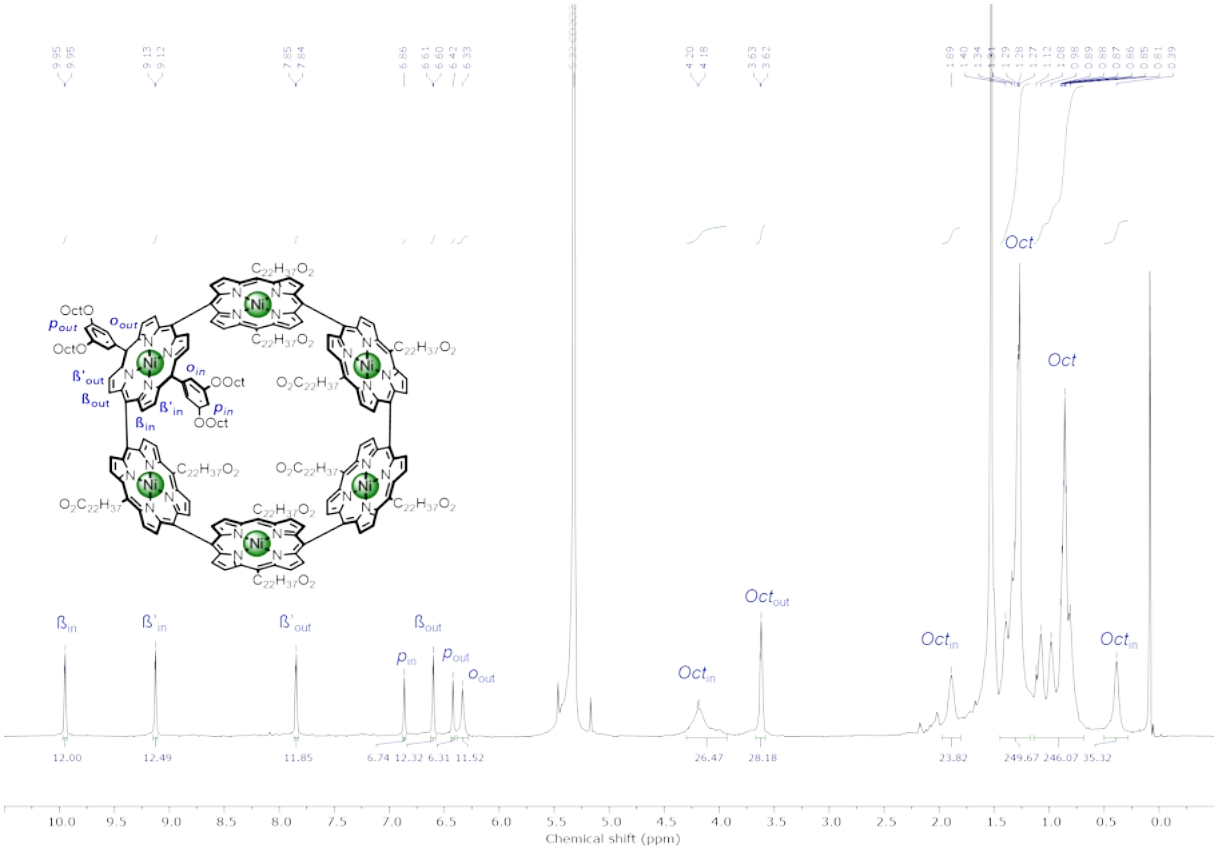

Figure S59. ^{1}H NMR (600 MHz) spectrum of ***cs*-P6$_{OOct}$** (CD_2Cl_2, 298 K).

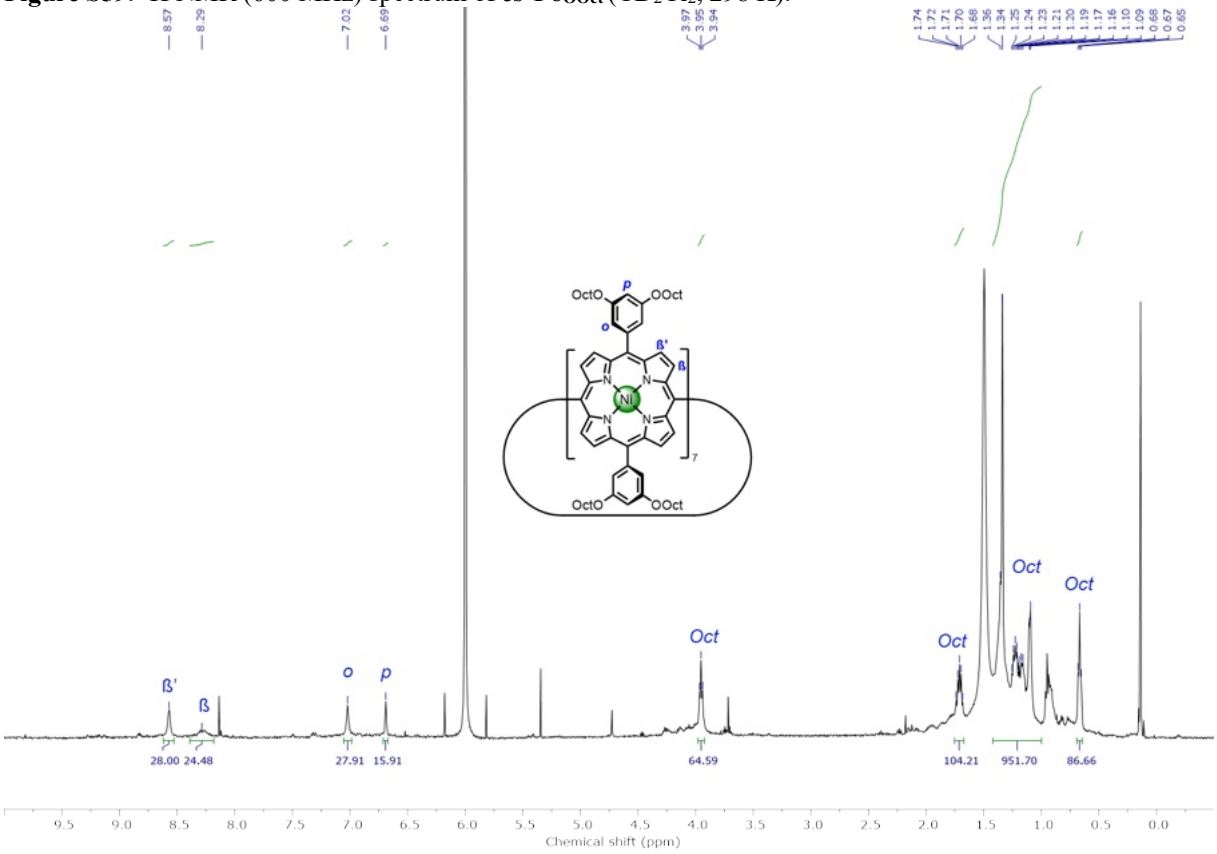

Figure S60. ^{1}H NMR (500 MHz) spectrum of ***cs*-P7$_{OOct}$** (TCE-d_2, 368 K).

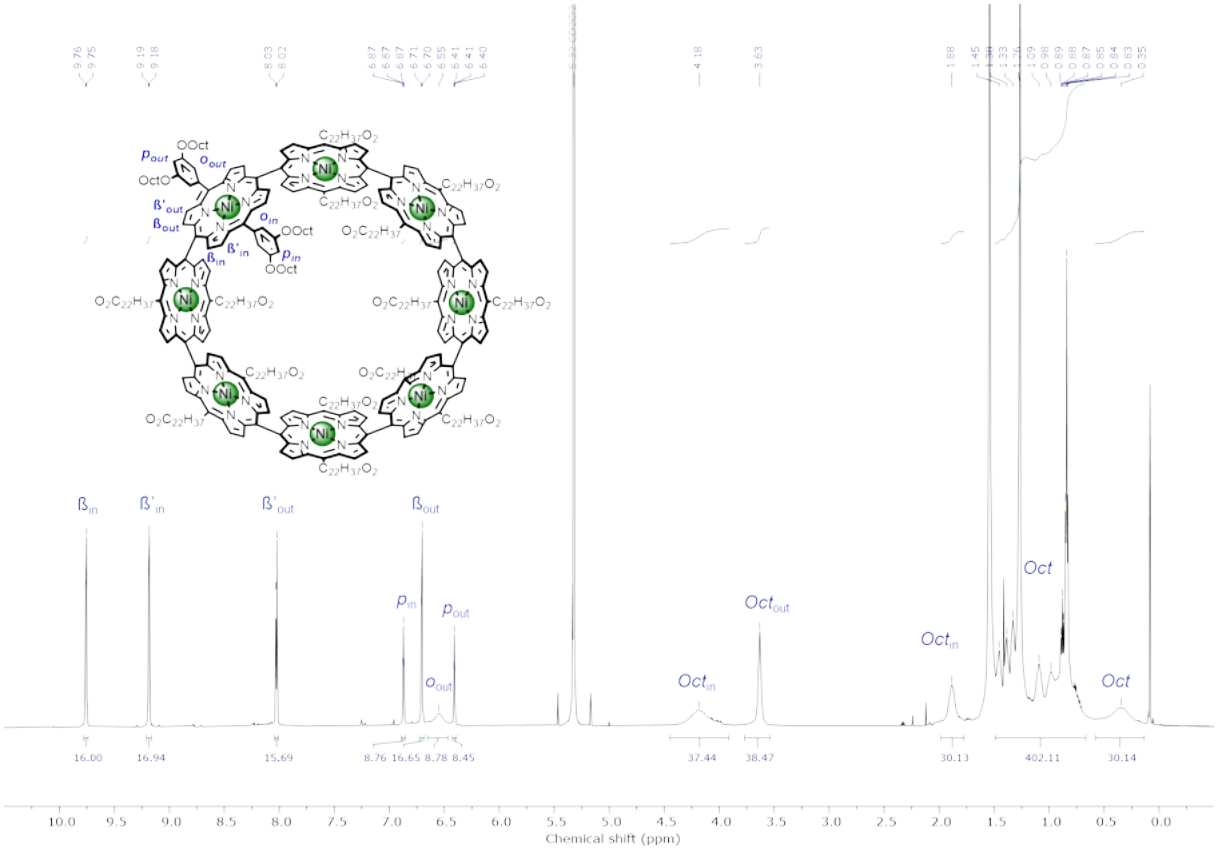

Figure S61. ^{1}H NMR (600 MHz) spectrum of ***cs*-P8$_{\mathbf{OOct}}$** (CD_2Cl_2, 298 K).

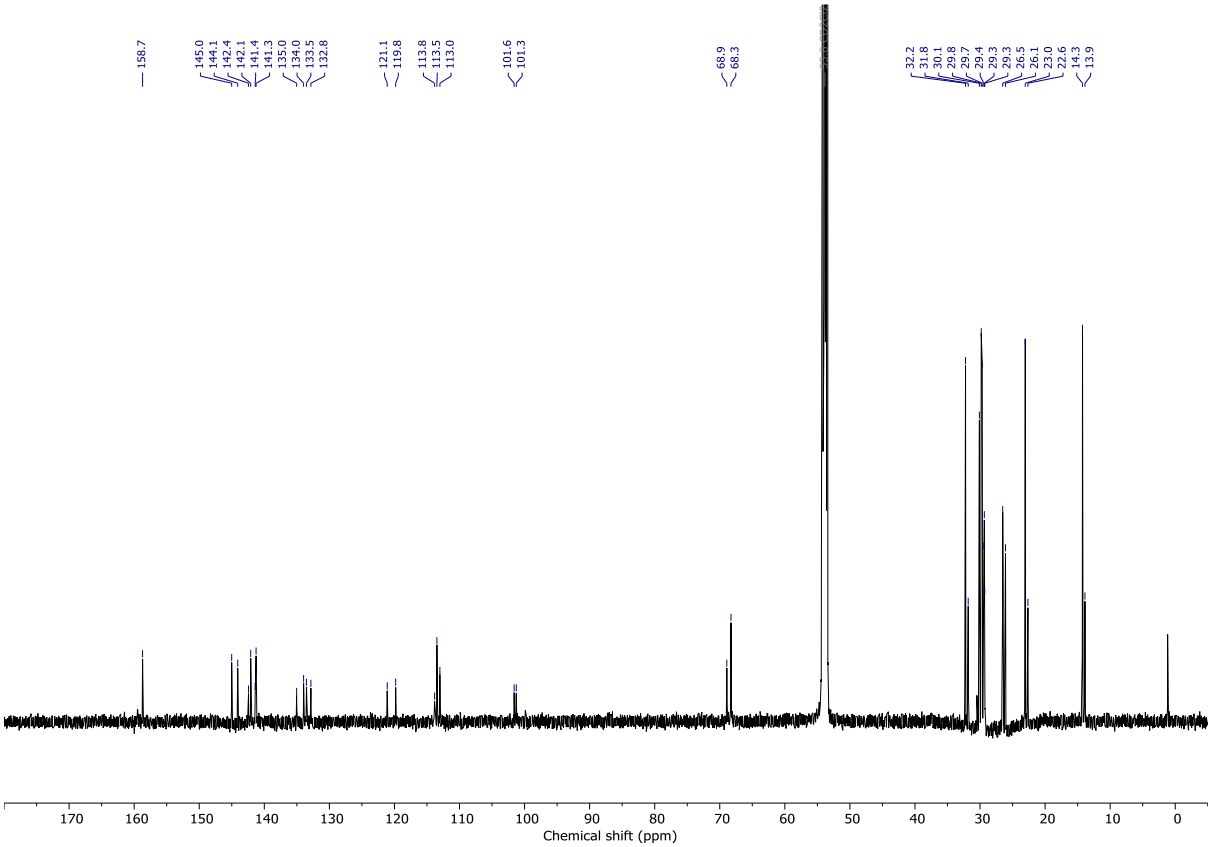

Figure S62. ^{13}C NMR (151 MHz) spectrum of ***cs*-P8$_{\mathbf{OOct}}$** (CD_2Cl_2, 298 K).

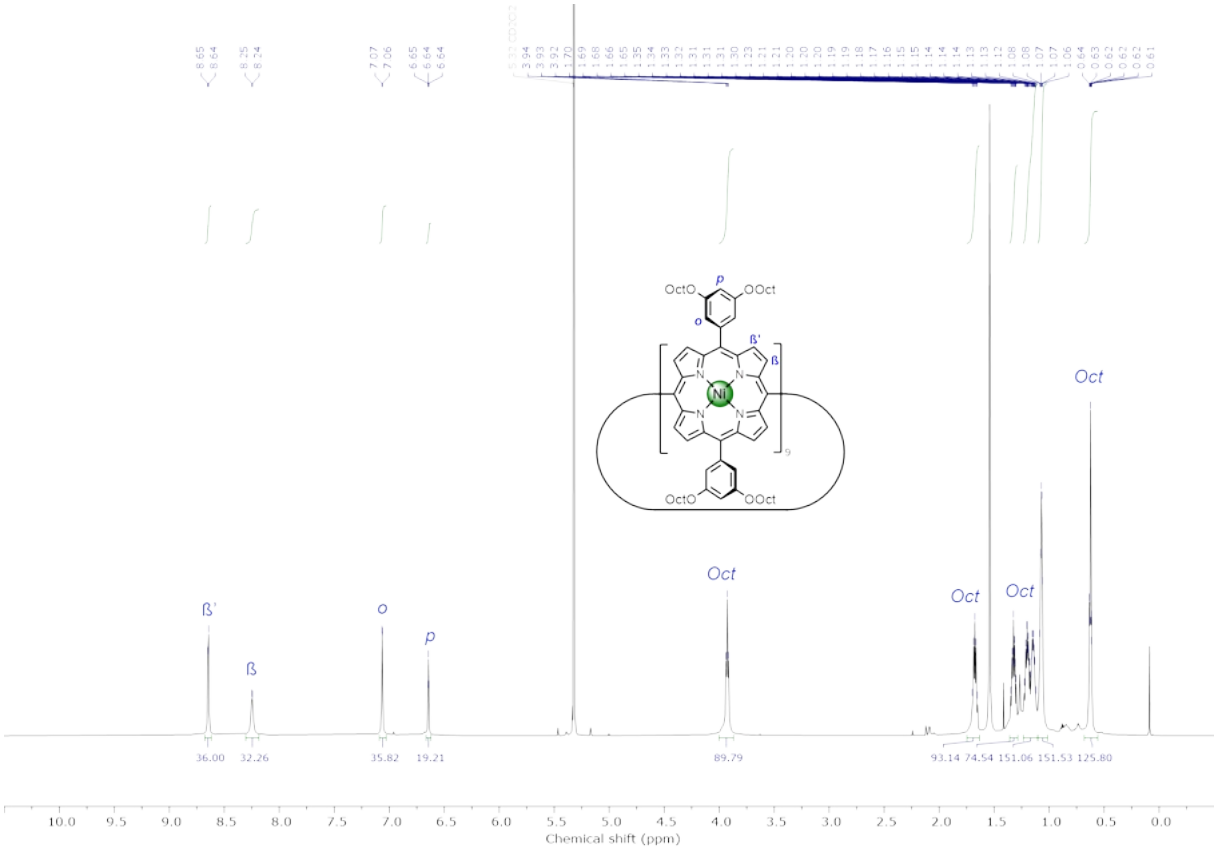

Figure S63. ^{1}H NMR (600 MHz) spectrum of ***cs*-P9$_{OOct}$** (CD_2Cl_2, 298 K).

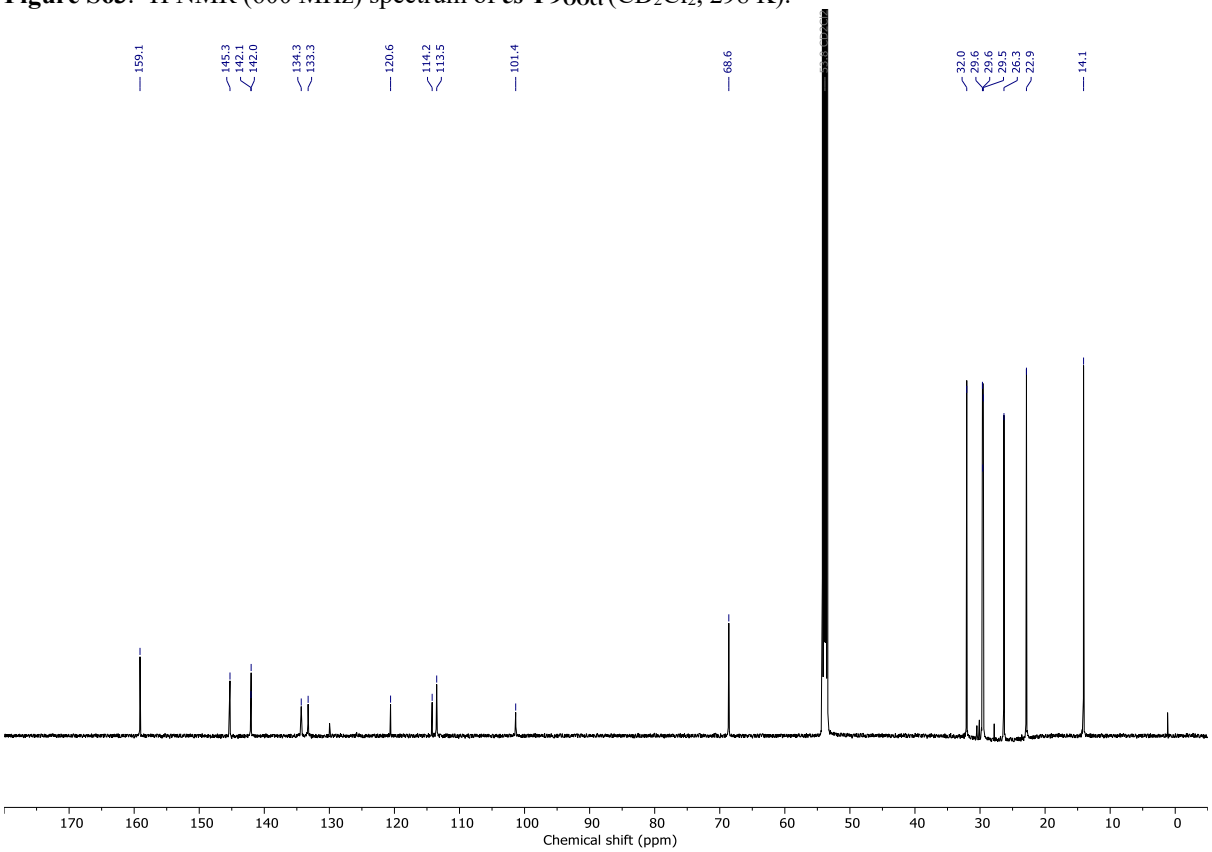

Figure S64. ^{13}C NMR (151 MHz) spectrum of ***cs*-P9$_{OOct}$** (CD_2Cl_2, 298 K).

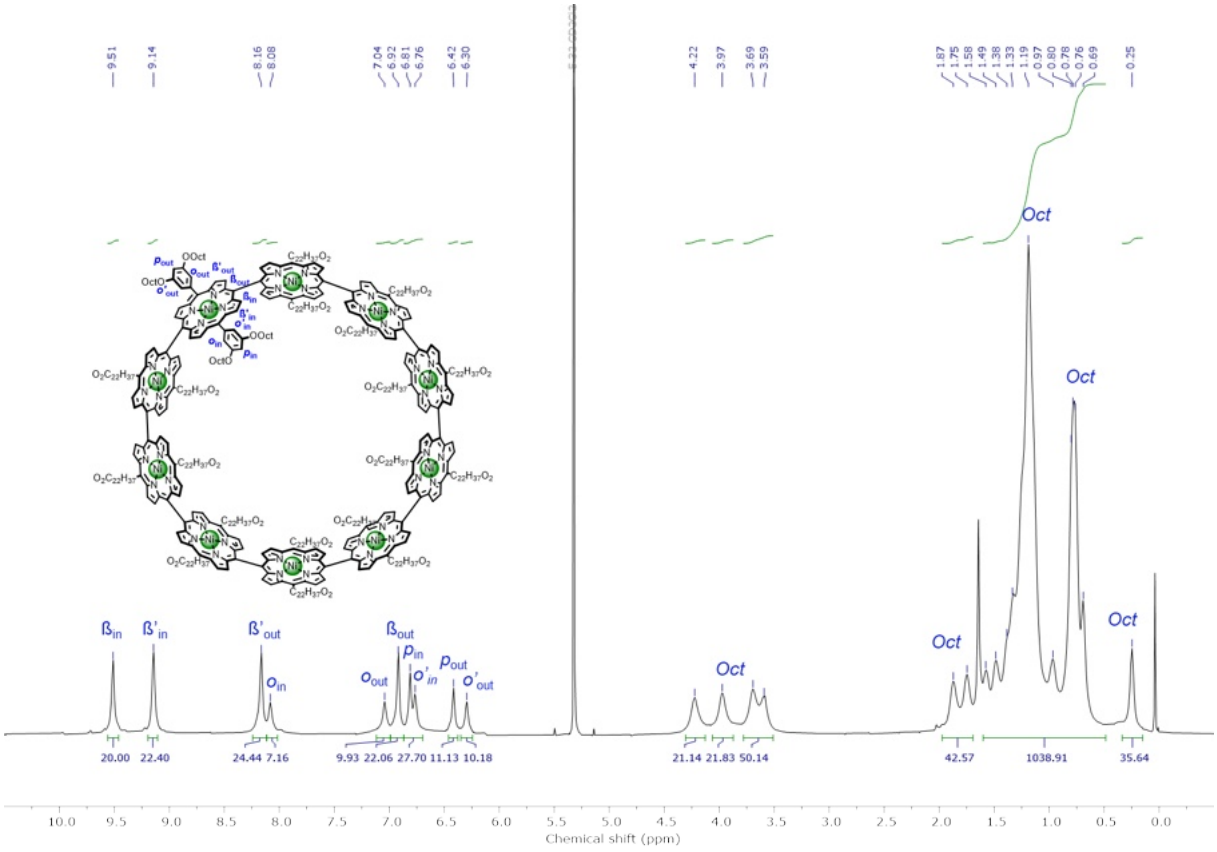

Figure S65. ^{1}H NMR (500 MHz) spectrum of ***cs*-P10$_{OOct}$** (CD_2Cl_2, 233 K).

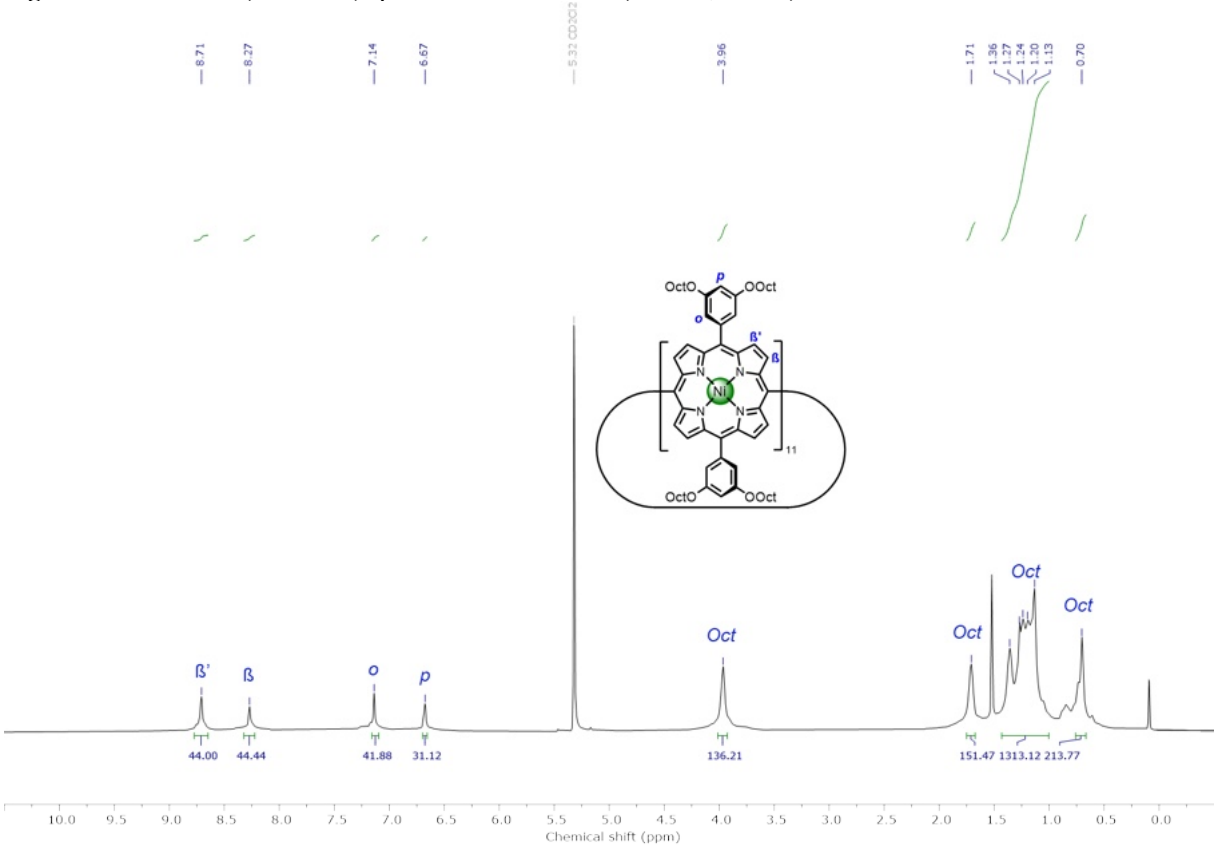

Figure S66. ^{1}H NMR (600 MHz) spectrum of ***cs*-P11$_{OOct}$** (CD_2Cl_2, 298 K).

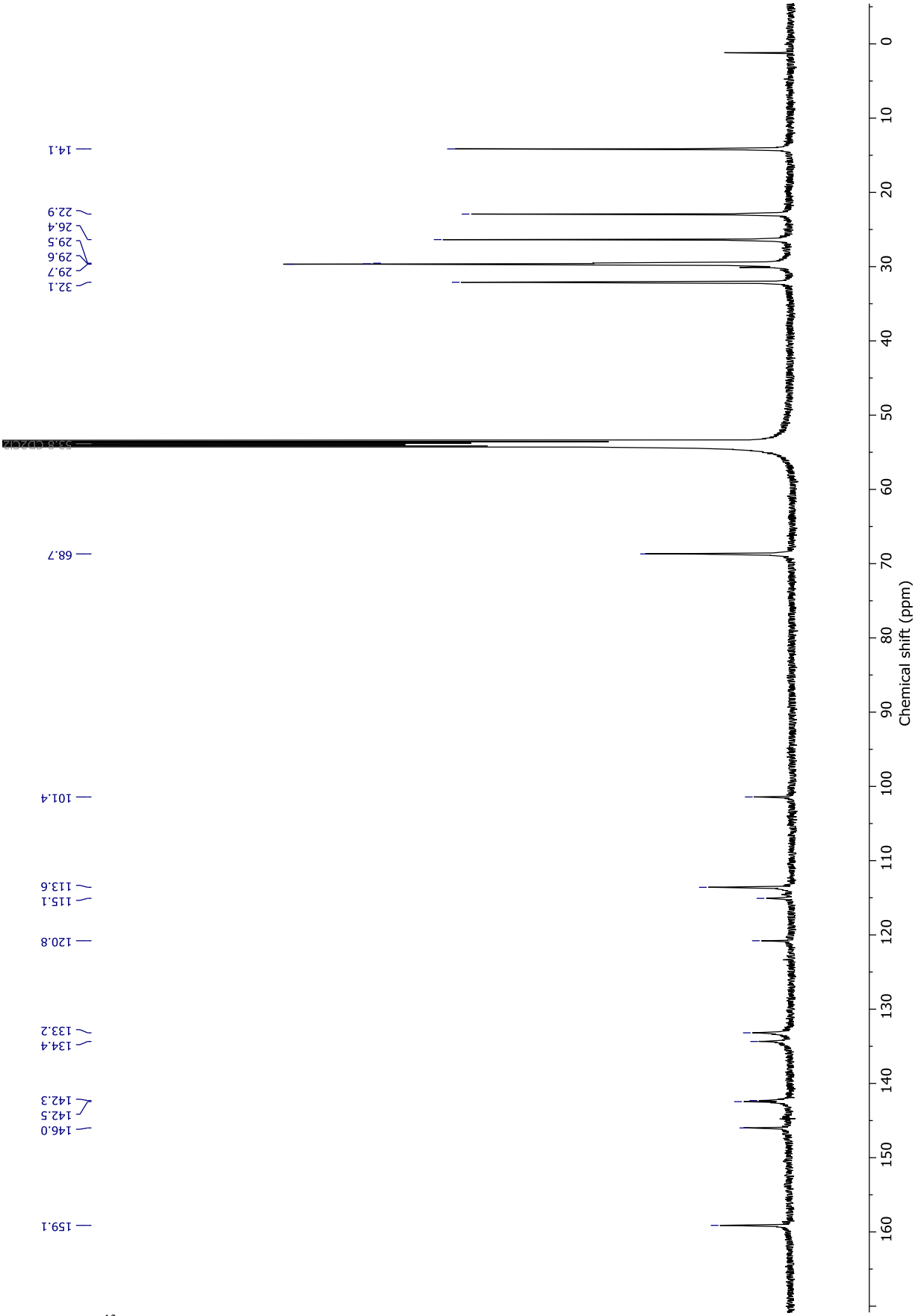

Figure S67. ^{13}C NMR (151 MHz) spectrum of ***cs*-P11$_{OOct}$** (CD_2Cl_2, 298 K).

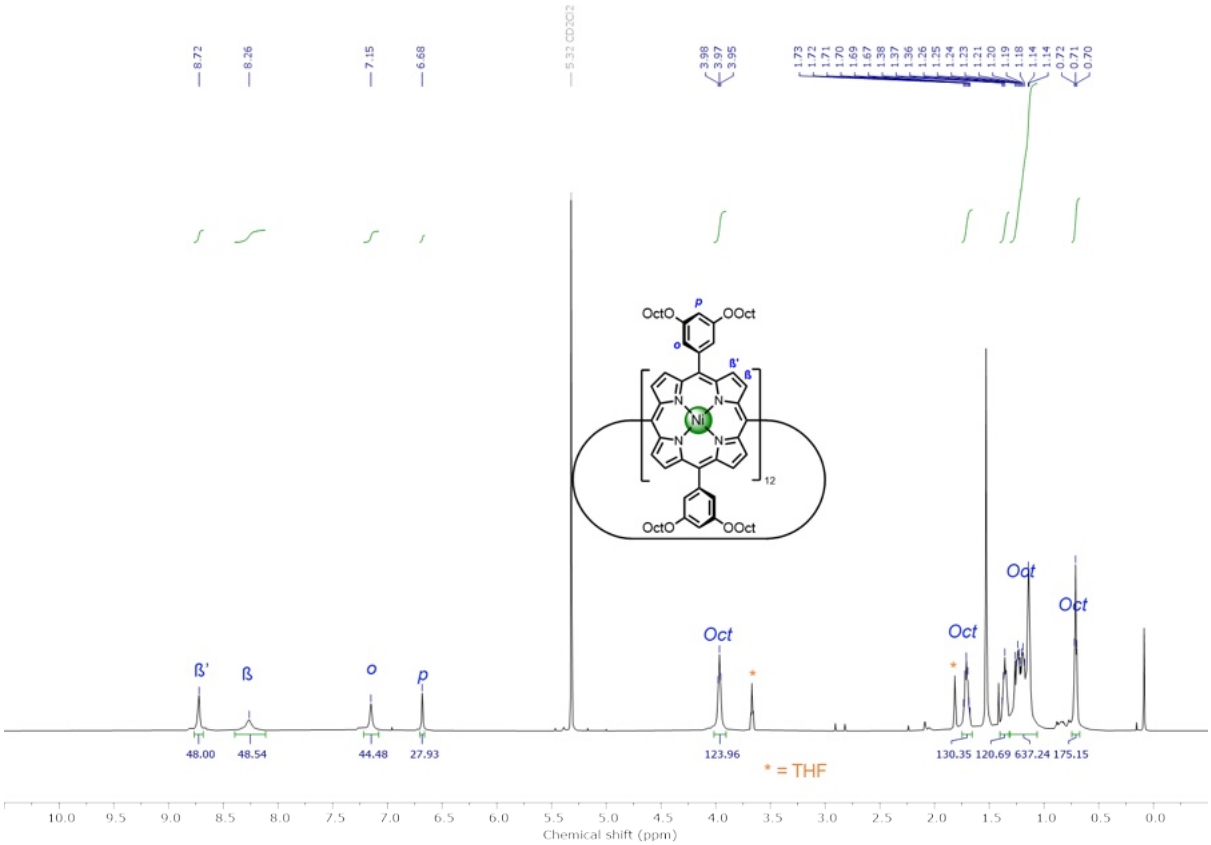

Figure S68. ^{1}H NMR (600 MHz) spectrum of ***cs*-P12$_{OOct}$** (CD_2Cl_2, 298 K).

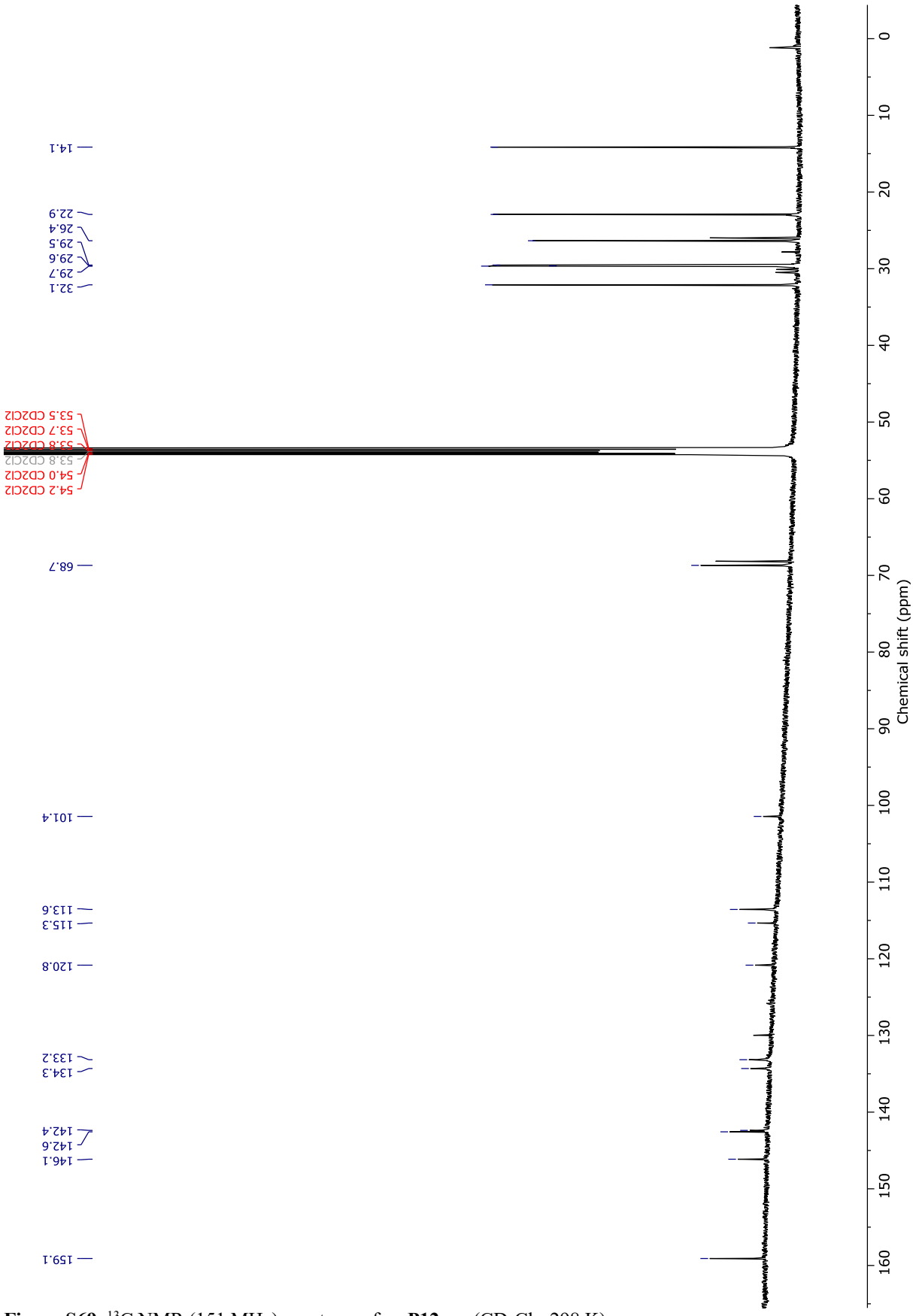

Figure S69. ^{13}C NMR (151 MHz) spectrum of ***cs*-P12$_{OOct}$** (CD_2Cl_2, 298 K).

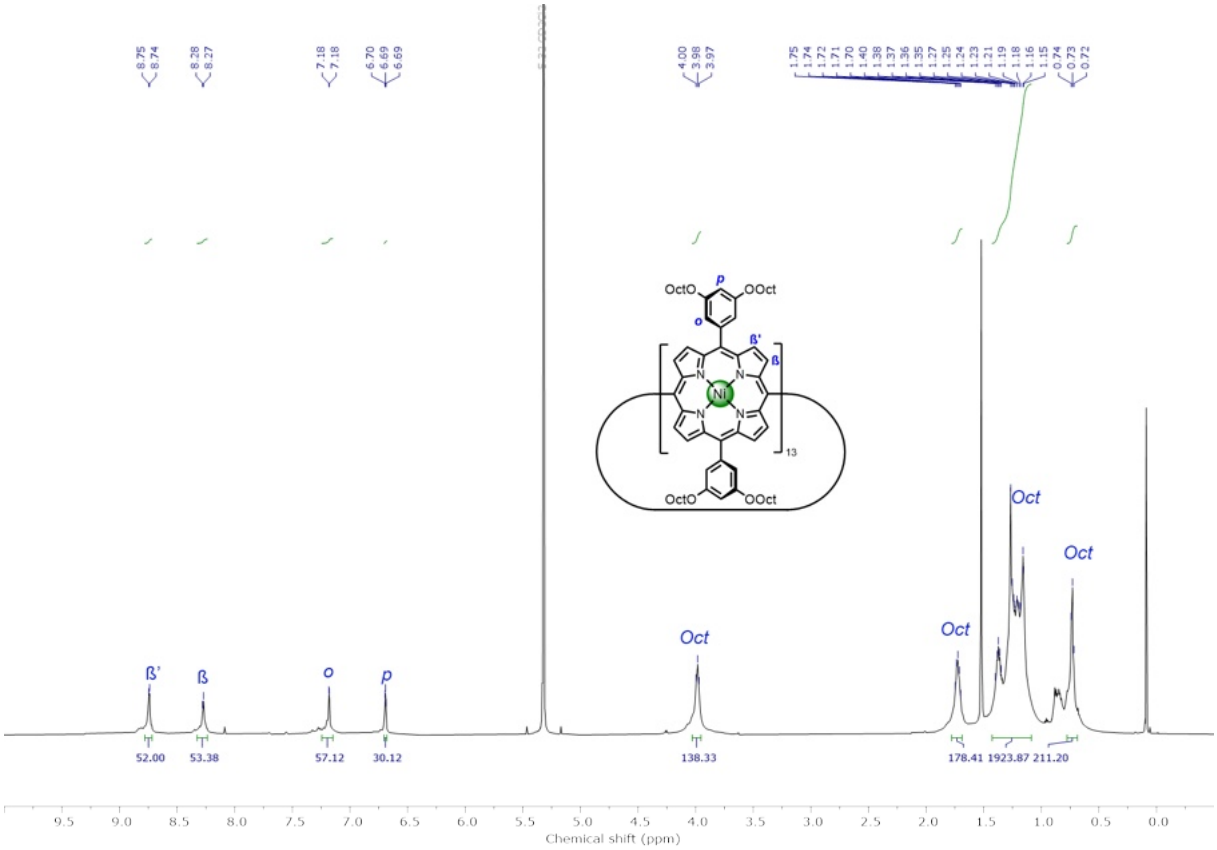

Figure S70. ^{1}H NMR (600 MHz) spectrum of ***cs*-P13$_{OOct}$** (CD_2Cl_2, 298 K).

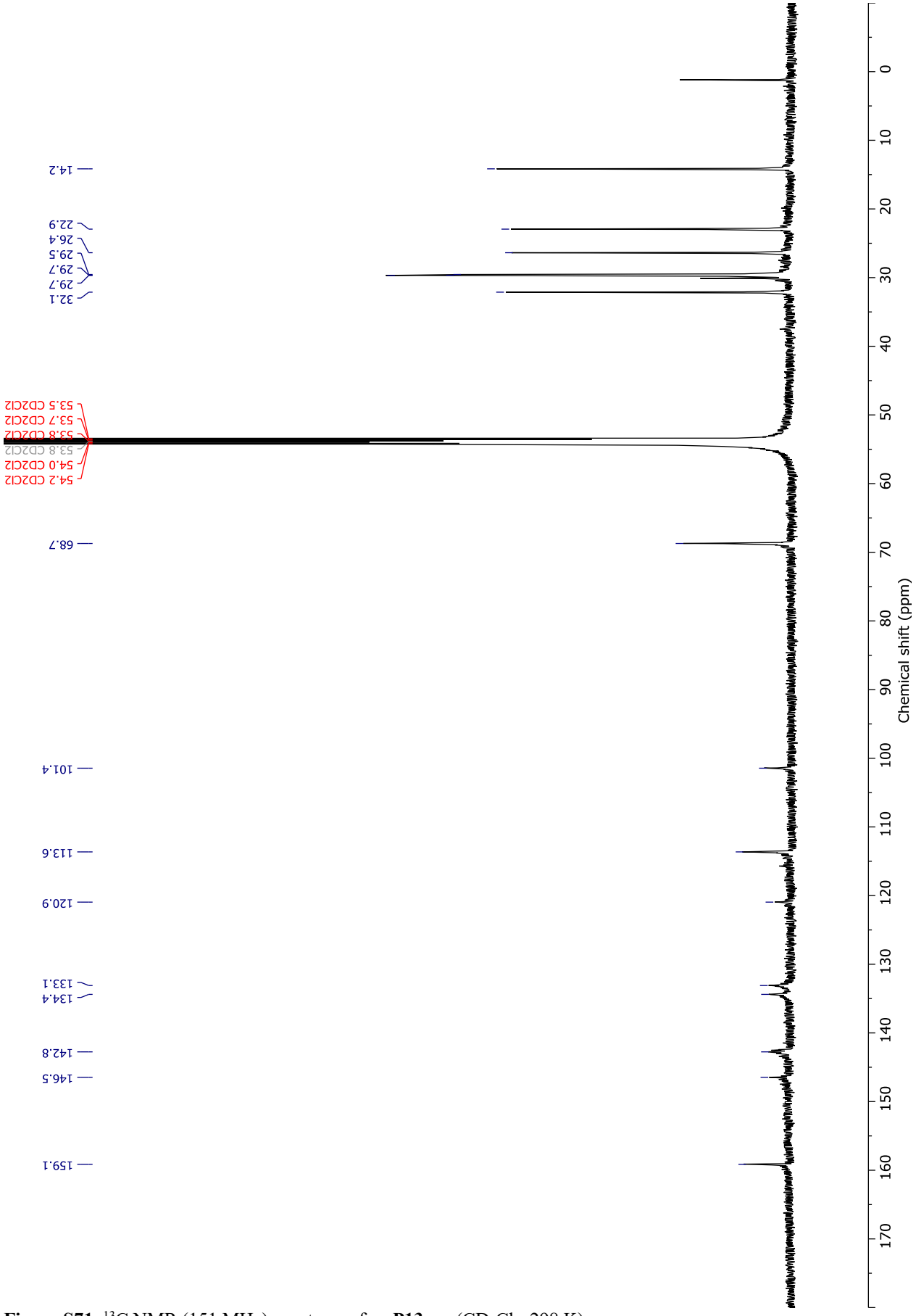

Figure S71. ^{13}C NMR (151 MHz) spectrum of ***cs*-P13$_{OOct}$** (CD_2Cl_2, 298 K).

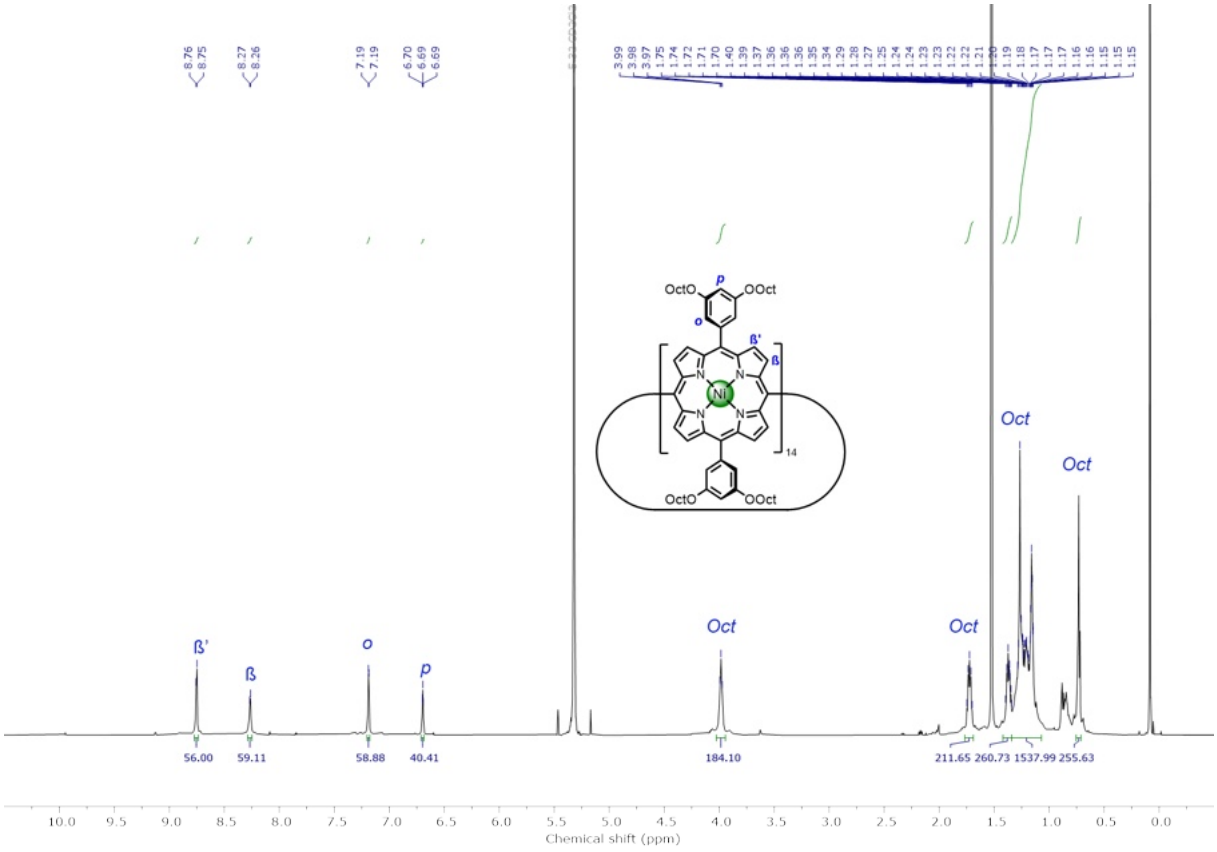

Figure S72. ^{1}H NMR (600 MHz) spectrum of ***cs*-P14$_{OOct}$** (CD_2Cl_2, 298 K).

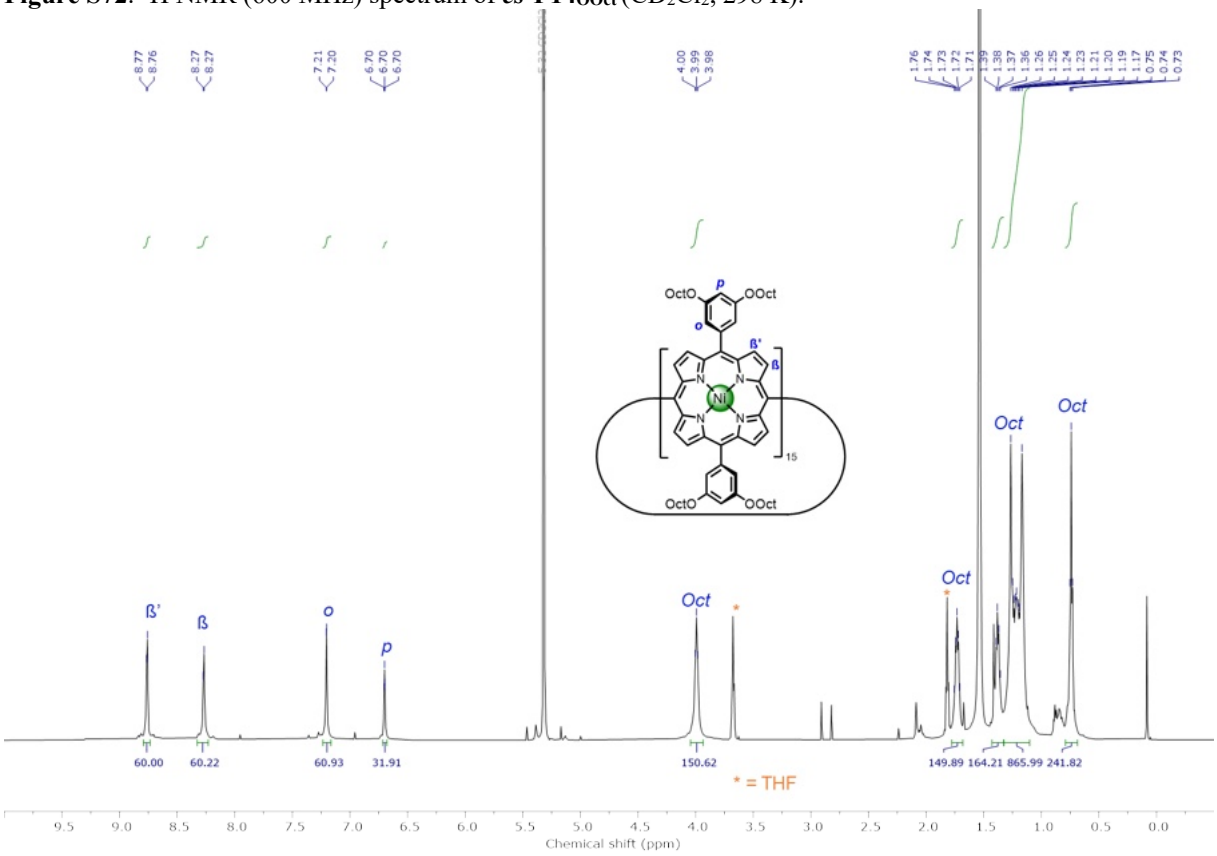

Figure S73. ^{1}H NMR (600 MHz) spectrum of ***cs*-P15$_{OOct}$** (CD_2Cl_2, 298 K).

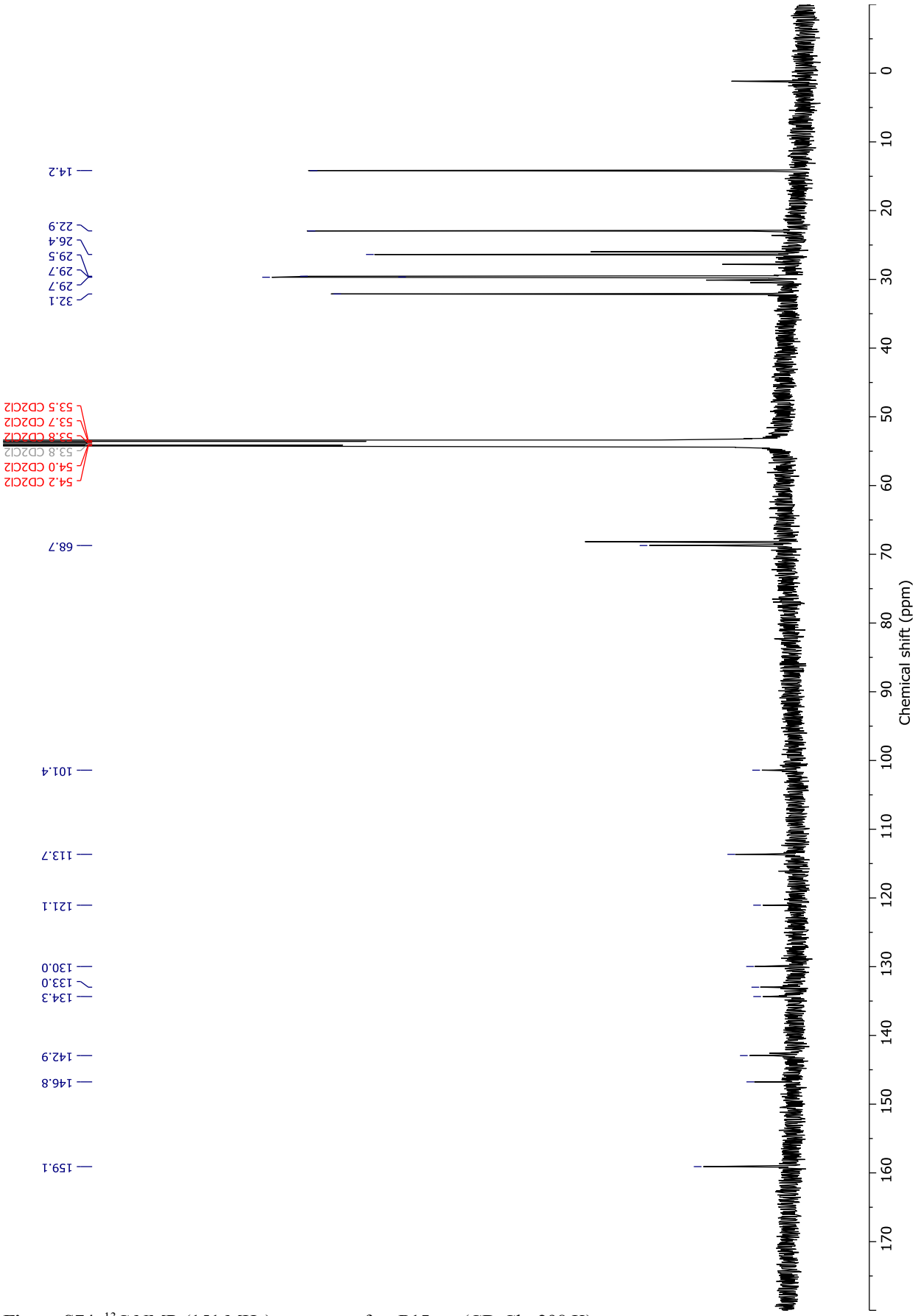

Figure S74. ^{13}C NMR (151 MHz) spectrum of ***cs*-P15$_{OOct}$** (CD_2Cl_2, 298 K).

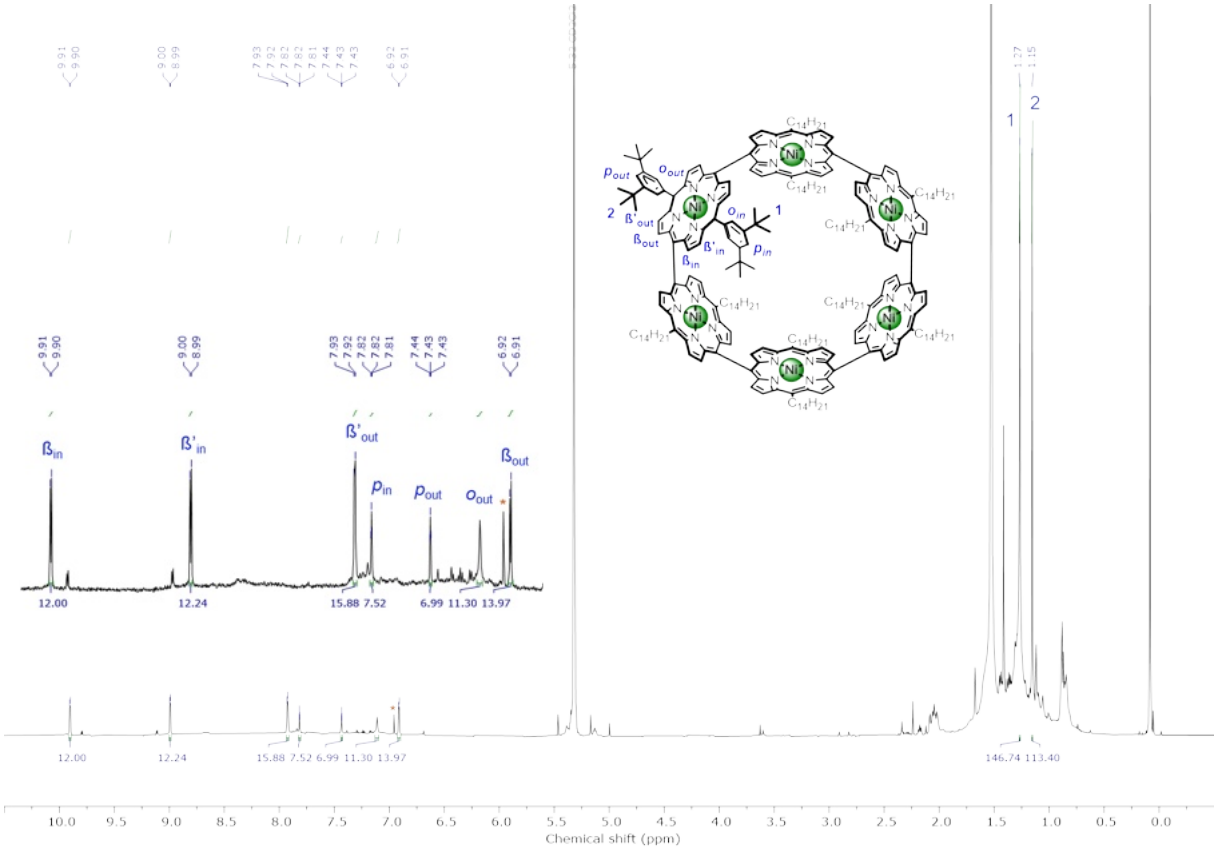

Figure S75. ^{1}H NMR (600 MHz) spectrum of ***cs*-P6$_{t\mathrm{Bu}}$** (CD_2Cl_2, 298 K).

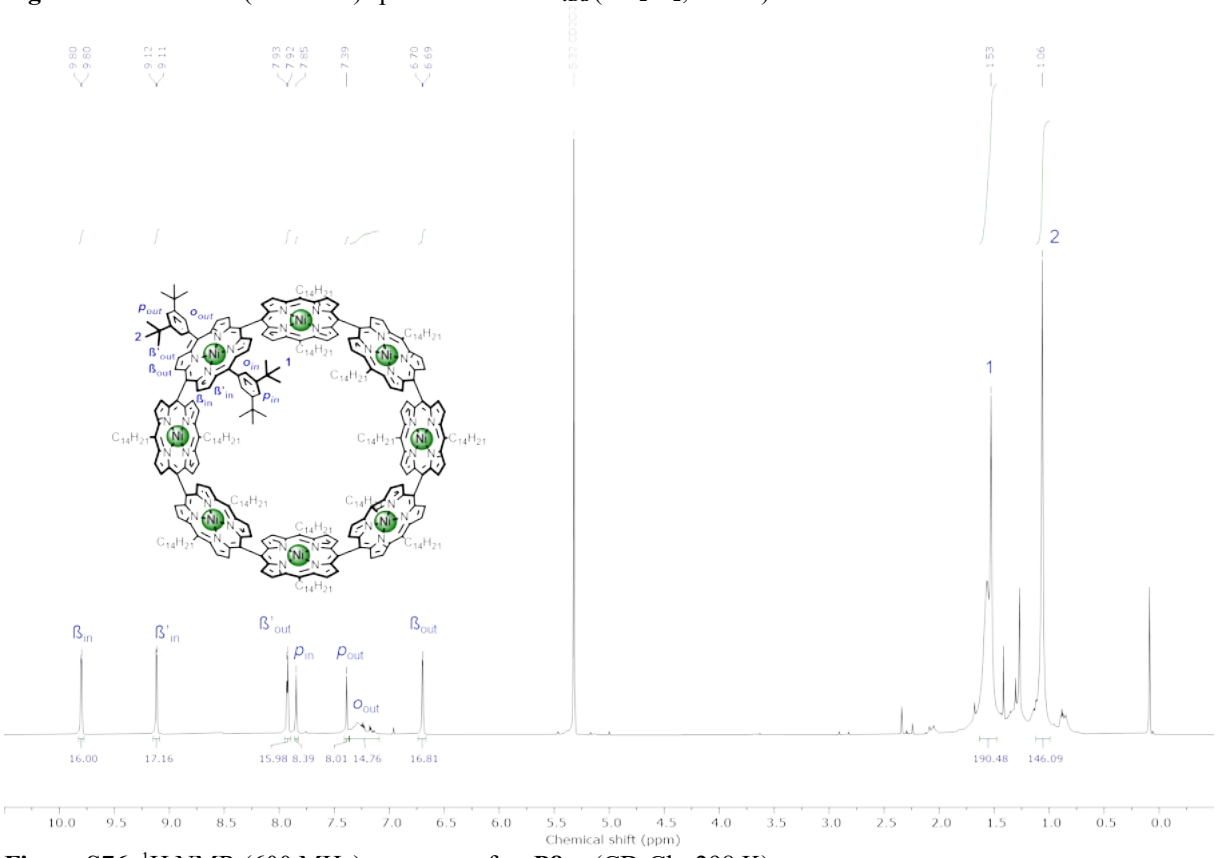

Figure S76. ^{1}H NMR (600 MHz) spectrum of ***cs*-P8$_{t\mathrm{Bu}}$** (CD_2Cl_2, 298 K).

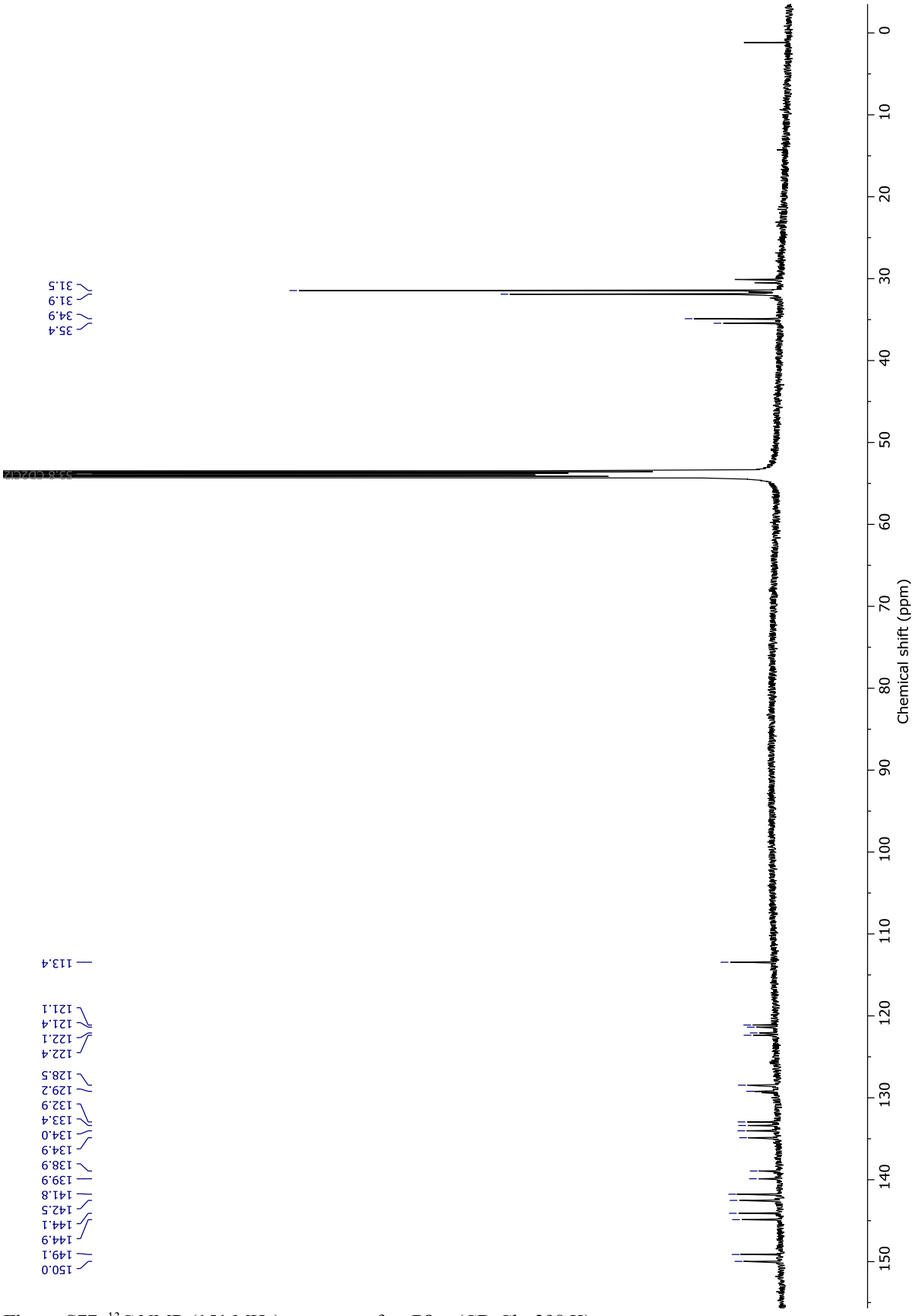

Figure S77. ^{13}C NMR (151 MHz) spectrum of ***cs*-P8$_{t\mathrm{Bu}}$** (CD_2Cl_2, 298 K).

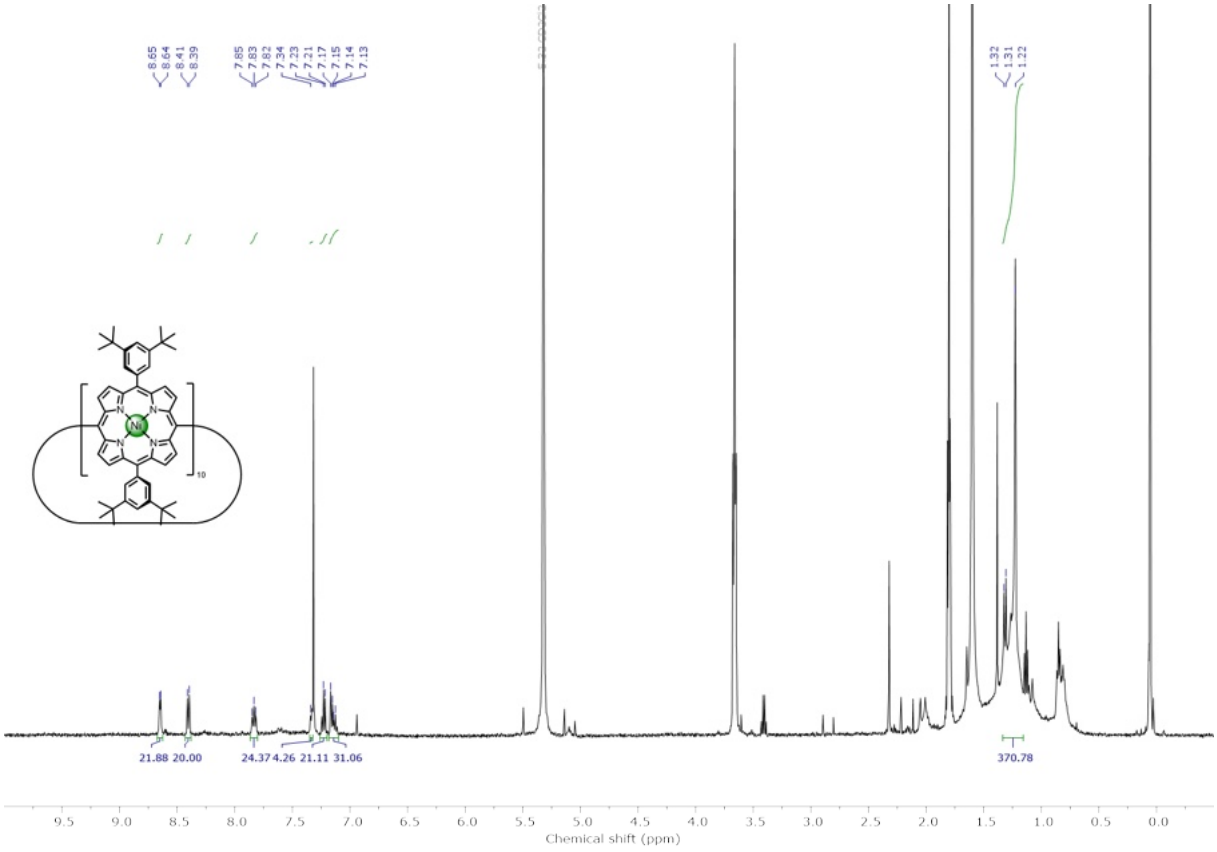

Figure S78. ^{1}H NMR (500 MHz) spectrum of ***cs*-P10$_{t\mathrm{Bu}}$** (CD_2Cl_2, 263 K).

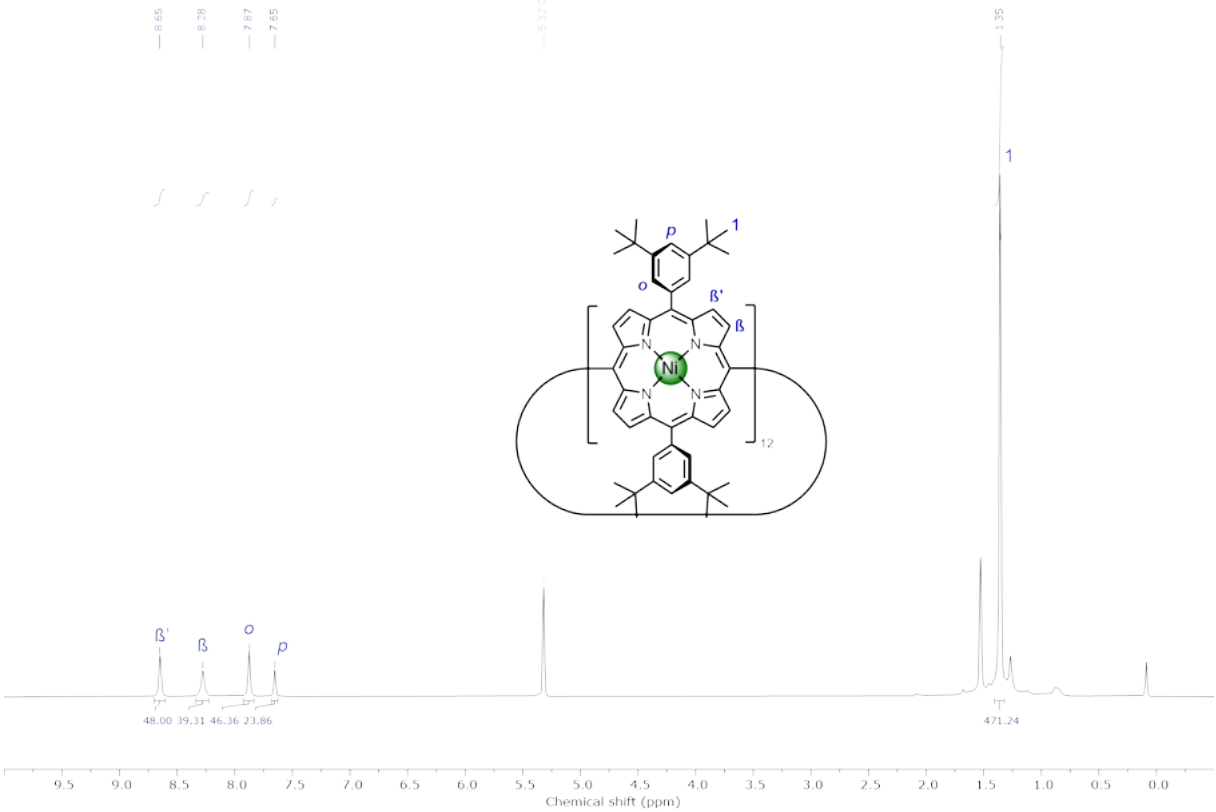

Figure S79. ^{1}H NMR (600 MHz) spectrum of ***cs*-P12$_{t\mathrm{Bu}}$** (CD_2Cl_2, 298 K).

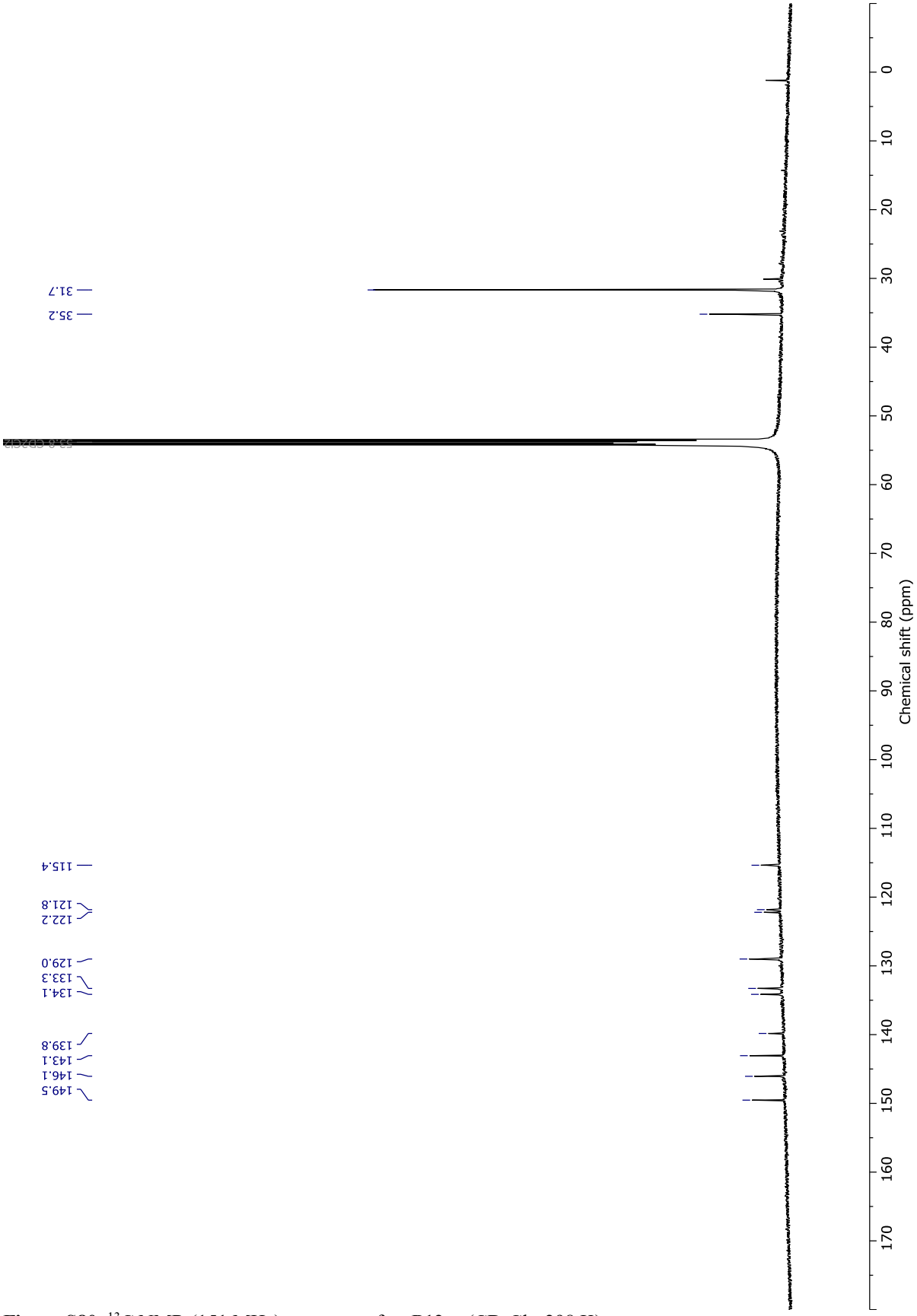

Figure S80. ^{13}C NMR (151 MHz) spectrum of ***cs*-P12$_{t\mathrm{Bu}}$** (CD_2Cl_2, 298 K).

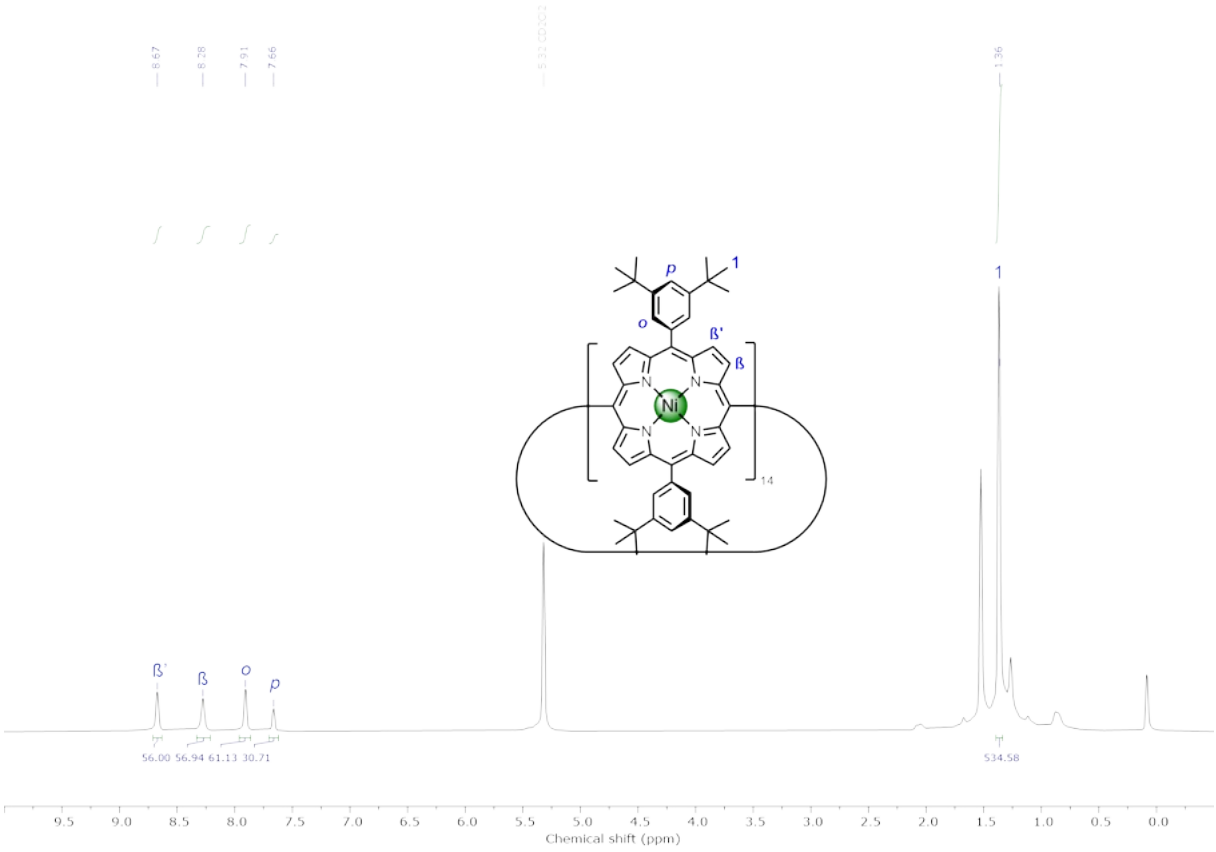

Figure S81. ^{1}H NMR (600 MHz) spectrum of ***cs*-P14$_{t\mathrm{Bu}}$** (CD_2Cl_2, 298 K).

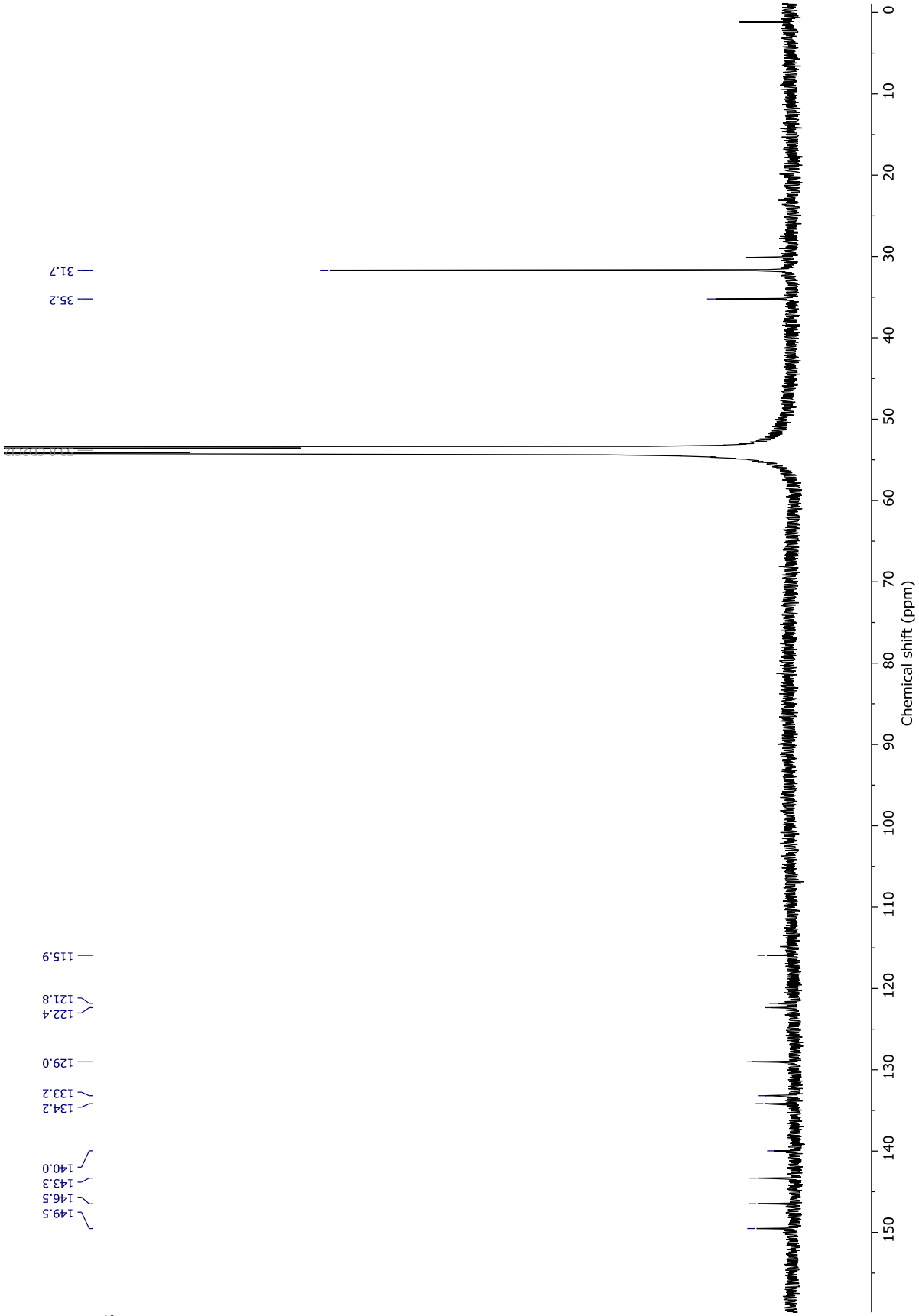

Figure S82. ^{13}C NMR (151 MHz) spectrum of ***cs*-P14$_{t\mathrm{Bu}}$** (CD_2Cl_2, 298 K).

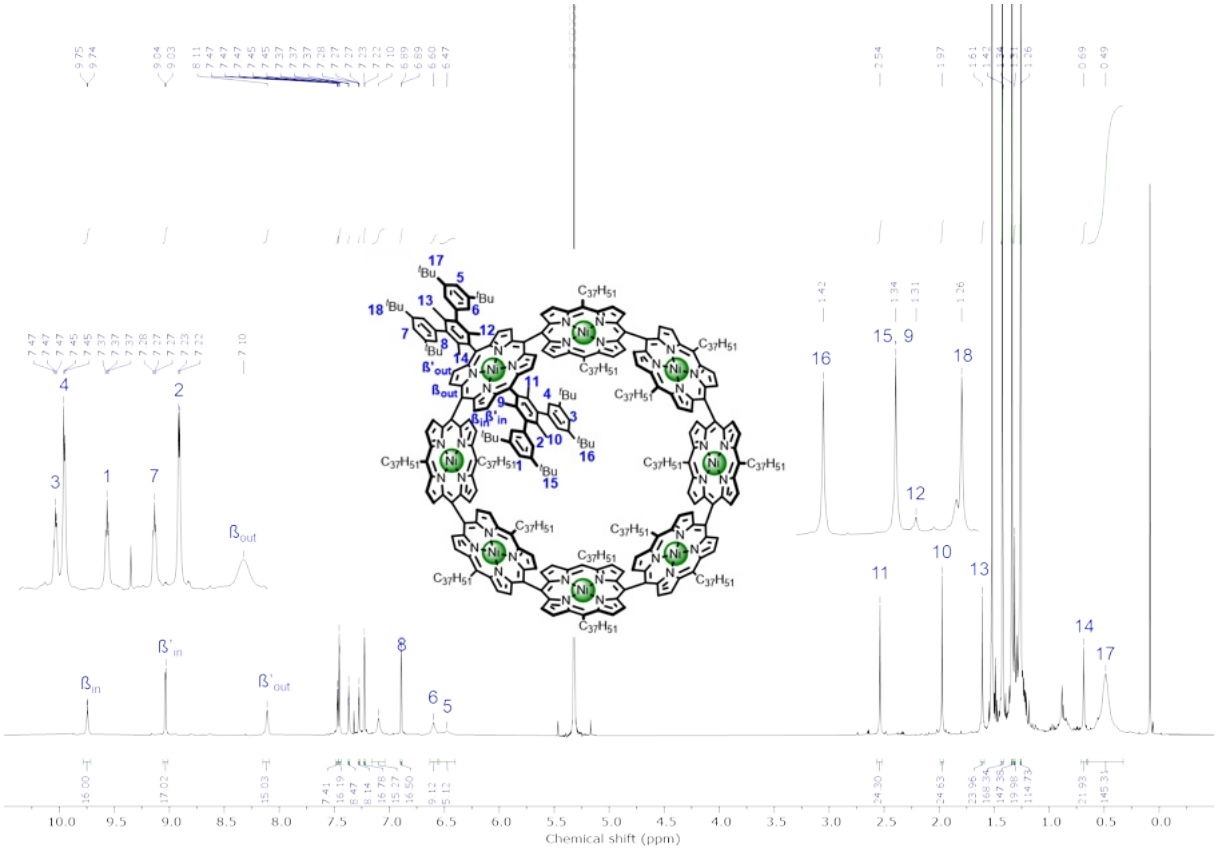

Figure S83. ^{1}H NMR (600 MHz) spectrum of ***cs*-P8$_{\mathbf{MesBu}}$** (CD_2Cl_2, 298 K).

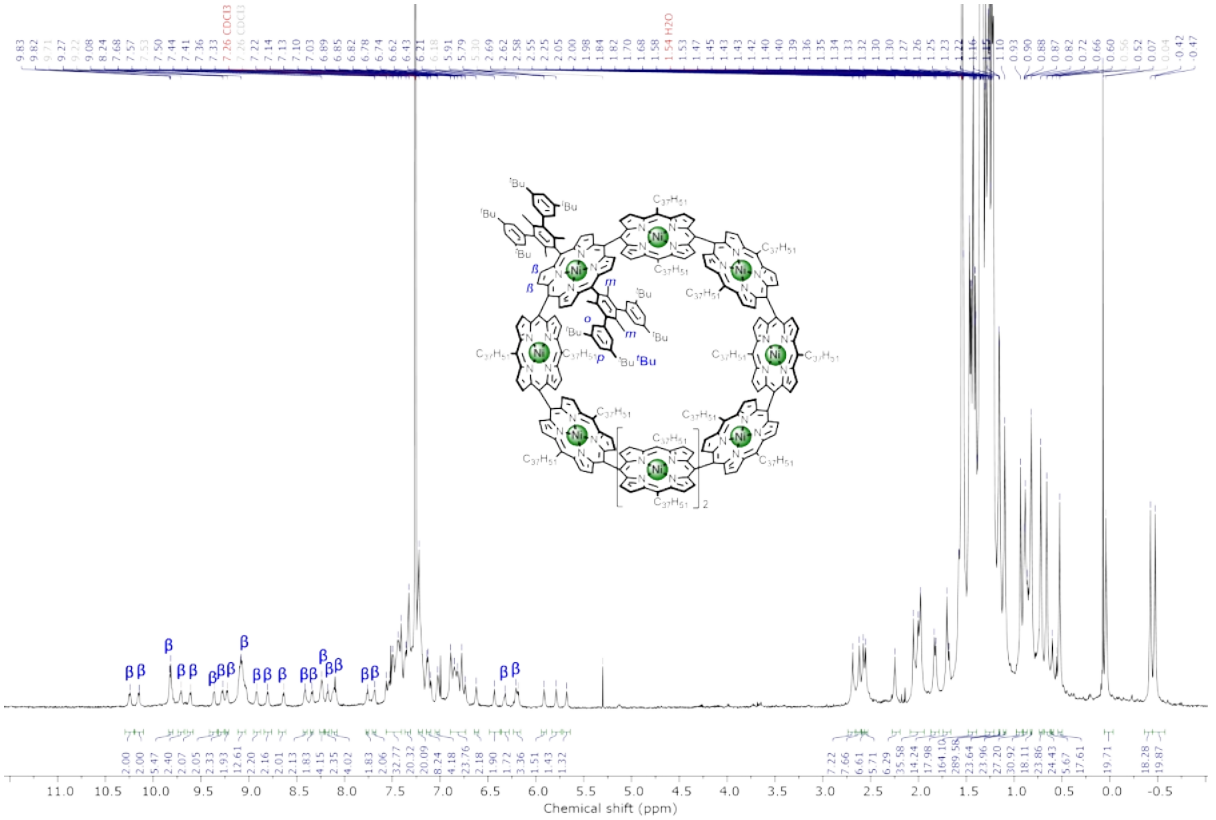

Figure S84. ^{1}H NMR (400 MHz) spectrum of ***cs*-P9$_{\mathbf{MesBu}}$** ($CDCl_3$, 298 K).

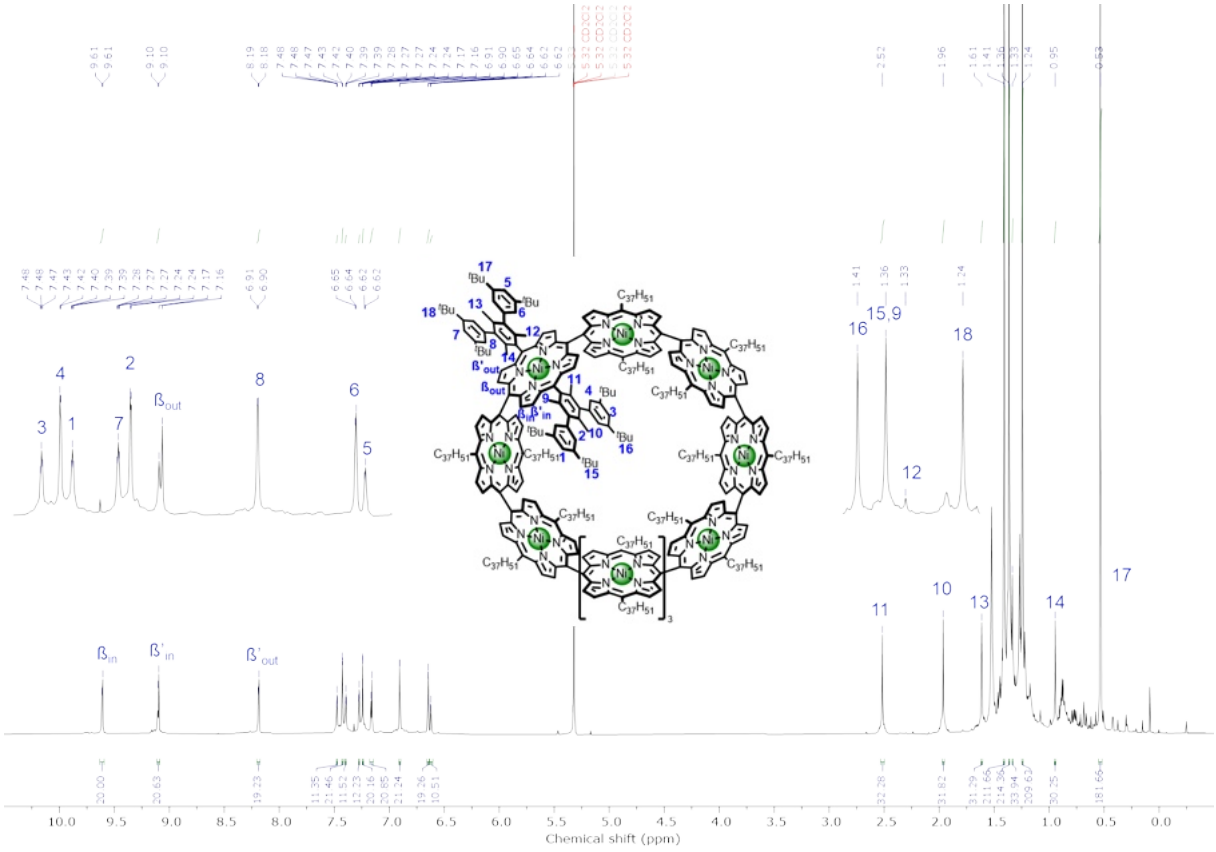

Figure S85. ^{1}H NMR (600 MHz) spectrum of ***cs*-P10$_{\mathbf{MesBu}}$** (CD_2Cl_2, 298 K).

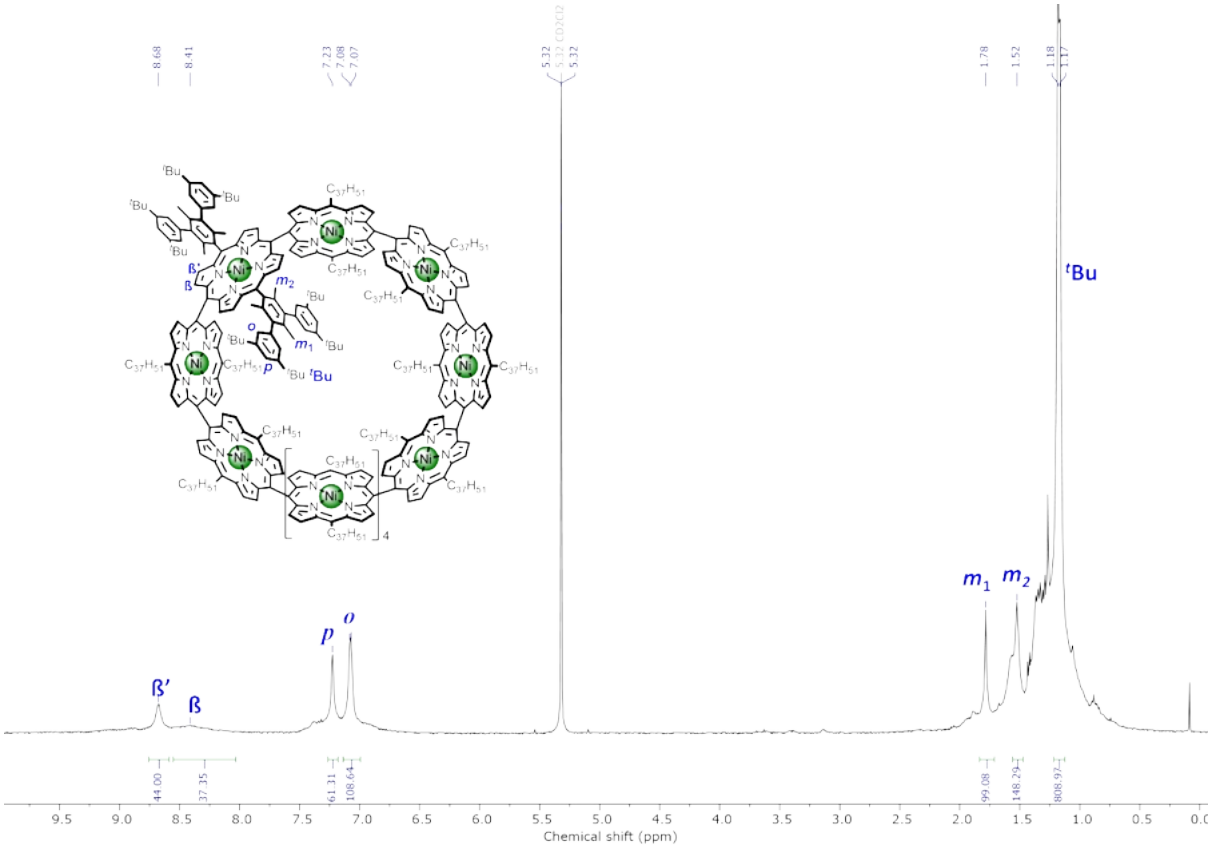

Figure S86. ^{1}H NMR (400 MHz) spectrum of ***cs*-P11$_{\mathbf{MesBu}}$** (CD_2Cl_2, 298 K).

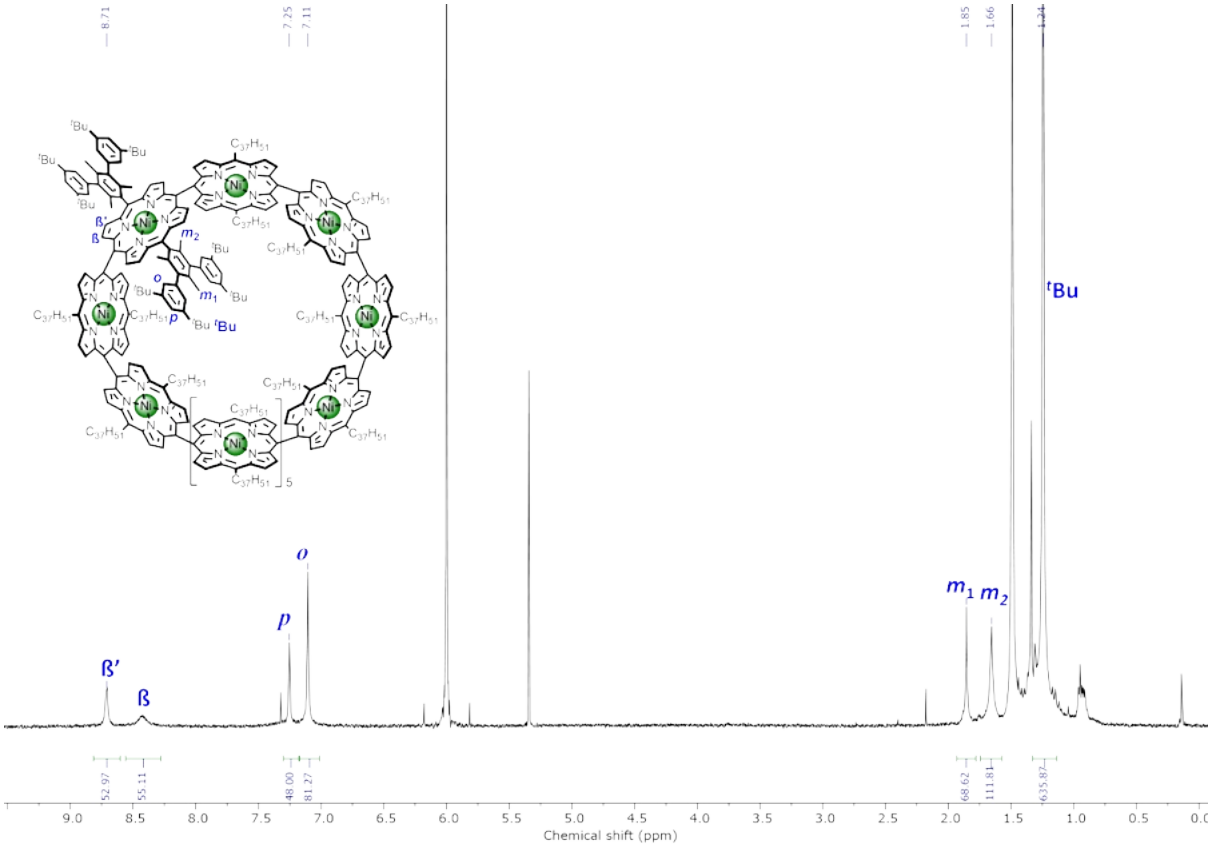

Figure S87. ^{1}H NMR (500 MHz) spectrum of ***cs*-P12$_{\mathbf{MesBu}}$** (TCE-d_2, 368 K).

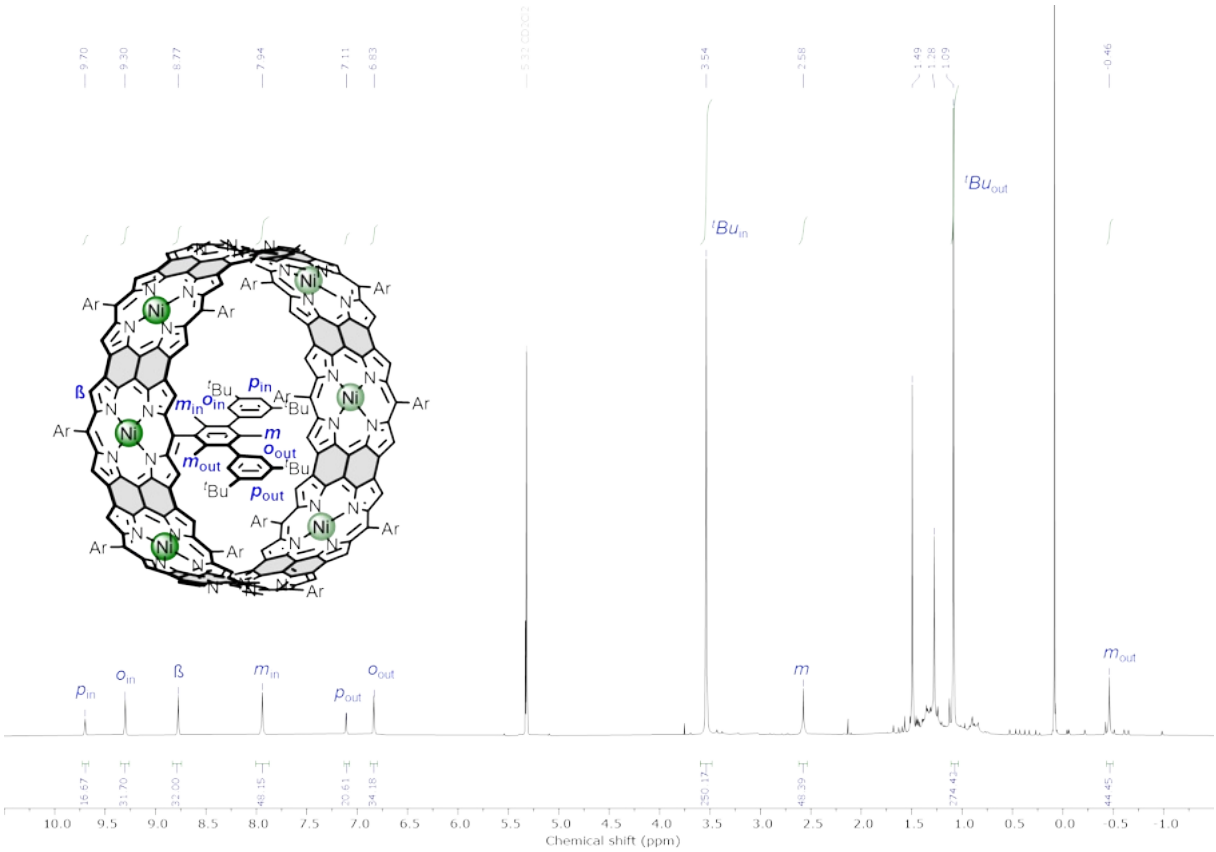

Figure S88. ^{1}H NMR (400 MHz) spectrum of ***cf*-P8$_{\mathbf{MesBu}}$** (CD_2Cl_2, 298 K).

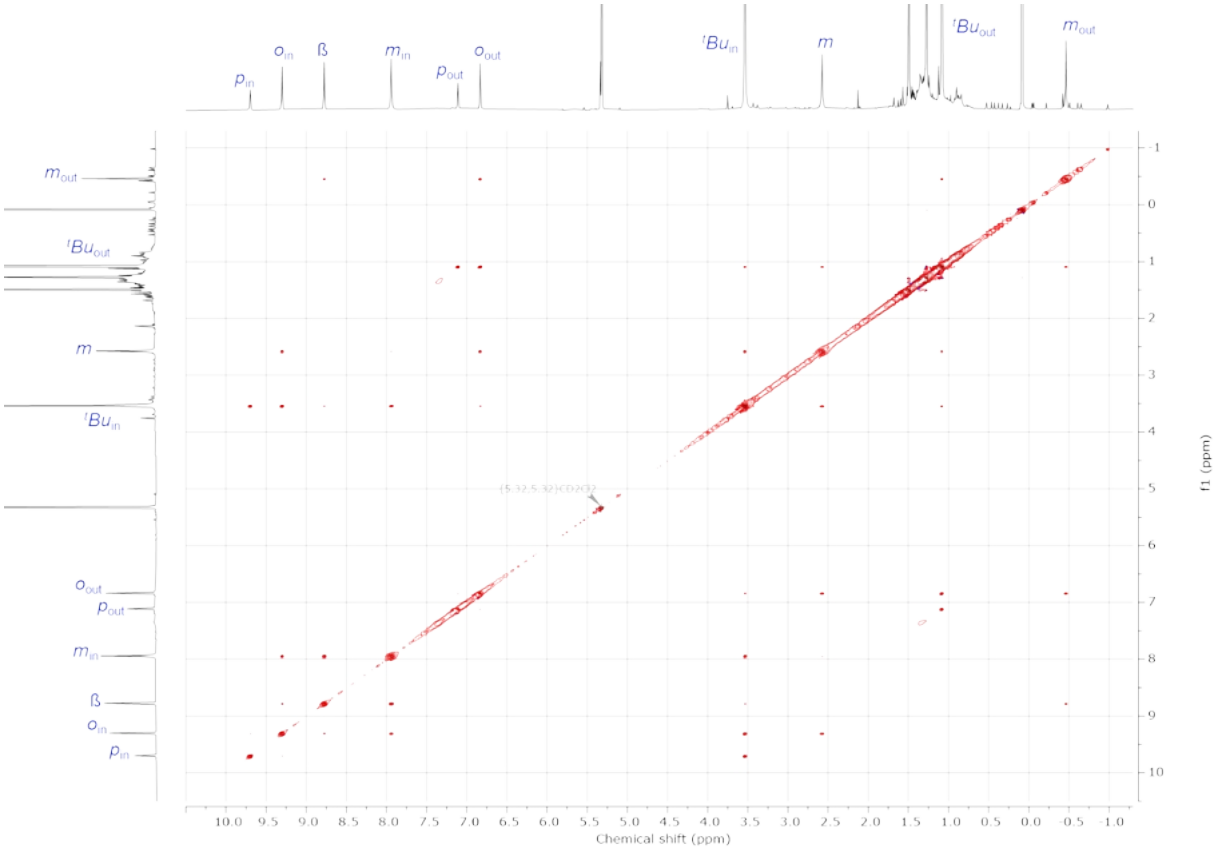

Figure S89. NOESY (400 MHz, CD_2Cl_2, 298 K, mixing time = 0.2 s) spectrum of ***cf*-P8$_{MesBu}$**.

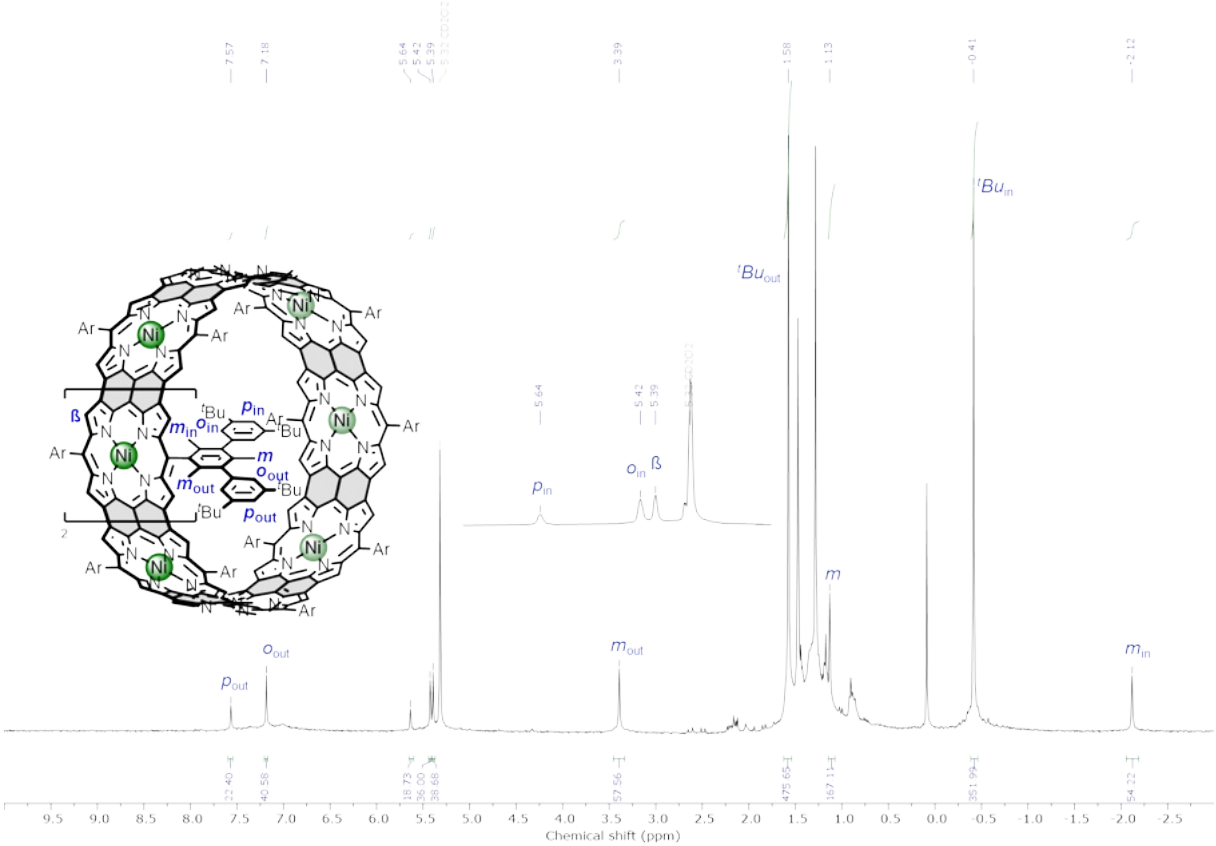

Figure S90. ^{1}H NMR (400 MHz) spectrum of ***cf*-P9$_{MesBu}$** (CD_2Cl_2, 298 K).

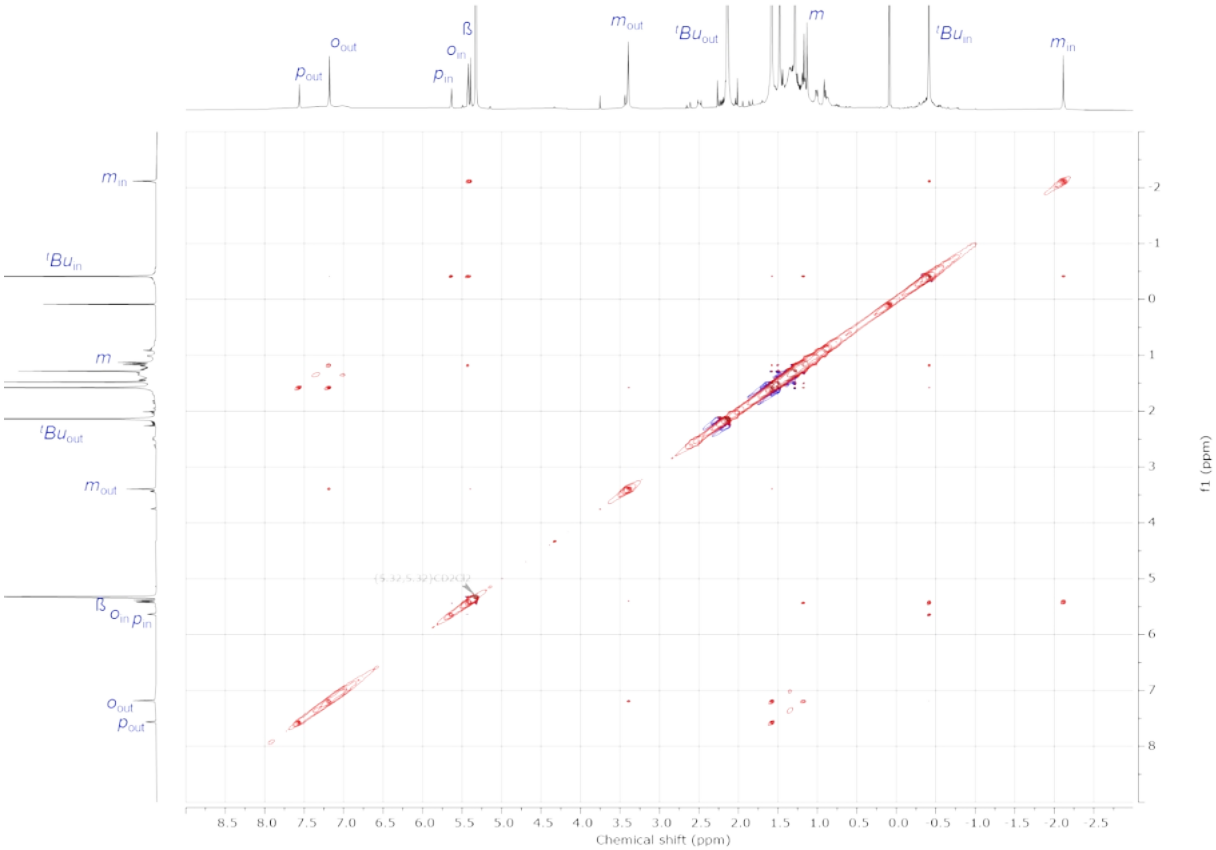

Figure S91. NOESY (500 MHz, CD_2Cl_2, 298 K, mixing time = 0.13 s) spectrum of ***cf*-P9$_{MesBu}$**.

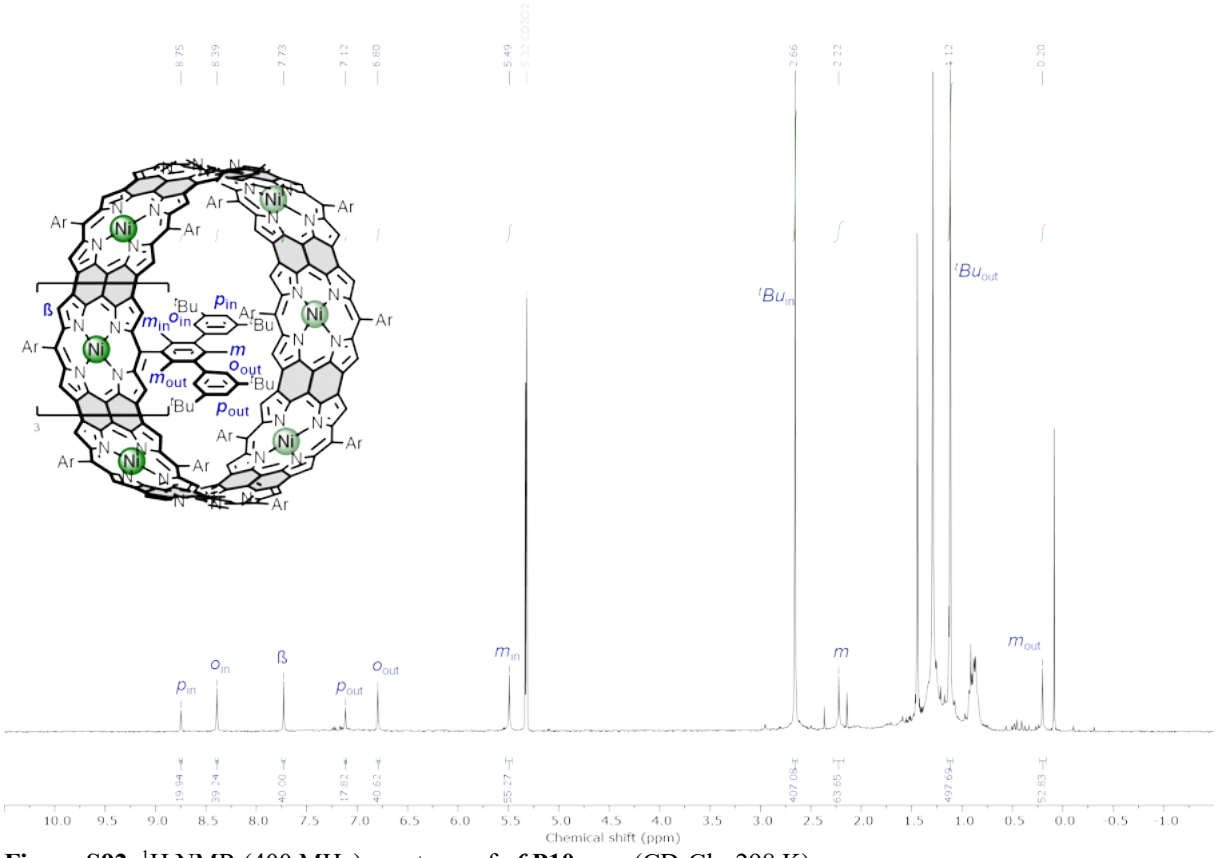

Figure S92. ^{1}H NMR (400 MHz) spectrum of ***cf*-P10$_{MesBu}$** (CD_2Cl_2, 298 K).

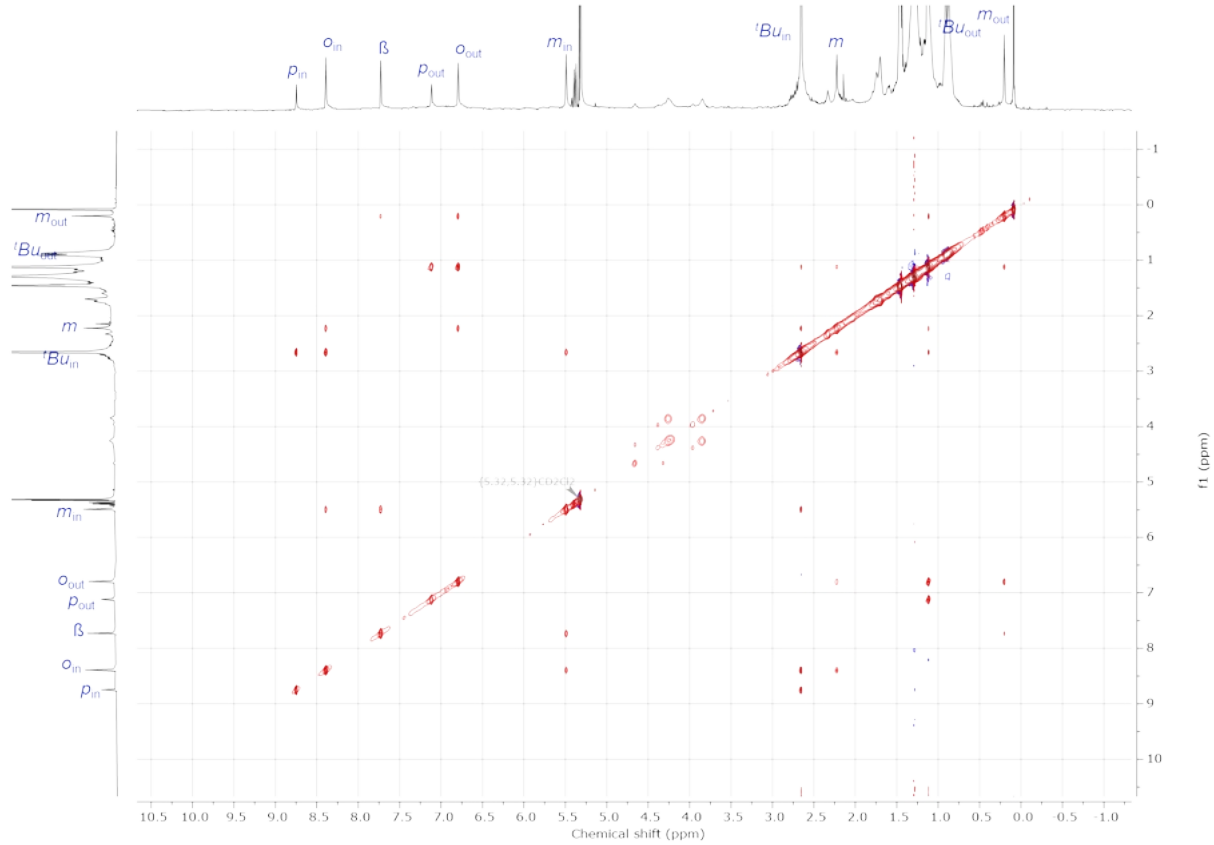

Figure S93. NOESY (500 MHz, CD_2Cl_2, 298 K, mixing time = 0.17 s) spectrum of ***cf*-P10$_{MesBu}$**.

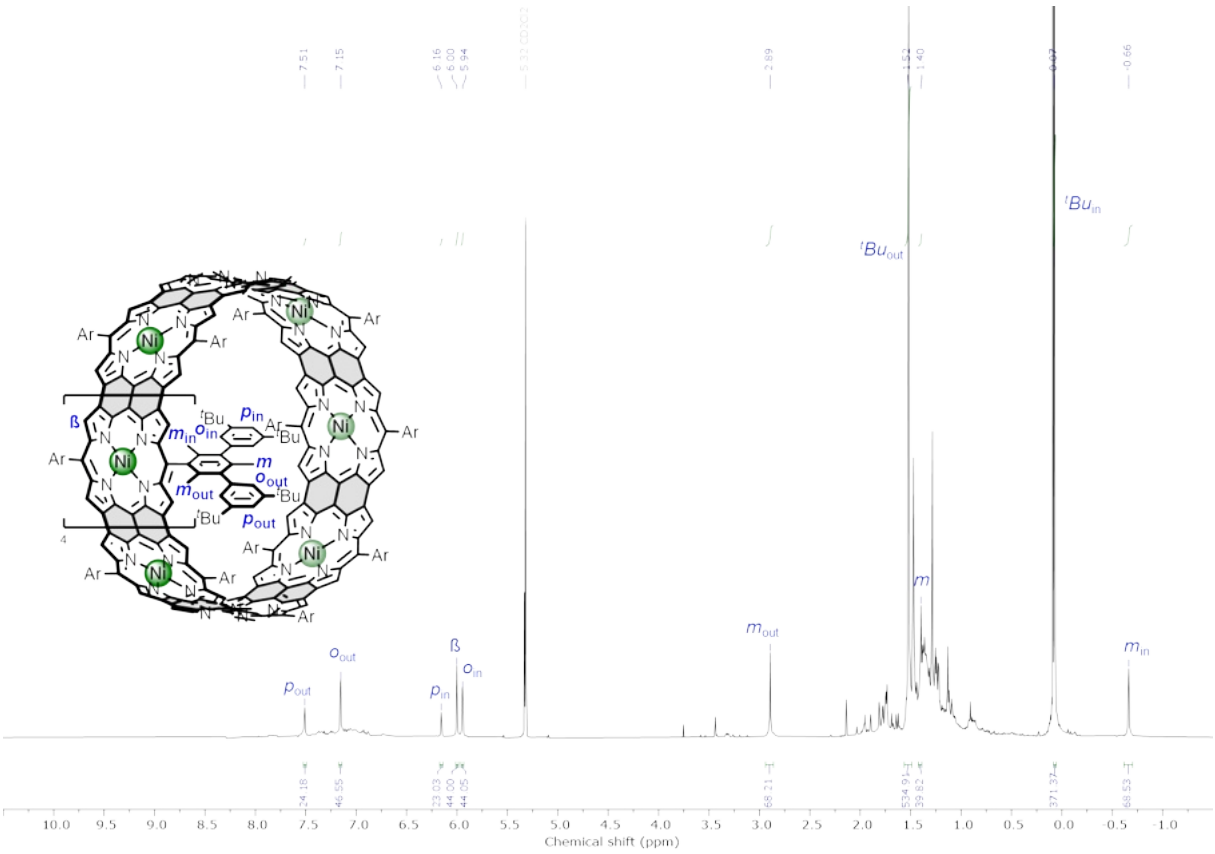

Figure S94. ^{1}H NMR (400 MHz) spectrum of ***cf*-P11$_{MesBu}$** (CD_2Cl_2, 298 K).

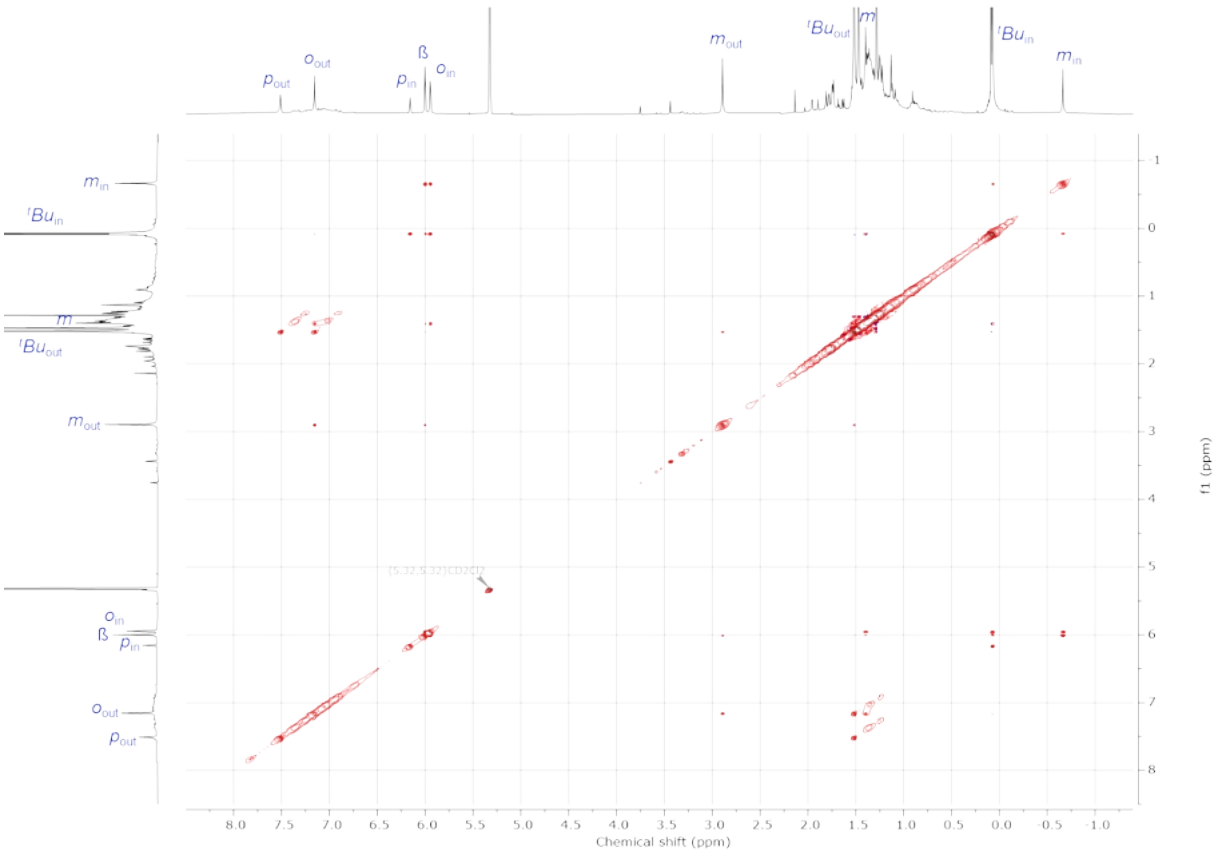

Figure S95. NOESY (500 MHz, CD_2Cl_2, 298 K, mixing time = 0.20 s) spectrum of ***cf*-P11$_{MesBu}$**.

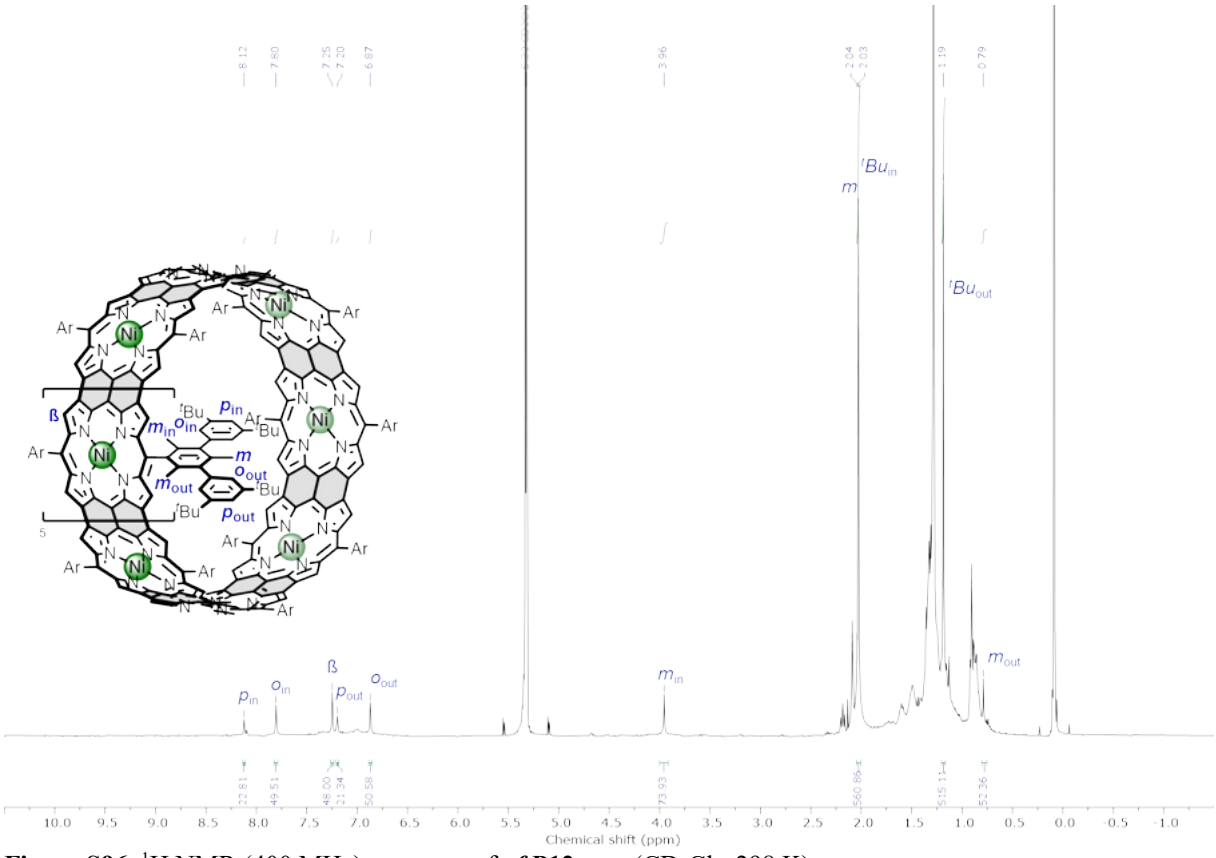

Figure S96. ^{1}H NMR (400 MHz) spectrum of ***cf*-P12$_{MesBu}$** (CD_2Cl_2, 298 K).

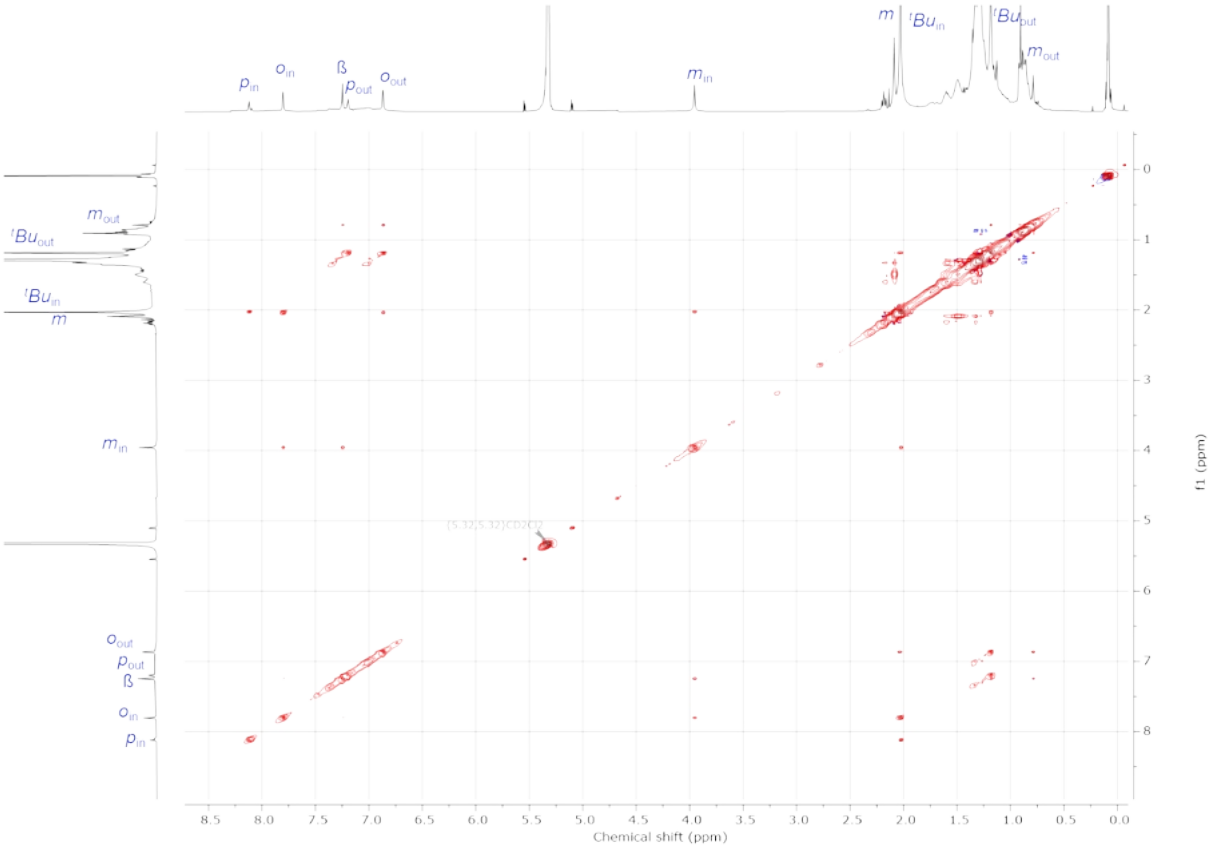

Figure S97. NOESY (400 MHz, CD_2Cl_2, 298 K, mixing time = 0.20 s) spectrum of ***cf*-P12$_{MesBu}$**.

Section 9. Absorption Spectra

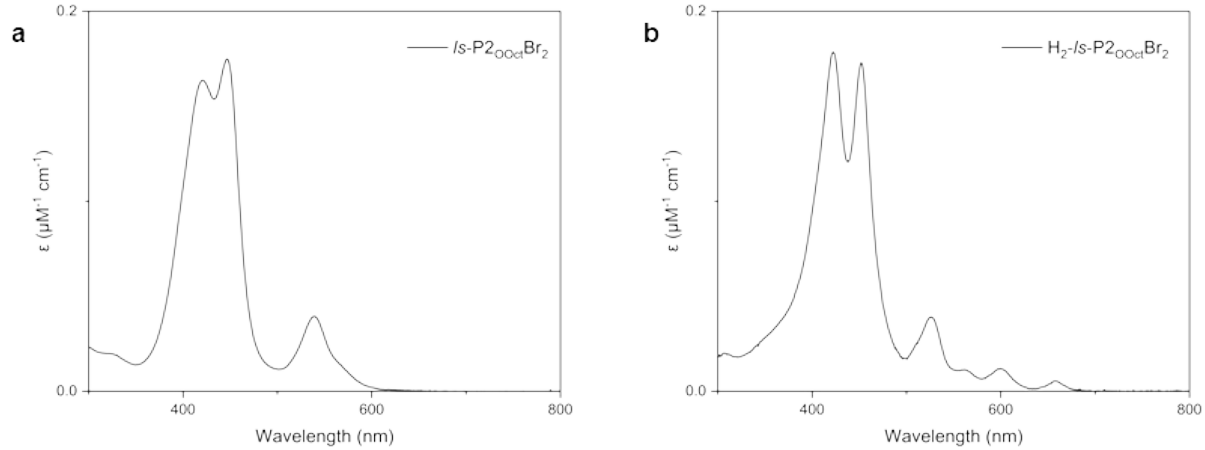

Figure S98. UV-vis absorption spectra of ***ls*-P2$_{OOct}$Br$_2$** (a) and **H$_2$-*ls*-P2$_{OOct}$Br$_2$** (b) in dichloromethane.

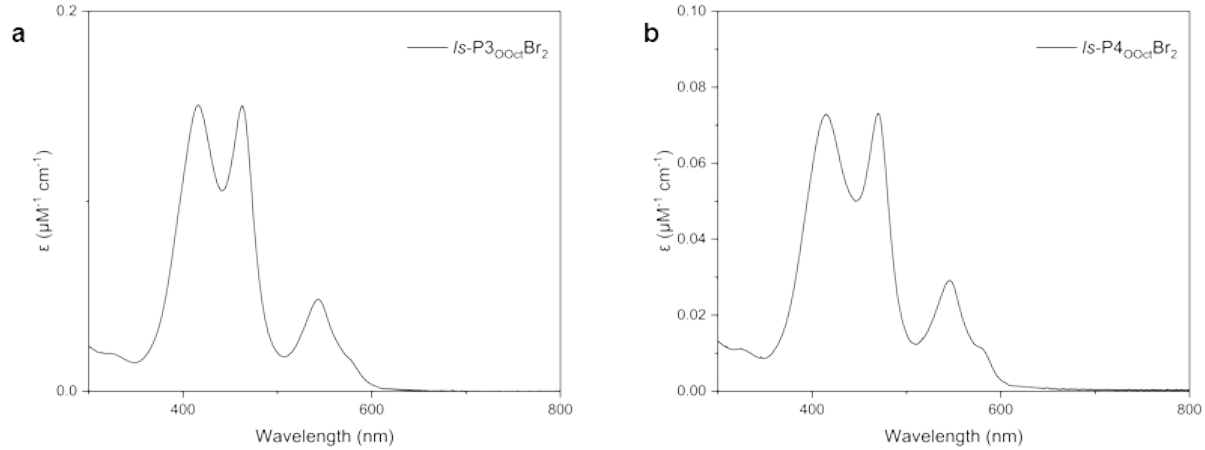

Figure S99. UV-vis absorption spectra of ***ls*-P3$_{OOct}$Br$_2$** (a) and ***ls*-P4$_{OOct}$Br$_2$** (b) in dichloromethane.

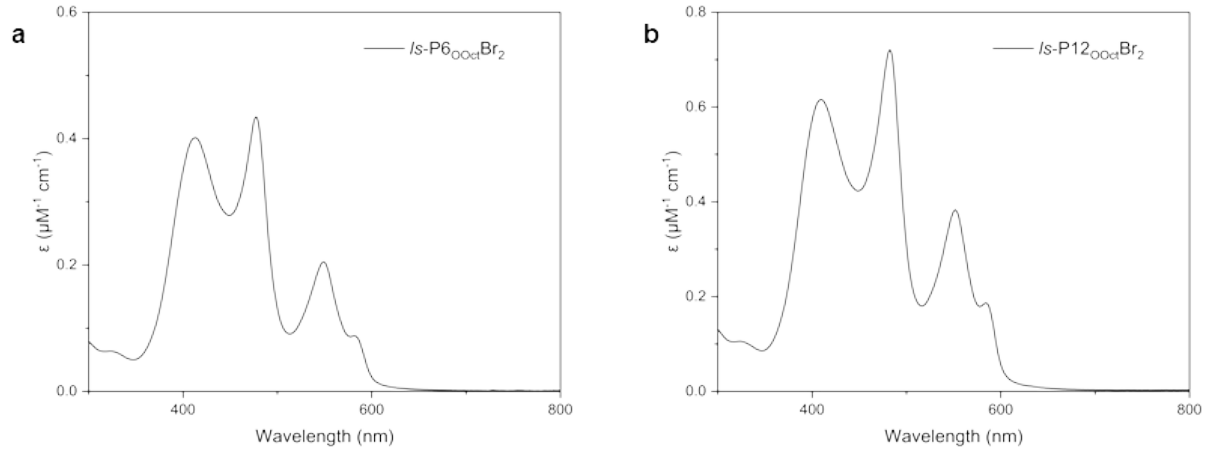

Figure S100. UV-vis absorption spectra of ***ls*-P6$_{OOct}$Br$_2$** (a) and ***ls*-P12$_{OOct}$Br$_2$** (b) in dichloromethane.

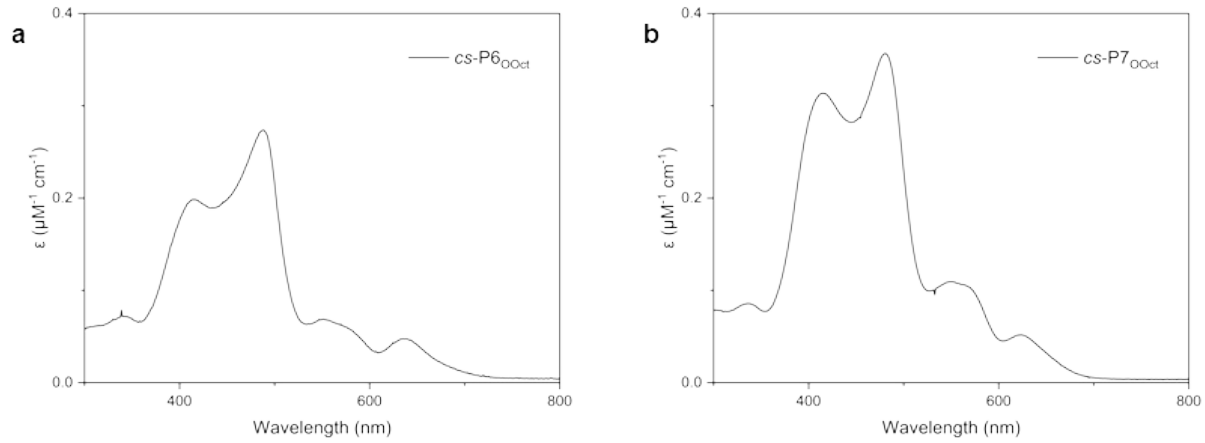

Figure S101. UV-vis absorption spectra of ***cs*-P6$_{OOct}$** (a) and ***cs*-P7$_{OOct}$** (b) in dichloromethane.

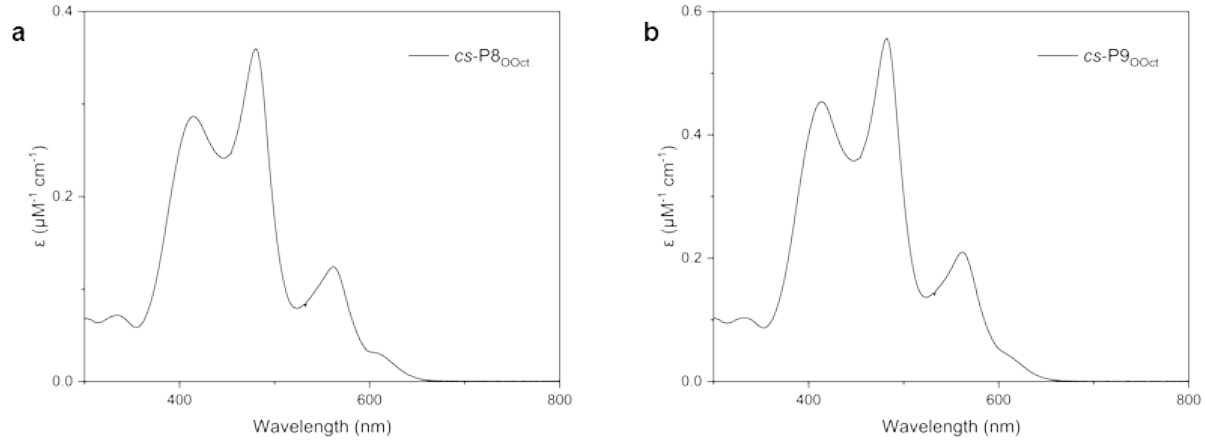

Figure S102. UV-vis absorption spectra of ***cs*-P8$_{OOct}$** (a) and ***cs*-P9$_{OOct}$**(b) in dichloromethane.

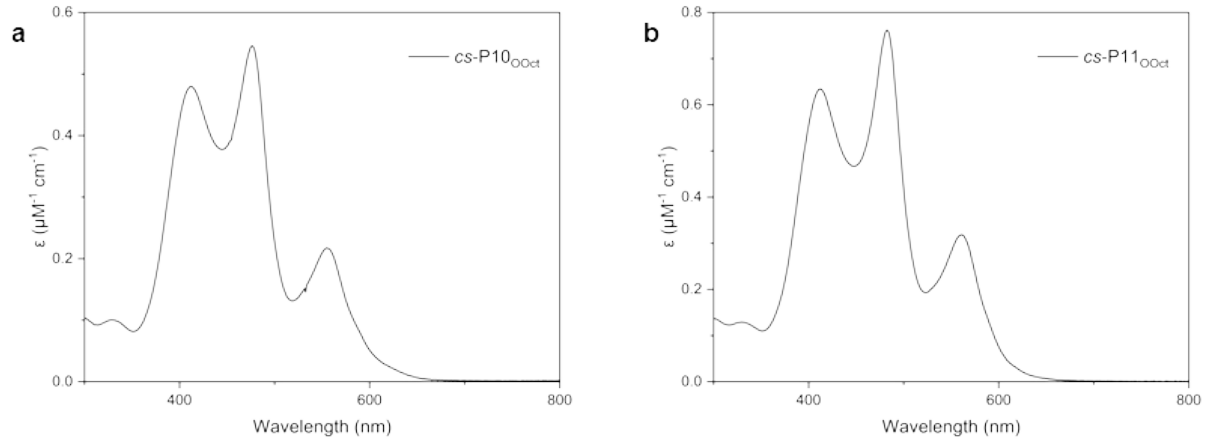

Figure S103. UV-vis absorption spectra of ***cs*-P10$_{OOct}$** (a) and ***cs*-P11$_{OOct}$** (b) in dichloromethane.

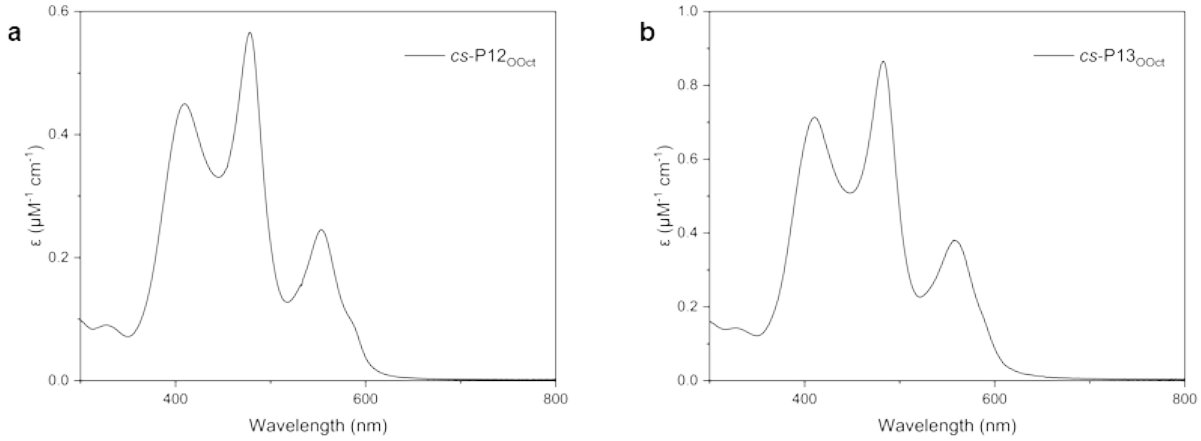

Figure S104. UV-vis absorption spectra of ***cs*-P12$_{OOct}$** (a) and ***cs*-P13$_{OOct}$** (b) in dichloromethane.

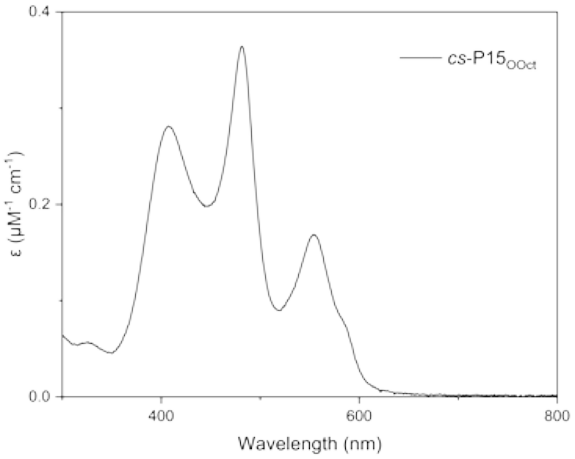

Figure S105. UV-vis absorption spectra of ***cs*-P15$_{OOct}$** in dichloromethane.

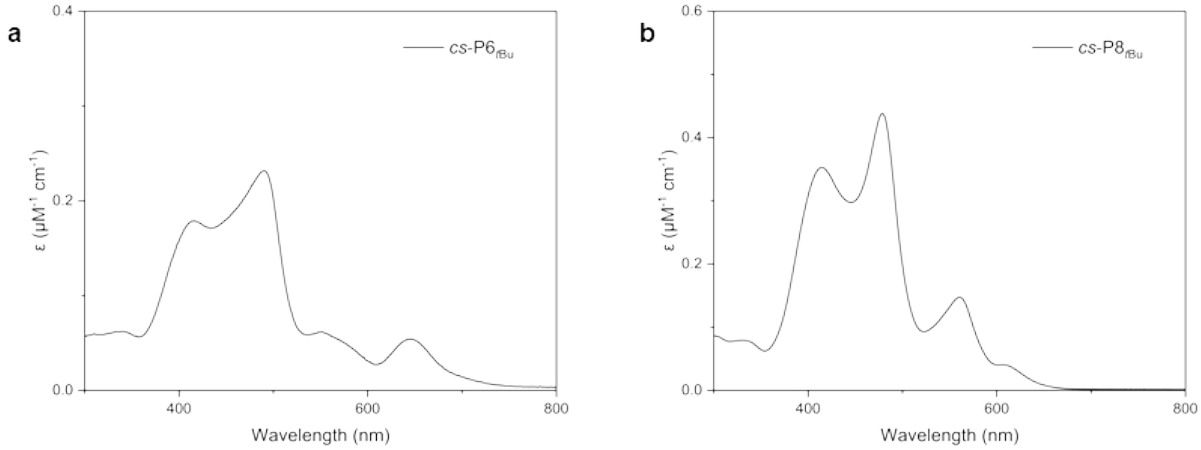

Figure S106. UV-vis absorption spectra of ***cs*-P6$_{tBu}$** (a) and ***cs*-P8$_{tBu}$** (b) in dichloromethane.

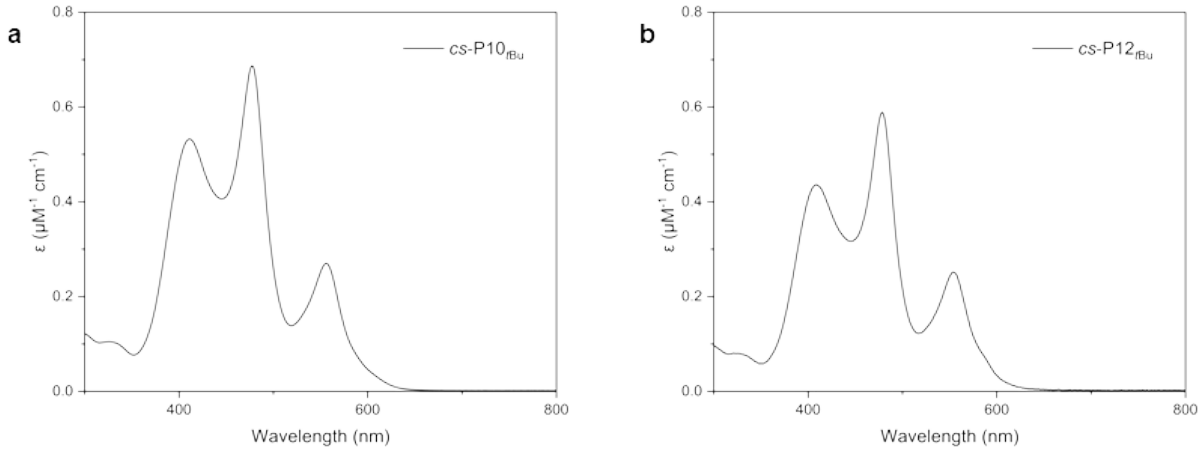

Figure S107. UV-vis absorption spectra of ***cs*-P10$_{tBu}$** (a) and ***cs*-P12$_{tBu}$** (b) in dichloromethane.

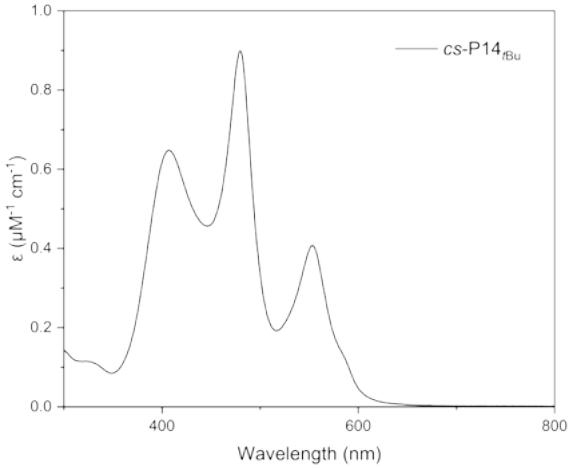

Figure S108. UV-vis absorption spectra of ***cs*-P14$_{tBu}$** in dichloromethane.

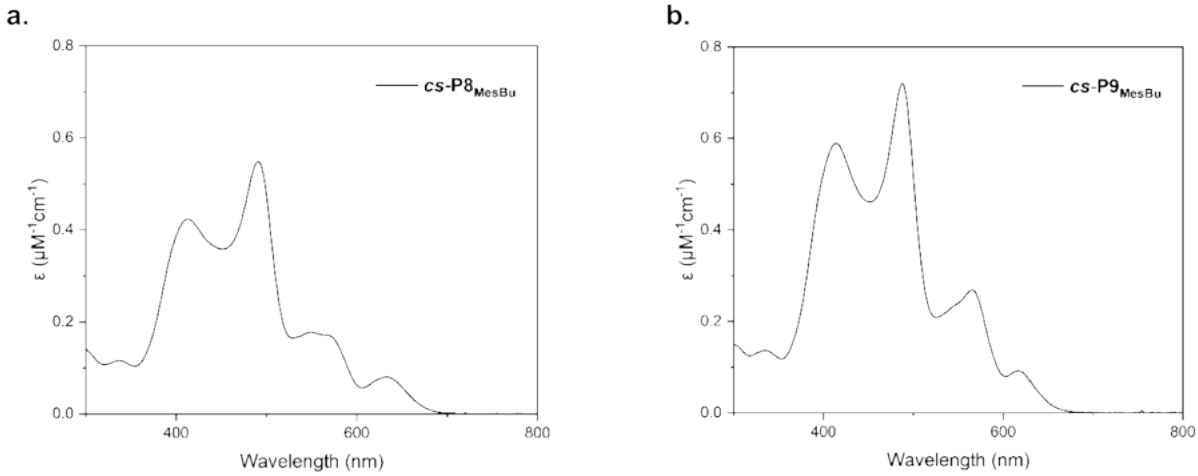

Figure S109. UV-vis absorption spectra of ***cs*-P8$_{MesBu}$** (a) and ***cs*-P9$_{MesBu}$** (b) in dichloromethane.

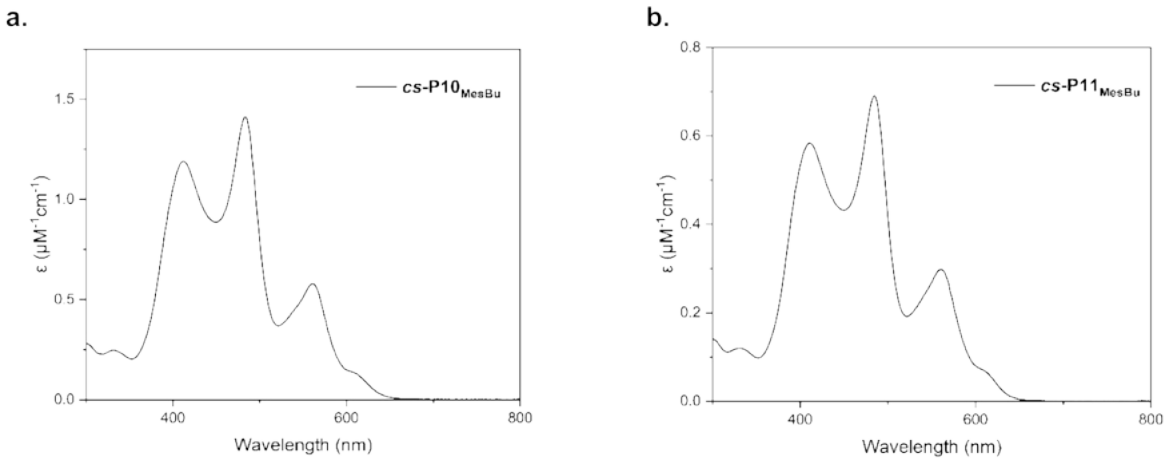

Figure S110. UV-vis absorption spectra of ***cs*-P10$_{MesBu}$** (a) and ***cs*-P11$_{MesBu}$** (b) in dichloromethane.

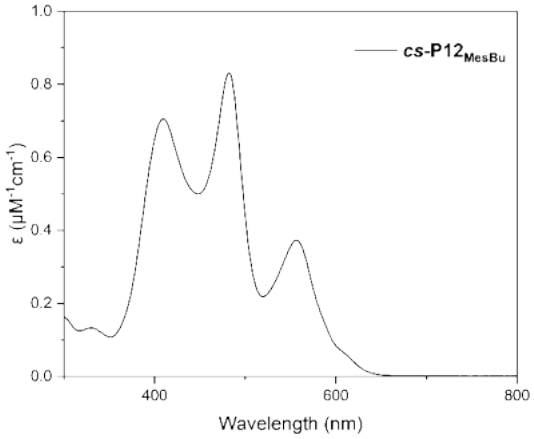

Figure S111. UV-vis absorption spectrum of ***cs*-P12$_{MesBu}$** in dichloromethane.

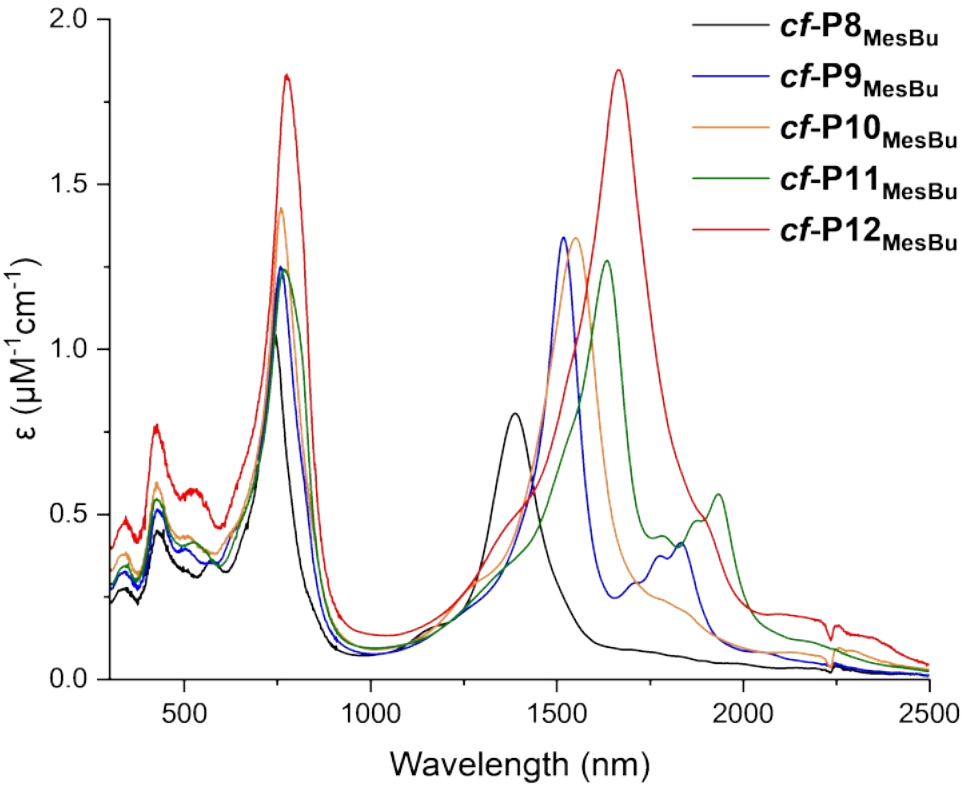

Figure S112. UV-vis-NIR absorption spectra of five belts in toluene-d_8.

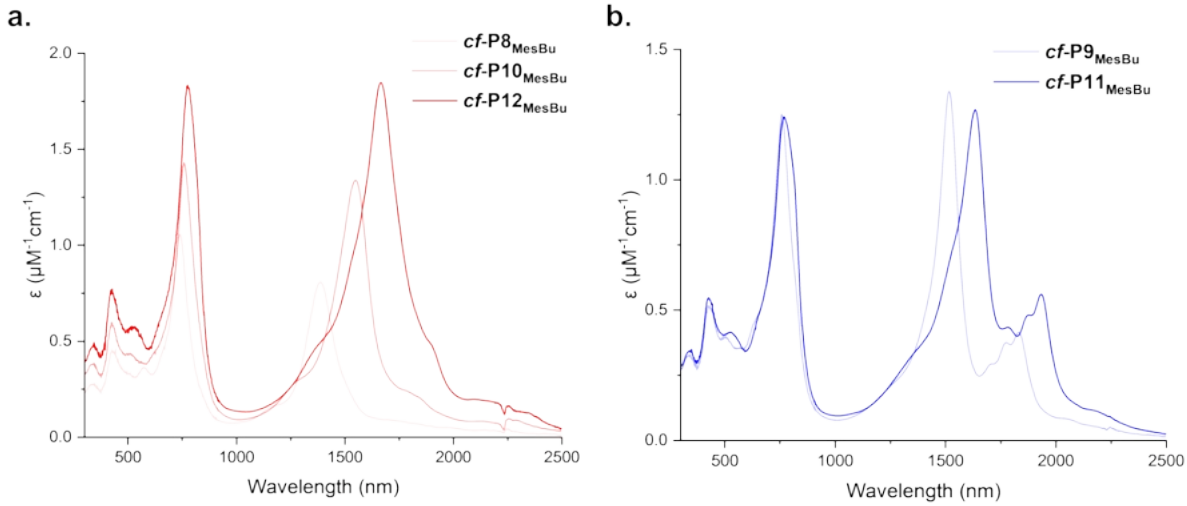

Figure S113. UV-vis-NIR absorption spectra of even-numbered belts (a) and odd-numbered belts (b) in toluene-d_8.

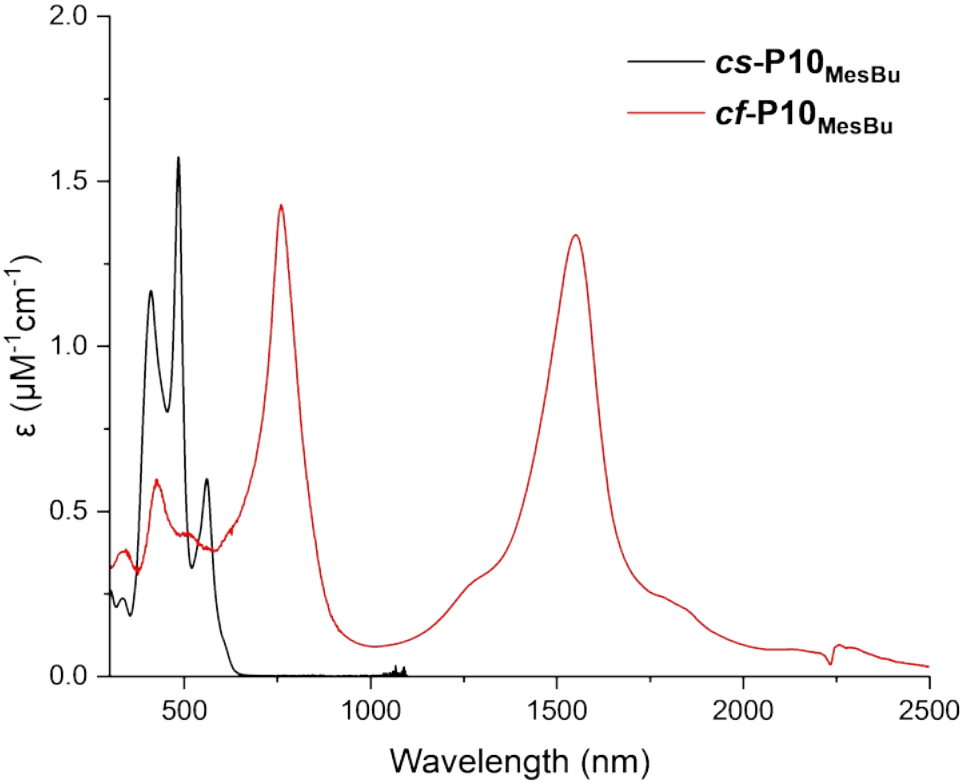

Figure S114. UV-vis-NIR absorption spectra of ***cf*-P10$_{MesBu}$** and ***cs*-P10$_{MesBu}$** in toluene-d_8.

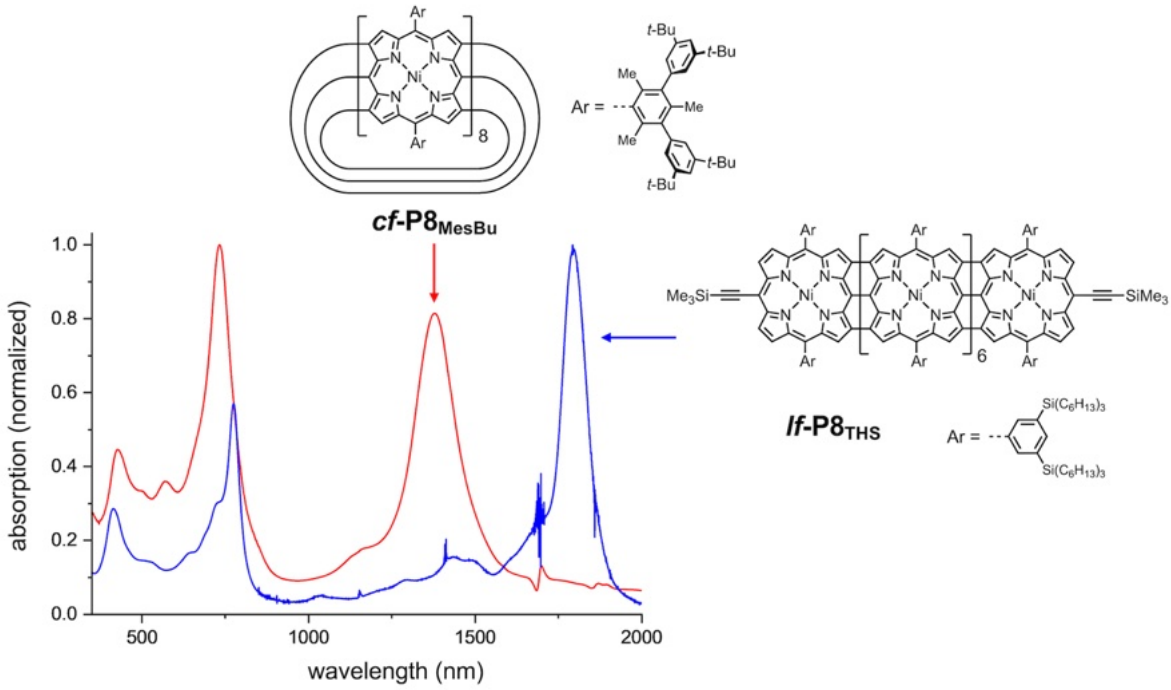

Figure S115. Comparison of the UV-vis-NIR absorption spectra of ***cf*-P8$_{MesBu}$** and ***lf*-P8$_{THS}$** in chloroform at 298 K. The spectrum of ***lf*-P8$_{THS}$** was reported in ref. (*30*).

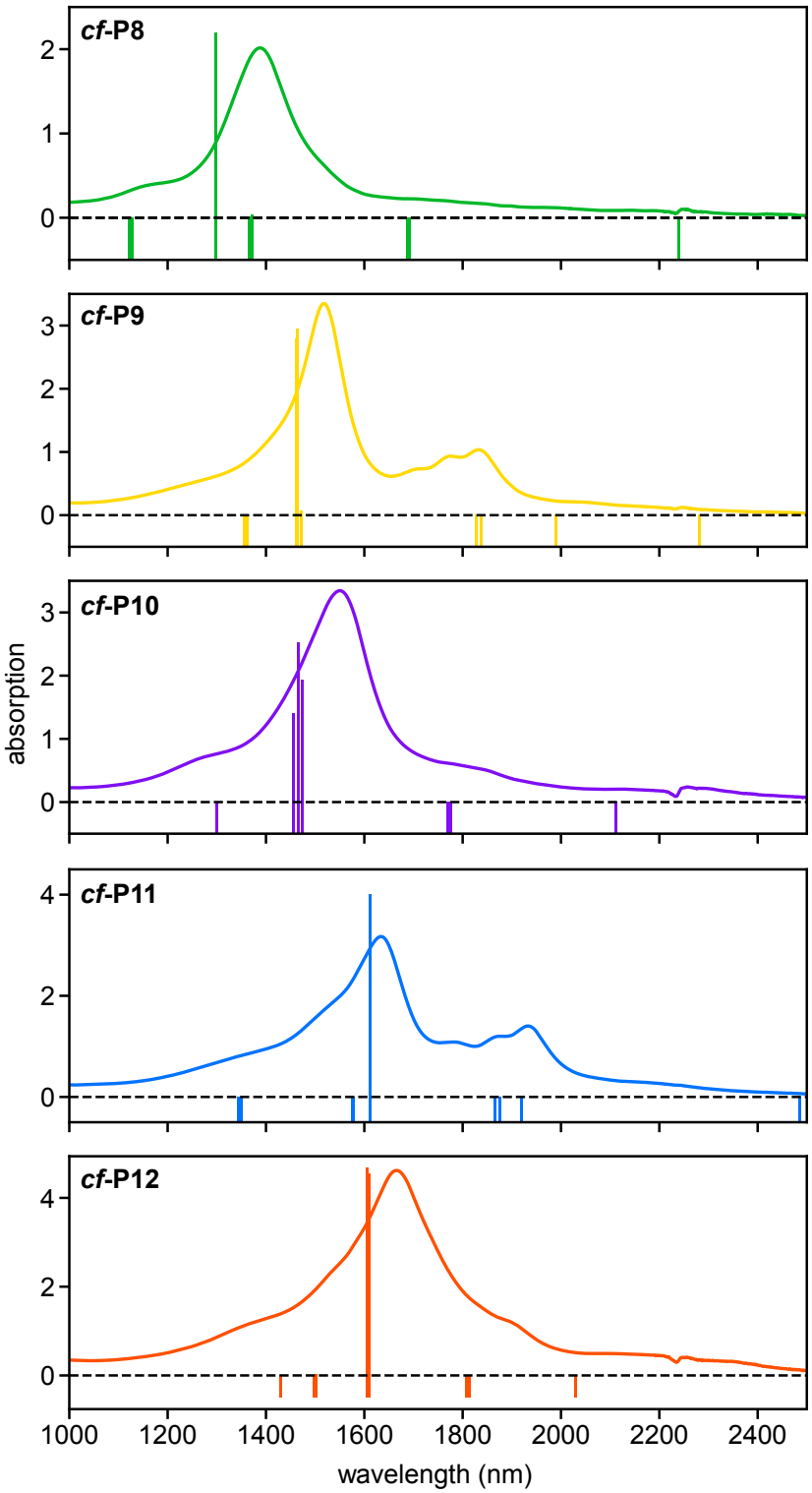

Figure S116. Experimental (curves, in toluene-d_8) vs. calculated (lines) absorption spectra of ***cf*-P8** (green), ***cf*-P9** (yellow), ***cf*-P10** (purple), ***cf*-P11** (blue), ***cf*-P12** (orange). Calculated oscillator strengths were obtained using TD-DFT with OX-B3LYP/def2-SVP (10 roots) and the polarizable continuum model with toluene as the solvent, at geometries with a single side-chain (to reduce the symmetry). The positive *y*-axis shows oscillator strength; the negative *y*-axis shows the computed energy spectrum. These results suggest that UV-vis-NIR signals at wavelengths longer than ~1800 nm originate from vibronic effects, which are not accounted for in these calculations due to the large size of the belts. The absence of shoulders at 1800–2000 nm in even-numbered belts relative to their odd-numbered counterparts may result from their (approximate) inversion symmetry, which imposes a parity constraint (Laporte's rule) on their allowed electronic transitions. This constraint is absent in odd-numbered belts, which lack inversion symmetry.